Experimental investigation and modelling of consolidation and layering mechanisms in high-shear granulation

The University of Sheffield

Faculty of Engineering

Department of Chemical and Biological Engineering

By

Stefan Aarnout Leonardus de Koster

Supervisors: Rachel Smith, Mike Hounslow, Jonathan Howse

A thesis submitted in partial fulfilment of the requirement for the degree of Doctor of Philosophy

Submission Date:

April 2018

Abstract

High-shear wet granulation is a particle size enlargement process widely used in industries such as the pharmaceutical, food and agricultural industries. Despite its predominance, knowledge on several of the key mechanisms of granulation is lacking, driving up the costs of the design of new processes, scale-up and control. For the rate mechanism of consolidation and layered growth, models can be found in literature, one of which has been validated for the case of growth in a static powder bed. However, these models remain to be experimentally validated for application in an actual granulator. This study is the first to develop a method to investigate consolidation and layered growth under such dynamic conditions, and presents a detailed investigation of the kinetics, as well as a model to describe them.

Initially, a high-shear mixer with three-bladed impeller was used for the method development of the study of the kinetics of consolidation and layered growth. However, experiments quickly showed that a dedicated piece of equipment was needed in order to isolate consolidation and growth from the other granulation phenomena, breakage in particular. Therefore, a novel, consolidation-only granulator (COG) was designed. Using the COG, the growth kinetics of a variety of powder-binder systems was evaluated. The granule mass was found to increase linearly with the square root of time, until a critical-packing liquid volume fraction had been achieved. This behaviour corresponds with surface tension-driven growth models. However, breakage and attrition were found to be prevalent for long granulation times, making it impossible to determine both the critical-packing liquid volume fraction and the final granulation time. Additionally, an unexpected rapid increase in initial granule mass was observed. Remarkably, the overall granule porosity was found to be constant. Tomography revealed that the granules developed a core-shell structure, with the higher-density shell becoming increasingly thick during granulation and the core becoming less dense.

A further study using a high-shear mixer with flat plate impeller was successfully performed to determine the critical-packing liquid volume fraction and final granulation time. Although the qualitative kinetic behaviour was found to match that predicted by the surface tension-driven growth model, the quantitative behaviour varied. Efforts to incorporate the observed core-shell structure into the existing model revealed that such an extension did not represent the observed behaviour. As such, no predictive expression was found for the critical-packing liquid volume fraction and final granulation time. However, these parameters can be obtained from experimental work. Finally, the initial rapid increase in granule was addressed, and it was deemed probable that this effect would not have a significant impact on in-situ nucleation in a granulator.

Finally, the results from all the studies were combined to adjust the existing model and convert it into two different population balance models (PBMs). The first, a three-dimensional PBM, was simply proposed. The second, a one-dimensional PBM, was solved by discretisation and compared to the experimental results to evaluate its performance. It was found that the discretisation method showed some deviation from the experimental results, but that this error could be reduced by decreasing the bin width.

This work has successfully identified the underlying kinetics of layered growth, elucidated the consolidation and growth behaviour of granules, and contributed to the modelling and design of granulation processes.

Acknowledgements

I would like to thank both my supervisor, Dr. Rachel Smith, for all her guidance, support and advice during my research project, and Professor Jim Litster for his valuable opinions on various parts of my project. I would also like to express gratitude to my co-supervisor, Professor Mike Hounslow, who taught me how to use Mathematica, as well as to my second supervisor, Dr. Jonathan Howse, for his advice on my doctoral development program. Many thanks go to Dr. Lian Liu for kindly allowing me to include her experimental data in my breakage studies. My thanks are also extended to include Dr. Kate Pitt, whose feedback on my writing has been invaluable, and Dr. Omid Tash, who put me on the right track for extending Hounslow et al.'s model for surface tension-driven growth.

Of course, my thanks also go to the all the wonderful members of the Particle Technology Group. Thank you all for your feedback, for providing a great working environment, for all your support, and for the wonderful activities you helped me organise. Special thanks go to Joshua Green and Stefan Bellinghausen for giving me feedback on my thesis and helping out with modelling. I could not have finished my PhD as I did without all of you people.

I would also like to thank the excellent technical staff at the University of Sheffield who helped me design my consolidation-only granulator. I would like to call out Andy Patrick, Mario Dorna and Sam Cripps in particular. My thanks are also extended to the wise men of the electronics workshop department: Oz McFarlane, Mark Jones, Usman Younis.

Finally, I would like to express thanks to my family and my best friend, Koen ter Horst, for their unwavering support during my studies.

Table of Contents

List of Figures

List of Tables

Nomenclature

Uppercase symbols

Symbol	Definition	Quantity
$\dot{A}$	Area that passes through the spray zone per time unit	area/time
AR	Particle shape factor	-
B	Birth rate	$(length*time)^{-1}$
$\underline{B}$	Birth vector	volume/time
B_0	Nucleation rate per volume	$(volume*time)^{-1}$
B_{lbr}	Critical interparticle space	-
B_v	Interparticle space of the granule	-
B_v''	Interparticle space between particles	-
B_{v0}	Interparticle space at granule formation	-
B_{va}	Interparticle space without reconfiguration	-
B_{va}^{*}	Interparticle space with reconfiguration	-
$C_{1,i}$	Constant for linear approximation of n	$length^{-2}$
$C_{2,i}$	Constant for linear approximation of n	$length^{-1}$
Ca	Capillary number	-
D	Death rate	$(length*time)^{-1}$
$\underline{D}$	Death vector	volume/time
D	Diameter	length
$\tilde{D}$	Reduced radius	length
D_{eff}	Effective diffusivity	area/time
De	Deformation number	-
Fr	Froude number	-
G	Growth rate	length/time
G_i	Granule growth rate in bin i	length/time
J, J_L	Liquid flux	length/time
L	Particle/granule size	length
L_i	Granule size at bin i	length
$L_{p,i}$	Representative granule size in bin i	length
N	Number of drum rotations	-
N	Number of intact granules	-
N	Total number of particles	-
N	Total number of particles per volume	$volume^{-1}$
N_0	Initial number of intact granules	-
N_i	Total number of particles in bin i	-
N_i	Total number of particles per volume in bin i	$volume^{-1}$
R	Pore radius	length
R	Radius of the granulator	length
S	Liquid saturation	-
S	Probability of particle breakage	-
S_i	Breakage selection rate constant for bin i	$time^{-1}$
St_{def}	Stokes deformation number	-
Str^{*}	Dimensionless peak flow stress	-
St_v	Viscous Stokes number	-
St_v^{*}	Critical Stokes number	-
$St_{v,max}$	Maximum Stokes viscous number	-

Symbol	Definition	Quantity
U_c	Representative collision velocity	Velocity
$\dot{V}$	Volumetric binder flow rate	volume/time
V_d	Droplet volume	volume
V_l	Liquid volume	volume
V_s	Solid volume	volume
W^*	Cut-off size	length
$W_{m,kin}$	Kinetic energy of the particle	energy
$W_{m,min}$	Minimum kinetic energy required for breakage	energy
Y_g	Dynamic yield stress	pressure

Lowercase symbols

Symbol	Definition	Quantity
a	Lumped growth parameter	time$^{1/2}$
a	Lumped particle breakage parameter	-
a	Volume of air of a single granule	volume
a_d	Dynamic lumped growth parameter	time$^{1/2}$
a_s	Static lumped growth parameter	time$^{1/2}$
b	High-liquid fraction core size	length
$\hbar$	Dimensionless core size	-
$b_{i,j}$	Number of granules from bin j assigned to bin i	-
d	Mean primary particle size	length
d_{10}	10th volume percentile size	length
$d_{3,2}$	Surface area mean diameter	length
$d_{4,3}$	Volume moment mean diameter	length
d_{50}	50th volume percentile size	length
d_{90}	90th volume percentile size	length
d_d	Droplet diameter	length
e	Coefficient of restitution	-
f	Frequency of rotation	time^{-1}
f	Impeller shape factor	-
f_{Mat}	Material parameter defining fracture behaviour	(length*energy)$^{-1}$
f_N	Nuclei size distribution	-
g	Acceleration due to gravity	length/time^2
h	Liquid layer thickness	length
h	Total granule size	length
$\hbar$	Dimensionless total granule size	-
h_0	Initial droplet diameter	length
h_1	Static-growth maximum granule size	length
$\hbar_1$	Dimensionless static-growth maximum granule size	-
h_2	Impact-driven maximum granule size	length
$\hbar_2$	Dimensionless impact-driven maximum granule size	-
h_a	Distance between two granules	length
h_{max}	The maximum attainable granule size	length
i	Index of the bin under investigation	-
j	Index of bin compared to bin i	-
k	Consolidation rate constant	-
k	Impact number	-

Symbol	Definition	Quantity
k_c	Compaction rate constant	time^{-1}
l	Volume of liquid of a single granule	volume
$\tilde{m}$	Reduced granule mass	mass
m_0	Initial granule mass	mass
$m_{0,extrapolated}$	Extrapolated initial granule mass	mass
n	Number density function	volume^{-1}
n	Number of impacts	-
n_i	Number density function in bin i	volume^{-1}
p	Pressure	pressure
q	Constant liquid flux	volume/time
q	Final bin size	-
$\underline{q}$	Volume vector	volume
r	Growth rate	length/time$^{1/2}$
r	Radius	length
r	Ratio between breakage zone and total area	-
r	Size ratio between bin $i+1$ and bin i	-
r_0	Initial radius of the granule	length
$r_{0,obs}$	Extrapolated initial radius of the granule	length
s	Position	length
s	Probability of granule breakage	-
s	Volume of solid of a single granule	volume
s_{max}	Maximum pore saturation	-
t	time	time
t'	Wetting time	time
$\hat{t}$	Dimensionless time	-
t''	Densification time	time
t_1	Static-growth t_{max}	time
t_2	Impact-driven t_{max}	time
t_c	Circulation time	time
t_{max}	Time until the granule has reached critical packing	time
$\hat{t}_{max}$	Dimensionless t_{max}	-
$t_{max,d}$	Observed t_{max} for dynamic experiments	time
$t_{max,s}$	Observed t_{max} for static experiments	time
$t_{max,theory}$	Calculated t_{max} for experiments	time
$t_{max,theory,d}$	Calculated t_{max} for dynamic experiments	time
$t_{max,theory,s}$	Calculated t_{max} for static experiments	time
t_{max}^{app}	Apparent t_{max}	time
t_p	Droplet penetration time	time
t_{real}	Actual granulation time	time
u_0	Granule velocity	velocity
$<v>$	Average velocity	velocity
v	Velocity	velocity
v	Granule volume	volume
v_0	Initial droplet volume	volume
v_0^{app}	Apparent initial liquid volume v_0	volume
v_1	Static-growth granule volume	volume
v_2	Impact-driven granule volume	volume
v_A	Granule air volume	volume
v_c	Granule impact velocity	velocity

Symbol	Definition	Quantity
v_{crit}	Critical solid volume	volume
v_i	Granule volume of bin i	volume
v_L	Granule liquid volume	volume
v_{max}	Maximum granule volume	volume
v_p	Relative granule velocity	velocity
v_S	Granule solid volume	volume
v_{S+L}	Total granule volume excluding air	volume
v_T	Total granule volume	volume
w	Liquid to solid mass ratio	-
x	Height coordinate	length
x	Particle size	length
x_i	Representative granule volume of bin i	volume

Greek symbols

Symbol	Definition	Quantity
α_i	Constant to prevent a negative approximation of n	-
$\beta_{i,j}$	Coalescence kernel at bins i and j	time^{-1}
γ	Liquid surface tension	force/length
δ	Difference between total granule size and core size	length
$\hat{\delta}$	Dimensionless granule-core size difference	-
ε	Porosity	-
ε_0	Initial porosity	-
ε_b	Bed porosity	-
ε_{end}	Porosity observed for long granulation times	-
ε_{min}	Minimum porosity	-
ε_{start}	Porosity observed for short granulation times	-
θ	Contact angle	angle
μ	Dynamic liquid viscosity	pressure*time
ρ_g	Granule density	density
ρ_l	Liquid density	density
ρ_s	Solid density	density
σ_p	Dynamic yield stress	pressure
τ_p	Dimensionless penetration time	-
ϕ_1	Static-growth critical-packing liquid volume fraction	-
ϕ_2	Impact-driven critical-packing liquid volume fraction	-
ϕ_{cp}	Critical-packing liquid volume fraction	-
$\phi_{cp,d}$	Dynamic ϕ_{cp}	-
$\phi_{cp,s}$	Static ϕ_{cp}	-
Ψa	Dimensionless spray flux	-
ω	Agitation intensity rate constant	time^{-1}
ω	Angular velocity	time^{-1}

Abbreviations

Abbreviation	Definition
CFD	Computational fluid dynamics
CGB	Continuous growth behaviour
COG	Consolidation-only granulator
DEM	Discrete element method
DSMC	Direct simulation Monte Carlo
ECT	Electrical capacitance tomography
EKE	Equipartition of kinetic energy
ETM	Equipartition of fluctuating translational momentum
HPMC	Hydroxypropyl methylcellulose
KTGF	Kinetic theory of granular flow
LB	Lattice Boltzman
MC	Monte Carlo
MOM	Method of moments
PBM	Population balance model
PEG	Polyethylene glycol
PEPT	Positron emission particle tracking
PIV	Particle image velocimetry
PSD	Particle size distribution
QMOM	Quadrature method of moments
SGB	Step-wise growth behaviour
SWA	Stochastic weighted algorithm

Chapter 1.   Introduction

1.1 Research background

Granulation is the process of creating larger, more easily processable particles called *granules* by agglomeration of powders [1]. The process is widely applied in many areas, including pharmaceuticals, food and agriculture. However, despite its prevalence in industry and many excellent studies over the past 60 years [2], the complexity of granulation processes still poses many challenges. The fundamental mechanisms of granulation are not yet fully understood. Consequently, designing new formulations [2,3], or scaling up existing processes [4,5] require extensive investigation. This work focuses on contributing to our understanding of two of the key mechanisms of granulation: consolidation and layered growth.

This introductory chapter highlights the current state of the field of granulation and the gaps of knowledge this study aims to address. Additionally, a detailed list of the aims of this work is provided, and the outline of this thesis is presented.

1.1.1 Granulation in industry

There are many reasons why granulation is widely employed in industry. Granulation of powders reduces dust formation, improves handling, tabletability and product appearance. Additionally, material properties can be controlled with granulation [1,3,6]. Of particular interest to this work is the widely applied method of *high-shear wet granulation*, which employs heavy-duty mixers to agglomerate powders using a liquid binder [3].

Although wet granulation using mixers is a common size enlargement method in industry, it is one of the most complex processes to scale up and control [6]. Predicting the effects of changes in formulation, or designing a production process for a defined product requires extensive experimental investigation [2,3], and even the processes that operate well may suffer from large recycle ratios, material wastage, energy and money [2]. Although heuristics for scaling up processes exist [6-10], some rules of thumb are extremely contradictory. Even granules produced from 'proven' methods that yield similar granule size distributions may have different properties, or vice versa [11].

The situation is not hopeless, however. Over the past 60 years [2], knowledge of granulation has vastly improved. Research in the field became more systematic with the conceptualisation of three distinct rate processes or mechanisms for granulation: wetting and nucleation; consolidation and growth; and breakage and attrition [2], as shown in Figure 1.1. These rate process can often be further divided into distinct mechanisms. Growth, for example, occurs either via agglomeration of granules (coalescence) or powder uptake (layering).

Regime maps were developed to better describe wetting and nucleation [12], granule coalescence [13], and granule growth [14]. Investigations of granule breakage at the granule scale [15] and process scale [16,17] improved the knowledge on the mechanisms and granule properties that govern breakage. All these advances in the field of granulation have improved granulation process design, and cleared the way for the development of predictive models. However, there are still gaps in knowledge, particularly for breakage, attrition [15,16], consolidation [18] and layered growth [19].

1.   Wetting and nucleation

2.   Consolidation and growth

3.   Breakage and attrition
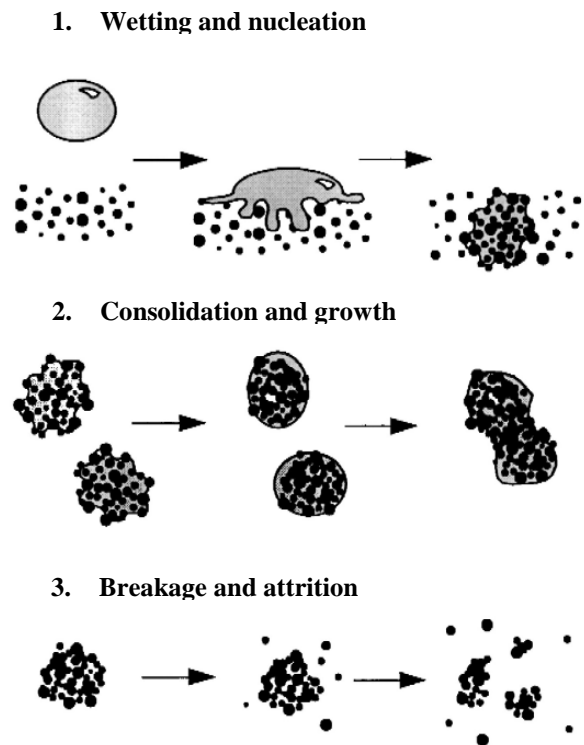
Figure 1.1: The three granulation mechanisms as presented by Iveson et al. [2]. Reproduced with permission from Elsevier.

1.1.2 The value of predictive models

Predictive models could greatly contribute to the reduction of the number of experiments needed to design processes for new products, as well as facilitate a more straightforward scale-up of existing processes. Additionally, the on-line monitoring and control of processes can be improved using simulations.

Attempts to simulate agglomeration processes have a long history in the literature [20-23]. Of particular interest are *population balance models* (PBMs), which track the frequency distributions of a property as a function of one or more other properties over time. For granulation, the number frequency distribution as a function of granule size is usually simulated [22], although more complex models also simulate frequency distributions as functions of properties like porosity and liquid content [24]. PBMs can be rather flexible, with different *kernels* representing the different rate processes, such as agglomeration, occurring during granulation.

Originally, models were mostly empirical, with parameters having to be fit to experimental data in order to obtain reasonable predictions [20-23]. However, a gradual shift towards more mechanistic models [25,26] and combinations with other physically relevant models such as the discrete element method (DEM) can be found in the literature [27-29]. By elucidating the various granulation mechanisms, it should eventually become possible to predict all granule properties, to select operating conditions to obtain a specific product, and to scale up granulation processes.

The study presented here aims to contribute to increasing the understanding of, and the development of a mechanistic PBM for two correlated rate phenomena in particular:

consolidation and layered growth. Hounslow et al. [30] proposed two different theoretical models to predict these two rate processes directly after nucleation. However these models were not validated until Pitt et al. [31] demonstrated that the model for surface tension-driven growth correctly predicted growth behaviour of nuclei in a static powder bed. However, so far, no studies have been performed to investigate the growth behaviour of granules in a dynamic situation.

1.2 Research objectives

The overall objective of this work was to provide a mechanistic model that describes the consolidation and layered growth mechanisms of high-shear wet granulation. In order to achieve this, a fundamental understanding of these phenomena was required. Therefore, it was necessary to develop an experimental method of investigating consolidation and layered growth by isolating them from the other granulation mechanisms. A method developed in this way is expected to be useful not only for the investigation of consolidation and layered growth in future studies, but also applicable to other mechanisms such as breakage and attrition. The layered growth kernel proposed in this study can be combined with other kernels to mechanistically simulate the phenomena occurring during granulation. The approach taken can be summarised into the following subgoals:

- To summarise the current state of the literature on granulation, granulation mechanisms and modelling of granulation to highlight the novelty and impact of this work.
- To develop an experimental method to isolate and study consolidation and layered growth.
- To use the developed experimental method to obtain kinetic consolidation and growth data for a variety of powder-binder systems:
  - To investigate the effect of particle size and shape
  - To investigate the effect of binder viscosity
  - To investigate the effect of binder drying
- To identify a model that describes the experimentally obtained kinetic consolidation and layered growth behaviour.
- To investigate the key parameters of the model and identify ways of either predicting these parameters or extracting them from experimental data.
- To convert and adapt the model into a mechanistic population balance model and evaluate its performance.

1.3 Thesis layout

This work explores several experimental methods, as well as population balance modelling methods. This thesis is structured to first provide an overview of the subject and the current state of the field of granulation. This information is then used to develop an experimental method, which is subsequently employed to collect experimental data. After the evaluation of the experimental data and comparison with the literature, a model is developed and evaluated using the data. Finally, all results are linked back to the objectives and

discussed. A graphic outline of this work is shown in Figure 1.2, and the chapter structure is presented as follows:
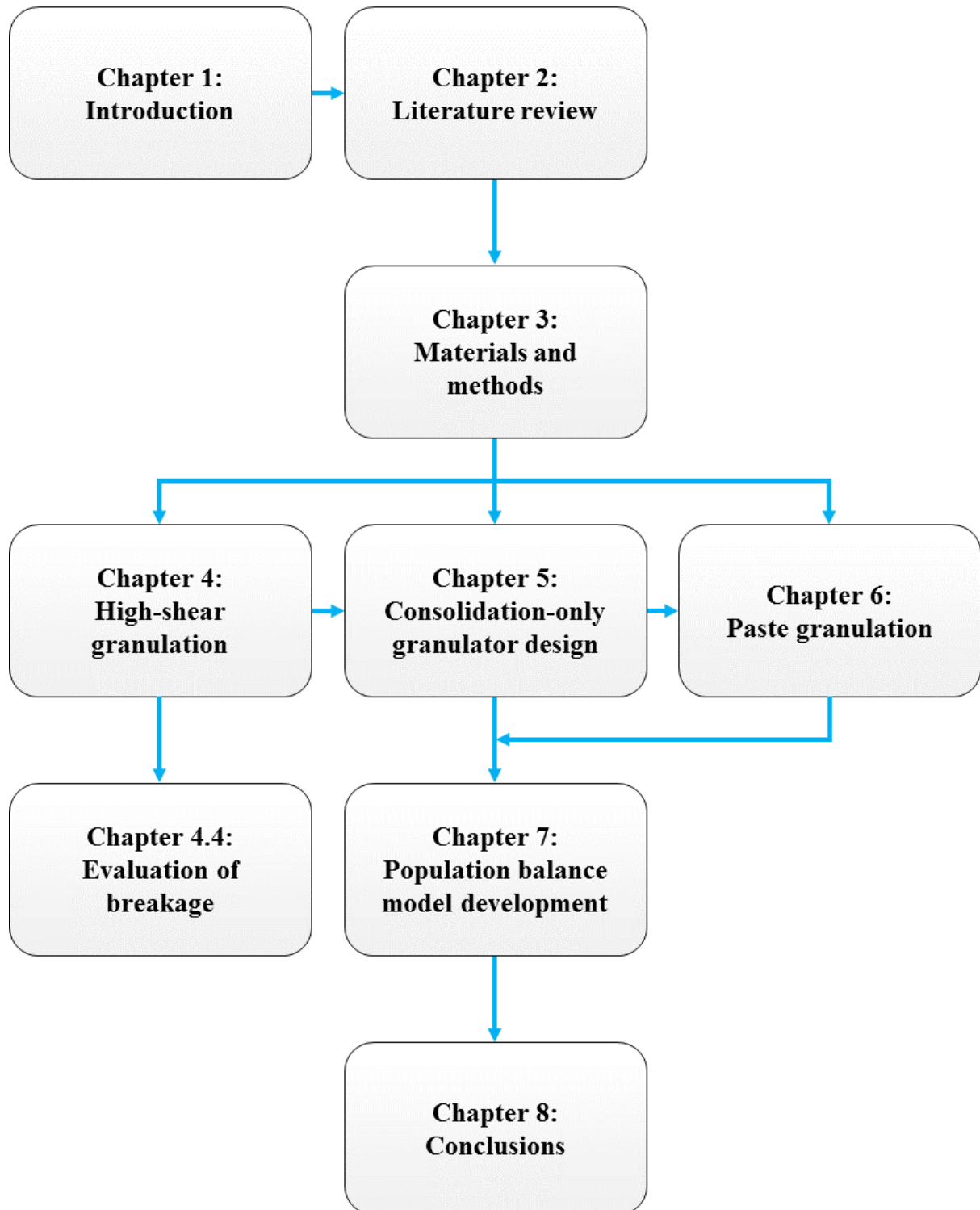
Figure 1.2: Graphic outline of this work showing the interdependency of the various chapters.

Chapter 2 presents the state of the literature. A brief overview of granulation equipment is given, and the current knowledge on the various granulation mechanisms is discussed. Additionally, the applications of population balance modelling in the field of granulation are discussed extensively. Finally, a brief overview of the issues with scale-up and control of granulation processes is presented.

Chapter 3 lists all materials and characterisation techniques used in this work. Additionally, the chapter provides a detailed overview of the various experimental methods employed throughout this study.

Chapter 4 details the experiments performed with a high-shear mixer, which laid the foundation for the design of novel consolidation-only granulator (COG). Additionally, the trends observed in the breakage behaviour are investigated.

Chapter 5 presents the design of the COG and describes the experiments performed with this novel granulator to obtain the kinetics of consolidation and layering for various powder-binder systems. The collected data is compared to models from the literature. The validity of the designed method is then discussed.

Chapter 6 addresses several of the deviations from the best model identified in the previous chapter. Experiments are performed using a high-shear mixer with a flat plate impeller and paste granules in order to determine of the key parameters of the model are investigated. Furthermore, extension of the model from the literature is proposed. Finally, the kinetics of the initial growth behaviour are discussed.

Chapter 7 proposes two different population balances models to describe layered growth. The second model is further developed, solved using various discretisation methods and compared to the experimental data reported in Chapter 5. Finally, the validity and limitations of the model are discussed.

Chapter 8 summarises the results of Chapters 4-7, and links the results back to the gaps of knowledge identified in Chapter 2 and the objectives of this work. Finally, the contribution of this work to the field of granulation is discussed and recommendations for further research are made.

Chapter 2.   Literature review

2.1 Introduction

Fine powders are difficult to handle. Many industries that use particulate materials, like the pharmaceutical, catalyst, food and fertiliser industries, use *granulation* to improve the processability of powders. Granulation is defined as the formation of agglomerates by sticking together smaller particles, usually by agitation methods [1]. In this thesis, agglomerates produced in this way are referred to as *granules*.

Using granules instead of powders offers many advantages. The hazards of dust explosions, caking and formation of lumps are reduced, bulk storage density is increased and handling and metering of the material are improved. The latter is especially important for industries that produce tablets from powders, such as the pharmaceutical industry. Another advantage of granulation is prevention of the segregation of powder mixtures. The dispersion and solubility of powders can be better controlled, which is relevant to the food industry. Properties like the porosity and surface to volume ratio can be controlled, which is important for the catalyst support industry. Furthermore, granulation improves the appearance of powder products [1,3,6]. Granulation can either be carried out with dry powder (*dry granulation*) or with a binder (*wet granulation*) [3]. This work focuses on wet granulation.

Despite its relevance and almost 60 years of research [2], granulation remains more of an art than a science. Ideally, the desired granule properties are used to determine the necessary formulations, operating conditions and equipment. Although knowledge of granulation has grown over the past years, extensive laboratory work is still necessary to determine which conditions result in the desired properties [2,3]. Furthermore, the scaling up of a granulation process requires considerable investigation [4,5].

In this chapter, an overview of literature relevant to this thesis is presented, with a focus on high shear wet granulation. First, a basic explanation of granulation equipment is given. Next, granulation mechanisms and methods to model granulation are explained. Finally, scaling and control of granulation processes are discussed.

2.2 Granulation equipment

In industry, many types of granulation equipment are used, each of which has advantages and disadvantages. In this chapter, four different types of wet granulators are compared:

- Tumbling granulators
- Fluidised bed granulators
- Twin screw granulators
- Mixer granulators

2.2.1 Tumbling granulators

Tumbling granulators impart motion to powders in a rotating drum or disc and can be operated continuously or in batch [1,6]. Liquid binder is added through spray nozzles and scrapers may be present to control cake build-up on the walls. This type of granulator is used by the fertiliser, iron and agro-chemical industries, among others [1], and is also used for particle coating [6].

Granules produced in tumbling granulators are relatively large, with sizes in the range of 0.5-20 mm, have a low porosity and are highly spherical [1]. Tumbling granulators can have a very high throughput (up to 800 t/h) [6].

When operated continuously, disc granulators make use of the natural segregation of particles to sort out the larger particles, resulting in narrow size distributions and greatly reducing the need for a recycle. Continuous rotating drum granulators have no particle sorting mechanism in place and, as a result, require much larger recycles. On the other hand, rotating drums can handle a much higher throughput than disc granulators [6].

2.2.2 Fluidised bed granulators

In a fluidised bed, particles are kept in motion by sending a gas through the powder bed. A liquid binder is sprayed either from above or within the bed. Fluidised beds can be operated either in batch or continuously for granulation. Industries using these types of fluidised beds include the pharmaceutical, food and agro-chemical industries [32].

Two types of fluidised beds are commonly used: bubbling and spouted beds. In a bubbling bed, particles are fluidised and large bubbles form, whereas in spouted beds most of the powder is not fluidised. Instead, a jet of air in the centre creates a spout of particles and gas [1]. A spouted bed offers more control over particle circulation and growth compared to a bubbling bed. Furthermore, spouted beds can be used when particles are difficult to fluidise. On the other hand, bubbling beds can be scaled up more easily [6].

Granules produced in fluidised beds generally have sizes in the range of 0.1-2 mm and a low density [1,6]. Fluidised beds have good heat and mass transfer and are relatively simple to operate and scale up, but running costs and wear of the granulator are higher compared to other types of equipment.

2.2.3 Twin screw granulators

The direct production of granules using twin screw granulation or twin screw extrusion has increasingly received attention in the past few years [33,34]. Twin screw granulation involves two augers transporting a wet mass to an extrusion zone. By using different kneading elements, the shape and granule size distribution can be varied [35]. Depending on the conditions, particles may be produced directly or after an extra cutting or milling step in which the extrudate particle size is reduced [36]. Since a twin screw extruder can be operated continuously, it could be used to replace high-shear granulation processes. A major disadvantage of twin screw granulation, however, is the complexity of parameters such as screw configuration, which make the design and optimisation of a granulation process laborious.

2.2.4 Mixer granulators

In mixer granulators, an agitator or impeller is used to impart motion to particles [1]. Such granulators are classified either as low-shear or high-shear mixers, depending on the impeller speed and presence of choppers that break up larger agglomerates. The axis of the impeller can either be horizontal or vertical. Horizontal mixers are used in, for example, the fertiliser industry, whereas vertical mixers are used by the detergent, agro-chemical and

pharmaceutical industries [1]. Mixer granulators can be operated either continuously or in batch and produce less spherical, denser granules than tumbling granulators [6]. Although granulation using mixers is used in many different industries, it is the most complex type of equipment to scale up and control [6]. In the following sections, both low- and high-shear mixers are discussed in more detail.

2.2.4.1   Low-shear mixer granulators

Low-shear granulators use less energy than their high-shear counterparts, and may produce denser granules than those obtained by fluidised bed granulation. This decreases tabletability, but reduces wear of the granules, which may or may not be desired, depending on the application for which the granules are used. There are five major types of low-shear mixers: ribbon or paddle blenders, planetary mixers, orbiting screw mixers, sigma blade mixers and rotating shape granulators [37]. A schematic drawing of each type of mixer is shown in Figure 2.1.

Ribbon blenders are mixers consisting of a shaft with metal ribbons and can be used for granulation, although the shaft may not be strong enough to withstand the torque. Therefore, sometimes paddles are used instead of ribbons. Ribbon or paddle blenders may be operated continuously [37]. Due to their slow operation, most industries have replaced this type of granulator with tumbling drums [6].

Planetary mixers consist of a bowl with vertical agitator elements and usually mix well in the horizontal plane, but not the vertical plane. This type of mixer is operated in batch [37]. Due to long mixing times, planetary mixer granulators have mostly been replaced by batch high-shear mixers [6].

Like the previously mentioned types of low-shear granulators, orbiting screw granulators are mainly used for mixing. The mixer consists of a cone with a moving screw that agitates the powder. By adding a chopper and spray nozzle, the mixer can be used as an effective low-shear granulator [37]. Orbiting screw granulators may be used when gentle granulation is required, for example when opting for formulations that yield granules with a low strength.

A sigma blade mixer has s-shaped, rounded blades that mostly compress powders and liquid into a paste. This type of kneading leads to a very uniform binder distribution [37] and is mostly used for dough mixing in the bread industry.

Rotating shape granulators usually consist of a drum with cylinder-based shape. The machine shell rotates along a horizontal axis. On the axis, a second rotating device agitates the powder in addition to the motion imparted by the shell. The shear in the device is usually low, which may be desired or undesired depending on the target product. This type of granulator is mostly operated in batch, although continuous types are also available [37].
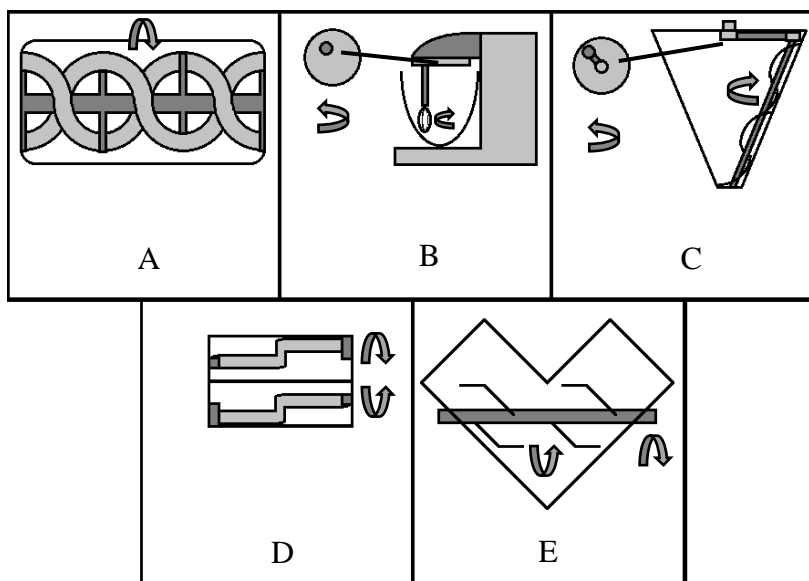
Figure 2.1: Different types of low-shear mixers: ribbon blender (A), planetary mixer (B), orbiting screw granulator (C), sigma blade mixer (D) and rotating shape granulator (E).

2.2.4.2   High-shear mixer granulators

High-shear mixer granulators usually consist of a bowl with many different possible geometries, an impeller to mix the powder and binder liquid, and a chopper to break down large agglomerates [38]. Advantages of high-shear granulators include the short processing time, efficient use of binder liquid, the possibility of handling cohesive materials and the production of stronger granules. However, there are also several disadvantages to using high-shear mixers. Granules in high-shear granulators experience stronger shear forces and, consequentially, significantly more breakage and attrition compared to other granulators [6]. As a result, the granules produced in this way have a higher density and, therefore, a lower compressibility (i.e. volume reduction when compressed) compared to granules produced in low-shear granulation. Furthermore, a narrow range of operating conditions is required in order to obtain reproducible results [38].

In the pharmaceutical industry, batch high-shear mixers are widely used due to their robustness, but at the same time, they are one of the most complex types of granulator [6]. This complexity is mainly caused by the influence of chopper and impeller geometry and the differences in shear and flow patterns between different high-shear mixer types. For example, chopper speed has little effect on granulation in vertical shaft mixers, whereas it has a much larger impact on granulation in horizontal shaft designs like the Lödige mixer [6]. A schematic of a horizontal and vertical mixer is shown in Figure 2.2.

Continuous high-shear mixers involve a horizontal or vertical shaft with blades or pins rotating at high speed. This type of granulator is used in, for example, the ceramic clays and detergent industries [6]. Residence times are usually in the order of minutes. A major advantage is that continuous granulators offer a more flexible throughput of material. In a recent study [39], a horizontal continuous granulator was compared to a high-shear mixer and fluidised bed. It was concluded that, for the formulation tested, the continuous granulator outperformed the others in terms of quality and control.
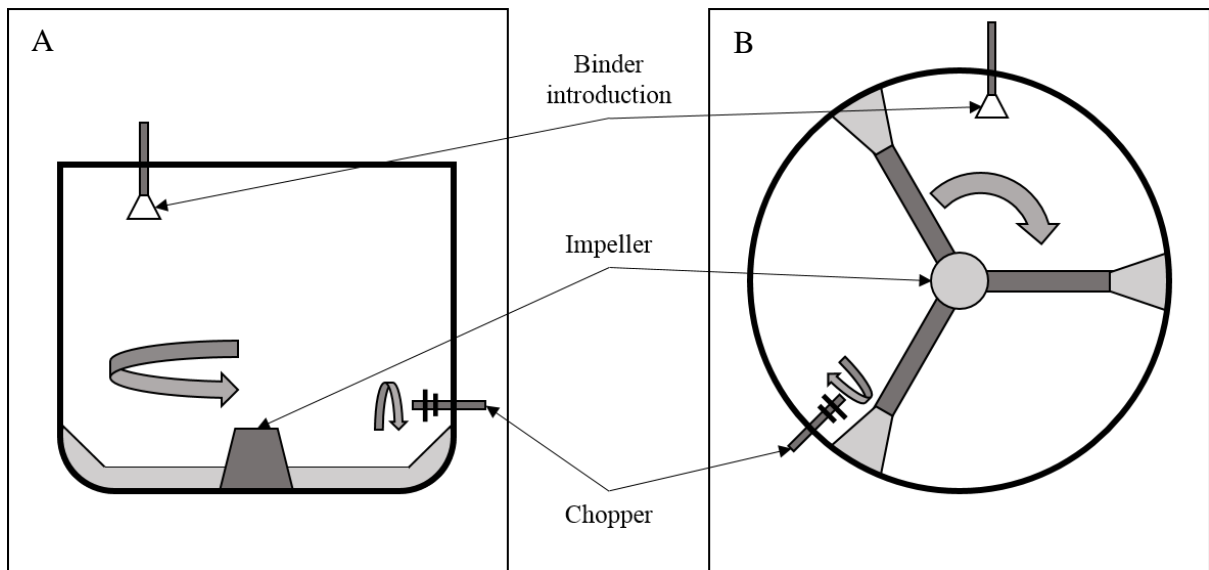
Figure 2.2: Schematic examples of high-shear mixer design: A vertical impeller shaft mixer (A) and a horizontal impeller shaft mixer (B).

High-shear batch granulation is one of the most widely applied granulation technologies [6]. In spite of this, developing a granulation process and formulation often requires thorough experimentation due to the number variables involved [38]. In the next subchapter, the reason for this complexity is explained.

2.3 Granulation phenomena

In order to design granulation processes, it is important to understand the different phenomena occurring during granulation. In a review at the start of the 21st century, Iveson et al. [2] distinguish three different rate processes: wetting and nucleation; consolidation and growth; and breakage and attrition. Each of these processes is discussed in the following sections, with a focus on granulation in high-shear mixers.

2.3.1 Wetting and nucleation

Wetting and nucleation occur when a dry powder is contacted and mixed with liquid binder [2]. Liquid displaces air in the dry powder and wetted powder particles agglomerate into seed granules called *nuclei*. Wetting and nucleation is an important process, since the product granule size distribution is related to the nucleation conditions [12], and poor wetting may lead to broad particle size distributions and poor liquid distribution [6]. Therefore, it is imperative to know what happens when a droplet hits the powder bed. Two extreme situations can be discerned. The droplet size can either be large compared to the particle size, or the particles can be large compared to the droplets [6].

In the case a droplet being larger than the primary particles, five nucleation steps occur [12]. First, the droplet is formed. It then impacts the bed, and, very rarely, breaks into smaller droplets. Next, the droplet coalesces at the powder surface and then penetrates into the powder pores. Finally, the liquid is mixed by mechanical dispersion. This mechanism is called *immersion*.

When the droplet impacts the powder bed in the immersion mechanism, several types of fragmentation of the droplet can occur, each of which results in different types of granules [40]. On loose, cohesive powder beds and at low velocities, *tunnelling* will occur. The droplet sucks in particles and penetrates into the bed. This mechanism usually forms spherical granules. For coarser powders, droplets instead *spread*, forming disc-shaped granules. At higher velocities, the impact causes *crater formation*, resulting in a droplet coated in particles. The shapes of granules produced in this way vary.

Charles-Williams et al. [41] compared droplet spreading and penetration on dry and pre-wetted static powder beds. Penetration is much slower in wet powders, and the viscosity greatly influences the penetration and spreading times. When the liquid contact angle is greater than 90°, e.g. for hydrophobic powders and aqueous binders, the liquid does not penetrate the bed [42]. Instead, powder particles form a shell around the droplet, essentially forming a hollow particle after drying. This mechanism is called *solid spreading*.

After nucleation, the binder liquid is distributed by mechanical dispersion. Depending on the shear, two types of nuclei can be discerned [43]. If shear is insufficient, the granules remain as they are, and the liquid distribution may be inhomogeneous. In the case of high shear, the nuclei will break, and the resulting granules are more homogeneous compared to a situation without breakage.

When a droplet is smaller than the primary particles, the relevant mechanisms are different from the situation described above [44]. *Distribution nucleation* is more akin to a coating and coalescence process and can also be divided into five steps. First, droplets are formed. Next, the droplet is deposited on a primary particle, and may spread across the surface or even penetrate into the pores of the particle [6]. As more and more droplets gather at the surface of the particle, the particle becomes coated in liquid. Since the powder bed in a granulator is moving, particles experience many collisions with other particles. Nucleation occurs when two colliding particles are sufficiently coated to form a liquid bridge [44].

An important development in the investigation of wetting and nucleation phenomena was the proposition of a dimensionless spray flux, Ψ_a [45], defined as the ratio of the wetted area covered by the nozzle to the spray area in the nucleation zone (Equation 2.1):

$$\Psi_a = \frac{3 * \dot{V}}{2 * \dot{A} * d_d} \tag{2.1}$$

where $\dot{V}$ is the volumetric binder flow rate, $\dot{A}$ is the area that passes through the spray zone each second and d_d is the droplet diameter. For low spray fluxes ($\Psi_a \ll 1$), drops do not overlap, and each drop forms a single nucleus. Using the concept of non-overlapping droplets, Wildeboer et al. [46] developed a nucleation-only apparatus, based on a conveyor belt with powder and a mono-sized drop nozzle. With this equipment, it is possible to continuously nucleate granules while mimicking a static powder bed. Droplets were found to coalesce due to the force of impact, thus creating nuclei composed of multiple droplets. Wildeboer et al. showed that the nuclei size distribution could be narrowed by increasing the powder bed velocity. This is in agreement with the definition of the spray flux, since increasing $\dot{A}$ leads to a decrease in Ψ_a.

Another way to improve the nuclei size distribution is by decreasing the drop penetration time, t_p [46]. When a drop of volume V_d is gently contacted with a static powder bed with porosity ε_b, the penetration time can be calculated according to Equation 2.2 [1]:

$$t_p = 1.35 \frac{V_d^{2/3} * \mu}{\varepsilon_b^2 * R * \gamma * \cos(\theta)} \tag{2.2}$$

where R is the pore radius, γ is the liquid surface tension, θ is the dynamic contact angle and μ is the liquid viscosity. This equation implies that, provided the powder and binder properties are known, liquid penetration times can be estimated.

Hapgood et al. [12] combined the concept of the spray flux with the liquid penetration time in a nucleation regime map, shown in Figure 2.3.
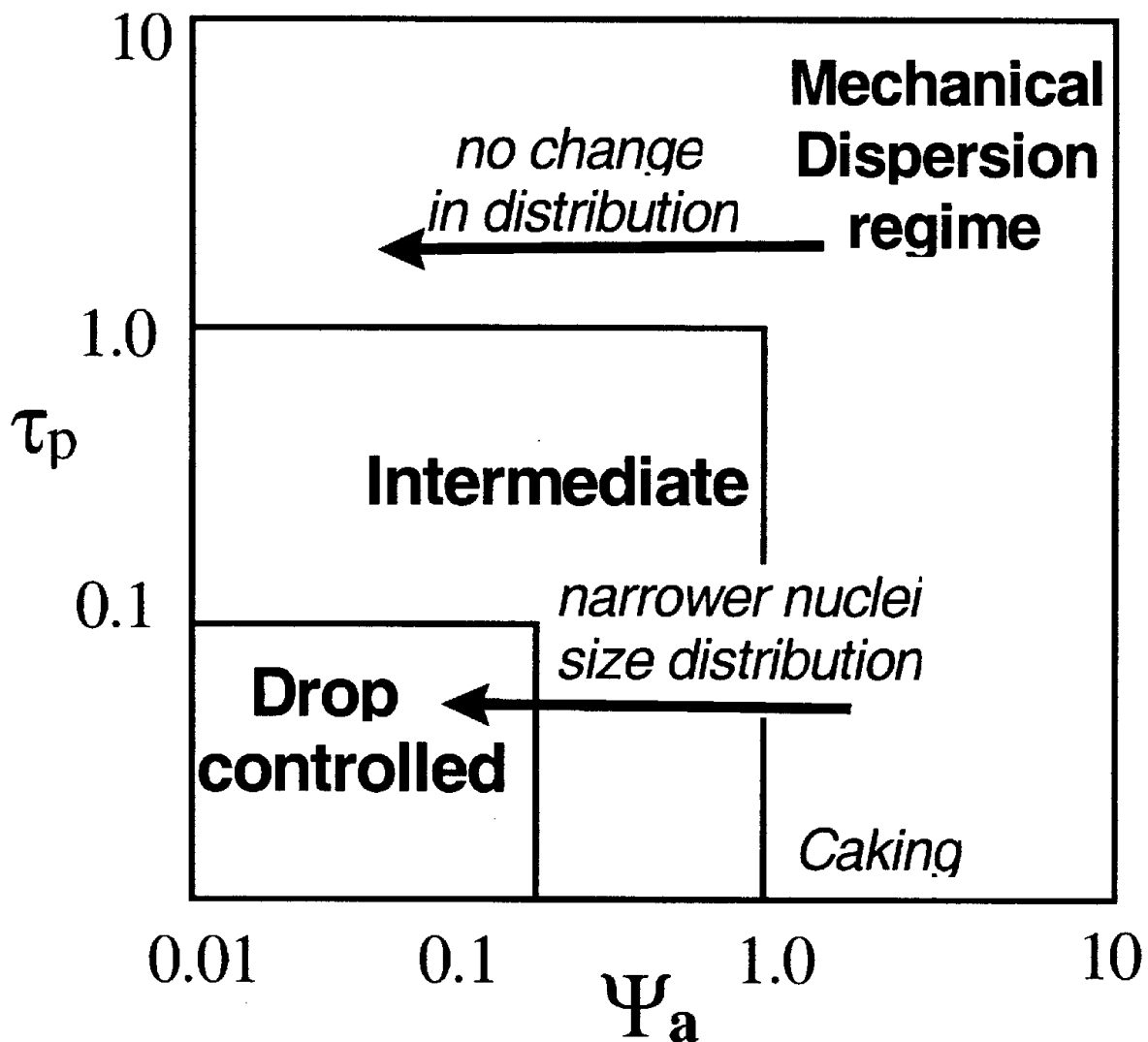
Figure 2.3: Nucleation regime map proposed by Hapgood et al. [12] showing the different regimes as functions of the dimensionless spray flux and drop penetration time. Reproduced with permission from Elsevier.

Using the time between which a section of powder leaves and re-enters the spray zone (circulation time t_c) to non-dimensionalise the penetration time (τ_p), the map was divided into three regimes. For high spray flux and long liquid penetration times, droplets have significant overlap. Therefore, mechanical mixing is needed to distribute the binder liquid. This usually leads to a broad nuclei size distribution. This regime is called the *mechanical dispersion regime.* When the drop penetration time and spray flux are much smaller than 1, each droplet forms a single nucleus. This is called the *drop controlled regime.* There is also an *intermediate regime* in which the process is sensitive to changes in nucleation zone conditions. In this way, the regime map enables the prediction of nucleation behaviour dependent on process parameters and liquid and powder properties.

2.3.2 Consolidation and growth

After wetting and nucleation, granules may grow and *consolidate* (i.e. increase in density). Since granulated products are often evaluated for size, size distribution and porosity or a related property [6], understanding when and how growth occurs is important for the industry. Granules can grow either by *layering* or *coalescence* [47]. Layering is the formation of a fresh layer of powder around an existing granule, causing slow growth. Coalescence, on the other hand, involves the collision and sticking together of two granules, causing granules to grow rapidly. In a high-shear mixer, both consolidation and growth occur at the same time scale due to strong agitation by the impeller. In the following sections, growth, consolidation and developments in this area are discussed.

2.3.2.1 Growth

When evaluating growth in a high-shear mixer, it is important to consider what happens when two surface-wet granules in the mixer collide. Basically, up to three different types of collisions can be discerned, depending on the type of granules involved [6].

For near elastic or non-deformable granules, only two phenomena occur. Colliding granules will either coalesce or rebound, depending on their kinetic energy. At low kinetic energies, the viscous liquid layer around the granules dissipates the kinetic energy sufficiently to prevent rebound. At high kinetic energies, the liquid bridge formed is not strong enough to keep the granules together, and rebound occurs. Ennis et al. [48] defined a criterion for this type of coalescence by using the viscous Stokes number, St_v, for unequally sized, spherical granules. The viscous Stokes number shows the ratio between kinetic energy and the work performed by the viscous forces, as shown in Equation 2.3:

$$St_v = \frac{8 * \tilde{m} * u_0}{3 * \pi * \mu * \tilde{D}^2} \tag{2.3}$$

where $\tilde{m}$ is the reduced mass of the granules, u_0 is the velocity of the granules, μ is the average viscosity of the liquid between the granules and $\tilde{D}$ is the reduced radius of the granules. By comparing the viscous Stokes number to a critical value, St_v^*, conclusions regarding the result of a collision can be drawn (Equation 2.4):

$$St_v^* = \left(1 + \frac{1}{e}\right) * ln\left(\frac{h}{h_a}\right) \tag{2.4}$$

Here, e is the particle coefficient of restitution, h is the liquid layer thickness and h_a is the gap distance between the two granules.

When the maximum viscous Stokes number, $St_{v,max}$ is much smaller than St_v^*, growth is in the *non-inertial regime*. In this regime, all collisions are successful. Therefore, granules grow by layering and coalescence. When St_v increases so that $St_{v,max} \sim St_v^*$, growth is in the *inertial regime*. In this regime, layering and both rebound and coalescence will occur and the overall growth is reduced. Finally, when the average viscous Stokes number increases even more so that it is in the order of the critical Stokes number, growth enters the *coating regime*. In this case, all collisions result in rebound and layering is the major growth mechanism.

Although Ennis et al. provided a useful description of elastic particles, granules in a high-shear mixer are generally deformable. For deformable particles, in addition to rebound and coalescence, deformation of the particles can occur [13]. When the viscous forces of the binder liquid are strong enough to fully dissipate the kinetic energy of the colliding granules, *type I coalescence* occurs; the granules do not actually touch and, therefore, do not deform. In the case where the kinetic energy is high enough to make the granules collide, either rebound or another type of coalescence occurs. After collision, the granules deform and rebound starts. As long as the liquid bridge formed is strong enough to keep the granules together, coalescence is successful. This is called *type II coalescence*. For high kinetic energies, the liquid bridge breaks and the two deformed particles separate.

Liu et al. [13] proposed coalescence maps for colliding particles by comparing the viscous Stokes number to the deformability of granules, expressed by the Stokes deformation number, St_{def} (Equation 2.5) [49]:

$$St_{def} = \frac{\rho_g * U_c^2}{2 * Y_g} \tag{2.5}$$

where ρ_g is the granule density, U_c is the representative collision velocity in the granulator and Y_g is the dynamic yield stress. The Stokes deformation number compares the kinetic energy to the energy required for deformation. The regime map is shown in Figure 2.4.

Using the proposed map, the collision behaviour of wet particles can be predicted. At low velocities, deformability is not significant, and particles generally show type I coalescence. Particles with a low deformation number and, therefore, low deformability, mostly show rebound behaviour at high velocities, whereas type II coalescence is dominant for highly deformable particles.

2.3.2.2 Consolidation

Consolidation, densification or compaction is the mechanism by which granules become denser due to collisions in the granulator [6]. During compaction, particle size is reduced, air is squeezed out of the pores, porosity decreases and binder liquid may be expelled to the granule surface. In the literature, two types of consolidation behaviour are discerned in high-shear mixers, depending on the deformability of granules [14].
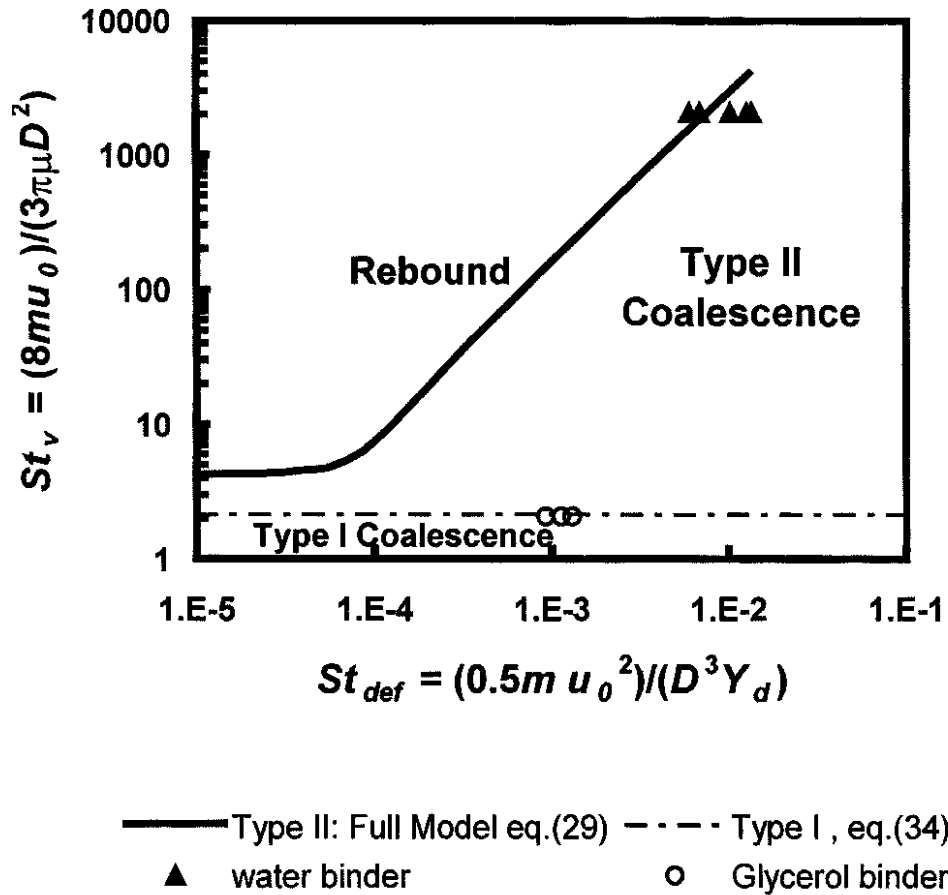
Figure 2.4: Coalescence regime maps depending on the Stokes deformation number for a particle collision (defined as $6/\pi * St_{def}$) and the viscous Stokes number [13]. Reproduced with permission from Elsevier.

In the case where granules are deformable, liquid is easily squeezed to the granule surface. This causes the granules to be surface wet most of the time, allowing for constant layering and coalescence. As a result, such granules show a constant growth over time [50]. This type of behaviour is referred to as *steady growth*. A low or medium binder viscosity and coarse particles promote steady growth behaviour.

Granules that deform slowly usually take some time to become surface wet [51]. During this time, which is usually referred to as the *induction period*, no growth occurs. After the induction period, rapid growth occurs [52]. The induction period can be reduced by increasing the binder content. Induction growth behaviour is typically observed for fine particles and high viscosities.

Iveson and Litster [18] investigated granule consolidation and proposed a simple model to describe the consolidation process (Equation 2.6):

$$\frac{\varepsilon - \varepsilon_{min}}{\varepsilon_0 - \varepsilon_{min}} = \exp(-k * N) \tag{2.6}$$

with ε, ε_0 and ε_{min} being the average porosity after N drum rotations, the initial porosity of the feed and the minimum achieved porosity, respectively, and k being a consolidation rate constant depending on yield stress, particle size and binder viscosity. More recently, it was suggested that the dependency of k on these properties could be related to the Stokes deformation number [6], at least for drum granulation.

Maxim et al. [53] further developed the consolidation model and proposed the following equations to describe the evolution of interparticle space over time (Equation 2.7):

$$\begin{cases} \dfrac{B_v - B_{va}}{B_{v0} - B_{va}} = \exp(-\omega * t) \ with \ t = t_{real} - t' \\[4mm] \dfrac{B_v'' - B_{lbr}}{B_{va}^* - B_{lbr}} = \exp(-\omega * t^*) \ with \ t^* = t_{real} - t'' \end{cases}$$

(2.7)

The two equations are valid for different times. After an initial wetting period, t', a particle is assumed to consolidate by bringing all the primary particles together. After a period t'', when all particles are packed together, further consolidation takes place by internal densification of the granule until a critical packing state is reached. t_{real} is the actual granulation time and ω is an agitation intensity rate constant, related to mixer speed. B_v and B_v'' are the interparticle space of the whole granule and interparticle space between primary particles, respectively. B_{va} and B_{va}^* are the interparticle space reached without and including reconfiguration of the primary particles, respectively. B_{v0} is the interparticle space at the formation of the granule ($t = 0$) and B_{lbr} is the critical interparticle space. The limiting binder to solid volume ratio, V_l/V_s is defined according to Equation 2.8:

$$\frac{V_l}{V_s} = \frac{B_{lbr}}{1 - B_{lbr}}, or \ B_{lbr} = \frac{V_l}{V_l + V_s}$$

(2.8)

where V_l and V_s are the volumes for binder liquid and solid particles, respectively. Although the model appears to be useful, this model has not been verified with experimental data. The rewritten form of the equation is important for the review of nucleation models in Section 2.3.2.4.

2.3.2.3 Regime maps

In order to identify and predict all types of growth behaviour observed during granulation, Iveson and Litster [14] proposed a regime map, an updated version of which [49] is shown in Figure 2.5. The map describes different regimes as a function of the Stokes deformation number and the maximum granule pore saturation, s_{max}, which gives the fraction of pores occupied by liquid (Equation 2.9):

$$s_{max} = \frac{w * \rho_s * (1 - \varepsilon_{min})}{\rho_l * \varepsilon_{min}}$$

(2.9)

where w is the mass ratio of liquid to solid and ρ_s and ρ_l are the densities of the solid particles and the binder liquid, respectively.
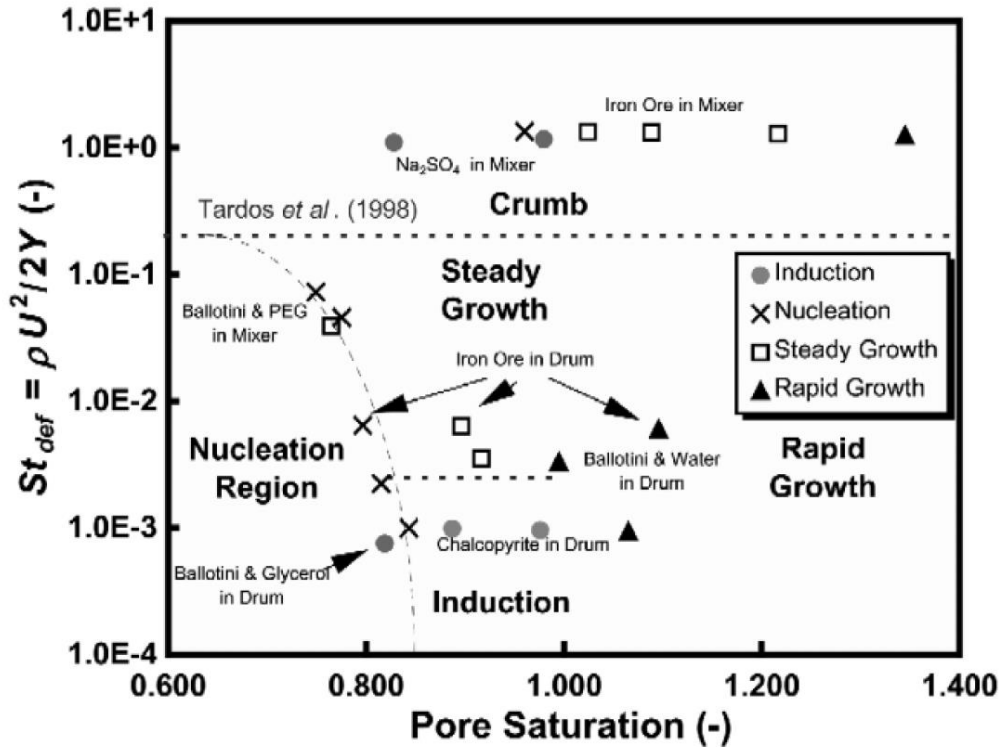
Figure 2.5: Regime maps proposed by Iveson and Litster [49], showing the different regimes during granulation as a function of the Stokes deformation number and the maximum pore saturation. Reproduced with permission from Elsevier.

The regime map allows for a qualitative prediction of growth behaviour. At low pore saturations, deformable powders remain free-flowing, whereas non-deformable powders form nuclei. Increasing the liquid content promotes the formation of nuclei, except for very weak (high St_{def}) powders, which form a crumb. Adding more liquid causes either induction growth for particles with a low Stokes deformation number or steady growth for deformable particles. Once the pore saturation is approximately 1, granules start growing rapidly. Increasing liquid content even further only results in the formation of an over-wet mass.

The regime map clearly shows how growth is related to powder and liquid properties and operation of the mixer. For example, increasing agitation intensity increases St_{def}, which is directly related to particle velocity. However, agitation intensity also promotes consolidation. Hence, growth is pushed from induction or steady growth to rapid growth and eventually crumb or slurry. Decreasing binder surface tension decreases consolidation and dynamic yield stress. Therefore, growth moves to the nucleation or crumb region. As expected, the map also shows that increasing binder viscosity or decreasing primary particle size leads to a transition from steady growth to induction growth.

In a later study [49], an attempt was made to verify and, more importantly, quantify the regime map. Although drum granulation data fitted the regime map well, mixer data did not. It was proposed that the cause of this was the estimation of the typical impact velocity; in the study it was assumed that the chopper speed could be used for this estimate. However, this assumption resulted in excessively large Stokes deformation numbers. Furthermore, the estimates of the dynamic yield strengths of the granules were possibly too low. It was pointed out that for proper use of the regime maps, better estimates for the Stokes deformation number are required.

Tu et al. [54] attempted to investigate the applicability of the regime map for high-shear mixers. Instead of the Stokes deformation number and the maximum pore saturation, both of which are inconvenient to determine, impeller speed and liquid to solid ratio were used. Since liquid to solid ratio is related to pore saturation and the Stokes deformation number is dependent on impeller speed, these choices appear valid. However, it should be noted that the influence of the dynamic yield stress of the particles is ignored.

In this study, it was observed that a single system of powder and binder showed completely different behaviours depending on impeller speed, liquid to solid ratio and binder addition rate. Nucleation only, steady growth, induction growth, rapid growth and unconstrained or extremely rapid growth regimes were observed. It was also shown that breakage occurred, something the regime map did not take into account. This study clearly demonstrated the applicability of growth regime maps, but also showed the need for improving their reliability.

2.3.2.4 Models for nucleation with subsequent consolidation and growth

Hounslow et al. [30] presented and compared two different models for nucleation and subsequent consolidation and growth. The models considered a pure binder liquid droplet surrounded by dry powder, simulating the immersion nucleation mechanism. Both models were developed for a planar and a spherical geometry.

The models both assume that the nucleus will eventually reach a critical packing density when the particles are packed as closely together as possible with the original amount of liquid added. This condition implies that the granule reaches a critical volume fraction, which is in agreement with the previously discussed consolidation model by Maxim et al. [53]. The critical volume fraction is defined as follows (Equation 2.10):

$$\phi_{cp} = \frac{V_l}{V_l + V_s}$$
(2.10)

This expression is based on exactly the same principle as the expression found in Equation 2.8, although Hounslow et al. do not provide an expression to calculate the critical packing liquid volume based on physical properties.

In Hounslow et al.'s first model, surface tension is considered the driving force at the three-phase interface, and viscous drag the retarding force. For a spherical geometry, nucleus growth can be described by Equation 2.11:

$$\frac{v - v_0}{v_{max} - v_0} = \sqrt{\frac{\gamma * d}{18.75 * \mu * h_0{}^2} * \frac{\phi_{cp}{}^3}{1 - \phi_{cp}{}^{1/3}} t} = \sqrt{\frac{t}{t_{max}}}$$
(2.11)

where v, v_0 and v_{max} are the volume, initial droplet volume and maximum attainable volume considering critical liquid volume fraction of the granule, respectively. γ is the liquid surface tension, d is the mean primary particle size, μ is the liquid viscosity, h_0 is the initial droplet diameter, ϕ_{cp} is the critical liquid volume fraction and t is the time after nucleation. The model shows that for a set time t_{max}, the volume of a granule increases with the square root of time. After the time exceeds t_{max}, no growth occurs. This model uses well understood physics,

but its weaknesses are the assumption of uniformity of the critical packing state and ignoring the collisions and deformations the nucleus may experience.

The second model, based on deformation driven diffusive flow, assumes that continuous small deformations cause transport into and out of the nucleus (Equation 2.12).

$$\frac{v - v_0}{v_{max} - v_0} = 1 - exp\left(-\frac{12 * D_{eff} * \phi_{cp}^{2/3}}{h_0^2} t\right) \tag{2.12}$$

where D_{eff} is the effective diffusivity and the other parameters are the same as in the previous model. As with the first model, the volume of the granule reaches a maximum value for the second model, but via a different path. Growth decreases according to exponential decay. Although the model incorporates the collisions and deformations experienced by the nucleus, the magnitude of the resulting diffusive flow or the dependence on liquid viscosity and primary particle size are unknown.

In essence, the model shows the same trend as the model proposed by Maxim et al. In fact, substituting the fraction in front of t with ω and rewriting the equation leads to Equation 2.13:

$$\frac{v - v_{max}}{v_0 - v_{max}} = \exp(-\omega * t) \tag{2.13}$$

As expected, this expression is very similar to those shown in Equation 2.7.

Pitt et al. [31] performed experimental and numerical studies on the consolidation and subsequent growth behaviour of granules by using the first, static immersion nucleation model proposed by Hounslow et al. By nucleating granules in a static powder bed and measuring the mass of the nuclei over time, the growth behaviour of the nuclei was determined. Lactose and zeolite were used as powders, and hydroxypropyl methylcellulose (HPMC) and silicone oil with various viscosities were used as binders. The growth behaviour fit the model very well for all systems tested. However, time scales were one to two orders of magnitude larger than those predicted by Hapgood's immersion nucleation model [55], indicating migration of liquid even after the drop had fully penetrated the bed.

2.3.3 Breakage and attrition

Of the three rate processes, breakage and attrition is the least understood in granulation [15,16]. However, breakage is an important process: breakage reduces the overall growth of granules, can be used for size control, and improves homogeneity [56]. Furthermore, knowing the breakage behaviour of granules can also provide information on the performance of the product during processing after granulation [15].

In the literature, several ways to study the breakage behaviour of granules are reported. Generally, the study of breakage can be divided into two main categories, based on the scale of the experiments [15]. Experiments on the granule scale focus on single or a small number of granules. This is important, since it shows how properties of the granules are linked to their strength. Breakage studies at the process scale instead consider the behaviour of granules during granulation. Both fields are briefly discussed in the following sections.

2.3.3.1   Breakage behaviour of individual granules

Methods of studying the breakage of individual granules involve measuring the force required to deform or break granules. Such tests result in a strength to express granule resistance to breakage [15]. The strength may vary depending on the technique used and can be measured either by static or dynamic methods.

Static methods include tensile and compressive strength, bending strength and hardness tests. Of these options, tensile and compressive strength tests are most frequently described in the literature [15].

Tensile strength tests involve the application of a tensile force to a particle. Tensile strength can be measured indirectly by applying a compressive force to granules, causing the generation of a tensile stress plane, which eventually leads to breakage. The compressive force required for failure is usually defined as the granule strength. This type of test is straightforward and requires no preparation of the sample [15], although a large number of granules must be sampled to attain reliable results. Antonyuk and et al. [57] investigated the deformation and breakage behaviour of several types of industrial granules with different properties. It was found that granules show different breakage behaviour, depending on their plasticity and microstructure. Elastic granules showed breakage at the major axis of stress, whereas elastic-plastic granules exhibited conical breakage at the area of contact.

For bending tests, granules are usually compressed into shapes that are easier to evaluate, such as bars or cylinders. A typical example of the method is the three-point bending test. The sample is supported at two ends from below, and a force is applied in the middle of the sample with a blunt wedge from the top, causing breakage. In this way, the propagation of a single crack can be evaluated. However, it is difficult to produce a sample that is representative of the original granules [15].

Hardness of a material is usually determined by indentation, which involves applying a load to an indenter at the granule surface [15]. The shape of the tip may vary. An advantage of indentation tests is their ease of use; provided the sample granule is large enough with respect to characteristic length scales like primary particle size and pore size. For smaller samples, nanoindentation can be used. Pepin et al. [58] found that hardness depends on three factors: the liquid binder surface tension and viscosity, and the interparticle friction.

Although static methods are useful and relatively straightforward to perform, their use for granulation is limited. In fact, Iveson et al. [59] state that due to the influence of the strain rate, traditional static strength measurement methods do not even give a qualitative indication of how materials will behave at high strain rates. Therefore, such methods would be invalid to predict any breakage behaviour during granulation. Consequently, different dynamic methods are needed to investigate breakage.

Antonyuk et al. [60] observed the dynamic breakage behaviour of single granules in granule impact tests, using different types of spherical granules. The breakage behaviour resembled that of static tests.

For their investigation of regime maps, Iveson and Litster [14] predicted the dynamic yield strength of granules by dropping granules from different heights and measuring the deformed contact area. In further research on breakage, Iveson et al. [61] used compression at various strain rates to measure the flow stress of pellets. They found that there was a critical strain rate below which strain rate did not matter, but above which flow stress increased with increasing strain rate. A follow-up study [62] using dynamic uniaxial compression tests at

different speeds revealed a relationship between the *dimensionless peak flow stress*, Str^*, and the c*apillary number*, *Ca*. These numbers are defined in Equations 2.14 and 2.15, respectively:

$$Str^* = \frac{\sigma_p * d_{3,2}}{\gamma * cos(\theta)}$$ (2.14)

$$Ca = \frac{\mu * v_p}{\gamma * cos(\theta)}$$ (2.15)

where σ_p, is the peak flow stress, $d_{3,2}$ is the primary particle Sauter diameter, γ is the surface tension, θ is the powder-liquid contact angle, μ is the binder viscosity and v_p is the relative granule velocity.

In the obtained relationship, two regimes where found; for low capillary numbers, Str^* flow stress was independent *Ca*, but for high values of *Ca*, there was a linear correlation between the two numbers. This relationship was further investigated by Smith and Litster [63] using dynamic diametrical compression tests to successfully define the difference between semi-brittle and plastic failure.

2.3.3.2   Breakage behaviour at the process scale

Breakage tests at the process scale are a useful tool to determine breakage behaviour because they directly provide information on what is happening during the granulation process. There are several ways to study breakage behaviour in a granulator. The two methods discussed in this section are the dye tracer and the breakage-only granulator.

Van den Dries et al. [56] used a dye tracer to investigate the influence of primary particle size and viscosity on the breakage behaviour of granules. Tracer granules were produced by mixing powder with the dye tracer, granulating and sieving out appropriate size fractions. Next, a reference batch was granulated under the same conditions, after which the tracers were added to the batch and granulation was continued. From the resulting batch, samples were taken, dissolved in water and analysed using UV-spectroscopy to determine the dye tracer content. It was concluded that increasing viscosity and decreasing particle size increases granule strength and decreases breakage.

Liu et al. [16] used a different approach. They filled a high-shear mixer with a cohesive sand mixture and added pre-made granule pellets. In this type of mixer, the only phenomenon that occurred was the breakage of granules. At set time intervals, the granules were removed from the bed and survivors were placed back in the granulator. Formulations with varying properties like binder saturation, viscosity and surface tension and primary particle size were evaluated. It was found that the extent of breakage decreased with an increase in binder saturation, viscosity and surface tension, and increased with an increase in primary particle size. Furthermore, Liu et al. state that the percentage of broken granules could be related to the Stokes deformation number. A critical Stokes deformation number of 0.2 was proposed, above which breakage occurred.

Smith et al. [17] investigated the effect of impeller speed and shape on breakage behaviour of granules in the breakage-only high-shear mixer. In addition to a bevelled edge impeller, which creates both shear and impact, a modified, flat impeller was used to maximise shear and reduce the effect of impact. The granulator was operated at two different speeds, and

instead of pellets, 2-5 mm sized granules prepared by single drop nucleation were used. The bevelled edge impeller caused significant breakage of the sample granules, and there was a clear correlation between the Stokes deformation number and breakage behaviour. For the flat impeller, however, only one of the samples showed significant breakage, even at the highest speed. It was concluded that impeller shape and speed have a strong effect on granule breakage. In particular, the impeller shape could be used to significantly control breakage behaviour.

2.4 Population balance modelling

Models and simulations can increase both the understanding of granulation and provide useful information for industry [64]. Applications include the verification of mechanism hypotheses, predicting granule properties, designing granular products, and optimisation and control. The following subsections discuss population balance modelling specifically, as well as synergy with other modelling methods.

Population balances are a frequently used modelling tool in various areas of research [64]. Models using population balances are capable of describing the evolution of one or more properties possessed by entities over the course of time. In the case of one-dimensional population balances in particle technology, such a model usually describes the evolution of the particle size distribution by volume, number or mass over time [26,65]. Generally, a population balance model (PBM) can be summarised as in Equation 2.16:

$$\frac{\partial n}{\partial t} + \frac{\partial (G * n)}{\partial L} = B - D \tag{2.16}$$

where n is the number-density function, L is the particle size, t is the time and G, B and D are expressions for growth, birth and death, respectively. Depending on the equations used, the model can incorporate granulation mechanisms like nucleation, coalescence, breakage, layering etc. For continuous processes, flow rates in and out of the systems may also be added [6]. The governing equations for these processes are *kernels*, which describe the rules for which these processes apply [64]. For example, an aggregation kernel describes the frequency and successes of collisions to predict growth rates. Kernels can be based on theoretical concepts, parameters fitted to experimental data, or physical models [66].

2.4.1 One or multiple dimensions?

PBMs in granulation can track multiple granule properties. In the case where only a single property is evaluated, PBMs are called *one-dimensional* (1-D). The earliest works focused on 1-D models that tracked particle volume, since this property has the advantage of being additive; when two granules coalesce, the volume of the resulting granule is the sum of the volumes of the original granules.

One of the earliest population balance methods successfully applied to particle growth was proposed by Hounslow et al. [22]. They proposed a solution method based on discretisation of the population balance equations and applied the model to a crystallisation process. The equations included terms for nucleation, agglomeration and growth. Since then, PBMs have

been extensively used in the field of granulation to predict granule properties and increase our understanding of the granulation process [65,67].

Although 1-D PBMs can be solved faster than *multidimensional* models, tracking a single property has its limitations [65]. Generally, properties such as porosity and liquid content are not homogeneously distributed over particle size classes. Depending on the application of the granules, it is imperative to be able to predict these properties. In such cases, tracking granule volumes alone is insufficient.

In a review in 2002, Iveson [24] confirmed such limitations and proposed a four-dimensional approach to population balance modelling. The author suggested balances for porosity and binder content in addition to granule volume, as well as a balance tracking composition in the cases of granulating with powder mixtures.

Verkoeijen et al. [68] expanded upon this concept and introduced a three-dimensional PBM. Instead of volume, liquid content and porosity, the model tracks volumes of solid, liquid and air. Although this method does not directly yield the properties Iveson [24] suggested, these properties can all be calculated when the three volumes are known. Similar to total volume in 1-D population balances, volumes in 3-D PBMs have the additional advantage of being additive, whereas changes in liquid content or porosity are much more complex to compute. As an example, a granule coalescing with another granule with a potentially different liquid content and porosity may yield a particle of equal, greater or lower liquid content and porosity, depending on the size difference of the original granules. Volumes of solid, liquid and air, however, are simply added, greatly simplifying calculations.

Darelius et al. [69] expanded upon the concept of the 3-D PBM proposed by Verkoeijen et al. and proposed a more mechanistic kernel. The authors assumed granules without any air, and added an additional balance for the liquid volume present inside the granules. The purpose of this change was to enable the calculation of the pore saturation, upon which the rate of compaction and the probability of coalescence were based. Their data was also compared to experimental data using a high-shear mixer and oversaturated granules. The model agreed reasonably well with the experiments for volume, pore saturation and porosity, demonstrating the usefulness of 3-D PBMs.

A major disadvantage of 3-D PBMs is their reduced computational efficiency. In the literature, several methods to reduce the complexity of multidimensional PBMs can be found. Both Hounslow et al. [70] and Biggs et al. [71] used a linked system of multiple 1-D PBMs. By assuming that all granules in a single size class have the same properties, such as liquid content, the model is reduced to two linked population balance equations. The model also assumes that time and size are the only parameters that influence the rates. This method will be referred to as the *lumped parameter* approach [72]. Both works show promising results, although Hounslow et al. point out several limitations of the assumptions. In the case where rates are interdependent, such as binder liquid content for aggregation kernels, the assumptions of lumped parameters are inappropriate.

Barrasso and Ramachandran [72] expand on the idea of a reduced order method by evaluating the validity of the assumptions of this lumped parameter approach. The authors numerically solve a four-dimensional PBM for a binary powder mixture with volume of solid, liquid, air and the additional solid component. Next, the lumped parameter approach is applied in several different ways, setting several parameters as bin properties. For some models, only a single parameter was considered lumped, whereas the most reduced model had three lumped parameters, with only the solid volume being a distributed parameter. The

accuracy and computational time were compared for the models evaluated. Solution times varied from almost 34 hours for the 4-D model to merely 3 seconds for the 1-D model. The authors conclude that the liquid content should be kept as a distributed parameter due to its importance in the agglomeration of granules. Depending on the required accuracy, the lumped parameter approach is a useful technique for the order reduction of multidimensional PBMs.

An alternative order reduction technique was proposed by Chaudhury et al. [73], using a combination of tensor decomposition, separation of variables and single variable decomposition. This method is based on splitting up the functions depending on multiple granule properties into equations that are more readily solved. The authors show that this method hardly reduces accuracy while greatly reducing computational time.

In summary of this subsection, the number of dimensions evaluated in a population balance model for granulation is dependent on the desired accuracy and the available computational time. If accuracy is the focus of a study, multiple dimensions should be used. The most important properties that should be included are solid or total volume, and liquid volume or liquid content, as these are the key factors in coalescence. However, if computational efficiency is the focus, such as in the case of control, a lumped parameter approach should be used to save time.

2.4.2 Solution methods

The previous subsection shows that there are several ways to set up population balance equations to model granulation. Often, the final reasoning why a specific model is selected is the result of a comparison of desired accuracy versus computational effort. These factors depend on the selected model, which can have varying degrees of complexity, and the solution method. This section will focus on the latter.

Often, population balance equations cannot be solved analytically. Therefore, either the model has to be simplified as explained in the previous section, or the system of equations has to be solved in a computationally efficient way. In the literature, myriad solution methods can be found [66]. However, most of such solution methods may be classified into three main categories: *discretisation*, *Monte Carlo* (MC) simulations, and the *method of moments* (MOM) [74]. These are discussed extensively in the following subsections. Other techniques that are briefly touched upon are the *Lattice Boltzmann* (LB) method and solution using *wavelets*. An overview of all references for the discussed methods can be found at the end of this section in Table 2.1.

2.4.2.1 Discretisation

One of the most common solution methods for PBMs is discretisation. Discretisation is based on the transformation of a continuous integral equation into a finite series of linked equations. The rationale behind this transformation is that, in practice, the particle size distribution of granules is not continuous. The cause of this discontinuity is twofold; the number of granules produced is not infinite, leading to discrete granule sizes, and the accuracy of measurement techniques is not continuous, resulting in a limit to the sizes covered. Usually, particle size distributions (PSDs) divide particles into size ranges or bins.

Therefore, it is logical to use a technique that evaluates changes to the number of granules per bin size.

An example of discretisation according to a granule size distribution is shown in Figure 2.6. The number frequency n, standardised by the bin width, is shown as a function of discretised volume v, much like an actual size distribution. The standardised number frequency is obtained by dividing the total number of particles N in bin i, or N_i in short, by the difference between the volume of the next bin, v_{i+1} and the volume in the current bin, v_i. A single bin contains all particles of volume v_i or greater, but smaller than volume v_{i+1}. Note that the bin distribution does not have to be linear. This concept is used in this section to discuss various discretisation techniques, an overview of which is provided by Figure 2.7.

One of the first discretisation schemes for population balance models was proposed and applied to a crystallisation process by Hounslow et al. [22]. The authors proposed a geometric series such that each bin was twice the size of the previous bin, as shown in Figure 2.7a. For collisions, a particle was assigned to a current bin if its size was equal to or larger than the minimum bin size, but smaller than the next bin size.
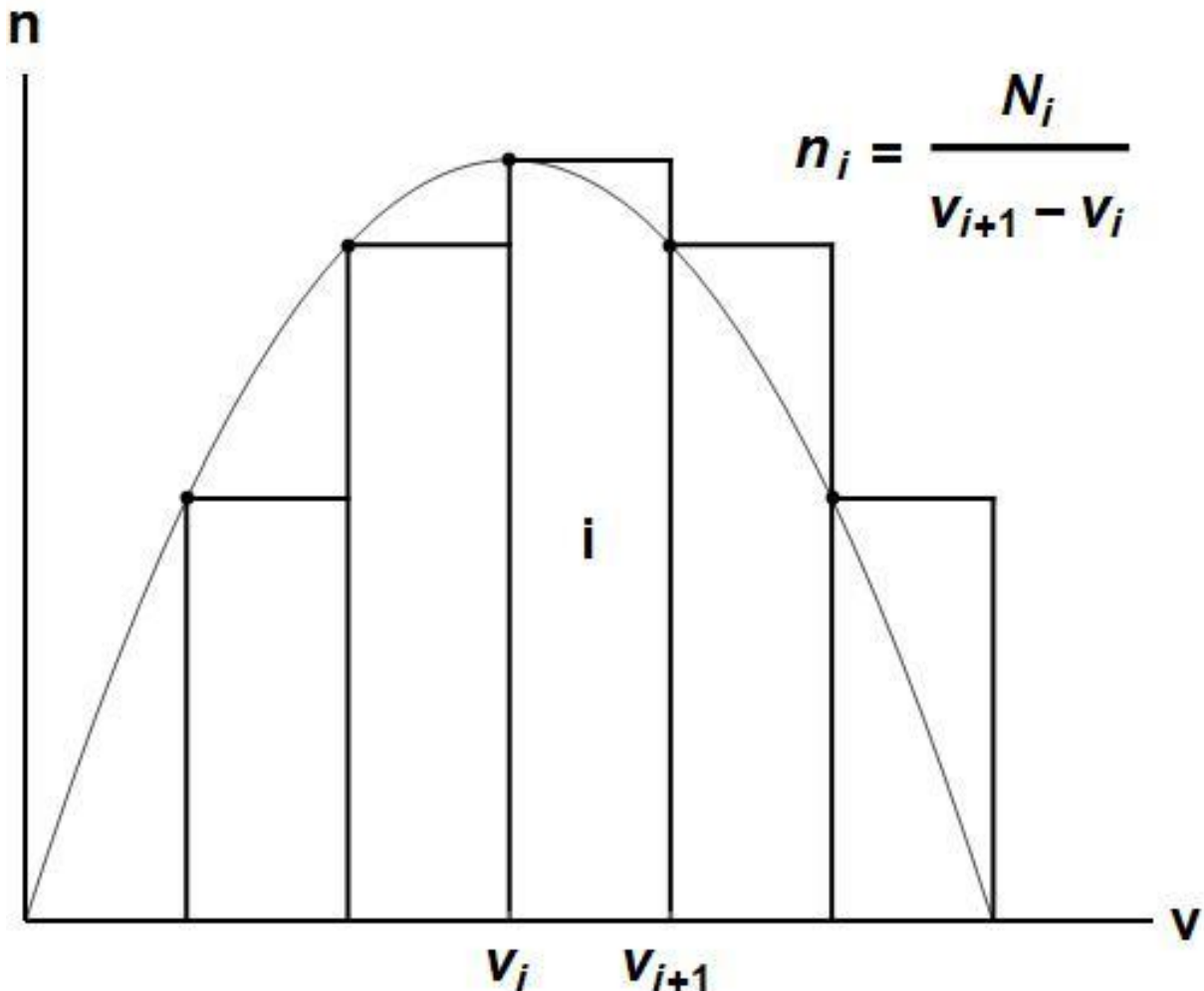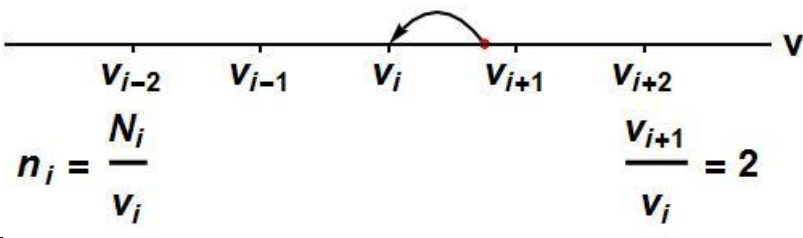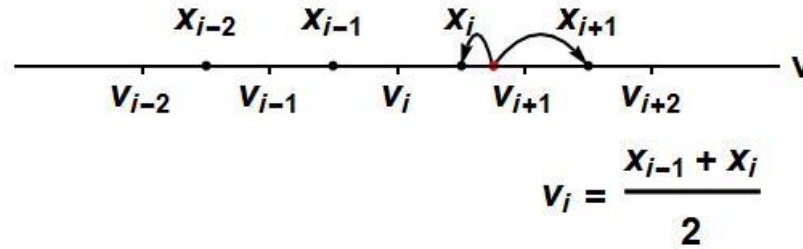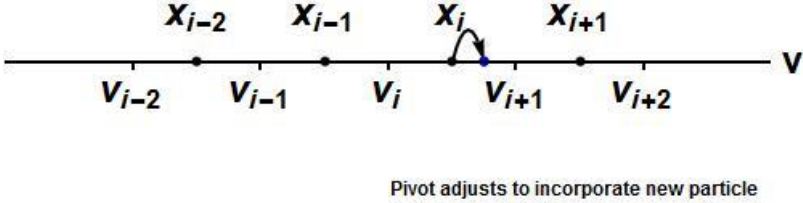
Figure 2.6: Example of discretisation using a granule size distribution. The volume of granules is divided into discrete bins on the x-axis, and the number density, the number of granules in bin *i* divided by the width of that bin, is displayed on the y-axis.

Scheme	Authors

A

● New particle

v_{i-2} v_{i-1} v_i v_{i+1} v_{i+2} **v**

$$n_i = \frac{N_i}{v_i} \qquad \frac{v_{i+1}}{v_i} = 2$$

Hounslow et al. [22]

B

● Pivot

x_{i-2} x_{i-1} x_i x_{i+1}

v_{i-2} v_{i-1} v_i v_{i+1} v_{i+2} **v**

$$v_i = \frac{x_{i-1} + x_i}{2}$$

Kumar and Ramkrishna [75]

x_{i-2} x_{i-1} x_i x_{i+1}

v_{i-2} v_{i-1} v_i v_{i+1} v_{i+2} **v**

C

● Average

x_{i-2} x_{i-1} x_i x_{i+1}

v_{i-2} v_{i-1} v_i v_{i+1} v_{i+2} **v**

Kumar and Ramkrishna [76]

Pivot adjusts to incorporate new particle

28

D
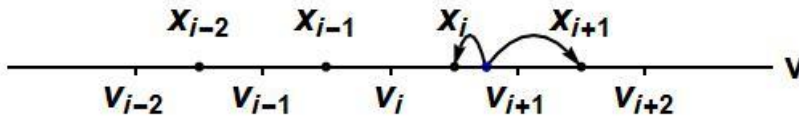
Kumar et al. [77]
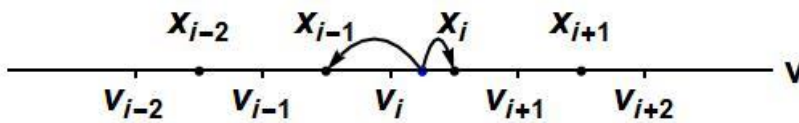
Figure 2.7: Discretisation schemes based on Hounslow et al.'s discretisation [22] (A), the fixed pivot method [75] (B), the moving pivot method [76] (C) and the cell averaged technique [77] (D).

The obtained numerical solutions were compared with analytical solutions from Gelbard and Seinfield [21]. This comparison showed that the model agreed reasonably well with the analytical solution. In addition, the discretised model was used to successfully predict experimental results from crystallisation data.

Although Hounslow et al.'s discretisation method [22] is promising, its key limitation is the use of a constant geometric grid. Kumar and Ramkrishna [75] addressed this issue by introducing a new discretisation method, shown in Figure 2.7b: the fixed pivot method. This method can use any grid, and assigns particles to so-called pivots, representative sizes for a bin. Particles born inside a bin are assigned to several pivots depending on their properties. The closer a particle size is to the actual representative size, the greater the percentage of its properties is assigned to that pivot. When applied to a geometric grid with a scaling factor of 2, the solution of the fixed pivot method becomes the same as the solution obtained by Hounslow et al. [22].

The discretised model agreed well with analytical solutions, although the method did not deal well with parts of a distribution that frequently showed steep changes in density. The authors remarked that a moving grid could be a solution in such cases. In a later work [78], the same authors combined the fixed pivot method with the method of characteristics to address the issue of changes in density. Although successful, the authors pointed out that the solution method only readily applies to crystallisation, as the required characteristic curves can be determined for this type of process.

Chakraborty and Kumar [79] later expanded the fixed pivot technique to make it suitable for solving multidimensional PBMs. Comparisons to analytical solutions showed that the method was viable, but quite dependent on the correct orientation of the grid elements.

Although the fixed pivot method has the advantage of being applicable to irregular grids, it cannot deal well with rapidly changing particle numbers. This weakness leads to the overprediction of number densities for the largest particles. In an attempt to address this, Kumar and Ramkrishna [76] proposed a moving pivot technique. Instead of using fixed pivots, the pivots automatically adapt according to the average particle size in a single bin, as shown in Figure 2.7c. In this way, the accuracy of the predictions for rapidly changing number densities is greatly improved, while keeping the advantages the fixed pivot technique offers. A trade-off for the increased accuracy, however, is a possible increase in computational time.

Nopens et al. [80] compared the performances of the Hounslow method and the fixed and moving pivot methods applied to a flocculation process. Solutions for various different situations were compared: pure aggregation, pure binary breakage and a combination of aggregation and binary breakage. It was found that for pure aggregation, the moving pivot method was the fastest method with the most accurate results, although accuracy could be sacrificed for speed when using the other two methods. For binary breakage, the fixed and moving pivot methods performed similarly and produced better results than the Hounslow method. Of these two, the moving pivot method was slightly faster and, therefore, preferred. For the kernel combining both breakage and coalescence, the moving pivot method produced the most accurate results, but it was slower than the Hounslow method.

This comparison shows that accuracy and computational time are not the only factors that should be considered when selecting a discretisation method; the types of mechanisms simulated are important as well. Methods of modelling different granulation mechanisms are addressed later in Section 2.4.3.

Although the moving pivot technique greatly increases accuracy, it is also a complex method of discretisation; the resulting set of population balance equations are stiff, meaning they can lead to incorrect solutions if a wrong step size is selected. This property complicates the solution of equations obtained with the moving pivot method. To address this problem, Kumar et al. [77] proposed a new discretisation technique; the cell averaged technique, shown in Figure 2.7d. This technique uses the fixed grid from the fixed pivot method, but uses averages of particle properties like the moving pivot method. However, instead of moving the pivots, the averages are simply assigned to pivots according to their proximity to the pivot values. In this way, the accuracy is improved at a lower computational cost than the load needed for the moving pivot method.

In 2008, two extensions were proposed for the cell average technique by Kumar et al. [77]. The first extension [81] introduced a coupling scheme, which links different rate processes such as nucleation and growth and treats them uniformly. In this way, accuracy is increased and computational time is reduced. A second extension proposed by Kumar et al. [82] expanded the cell average technique to two-dimensional PBMs. Although this expansion conserved only two moments for the cell average technique compared to three for the fixed pivot technique, the cell average technique is preferred for size-dependent kernels. The authors remark that although it is possible to solve three-dimensional equations with the developed discretisation technique, the computational time would increase.

A successful attempt at expanding the cell average technique to three dimensions was made by Chaudhury et al. [83]. In order to offset the extra computational load, the calculations were parallelised across multiple cores. In this way, simulation time was significantly decreased.

Bertin et al. [84] created a technique based on the moving pivot method for aggregation and breakage by incorporating the property redistribution of the cell averaged method. Although the new technique is computationally more expensive than other techniques, it outperforms such methods in terms of accuracy. In the case of growth and attrition only, the computational time for the solution method is greatly reduced. In this situation, the solution method should be preferred over other solution methods.

Apart from the techniques shown in Figure 2.7, several other successful discretisation techniques can be found in the literature. A family of commonly applied solution techniques are the finite element, finite difference and finite volume methods [66]. These are grouped in such a way here because their intention is the solution of the population balance equations using a discretisation technique different from the discretisation methods mentioned above. An example from literature is the solution of coagulation by Filbet and Laurençot [85], which is based on a finite volume scheme. This method has been further expanded by Qamar and Warnecke [86] for two-component aggregation. The same authors [87] combined the finite volume scheme with the method of characteristics, which is a solution method for partial differential equations.

Immanuel and Doyle [88] developed a hierarchical two-tier technique for the solution of one-dimensional population balance equations. The technique, based on finite volume discretisation, divides the particle size distribution (PSD) into bins and assigns a uniform particle distribution to each bin. In this aspect, the method is more similar to the cell averaged and moving pivot methods than the Hounslow and fixed pivot methods. However, this method differentiates itself by using a two-tier algorithm to solve the differential equations. In a single time step, rates are calculated separately first by keeping the PSD constant. Next, the PSD is updated using the determined rates. This step may be iterated several times before updating the time. The technique was later extended to 3-D [89] and multidimensional [90] PBMs using mathematical kernels. More mechanistic kernels were successfully introduced in follow-up studies [91,92]. Overall, an advantage of the two-tier technique is its efficiency, yielding relatively fast results with acceptable error.

From the examples mentioned above, it can be concluded that discretisation is a versatile solution technique for population balance equations. However, the computational time increases rapidly when a fine grid is required and when multiple dimensions are involved. Accuracy and computational time have to be balanced. In addition, the equations needed to model the rate processes in PBMs should influence the choice of the discretisation method, as some methods are better at handling certain mechanisms than other methods.

2.4.2.2   Monte Carlo method

The Monte Carlo (MC) method is a stochastic solution technique. In general, MC methods are slower than discretisation methods, but they are more straightforward to parallelise. This makes them ideal for solving multidimensional PBMs. Furthermore, MC methods provide more insight into, for example, the particles involved in collisions and the exact composition of particles.

MC methods can be divided into two subcategories. For *event-driven* MC simulations, events occur based on their probability within a time step determined by the rate of the process. An example of this would be the collision of two particles, and the resulting

rebound, coalescence or breakage that can occur. This method is preferred over more complex *time-driven* MC simulations, which require the discretisation of time [93].

It is possible to classify event-driven MC simulations even further into *constant volume* and *constant number* MC. For the former, the total volume of the particles is conserved. Therefore, the number of particles can increase due to nucleation and breakage, and decrease by coalescence. A disadvantage of this method is statistical errors introduced when the number of simulated particles is insufficient. Particularly, in the case where coalescence is prevalent, this weakness will affect the accuracy of the results. On the other hand, excessive breakage slows down the simulation significantly due to the need to account for an increasing number of particles.

Constant number MC prevents such problems by keeping the number of particles constant. Breakage and coalescence are handled by adjusting the simulation volume, thereby circumventing any problems that constant volume MC has. For this reason, constant number MC is the preferred event-driven MC method.

An example of a successful application of a constant volume MC method is the work by Gantt and Gatzke [93]. In this work, a series of multidimensional PBMs is solved by an algorithm that combines the discrete element method (DEM), discussed in Section 2.4.4, with stochastic techniques. Although the authors pointed out that accurate information on parameters such as granule strength and Young's modulus were lacking in the model, the simulations agreed well with experimental data.

Other examples of the application of event-driven MC are works by Braumann et al. [94] and Braumann et al. [95]. Both works involved the direct simulation Monte Carlo (DSMC) technique to solve a multidimensional PBM. The former work combined granulation with a chemical reaction, whereas the latter focused on increasing understanding the numerical error of stochastic models.

A different solution approach from DSMC is the stochastic weighted algorithm (SWA) [96]. This method assigns weights to different groups of computational particles. In this way, inaccuracies due to low numbers of particles are addressed. Follow-up studies further developed SWAs to allow for compartmentalisation (discussed in Section 2.4.3) of the model [97] and improve performance [98]. Although the algorithms by themselves are slower than DSMC, they are more accurate. This increase in accuracy results in an overall improved efficiency, especially for wide PSDs.

Yu et al. [99] investigated optimal strategies for MC simulations. It was found that the number of bin sizes increased resolution, but decreased accuracy. Furthermore, the authors presented guidelines for the number of simulated particles versus the number of replicates needed at minimum CPU cost.

Ultimately, the choice of MC solution method depends on the system investigated. For broad particle size distributions, the stochastic weighted algorithm is a good choice, although most number constant MC techniques should also give good results. For narrower PSDs, DSMC could be sufficient.

2.4.2.3 The method of moments

A final important technique in the literature is the method of moments (MOM), or more specifically, the quadrature method of moments (QMOM). Moments contain information on the shape of the PSD, such as the mean and variance. The higher the order of moments

considered, the more detailed the PSD can be described. MOM tracks the lower order moments. In this way, the general characteristics of a PSD can be rapidly calculated. However, MOM requires the PSD to be in a mathematical form. QMOM is an improved method, proposed by McGraw [100], which has no such requirement.

Alopaeus et al. [101] applied QMOM to breakage, agglomeration and a combination of the two. The authors found that high accuracy could be achieved by setting the first six moments to be conserved while only doubling the computational time compared to a situation in which only two moments were conserved. A study by Rajniak et al. [102] employed QMOM to a PBM for a Wurster fluidised bed. The model was combined with computational fluid dynamics (CFD) and used to obtain collision rate constants by fitting with experimental data. The simulations successfully predicted experimental observations, but there were also discrepancies.

In a study by Marshall et al. [74], QMOM was compared to a discretised PBM and an event-driven MC for the case of bicomponent aggregation. It was found that the discretised solution mostly agreed with the early stages of granulation, whereas the event-driven MC showed great accuracy over the entire time range investigated. QMOM was fast and accurate for a composition-independent model, but showed errors when the second component was introduced. The authors noted that this problem could probably be solved by increasing the number of moments tracked.

In summary, QMOM is a suitable, fast method of solving a PBM, and it has the added advantage of allowing for the incorporation of CFD. However, QMOM only provides information on the moments instead of the more detailed information provided by other methods. For more detailed results, solution of the full population balance equations by discretisation or MC is required.

2.4.2.4   Other solution strategies

This review on solution methods has limited itself to discussing the most popular solution methods. Two other methods are worth mentioning. The first method is the Lattice Boltzmann method [103,104]. This method draws an analogy to lattice methods used to model hydrodynamics and excels at modelling nucleation and growth. However, the method is less accurate for aggregation and breakage, and needs to be combined with other methods to yield reliable results.

The other method is the method of wavelets [105] which performs a wavelet transformation on the population balance equations to make them solvable. This method has the advantage of tuneable resolution, allowing for the quick computation of rough information on the solution, or more accurate solution with increased computational time. Although the method is promising, the method has not been frequently applied to population balance modelling in the literature [106].

2.4.2.5   Concluding remarks on solution strategies

The balance of computational time and accuracy has been a recurring theme throughout this review. Some methods, such as the moving pivot method, can be tuned to have high accuracy, but at the cost of increased CPU usage. Some methods are fast, but offer little detail, such as the quadrature method of moments (QMOM). Monte Carlo (MC) has the

advantage of being able to provide information on particle collision history, whereas QMOM is easy to combine with computational fluid dynamics (CFD). Some solution methods are particularly useful for modelling wide particle size distributions (PSDs), or are good at dealing with specific mechanisms such as breakage or nucleation. MC simulations have the advantage of being able to be split over multiple cores, greatly decreasing computational time.

In summary, the following factors need to be considered when selecting a solution system:

- Dimensionality of the population balance equations
- Mechanisms considered (e.g. nucleation, coalescence, breakage, growth)
- Required accuracy for the application
- Acceptable computational time for the application
- Hardware (e.g. number of cores, available CPU)
- Desired synergy with other models, such as CFD and DEM

2.4.3 Different rate processes and the population balance

The performance of population balance models greatly depends on the rate processes simulated. In the literature, a shift to more mechanistic models [25,26] and combinations with DEM simulations can be found [27-29]. In this section, the principles behind different representations of mechanisms and kernels are discussed.

Nucleation is a mechanism of 'birth' in population balance modelling. Hounslow et al. [65] describe birth according to the following equation (Equation 2.17):

$$\frac{dn}{dt} = B_0 f_N \tag{2.17}$$

where n is the number density function, t is time, B_0 is the nucleation rate per volume per second and f_N is the nuclei size distribution. A common assumption is setting the distribution to monodisperse, in which case the number density function is a Dirac delta function. Assuming nuclei are the smallest class of granules formed in the system, Equation 2.17 can be discretised according to Equation 2.18:

$$\frac{dN_1}{dt} = B_0 \tag{2.18}$$

where N_1 is the number of particles per volume in the lowest bin. Even with this assumption, determining the actual nucleation rate is a challenge.

Poon et al. [91] developed a nucleation and wetting kernel based on the drop-controlled regime. The model accounted for slow wetting and penetration times, but assumed no overlap of droplets and a preference for binder distribution over fines instead of existing granules. The kernel was successfully applied in a three-dimensional model.

In the literature, coalescence kernels are the most commonly studied type of kernel [107]. An example of a discretised agglomeration kernel [22] is shown in Equation 2.19.

Table 2.1: Overview of solution methods discussed in Section 2.4.2.

Solution method	Study
Linear discretisation	Hounslow et al. (1988) [22]
Fixed pivot discretisation	Kumar and Ramkrishna (1996) [75]
	Chakraborty and Kumar (2007) [79]
	Kumar and Ramkrishna [78]
	Lee et al. [108]
Moving pivot discretisation	Kumar and Ramkrishna (1996) [76]
Cell averaged discretisation	Kumar et al. (2006) [77]
	Kumar et al. (2008) [81]
	Kumar et al. (2008) [82]
	Chaudhury et al. (2013) [83]
	Bertin et al. (2016) [84]
Finite volumes	Filbet and Laurençot (2004) [85]
	Qamar and Warnecke (2007) [86]
	Qamar and Warnecke (2007) [87]
Two-tier hierarchical method	Immanuel and Doyle (2003) [88]
	Immanuel and Doyle (2005) [89]
	Pinto et al. (2007) [90]
	Poon et al. (2008) [91]
	Poon et al. (2009) [92]
Event-driven Monte Carlo	Gantt and Gatzke (2006) [93]
	Braumann et al. (2007) [94]
	Yu et al. (2015) [99]
	Braumann et al. (2010) [95]
Stochastic weighted approach	Patterson et al. (2011) [38]
	Lee et al. (2015) [97]
	Lee et al. (2015) [98]
Quadrature method of moments	Alopaeus et al. (2006) [101]
	Rajniak et al. (2009) [102]
	Mortier et al. (2011)
Lattice Boltzmann	Majunder et al. [103]
	Majunder at al. [104]
Daubechies orthonormal wavelets	Liu and Cameron (2001) [105]

$$\frac{dN_i}{dt} = \underbrace{N_{i-1}\sum_{j=1}^{i-1}2^{j-i+1}\beta_{i-1,j}N_j}_{(1)} + \underbrace{\frac{1}{2}\beta_{i-1,i-1}N_{i-1}{}^2}_{(2)} - \underbrace{N_i\sum_{j=1}^{i-1}2^{j-1}\beta_{i,j}N_j}_{(3)} - \underbrace{N_i\sum_{j=i}^{\infty}\beta_{i,j}N_j}_{(4)} \quad (2.19)$$

where N is the number of particles per volume in a specific bin, i is the bin being currently investigated, j is the bin compared to i, $\beta_{i,j}$ is the coalescence kernel at bins i and j in volume per unit of time and t is the time. The terms, numbered 1-4, can be explained as follows:

Terms 1 and 2 show the increase in the number of particles in bin i due to the coalescence of a particle in the previous bin with a particle from any bin equal to or smaller than the previous bin size. Terms 3 and 4 represent the reduction of the number of particles due to agglomeration with a particle in a previous bin or a particle in the current bin or greater, respectively. It is important to note that the coalescence kernel, $\beta_{i,j}$, is of great importance for

the actual kinetics of the agglomeration process. Many studies focus on finding an expression for this kernel.

For example, Adetayo et al. [109] incorporated a mechanistic element into their empirical kernel by adopting a two-stage coalescence approach. The two stages were based on the non-inertial and inertial growth regimes, and were dependent on the viscous Stokes number. In later studies [110,111], a cut-off kernel based on granule size was introduced. Collisions with granules below the cut-off size W^* were considered successful. With this model, seemingly contradictory experimental data could be explained, although the authors emphasised that W^* was only understood qualitatively.

Liu and Litster [112] developed a more physically based kernel incorporating type I and II coalescence. Only collisions satisfying either type of coalescence were considered successful. It was found that type I coalescence favoured small granules, whereas type II coalescence showed a preference to larger granules. This result indicates that the effect of granule size on coalescence is also dependent on granule and binder properties, as the Stokes deformation number is partially responsible for coalescence behaviour. The model was not fitted to any experimental data. In spite of this, it agreed better with experimental data in the early stages of granulation than the experimentally fitted work by Adetayo et al. [109]. In addition, it showed good agreement with various experimental data sets in general.

A comparison of four different collision frequency kernels was made by Darelius et al. [113]. The kernels were combined with a collision efficiency kernel in order to develop a mechanistic population balance model. Collision frequency kernels compared were a size independent kernel [70], Smoluchowski's shear kernel [114], a kernel based on equipartition of kinetic energy (EKE kernel) [65] and a kernel based on equipartition of fluctuating translational momentum (ETM kernel) [65]. The first kernel considers all collisions equally likely; the second bases collisions on powder flow in suspension; the third assumes that the average velocity does not depend on size, but a random component does; the fourth assumes full randomness of velocity, but a constant translational momentum for all granules.

The ETM kernel turned out to describe results for high impeller speeds best, whereas the EKE kernel fit the data for low impeller speeds better. Since the EKE kernel emphasises granule size more than the ETM kernel, this result implies that granule size is more important for growth at lower impeller speeds. It was also shown that a general trend could be observed for the collision efficiency by including the liquid saturation in the efficiency expression. Since liquid saturation plays an important role in growth behaviour, as demonstrated by regime maps [14,49], this finding appears to be consistent with theory.

In a semi-mechanistic model, Chaudhury et al. [115] decoupled coalescence and consolidation. The model was capable of capturing both steady growth and induction growth behaviour. Although the kernel is practical for modelling, it needs as few empirical parameters as input. Another semi-mechanistic induction growth kernel was proposed by Pohlman and Litster [116]. The model in this work is based on the types of coalescence and rebound discussed in Section 2.3.2, whereas the model proposed by Chaudhury et al. focuses on droplet spreading.

As with nucleation kernels, there are few breakage kernels to be found in the literature [107]. Hounslow et al. [70] used tracer data to propose a kernel based on bimodal breakage. The kernel used is shown in Equation 2.20:

$$\frac{dN_i}{dt} = \sum_{j=i}^{n} b_{i,j} \, S_j N_j - S_i N_i \tag{2.20}$$

where, N_i is the number of particles per volume in a specific bin, i is the bin being currently investigated, j is the bin compared to i, S_i is the breakage selection rate constant per unit of time, $b_{j,i}$ is the number of fragments from bin j assigned to bin i, and t is the time. The challenge here is finding definitions for both S and b. Particularly b, which determines the size of the newly formed granules, is particularly difficult to determine reliably.

The model assumed that the only variables involved were time and granule size. Using these assumptions, the model was capable of describing both granule size distributions and tracer-mass distribution accurately. The authors pointed out that it was unusual that some rate constants depended on time and implied that some other variable must change with time.

Vogel and Peukert [117] attempted to introduce a mechanistic breakage kernel by using a probability of breakage. The breakage selection rate constant S was set to be dependent on the kinetic energies of the particles, and the breakage function was determined by the sizes of the particles involved in a collision. Experimental data was used to determine particle properties.

A mechanistic breakage model was developed, incorporated in population balances and experimentally validated by Ramachandran et al. [107]. The method involved the three-dimensional approach proposed by Verkoeijen et al. [68], using solid, liquid and air volumes. The breakage kernel itself was based on a method similar to Stokes deformation criteria, using external stress applied and the intrinsic granule strength. For the external stress, particle-particle, particle-wall and particle-impeller collisions were taken into account. Capillary forces, viscous forces and frictional forces determined the intrinsic strength of the granules. The kernel performed well compared to empirical and semi-empirical kernels and accurately described breakage kinetics.

A commonly applied equation to determine densification in 3-D PBMs was introduced by Verkoeijen et al. [68]. This method, based on Equation 2.6 by Litster et al. [18] is shown in Equation 2.21:

$$\frac{da}{dt} = -k_c \left(\frac{(l+a)(s+l+a)}{s} - \frac{\varepsilon_{min}(s+l+a)^2}{s} \right) \tag{2.21}$$

where s, l and a are the volume of solid, liquid and air, respectively, t is the time, k_c is a compaction rate constant and ε_{min} is the minimum attainable porosity. The constant k_c has to be determined experimentally.

An example of an equation for the growth rate by Hounslow et al. [22] is shown by Equation 2.22:

$$\frac{dN_i}{dt} = \frac{2G}{(1+r)L_i} \left(\frac{r}{r^2-1} N_{i-1} + N_i - \frac{r}{r^2-1} N_{i+1} \right) \tag{2.22}$$

where G is a growth rate in units of length over time, r is the ratio between the lengths of the current bin and the next bin, N_i is the number of particles per unit of length in bin i, and t is the time. Again, G must be determined experimentally.

In general, describing a mechanism as a single set of equations does not represent the actual phenomena in a granulator. Breakage, for example, is much more likely to occur near

walls or the impeller, and nucleation will take place in the spray zone. The rates mentioned above attempt to describe overall growth, birth and death rates, representing the granulator as a single black box, or a grey box in the case of semi-mechanistic models. Another option to this problem is compartmentalisation of the equations, which is the representation of different locations in the granulator by different sets of equations. Compartmentalisation is especially important when moving to more mechanistically accurate models.

Chaudhury et al. [118] investigated a compartmentalised model using a spray zone, a bulk high velocity zone, a bulk low velocity zone, and a shear zone. It was found that the PSDs varied between zones initially, but the granulator contents became more homogenous as time passed. This finding implies that a single-compartment model is suitable for longer granulation times, but does not accurately capture initial granulation behaviour.

Yu et al. [119] focused specifically on the spray zone of a high-shear mixer for the incorporation into compartmentalised population balance modelling. By comparison with experimental data, it was found that the spray zone is a well-mixed, thin surface layer of the powder bed.

Since twin screw granulation (Section 2.2.3) is mostly a linear process, it is especially suitable for compartmentalised models with well-defined boundaries based on the screw elements. Barrasso and Ramachandran [120] developed and evaluated a twin screw granulator PBM, combined with DEM to obtain residence times per compartment. Results agreed qualitatively with experimental data. The possibility of evaluating the effect of different screw configurations on granule properties, in particular, opens up quality-by-design approaches for twin screw granulation.

In summary, the equations that represent a granulation process in a PBM may vary greatly in complexity depending on the requirements of the model. If the model has to be accurate and mechanistically relevant, experimentally obtained fitted parameters are not sufficient. Although mechanistic representations of coalescence and to some extent breakage exist, further development of mechanistic nucleation, consolidation, layered growth and breakage equations are necessary. Furthermore, considering the granulator to be a single well-mixed compartment does not represent the actual situation, and may lead to inaccuracies when modelling early-stage granulation. On the other hand, if time is the most important factor, for example for on-line control, simple, fast models might be needed.

2.4.4 Other modelling techniques and synergy with population balances

Population balances are a useful modelling tool, but they do not describe what is happening at the granule and sub-granule scale. Although more mechanistic population balance models have been developed, such models do not fully describe a system. In order to increase the understanding of granulation, other models should also be used. In some cases, models can be combined with population balances in order to increase physical relevance.

A commonly used method for modelling granulation is the discrete element method (DEM) [66], which considers the interactions between individual particles. DEM has the advantage of incorporating physically relevant phenomena such as interparticle collisions into the simulation, and allows for the investigation of granulation at the particle scale. As a downside, the number of particles that can be modelled is limited.

Gantt and Gatzke [121] used dynamic DEM to simulate type I and II coalescence, consolidation and breakage in order to predict final granule size distributions of a high-shear

granulation process. Consolidation was modelled with a porosity-related exponential relationship. For breakage, a critical Stokes deformation number was used. The model showed results very similar to those obtained with population balances.

DEM can also be combined with population balance modelling in order to create a model that covers multiple scales. Gantt et al. [122] developed a coalescence model for a high-shear mixer using DEM specifically for the purpose of incorporation into population balance models. In order to reduce computational time, periodic boundary conditions and a radial boxing scheme were used to check for collisions. Other examples in the literature include Gantt and Gatzke [93], as discussed above, and Bouffard et al. [28].

Barrasso and Ramachandran [123] coupled a 2-D population balance model with DEM simulations in order to develop a hybrid framework. The model does not take nucleation into account, but it does allow for the incorporation of breakage and consolidation. Using the model, 10 seconds of rolling drum granulation with 5 seconds of liquid addition were successfully simulated. The results were not compared to experimental data.

In their study of twin screw granulation Barrasso et al. [124] developed a bi-directional coupling grid between DEM and PBM. DEM provides input for PBM, and if a significant change occurs in the PBM, the DEM simulation is repeated to obtain new data. In this way, PBM and DEM interact to create a model based on actual particle behaviour. This coupling scheme was used in the compartmentalised model described above [120].

Kulju et al. [125] used a one-way coupled DEM-PBM scheme to model a continuous high-shear mixer. DEM was able to predict the effect of shaft speed on the accumulation of material in the spray zone. In this way, the effect of shaft speed was incorporated into the PBM.

Another possible use of DEM is to train an artificial neural network (ANN). Barrasso et al. [126] used a reduced order model and DEM results to train an ANN to relate particle size, PSD and impeller speed to collision frequency. In this way, it is not necessary to perform DEM simulations while running the actual simulation, as all collision data is generated by the ANN. This method greatly reduces the required computational time, while the results are similar to a fully coupled DEM-PBM set-up.

Other examples of the application of an ANN are the studies performed by Yu et al. [127] and AlAlaween et al. [128]. In the work of Yu et al., an ANN capable of directly predicting the average particle size and standard deviation of a PSD was trained using experimental data and interpolation. AlAlaween et al. developed a network that was capable of predicting granule size, binder content and porosity using a similar method.

A different method of obtaining rate collision data is the kinetic theory of granular flow (KTGF). Tan et al. [129,130] showed that a collision kernel based on the equipartition of kinetic energy (EKE) derived by Hounslow [65] yields results to those obtained with KTGF.

Khalilitehrani et al. [131] compared two models to simulate the different phases in a high-shear mixer using computational fluid dynamics (CFD). Dilute regions were modelled with KTGF, whereas dense regions were modelled with a viscosity divergence model. The latter model relates shear to solid volume fraction. A rheology model incorporating shear stress and strain rate was used for the transitional zone between the dense and dilute phase. This model was compared to a model in which KTGF was used for the dilute and transitional zones, and the rheology model for the dense phase. The results were then compared to experimental data. It was concluded that the former model described the flow behaviour much better than both conventional models and the latter model.

Some models are simply developed in order to improve the understanding of granulation rate processes. A model to predict nucleation sizes as a result of droplet impact on static powder beds was developed by Lee et al. [132]. The analytical model was based on experimental observations. After impact, the droplets spread in a hemisphere and liquid penetrated into the bed. The droplet then recoiled and a nucleus formed. Although the simulations could predict nucleation sizes within 1.5% accuracy, the model required calibration with experimental data.

Liu et al. [133] developed a nucleation model based on a nuclei size-prediction method by Hapgood et al. [134]. The model used the Stokes deformation number to include the breakage of nuclei by binder impact. The model was validated with experimental data.

A capillary force model for use in a model for solid, liquid and gas three-phase flow combining CFD and DEM was proposed by Washino et al. [135]. The results produced by the model were compared to experimental data and showed reasonable agreement.

Talu et al. [136] modelled shear flows of a mixture of dry particles and wet particles with a liquid surface layer. Two types of simulations were run. The first type modelled agglomeration, and clearly showed growth and breakage regimes, depending on the type of mixer selected. From the results, the final granule size distribution could be calculated. In a second type of simulation, the deformation and break-up of a single granule in a powder medium was modelled and a critical Stokes deformation number was identified. Below the critical number, no breakage or deformation occurred. The granule deformed around the critical value, and breakage occurred at higher numbers.

The evolution of the porous microstructure of granules by layering was simulated by Ŝtêpánek and Ansari [19]. The volume-of-fluid-based model involved the wetting of a dry power bed and subsequent granule growth. The effect of various properties on the granule porosity was monitored and documented in maps.

Overall, the incorporation of different techniques into PBM allow for a more mechanistic simulation of the granulation process. Some techniques, such as DEM, make the model more physically relevant by considering granulation at the particle level. Other techniques, such as models that use physical phenomena to predict properties like nuclei size, capillary force, shear flow and layering allow for the development of physically relevant kernels.

2.5 Scaling and control

Scaling and control are very relevant to industry. Scaling up a granulation process is not straightforward and requires additional investigation [4,5], since the scale of a process can influence product properties [8]. Operation of the equipment needs to be controlled in order to guarantee consistent product quality. However, control can prove to be difficult when the effects of process conditions on the final product are uncertain. Therefore, some kind of framework for scale-up and control is needed [8]. The following sections describe the various scaling and control methods found in the literature.

2.5.1 Scaling methods

When scaling up, there are several possible strategies to consider. It is important to identify the key properties that have to be maintained and to choose the key processes that influence such properties [6]. Although scaling methods may be combined for better results,

some combinations have contradictory requirements or are economically unfeasible. In this section, a few of the most important scaling methods are discussed and compared.

First of all, some geometric scales should be kept constant [7]. The ratio between the impeller/bowl diameter and the chopper should be maintained, as well as the ratio between the fill height and the diameter. Furthermore, the granulator should be geometrically similar, and the position and shape of the impeller and chopper should be the same on scale-up. It is not always possible to satisfy all the geometrical requirements, simply because precisely scaled pieces of equipment might not be available. In a study of scale-up using shear forces, Tardos et al. [10] specifically emphasise the difficulty of scaling up granulators with different geometries and impeller shapes, although they claim that it is possible.

Another parameter that should be kept constant is the dimensionless spray flux Ψ_a [45]. In doing so, a good binder distribution is ensured. At larger scales, however, this may imply using multiple spray nozzles in order to keep the spray zone sufficiently large [3], which is economically unattractive. Plank et al. [137] modified the spray flux in order to incorporate the effect of surface velocity on granulation into the model, and used this concept for scale-up. Regardless of spray flux, the liquid content should be kept constant between scales.

A commonly applied scaling method is using a constant Froude number [8,9]. The definition of the Froude number is given in Equation 2.23:

$$Fr = \frac{\omega^2 * R}{g} \tag{2.23}$$

where ω is the angular velocity, R is the radius of the granulator and g is the acceleration due to gravity. The Froude number compares inertial and gravitational forces, and can be used to characterise flow patterns. Simply put, a constant Froude number ensures a similar flow pattern in the granulator. Maintaining a constant Froude number implies decreasing the impeller speed proportional to the increase in diameter squared. Using the Froude number is not always an effective scale-up method [9]. Mort [138] states that, rather than keeping the Froude number constant, it is better to ensure that the Froude number remains high enough to maintain a roping flow pattern. Hibare and Acharya [11] found that although keeping the Froude number constant resulted in a similar granule size distribution, properties such as granule strength were not the same [10].

An additional important parameter to consider is the Stokes deformation number [3]. By keeping this number constant, the collision velocity of the granules remains constant, and it ensures granules are in similar regimes. This can only be achieved by maintaining a constant impeller tip speed, which means the impeller speed is decreased proportional to the increase in diameter. Therefore, it is impossible to combine this technique with a constant Froude number. As long as the Froude number is high enough, this method produces better results compared to maintaining a constant Froude number [138] and better conserves granule properties like strength [9]. Nakamura et al. [139] recommend that when maintaining a constant tip speed during scale-up, the granulation time should be increased in order to achieve constant cumulative particle collision energy.

In order to account for possible changes in geometry as a result of scale-up, the swept volume approach can be used [3]. This method aims to keep the volume swept by the impeller proportional to the total batch volume. For geometrically similar granulators, this method is equal to the constant tip speed approach. Hibare and Acharya [11] obtained

comparable granule properties with this approach, although the granule size distribution varied slightly.

Tardos et al. [10] proposed a scale-up power law for the relationship between impeller speed and granulator diameter in order to maintain shear. It was concluded that neither a constant Froude number nor a constant tip speed maintain the shear forces during scale-up. Hassanpour et al. [9] further investigated the use of constant shear and found that it produced similar results for larger scales. At lower scales, however, the flow patterns were completely different under the constant shear condition, which led to significantly weaker granules.

2.5.2 Control

Like scale-up, control requires detailed knowledge on the effects of operating conditions on the properties of granules. For high-shear mixers in particular, control is difficult due to the complex interactions of the different rate processes [140]. In this section, some of the most common methods to apply control to high-shear granulation are discussed. Such methods include observation of flow patterns, inline probes and measuring conditions such as torque or impeller work.

2.5.2.1 Flow patterns

It becomes clear from Section 2.5.1 that flow patterns are an important factor influencing granule properties. Flow patterns determine mixing and shear among others, and it appears logical that flow patterns should give an indication of the state of a granulation process. One of the methods used to determine flow fields is *positron emission particle tracking* (PEPT) [9,141,142], which involves tracking a single tracer particle to determine flow patterns. Using this technique, Hassanpour et al. [9] showed that different flow patterns were present at different scales, even though a granulator with a similar geometry was used. In this way, it was possible to explain observed differences in granule properties. Saito et al. [142] showed that there are regions with different flow patterns in a high-shear granulator, which could account for variation in batch quality.

Another method to observe flow patterns is *particle image velocimetry* (PIV) [137,143,144]. For this method, a high-speed camera is used to analyse particles at the surface of a moving powder bed in a high-shear mixer. By using Fourier transforms, the velocity changes in the bed can be linked with material properties like binder viscosity [143]. Darelius et al. [144] used a transparent granulator and measured the velocities at the walls of the granulator, as opposed to the surface velocities. The flow fields were linked to frictional data to predict the torque. Plank et al. [137] incorporated the surface velocity values into the dimensionless spray flux in order to describe the change in liquid coverage during scale up.

Flow patterns can also be observed using *electrical capacitance tomography* (ECT) [145]. Tomograms produced in this way can be used to determine mixing efficiency, granule state and suitable times for stopping the addition of liquid or terminating the granulation process.

2.5.2.2 In-line probes

Using in-line probes to measure particle size and shape during granulation can provide valuable information for control. However, such probes are difficult to use in mixers because

the powder phase is not fully fluidised [6]. Watano et al. [146] solved this problem by using a high resolution, high speed camera and a stroboscope with a very narrow slit. This set-up allowed for the analysis of a very small plane, which enable the accurate measurement of granule size. The images were digitised and successfully used in a fuzzy control system for high-shear granulation.

Wenzel et al. [147] performed various experiments with a particle probe to determine the optimal position and settings for the probe. With the in-line probe, it was possible to directly see the effect of changing operating conditions on the particle size distribution.

2.5.2.3 Power consumption/torque and impeller work

Measurement of power consumption or torque is frequently used as an indirect technique for control in high-shear granulation processes [6]. By measuring the torque over time, a power curve can be constructed. When liquid is added to a dry powder, the power required to mix the powder increases. Once granulation starts, the torque increases even further. Finally, when the granules stop growing, the curve levels off. In this way, power torque can be used to monitor a granulation process [148,149]. However, due to batch to batch variation, it is dangerous to rely on power consumption alone [6].

Goldszal and Bousquet [150] investigated the evolution of the power consumption profile as a function of the moisture content and were able to discern the pendular, funicular, capillary and dispersion states of nucleation. A distinction was made between step-wise growth behaviour (SGB), which contains several torque 'plateaus' during nucleation and growth, and continuous growth behaviour (CGB), with a much smoother torque profile. It was claimed that SGB-type powders were more suitable for granulators, since CGB powders tend to form a paste instead of granules.

An alternative to power consumption is the impeller work, which can be obtained by integrating the power consumed over time [140]. In this way, the extent of the granulation process is expressed in terms of total work. The advantage of this method is that it is less sensitive to particle properties. Moreover, it can be combined with the power consumption for better accuracy.

2.6 Literature review conclusions

Granulation has been extensively researched in the literature since the second half of the previous century, and there is a clear shift to more science and less art in the field of granulation. Mechanisms in granulation have been characterised. Nucleation and wetting behaviour can be explained with nucleation regime maps, typical time scales and the dimensionless spray flux. Collision behaviour between granules can be predicted by using the viscous Stokes number. All of the granulation regimes observed during granulation can be described qualitatively by the pore saturation and the Stokes deformation number. Breakage behaviour appears to be related to the Stokes deformation number, dimensionless peak flow stress and capillary number. Additionally, dynamic breakage behaviour is receiving more attention in the literature. In spite of all the advances in the field, however, there is still a requirement for further understanding of granulation phenomena. Breakage and attrition behaviour cannot be reliably predicted. Consolidation and layering are not fully understood.

Models are constantly improving and are becoming more mechanistic. Population balances, especially when combined with mechanistic kernels and DEM, are becoming more physically relevant. Solution methods become increasingly efficient and allow for larger and more complex simulations. However, although many models are available, experimental data is required for validation.

This thesis aims to address the gap of knowledge on consolidation and layered growth, and develop a mechanistic model to predict these rate processes. In order to understand consolidation and layered growth, an experimental method must be developed to obtain useful kinetic data. Therefore, one of the objectives of this work is to develop such a method. Three different set-ups are used, as described in Chapter 4, Chapter 5 and Chapter 6. Additionally, Chapter 5 and Chapter 6 describe how the experimental data is compared to models from the literature, Hounslow et al.'s models for surface-tension drive growth and deformation-driven diffusive growth [30] in particular. Based on the models from the literature, this work then identifies the key parameters that govern granule layered growth. The final objective of this work is to develop a layered growth kernel for population balance modelling using these parameters so that this rate process can be predicted for the design of industrial granulation processes.

Chapter 3.   Materials and methods

3.1 Introduction

This chapter provides an overview of all materials and experimental methods used in this study and serves as a reference for the experiments described in the following results chapters. In addition, this chapter describes the characterisation and analysis methods used and discusses various properties of the materials employed.

Section 3.2 describes the different characterisation techniques, and provides some background information. The Sections 3.3 and 3.4 focus on the powders and liquid binders employed, respectively. Next, Section 3.5 elaborates on the properties of the different powder-binder systems used in the experiments. Finally, the different experimental methods are described in Section 3.6.

Three different types of experiments were performed. The first type focuses on exploring the use of a high-shear mixer for investigating granule consolidation and layered growth kinetics. The second type is an investigation of granule consolidation and layering in a purposefully designed consolidation-only granulator (COG). The third and final type of experiments were performed to further elucidate granule consolidation and layering by using a high-shear mixer with flat plate impeller to granulate paste particles.

3.2 Characterisation and analysis methods

Several methods were employed to characterise and analyse both the primary materials used and granules produced in this study. The most important of these techniques are particle size measurements via laser diffraction, viscosity measurements, contact angle measurements, interfacial tension measurements, liquid density measurements, envelope and true density measurements using powder and helium pycnometry, respectively, and X-ray tomography to study the internal granule structure. The principles and operation of these methods are discussed briefly below.

3.2.1 Laser diffraction

All powders used in this study were analysed with dry cell laser diffraction (Malvern Mastersizer 3000 PSA) to obtain their particle size distributions (PSDs) and characteristic particle sizes. The principle of laser diffraction is based on the scattering of a laser beam on particles [151]. Large particles have a small scattering angles, whereas small particles have a large scattering angle. The scattering angle is also influenced by the refractive index of the material.

The output of the laser diffraction characterisation is a table with size classes, or bins, and the volume of the particles inside each bin. This table can be used to plot a *volume frequency distribution* (referred to as *standardised PSD* in this work) or q_3, the volume percentage of particles in a bin divided by the bin width. The shape of the standardised PSD gives information on powder properties such as uniformity of the particle size, the *surface area mean diameter* or $d_{3,2}$, and the *volume moment mean diameter* or $d_{4,3}$. The $d_{3,2}$, or Sauter mean diameter, is the diameter of a sphere that has the same volume to surface area ratio as the particle investigated, and is mostly used when the surface area of the particles is important. The $d_{4,3}$, or De Brouckere mean diameter, shows where the bulk volume of the sample is located. This value is logical to use for laser diffraction, as laser diffraction

measures volume frequency. It is, however, less useful when the sample has a large quantity of fines, such as for the zeolite powder used in this study.

From the standardised PSD, the *cumulative particle size distribution* (cumulative PSD) by volume, or Q_3, can be calculated. This distribution yields three important percentile values: the d_{10}, d_{50} and d_{90}. A d_X indicates the maximum particle size at which X percent of the particles is equal to or smaller than that size. This means that a d_{10} contains the smallest 10 % of the particles by volume, the d_{50} the smallest 50 % of the particles by volume, and the d_{90} the smallest 90 % of the particles by volume. The closer the d_{10}, d_{50}, and d_{90} are to each other, the narrower the standardised and cumulative PSD.

In order to give a clear representation of the particle size distributions, the $d_{4,3}$, $d_{3,2}$, d_{10}, d_{50} and d_{90} are reported for all powders used. Additionally, the q_3 and Q_3 are shown for all samples.

3.2.2 Viscosity measurements

To determine the viscosity of the binder liquids, an MCR502 Anton Paar Rheometer was used with a CP50-2/TG conical plate. The rheometer operates on a simple principle. Liquid is placed on a stationary plate and a second plate is placed on top of the liquid. The top plate is then rotated at a velocity to impart motion to the liquid. The *shear rate* that is applied depends on the velocity of the plate and the height of the gap between the static and rotating plate. The apparatus then calculates the *shear stress*; the force measured divided by the area. The viscosity is simply the shear stress divided by the applied shear rate [152]. For this study, the applied shear rate varied between 0.01 and 1000 s^{-1}.

3.2.3 Contact angle measurements

To investigate the interaction between the different powders and binders used, contact angles were measured for each system with a First Ten Ångstroms FTÅ200 goniometer. This type of equipment uses imaging of a liquid droplet on a solid surface to calculate the contact angle between the solid and liquid.

A thin layer of powder was spread out on a microscope slide with double adhesive tape on top of it. In this way, the effect of droplet penetration was reduced. Next, a droplet was deposited from a 22 G (0.41 mm internal diameter) blunt needle on the powder layer. This was done in such a way that the droplet was completely detached from the needle before touching the powder. Over the course of 75 seconds, a 25-frame movie was recorded of the sessile droplet. The FTA32 software on the apparatus then automatically calculated the contact angle. However, there were limitations to the software for low contact angles (around 20°). In such cases, the baseline for the droplet had to be defined manually. This limitation has been reported in the literature [153], and 20° is known to be the minimum contact angle that can be measured accurately using this equipment.

3.2.4 Interfacial tension measurements

The interfacial tension of all liquids was measured with a First Ten Ångstroms FTÅ200 goniometer. For this measurement, the pendant drop shape method was used [154]. This method is based on the Young-Laplace equation[155], and it uses the radii of curvature of the droplets and their density to calculate the surface tension using FTA32 software. The pendant droplet was created from a 22 G (0.41 mm internal diameter) needle, and a single snapshot was taken of the droplet, after which the image was analysed by the software. In order to determine the precision of the values, the average surface tension was calculated based on the analysis of ten different droplets.

3.2.5 Liquid density measurements

For the measurement of liquid density, a 25 mL density flask was used. This type of flask has a stopper with a capillary, which allows for very accurate filling of the flask. The empty flask was weighed and filled with the liquid of interest, after which the cap was used to remove any excess liquid through the capillary. After careful removal of excess liquid from the exterior of the flask, the filled flask was weighed again. The density was calculated from the obtained liquid mass and the known flask volume.

3.2.6 Powder pycnometry

The envelope density of granules, i.e. the density including all internal and external cavities, was measured using a Micromeritics GeoPyc1360 powder pycnometer. The density measurement is based on volume displacement; first the volume of a chamber filled with free flowing DryFlo powder is measured, after which a sample with a known mass is introduced into the partially filled chamber. The equipment then measures the combined volume of the DryFlo powder and sample several times before determining the density using the known mass and the volume. For this study, a 12.7 mm sample chamber was used, and consolidation force was set at 28 N.

Due to the small size of the granules, several granules had to be analysed for each measurement. The use of multiple granules occasionally led to poor overall flow due to mechanical friction between the granules, lowering the accuracy of the measurement. In order to maintain reliable results, several repeats were performed. When sufficient granules were available, repeats were performed with new, previously untested granules. However, in cases where only a few granules were available, or where large numbers of granules were required, repeats were performed using the same granules.

3.2.7 Helium pycnometry

The true density of powders and granules was calculated using a Micromeritics AccuPyc 1340 helium pycnometer. Like the GeoPyc, the AccuPyc measures a volume, although it uses helium gas instead of DryFlo powder. A sample of known mass is placed into a sample chamber with a known volume. Then, the equipment fills the remaining volume of the sample chamber with helium, which penetrates into the pores of the sample. Using the initial pressure and the equilibrium pressure after addition of the helium, the software calculates the volume

of the sample chamber occupied by the sample. Next, it uses the mass of the sample to calculate the true density. However, if the sample has any inaccessible internal pores, the equipment gives an overestimation of the true volume, and therefore an underestimation of the true density. Whenever possible, a pressure of 19 psig was used for both the purges and the analysis. A minimum number of 20 purges was used, and the equilibrium rate was set at 0.005 psig/min.

3.2.8 X-ray tomography

A select number of granules were analysed using a Skyscan 1172 Micro-CT to obtain three-dimensional X-ray images of their internal structure. In the literature, X-ray computed tomography has been used to obtain porosity values for granules [156]. A limitation of this technique is its accuracy, which relies on the resolution of the equipment. On the other hand, the technique shows the internal structure of samples and can be used to calculate the volume of inaccessible pores, unlike helium pycnometry. For this study, X-ray computed tomography was mostly used to identify the denser and less dense zones in the granules, as the resolution was not high enough to obtain reliable porosity data.

3.3 Powder properties

In this work, four different powders were used for the experiments performed. These powders were glass beads, lactose monohydrate, plastic beads and sodium aluminosilicate zeolite. Lactose monohydrate, a cohesive powder with nonspherical particles, was selected for its common use as an excipient in the pharmaceutical industry. The other powders were selected to investigate a broader range of particle properties; sodium aluminosilicate is more cohesive than lactose monohydrate and has a significantly lower $d_{4,3}$; glass beads and plastic beads have highly spherical particles with different densities. All powders were analysed with dry cell laser diffraction to obtain their particle size distribution (PSD). Additionally, helium pycnometry was used to obtain the true density of the powders. A summary of all powders used, including some of their key properties, is shown in Table 3.1.

Table 3.1: Powders used and their properties. Standard errors are shown in brackets.

Powder	$d_{3,2}$ (μm)	$d_{4,3}$ (μm)	d_{10} (μm)	d_{50} (μm)	d_{90} (μm)	ρ_{true} (g/cm^3)
Glass beads	72.50 (0.08)	74.0 (0.1)	61.1 (0.3)	73.34 (0.08)	87.5 (0.6)	2.496 (0.001)
Lactose monohydrate	5.36 (0.04)	49 (1)	4.25 (0.06)	38.2 (0.2)	108 (2)	1.569 (0.001)
Plastic beads	51.4 (0.03)	52.02 (0.02)	45.1 (0.3)	51.73 (0.03)	59.2 (0.3)	1.219 (0.002)
Sodium aluminosilicate	0.943 (0.009)	2.84 (0.01)	0.280 (0.002)	2.744 (0.008)	5.32 (0.02)	2.10 (0.01)

3.3.1 Glass beads

Glass beads, provided by Mo-Sci Corporation, were used as a model particle. The particles are highly spherical, with a minimum sphericity of 0.85 (Mo-Sci Corporation). Due to their high sphericity and excellent flowability, glass beads allow for rapid separation of primary powder and granules produced after experiments.

3.3.1.1 Particle size distribution

In order to analyse the particle size of the glass beads, three different laser diffraction measurements were performed. The resulting PSDs were used to obtain three sets of $d_{3,2}$ and $d_{4,3}$ values, as well as the d_{10}, d_{50} and d_{90} values, which were then averaged to obtain the mean values. Figure 3.1 shows the standardised PSD and the size values.

Glass beads show a fairly narrow unimodal size distribution, with a d_{10} of 61.1 μm, and a d_{90} of 87.5 μm. This is in reasonable agreement with the guarantee given by the manufacturer that 80 % of the particles are in the range of 63-90 μm. The d_{50}, $d_{3,2}$ and $d_{4,3}$ are close, as expected of a narrow distribution of spherical particles. A cumulative PSD is shown in Figure 3.2. The curve is S-shaped, which is normal for narrow PSDs.
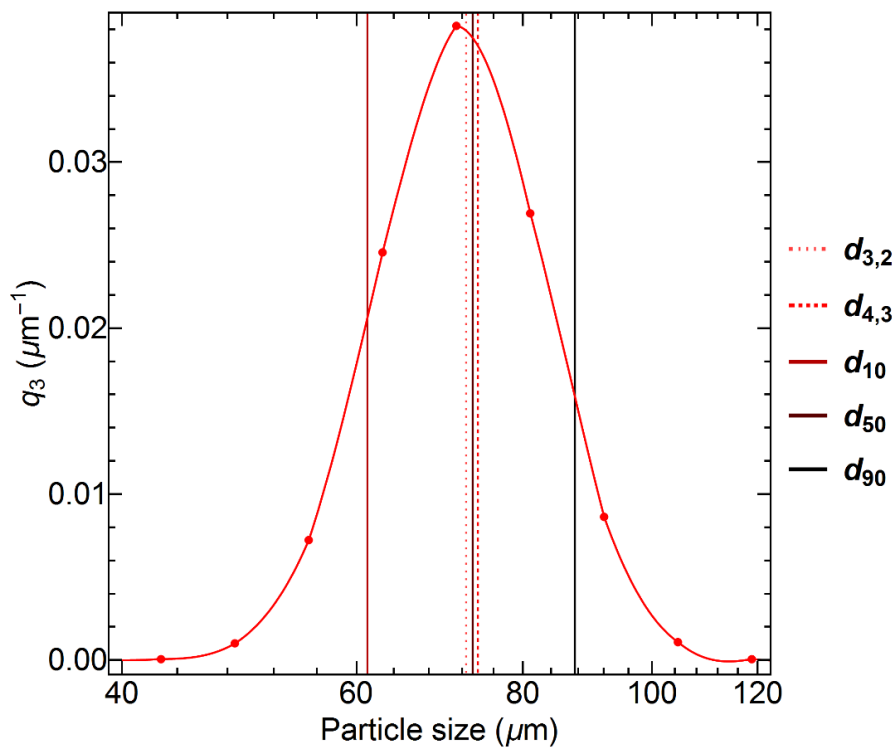
Figure 3.1: Standardised particle size distribution of glass beads obtained via laser diffraction, identifying the $d_{3,2}$, $d_{4,3}$, d_{10}, d_{50} and d_{90} values.
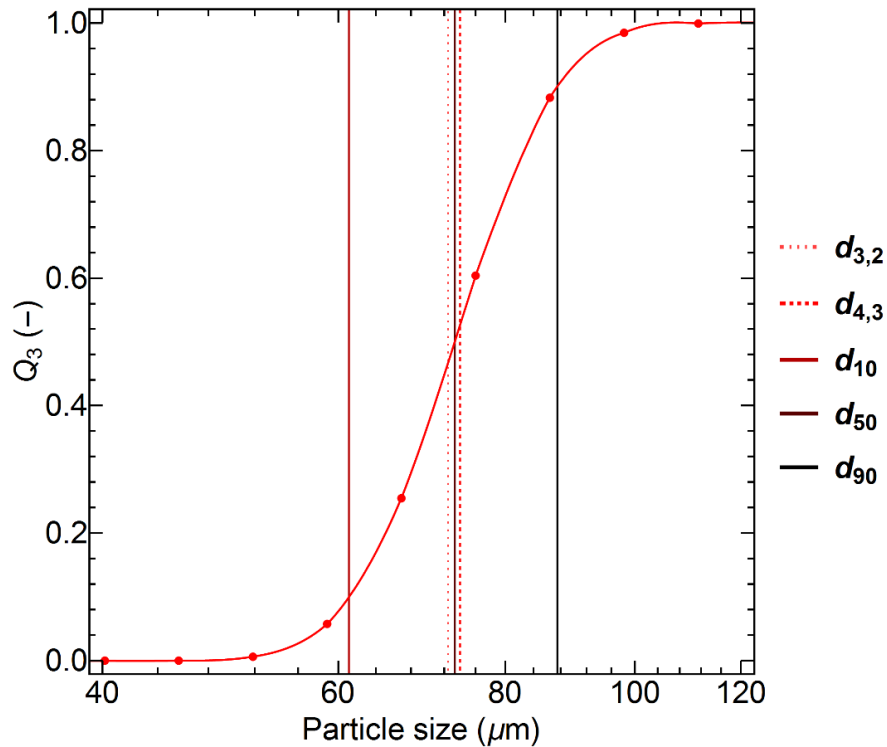
Figure 3.2: Cumulative particle size distribution of glass beads obtained via laser diffraction, identifying the $d_{3,2}$, $d_{4,3}$, d_{10}, d_{50} and d_{90} values.

3.3.1.2 Density

The true density of the powder, determined by a triplicate series of helium pycnometry experiments, was found to be 2.496 g/cm^3, making it the highest density powder used. This value was in agreement with the manufacturer's reported value of 2.5 g/cm^3.

3.3.2 Lactose monohydrate

Crystalline α-lactose monohydrate (Pharmatose 200M), which will be referred to as simply 'lactose' in this work, was provided by DFE Pharma. Compared to glass beads, lactose is much more cohesive, although it flows through a sieve fairly well when mild shaking is used. This reduction in flowability is mostly caused by the irregular shape of lactose particles, which allows the particles to interlock.

3.3.2.1 Particle size distribution

In order to determine the PSD, a series of four laser diffraction experiments was performed. A triplicate was insufficient as the values showed more variation than the other powders, with standard error percentages ranging from 0.6 to 2 %, whereas the standard errors of the other powders were consistently below 1%. Due to the reduced flowability of the powder compared to glass and plastic beads, a 1 cm diameter steel ball was used to promote the flow of the powder through the feed sieve. The standardised PSD, including relevant particle sizes, is shown in Figure 3.3.

51
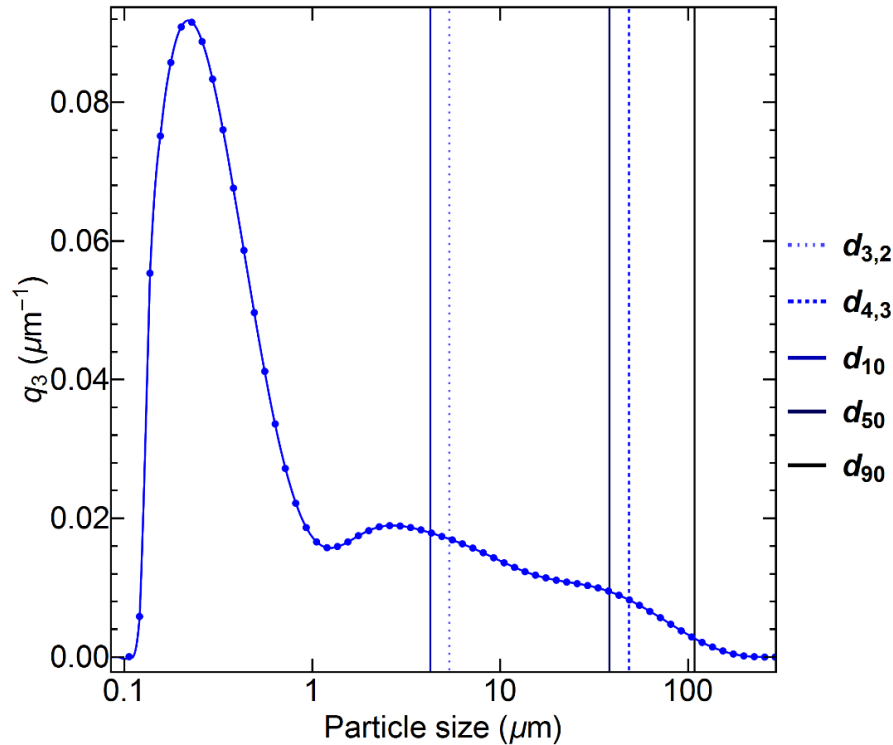
Figure 3.3: Standardised particle size distribution of lactose, obtained via laser diffraction, identifying the $d_{3,2}$, $d_{4,3}$, d_{10}, d_{50} and d_{90} values.

The PSD is clearly different from glass and plastic beads. A large fraction of fines is present in the lactose. With a d_{10} of 4.25 and a d_{90} of 108 μm, the size range is also much wider than that of glass beads. The manufacturer reports a fraction of 50-65% below 45 μm, which is reasonable considering the d_{50} is 38.2 μm. The d_{90} of 100 μm reported by the manufacturer is slightly lower than the measured d_{90}. The cumulative size distribution, shown in Figure 3.4, is fairly smooth, but it shows a long tail at the lower particle sizes.

3.3.2.2 Density

The true density of lactose, determined by a triplicate of helium pycnometry experiments, was found to be 1.569 g/cm^3. This is in reasonable agreement with the value of 1.54 g/cm^3 reported by the manufacturer.

3.3.3 Plastic beads

Plastic beads (Spheromers CA50) were provided by Microbeads AS. Like glass beads, plastic beads are highly spherical and unimodal, with excellent flow properties.
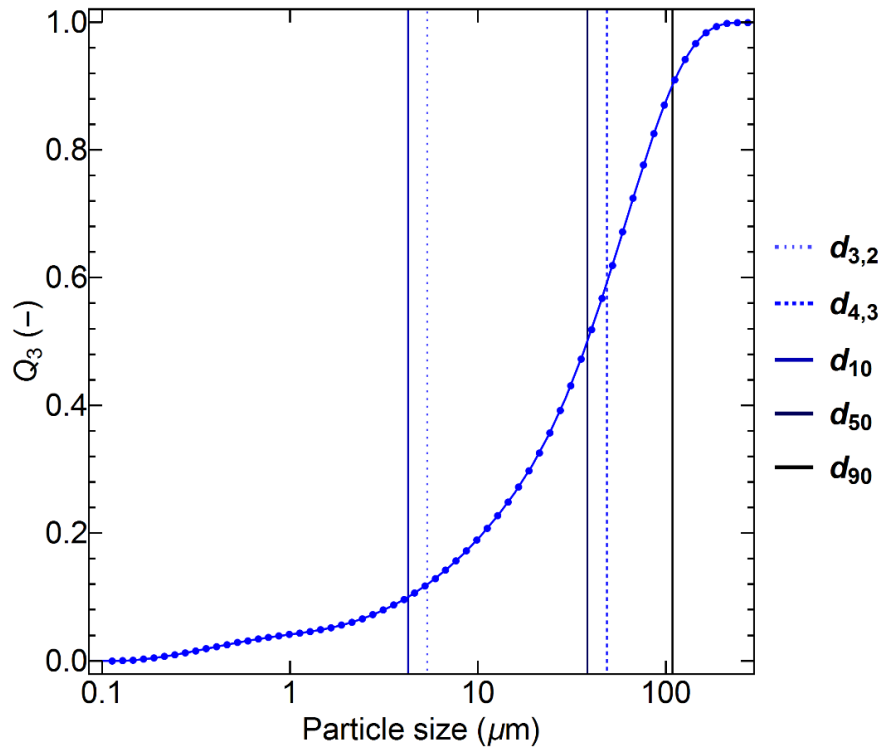
Figure 3.4: Cumulative particle size distribution of lactose obtained via laser diffraction, identifying the $d_{3,2}$, $d_{4,3}$, d_{10}, d_{50} and d_{90} values.

3.3.3.1 Particle size distribution

A triplicate of laser diffraction experiments was performed to determine the PSD for the plastic beads. The standardised PSD and all relevant particle sizes determined are shown in Figure 3.5.

The PSD is narrower than that of glass beads, with a d_{10} of 45.1 and a d_{90} of 59.2. The $d_{4,3}$ of 52.02 μm is within the error margin of 50 μm ± 5% reported by the manufacturer. The cumulative PSD, shown in Figure 3.6, is smooth and steep, as expected from a unimodal powder.

3.3.3.2 Density

A triplicate of helium pycnometry experiments was used to determine the true density of plastic beads, which was found to be 1.219 g/cm^3. This density is consistent with the value of 1.2 g/cm^3 reported by the manufacturer. Of all powders used, plastic beads has the lowest density.
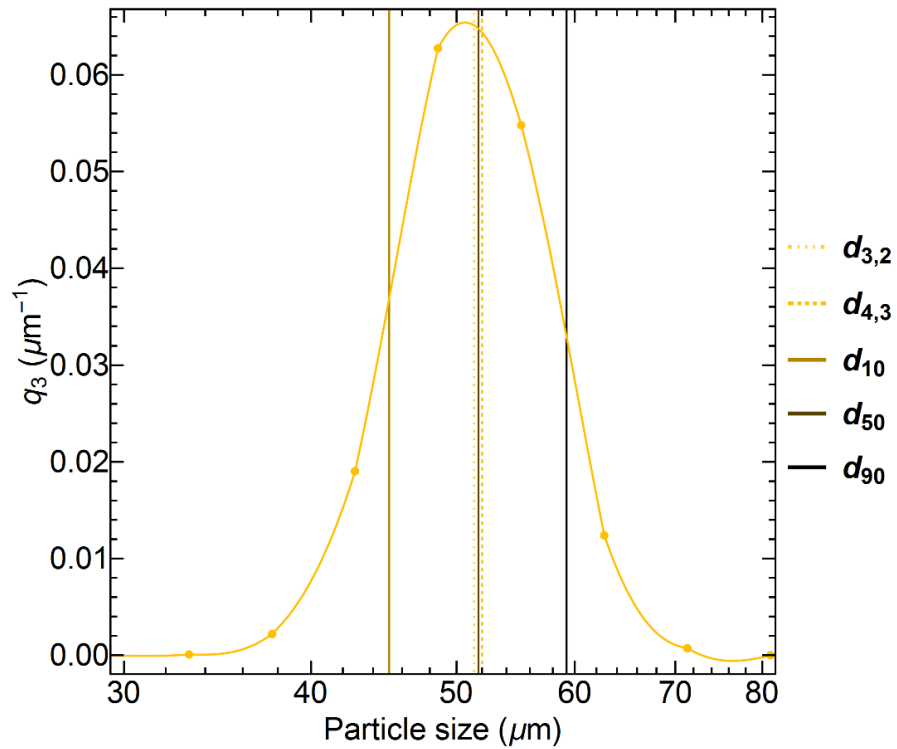
Figure 3.5: Standardised particle size distribution of plastic beads, obtained via laser diffraction, identifying the $d_{3,2}$, $d_{4,3}$, d_{10}, d_{50} and d_{90} values.
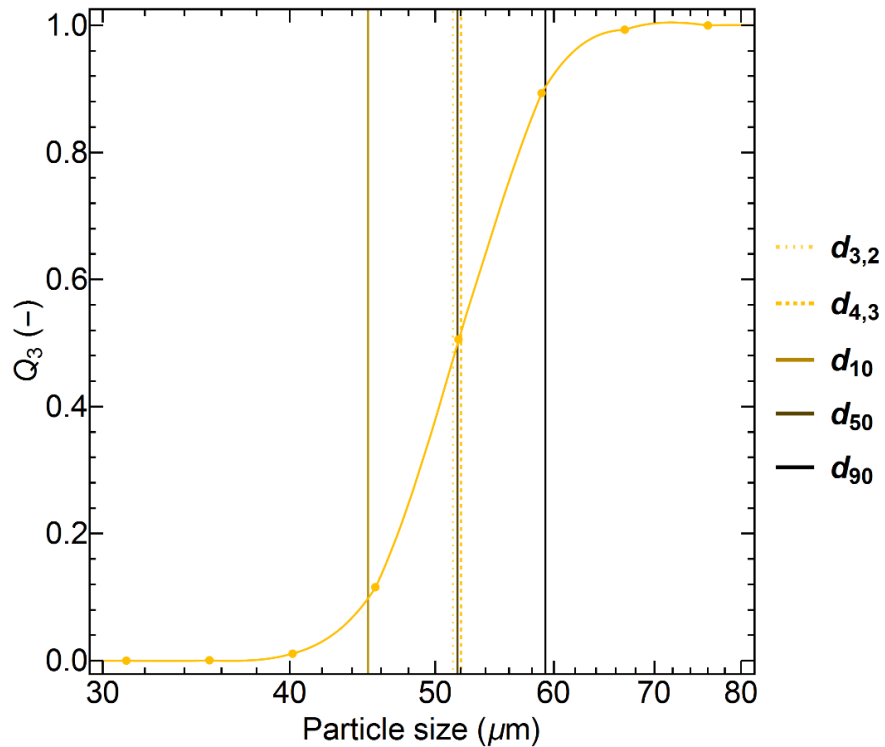
Figure 3.6: Cumulative particle size distribution of plastic beads, obtained via laser diffraction, identifying the $d_{3,2}$, $d_{4,3}$, d_{10}, d_{50} and d_{90} values.

3.3.4 Sodium aluminosilicate zeolite

Sodium aluminosilicate zeolite (Docil 4A), referred to as 'zeolite' in this work, was provided PQ Corporation. Zeolite is extremely cohesive, making sieving a laborious process. Additionally, the powder is much finer than any of the other powders tested.

3.3.4.1 Particle size distribution

The PSD for zeolite was determined with a triplicate series of laser diffraction experiments. A 1 cm steel ball was used to promote flow through the feed sieve by causing additional vibrations. Figure 3.7 shows the resulting standardised PSD. Interestingly, a bimodal distribution is obtained, whereas the manufacturer reports a narrow unimodal particle size distribution with a d_{50} of 3 μm and an average particle size of approximately 3 μm. The second peak corresponds quite well with the PSD shown by the manufacturer, and the $d_{4,3}$ and d_{50} of 2.84 and 2.744 μm, respectively, agree with the reported values. Two different explanations can be offered for this phenomenon. First of all, attrition could have caused an increase in the fractions of fines, resulting in the large first peak. Second, the analysis method can pick up unimodally distributed elongated particles as two different sizes, depending on the face turned towards the laser. However, since the manufacturer reports that the zeolite particles are mostly cubic in shape, this second explanation is unsatisfactory. It is, therefore, reasonable to assume that the zeolite particles have suffered attrition. The cumulative PSD, shown in Figure 3.8, mostly confirms the findings of the standardised PSD.
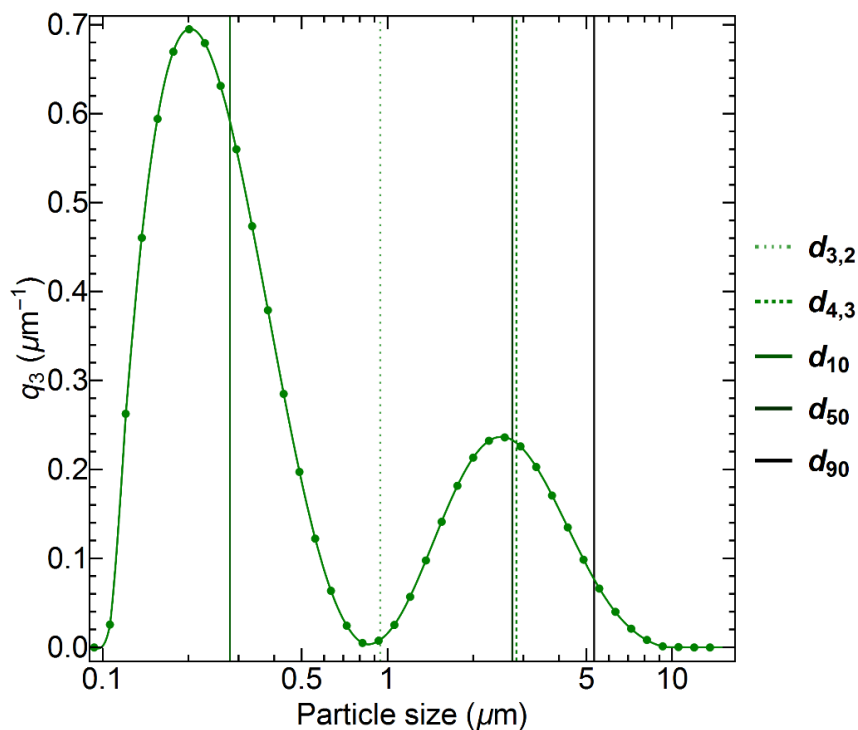
Figure 3.7: Standardised particle size distribution of zeolite, obtained via laser diffraction, identifying the $d_{3,2}$, $d_{4,3}$, d_{10}, d_{50} and d_{90} values.
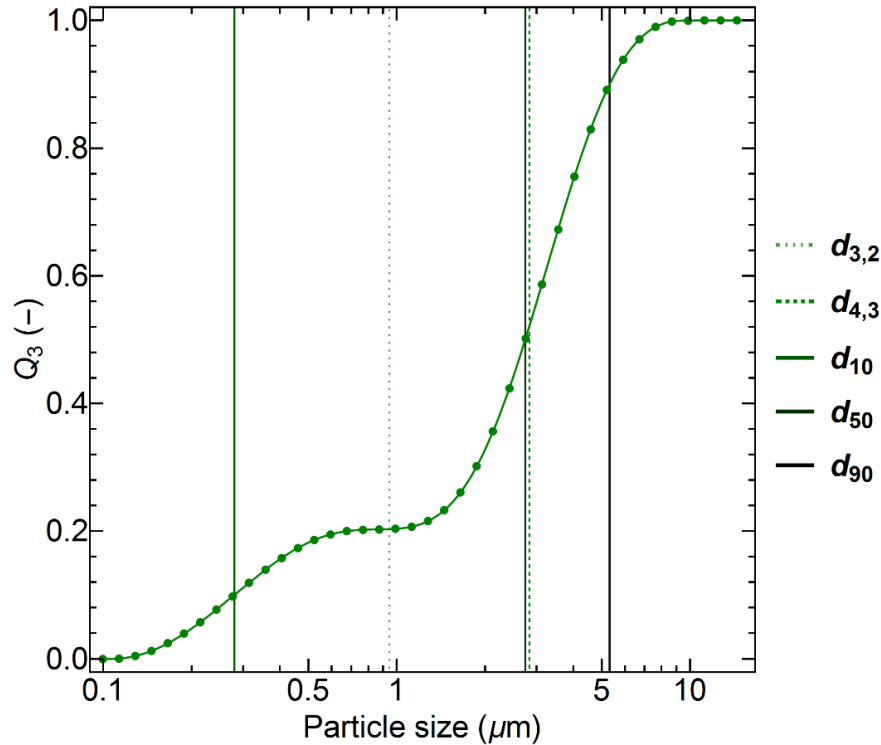
Figure 3.8: Cumulative particle size distribution of zeolite, obtained via laser diffraction, identifying the $d_{3,2}$, $d_{4,3}$, d_{10}, d_{50} and d_{90} values.

3.3.4.2 Density

The true density of zeolite, determined with a triplicate of helium pycnometry experiments, was found to be 2.10 g/cm^3. The manufacturer reports no density value for comparison.

3.4 Liquid properties

For the experiments performed in this study, four different binder liquids were used: silicone oil, aqueous hydroxypropyl methylcellulose (HPMC) solution, aqueous polyethylene glycol (PEG) solution and liquid PEG. Viscosities were varied by using different grades of silicone oil and PEG; a single HPMC solution was used. All liquids were analysed using rheometry to determine their viscosities. Liquid densities were determined using density measurement flasks; the liquid surface tension and liquid-powder contact angles were determined with a goniometer. A full list of solutions used and their properties is shown in Table 3.2.

Table 3.2: Liquids used and their properties. Standard errors are shown between brackets.

Liquid	Types	Density (g/cm^3)	Viscosity (mPa·s)	Surface tension (mN/m)
Silicone oil	10 cSt	0.9407 (0.0001)	12.95 (0.06)	19.49 (0.07)
	50 cSt	0.9640 (0.0001)	51.74 (0.09)	21.11 (0.05)
	100 cSt	0.9684 (0.0001)	104.8 (0.1)	19.92 (0.06)
	1000 cSt	0.9715 (0.0001)	1042.8 (0.9)	20.25 (0.08)
HPMC-solution	12 wt% saturated	1.0944 (0.0004)	200 (2)	45.3 (0.7)
PEG solution	50 wt% PEG4,000	1.0942 (0.0001)	130 (1)	52.4 (0.6)
	50 wt% PEG20,000	1.0953 (0.0001)	3192 (9)	53.0 (0.3)
PEG600	PEG600, 25.0 °C	-	131.6 (0.2)	-
	PEG600, 30.0 °C	-	103.1 (0.2)	-
	PEG600, 32.5 °C	1.1172 (0.0001)	94.54 (0.07)	42.9 (0.2)
	PEG600, 35.0 °C	-	82.6 (0.2)	-
	PEG600, 40.0 °C	-	66.3 (0.1)	-

3.4.1 Silicone oils

Silicone oils, provided by Sigma-Aldrich, were selected as one of the liquids investigated due to their low vapour pressure. Granules produced with this binder will, therefore, not dry. This allows for straightforward calculation of granule growth via mass measurements. Four different grades of oil with varying viscosities were used: 10 cSt, 50 cSt, 100 cSt and 1000 cSt. In order to increase the visibility of the silicone oils, the liquids were dyed with Solvent Blue 59 (Sigma-Aldrich). This was done by slowly adding small amounts of dye until the liquid reached a clearly visible blue colour. The densities of the dyed oils were 0.94, 0.96, 0.97 and 0.97 g/cm^3 for 10, 50, 100 and 1000 cSt silicone oil, respectively. These values are close to values for the undyed oils provided by Sigma-Aldrich. The interfacial tension was found to be approximately 20 mN/m for all silicone oils.

3.4.1.1 Viscosity

The viscosity of the silicone oils was measured by a single measurement using rheometry. For 10 cSt silicone oil, the measurement was performed in a shear rate range of 0.1-1000 s^{-1}, as the equipment is more tuned for higher-viscosity liquids. The full measurement range is shown in Figure 3.9.

Overall, the curves show linear behaviour, although the lines fluctuate more below a shear rate of 1 s^{-1}. Measurements below this value are used to determine whether a liquid is shear-thickening or shear-thinning and, overall, measurements in this range show more variation for all liquids explored. In the case of the silicone oils analysed, the values mostly fluctuate around the same value at low shear. During the experimental work, shear is expected to be higher than this range.

The average viscosity was calculated from the values obtained at a shear rate of 1-1000 s^{-1}, as this range shows the most constant behaviour. The viscosities determined were 12.95, 51.74, 104.8 and 1042.8 mPa•s for 10, 50, 100 and 1000 cSt silicone oil, respectively. This is slightly more viscous than expected from the kinematic viscosities provided by Sigma-Aldrich, and may be caused by the presence of dye in the liquid.
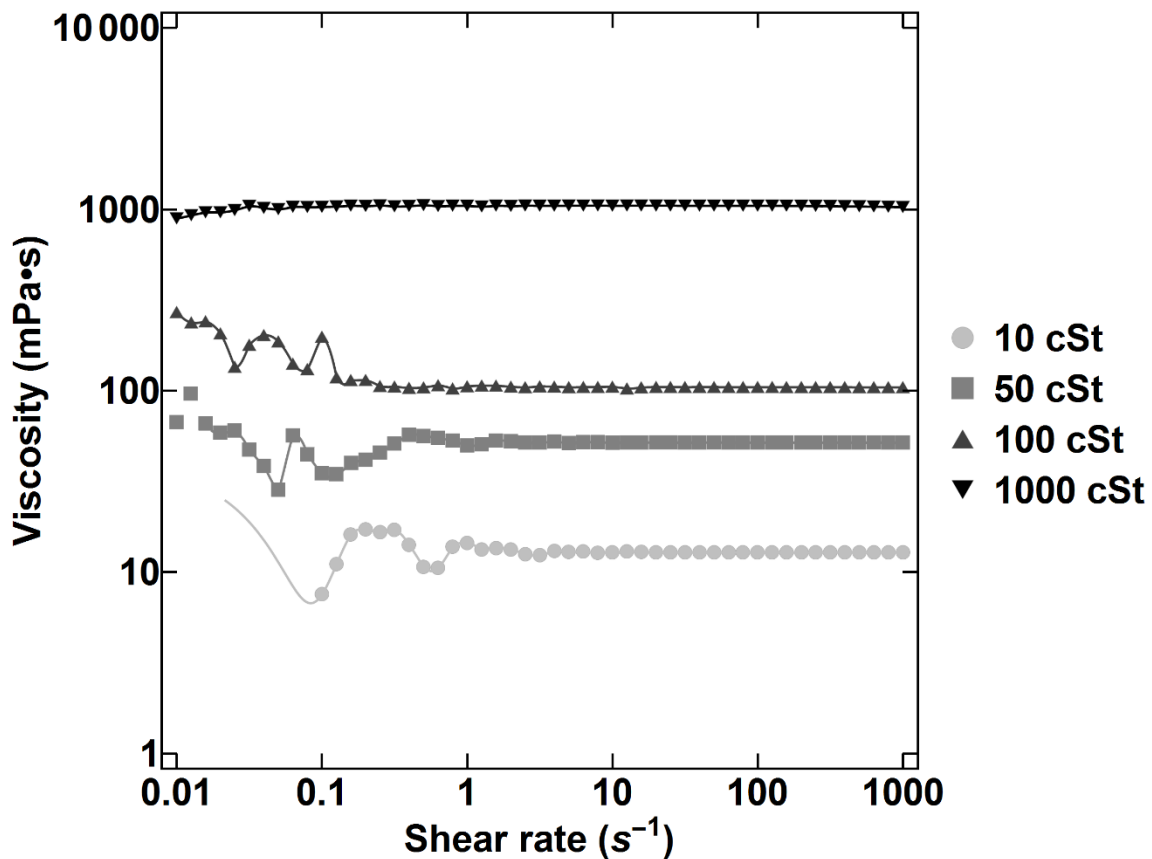
Figure 3.9: Viscosities of dyed 10, 50, 100 and 1000 cSt silicone oils as a function of the shear rate, shown on logarithmic axes.

3.4.2 Hydroxypropyl methylcellulose solutions

Hydroxypropyl methylcellulose (HPMC: Tylopur 603, provided by Shin-Etsu Chemical Ltd.) was dissolved in water saturated with lactose in order to reduce the effect of lactose dissolution during the experiments using lactose as the powder component. Saturation was performed by first dissolving a surplus of lactose in distilled water and filtering the resulting suspension. The filtrate was then used for the preparation of HPMC. A volume of lactose solution equivalent to the volume of water needed to create a 12 wt% HPMC solution was added. After the preparation of the solution, Erythrosin B (Sigma-Aldrich), a red dye, was added to improve visibility of the liquid. The shelf life of HPMC solution saturated with lactose is short (about 2 weeks) due to degradation of the lactose. For this reason, three freshly prepared solutions were used for characterisation of the liquids.

The densities and surface tensions of all HPMC solutions were similar, with an average density of 1.09 g/cm^3, and interfacial tension of 45.3 mN/m.

3.4.2.1 Viscosity

To estimate the viscosity of the HPMC solution used for granulation, three separately prepared solutions were analysed using rheometry. A comparison of the three obtained curves is shown in Figure 3.10.

Unlike the silicone oils, HPMC solutions show a clear increase in viscosity at low shear rates. This is a typical example of shear thinning behaviour. Interestingly, the second solution prepared shows less viscous behaviour at low shear rates. This could indicate that there is some variation between prepared batches. However, at higher shear rates, the solutions appear to be very similar. During granulation, high shear rates are more likely to occur than low shear rates, so the variation between granules produced by different solutions should be minimal.

Due to its shear thinning properties, the viscosities of the HPMC solutions were calculated from values obtained at shear rates varying between 10 s^{-1} and 1000 s^{-1}. Viscosities were found to be 188, 200 and 202 mPa•s, giving an average viscosity of 197 mPa•s.

3.4.3 Aqueous polyethylene glycol solutions

Polyethylene glycol (PEG, provided by Sigma-Aldrich) solutions were prepared with distilled water with acid red 1 dye (Sigma-Aldrich). First, a 1 wt% dye solution was prepared. Next, polyethylene glycol was dissolved in the dye solution in a 1:1 mass ratio. In this way, a 50 wt% PEG solution was produced. Two different PEGs were used to create solutions of different viscosities: PEG 4000 and PEG 20000. The liquids had similar densities of 1.0942 and 1.0953 g/cm^3 and surface tensions of 52.4 and 53.0 mN/m, respectively.
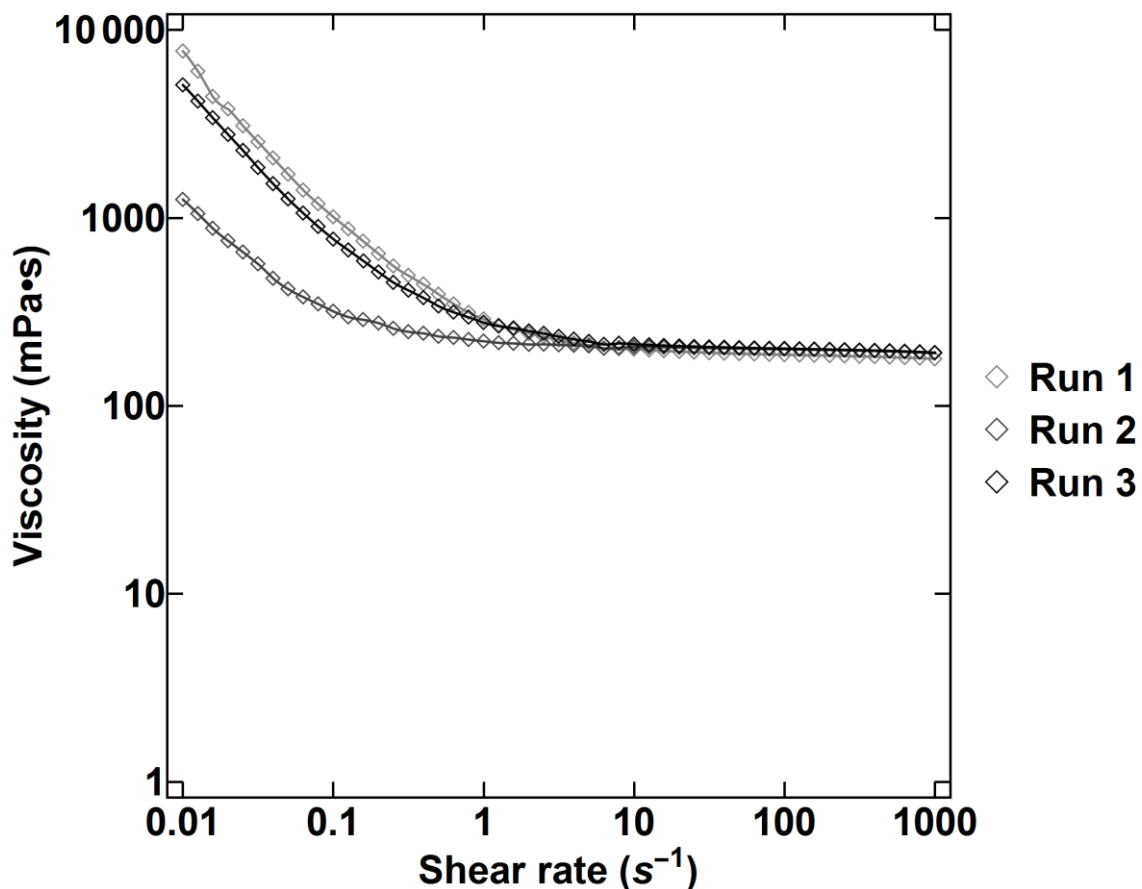
Figure 3.10: Viscosities of three lactose-saturated 12 wt% HPMC solutions as a function of the shear rate, shown on logarithmic axes.

3.4.3.1 Viscosity

Both the PEG 4000 and the PEG 20000 solutions were analysed using rheometry to obtain their viscosities. A comparison between the two solutions is shown in Figure 3.11. The behaviour of both liquids differs at low shear rates. The PEG 4000 solution shows shear thinning behaviour, whereas the PEG 20000 solution has a fairly constant viscosity. However, both solutions show constant behaviour in the shear rate range of 1-1000 s^{-1}, which is probably the most relevant range for granulation.

Viscosities calculated in the standard shear rate range were found to be 130 and 3192 mPa•s, for the PEG 4000 and the PEG 20000 solution, respectively.

3.4.4 Molten polyethylene glycol

A single experiment was performed using granulation with molten PEG 600. PEG 600 is a waxy solid at room temperature, with a melting point of 20-25 °C. This range allows for granulation with the pure liquid, but analysis of granules without a liquid component by cooling the granules down below the melting point. At 32.5 °C, the starting temperature of the experiments, the density of liquid PEG 600 was measured to be 1.1172 g/cm^3, and its surface tension 42.9 mN/m.
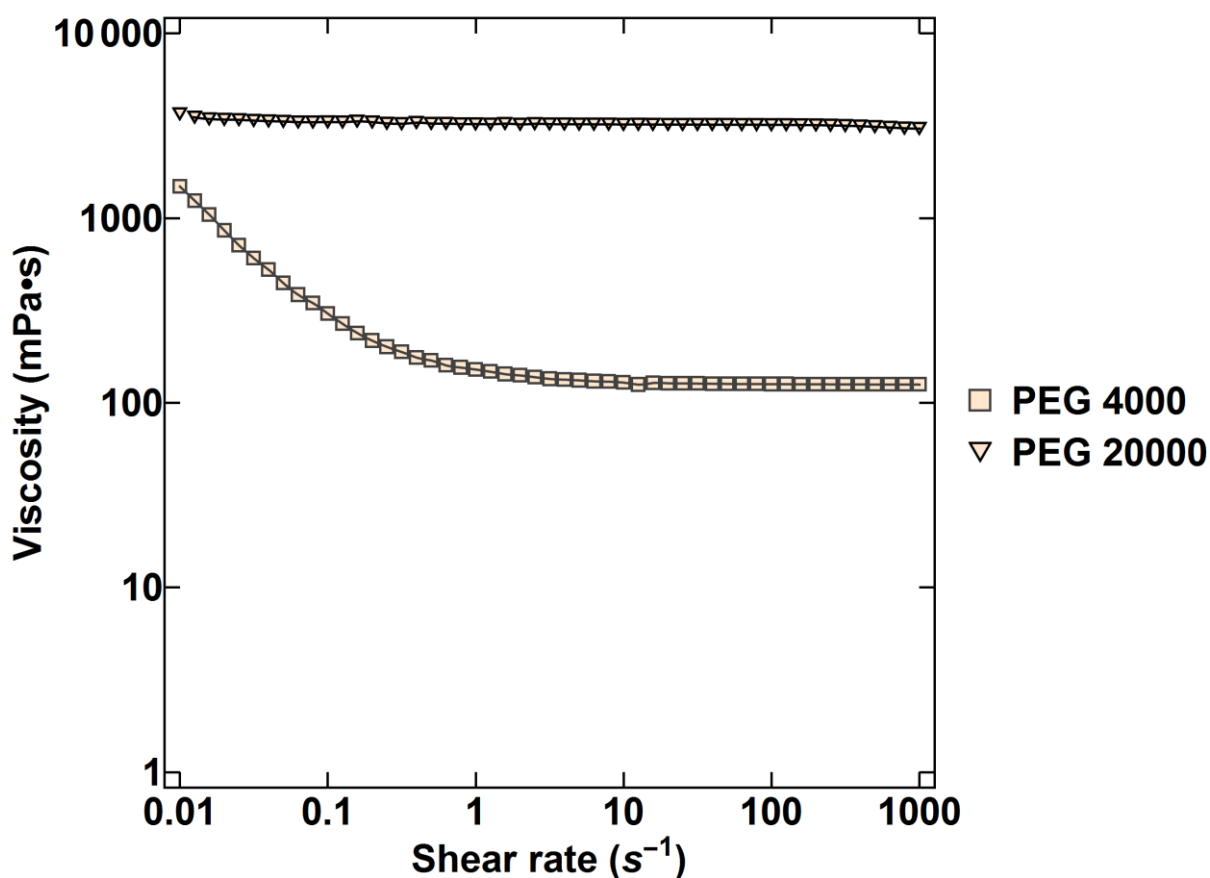
Figure 3.11: Viscosities of 50 wt% PEG 4000 and PEG 20000 solutions as a function of the shear rate, shown on logarithmic axes.

3.4.4.1 Viscosity

Since PEG 600 is a solid at room temperature, it was heated to 32.5 °C to melt it before use in the experiments. In order to obtain information on the viscous behaviour of liquid PEG 600 in the temperature range, rheometry was used to determine the viscosity at four different temperatures: 25, 30, 35 and 40 °C. A comparison between these measurements is shown in Figure 3.12.

At all four different temperatures, PEG 600 has a consistent viscosity for the largest part of the evaluated shear rate range of 0.01-1000 s^{-1}. For shear rates between 0.01 and 0.1 s^{-1}, there are more fluctuations in the measurements, but not enough to draw any conclusions on shear thinning or thickening. As expected, the viscosity of PEG 600 decreases with increasing temperatures. The viscosities, calculated from the standard shear rate range of 1-1000 s^{-1}, were found to be 131.6, 103.1, 94.5, 82.6 and 66.3 mPa•s for 25, 30, 32.5, 35 and 40 °C, respectively. Since PEG 600 is heated to about 32.5 °C before use, the viscosity is expected to be at least 94.5 mPa•s during granulation, becoming more viscous due to cooling as the experiment progresses.
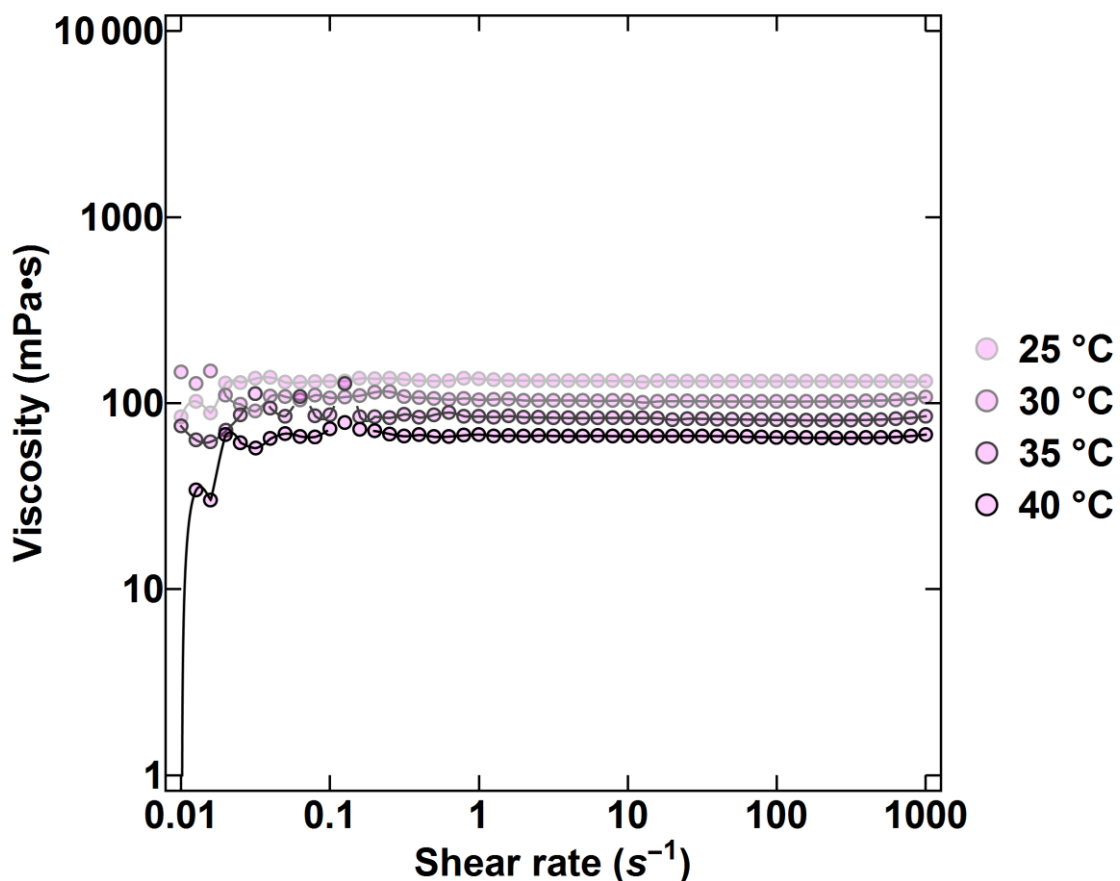
Figure 3.12: Viscosities of PEG 600 at 25 °C, 30 °C, 35 °C and 40 °C as a function of the shear rate, shown on logarithmic axes. 32.5 °C is not shown for clarity of the graph.

3.5 Powder-binder systems

In this study, fourteen different powder-binder were used overall. All systems used are shown in Table 3.3. The table also lists all contact angles for the powder-binder systems evaluated. As expected, most liquids wet well. For most systems, the liquid droplet spread almost instantly, making the contact angle so low that it could not be measured accurately. For such systems, the contact angle is denoted as *<20°*. Only two systems spread slow enough to determine an actual contact angle: glass beads-PEG 4000 (55.23°) and lactose-PEG 20000 (71.18°). It should be noted, however, that for both systems, the liquid continued to move very slowly after these measurements, and a stable point was never reached. It is highly likely that the liquid would continue to spread further on the powder material.

In order to verify this, the droplet was left for 2 minutes after the initial measurement. Both systems showed further spreading. An example snapshot is shown in Figure 3.13. Clearly, the liquid has spread further, as confirmed by the contact angle, which is 10° lower than the originally measured contact angle. This finding suggests that these liquids are expected to wet, but that the kinetics are much slower, which might affect granulation. Where relevant, such effects are discussed in the chapters where these two systems are used.

3.6 Methods

This section provides a brief general description of the experiments performed in this work. More detailed descriptions can be found in Chapter 4.2, Chapter 5.3 and Chapter 6.3. Every study used the same overall experimental method. Granules were first prenucleated and subsequently granulated, extracted and analysed. For a single powder-binder system, multiple experiments were performed at different granulation times in order to study the consolidation and layered growth behaviour of the granules.

A detailed description of all the granulation equipment and analysis methods is given in the relevant experimental chapters.

Table 3.3: Overview of all powder-binder systems used in this work

Powder	Binder	Contact angle (°)
Glass beads	Silicone oil 50 cSt	<20
	Silicone oil 100 cSt	<20
	Silicone oil 1000 cSt	<20
	50 wt% PEG 4000	55.23 (0.53)
Lactose monohydrate	Silicone oil 10 cSt	<20
	Silicone oil 50 cSt	<20
	Silicone oil 10 cSt	<20
	Silicone oil 1000 cSt	<20
	12 wt% HPMC	<20
	50 wt% PEG 4000	<20
	50 wt% PEG 20000	71.18 (0.97)
	PEG 600, 32.5 °C	<20
Plastic beads	Silicone oil 10 cSt	<20
Sodium aluminosilicate	Silicone oil 100 cSt	<20
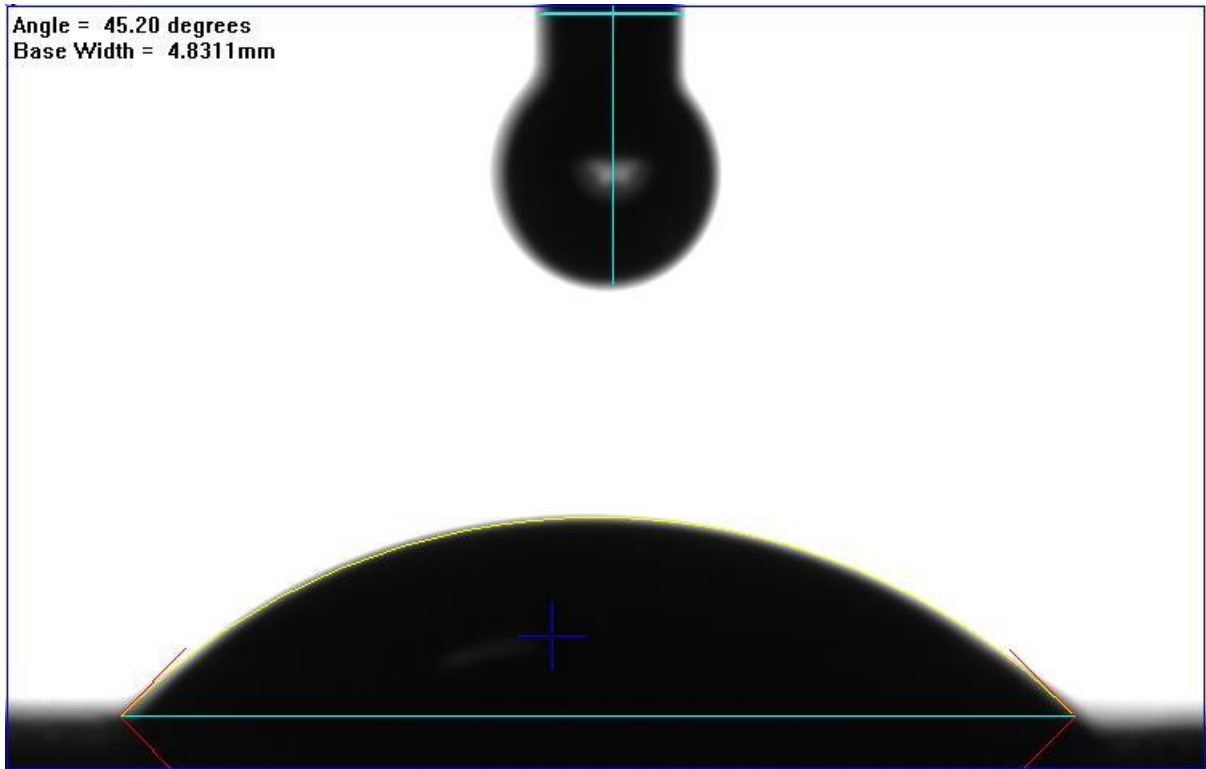
Figure 3.13: Snapshot of glass-PEG 4000, two minutes after the measurement. The contact angle is 10° lower than the originally measured contact angle.

Prenucleation outside of the granulator was done in order to reduce the complexity of the granulation process. By prenucleating granules, there was no need to add binder liquid during the granulation process. Consequently, the effects of nucleation and coalescence during granulation could be ignored. Various set-ups were used for prenucleation. For the experiments described in Chapter 4, granules were mostly nucleated manually with a syringe. The set-up described in Chapter 5 used a syringe pump for prenucleation. In Chapter 6, granules were prenucleated by making a paste of powder and binder and cutting the paste into pieces. Details of these procedures are given in the relevant experimental chapters.

Three different types of granulation equipment were used. Initially, experiments were performed with a high-shear mixer and a three-bladed impeller (Chapter 4). For the second series of experiments, a custom, consolidation-only granulator (COG) was designed to reduce granule breakage, as described in Chapter 5. The paste-based granules were granulated using a high-shear mixer with a flat plate impeller (Chapter 6).

After granulation, product granules were extracted from the granulator and separated from the powder by gentle sieving. The granules were then weighed in order to gain insight in their growth behaviour. Product granules produced in the studies with the COG (Chapter 5) and high-shear mixer with flat plate (Chapter 6) were also analysed for their true and envelope density by helium and powder pycnometry, respectively. In this way, the consolidation behaviour of these granules could be studied. Finally, a few representative granules were analysed for their internal structure using X-ray tomography.

Chapter 4.   Consolidation and layering in a high-shear mixer

4.1 Introduction

From the literature review in Chapter 2, it becomes clear that there are knowledge gaps in the field of granulation. One such gap is the kinetics of consolidation and the resulting layered growth. Hounslow et al. [30] proposed models for this mechanism in both static and dynamic situations. Pitt et al. [31] found that the static model, based on surface-tension driven growth, described consolidation and layered growth exceptionally well in static powder beds. However, a mechanistic study of consolidation and layered growth in dynamic powder beds, which is more realistic than static beds for granulation, has not been performed in the literature.

The purpose of this initial study was to develop an experimental granulation method that allows for the study of consolidation and layered growth in a dynamic situation. This method should separate the phenomena of interest from other granulation phenomena, i.e. breakage, attrition, agglomeration and nucleation. The method should, therefore, meet the following criteria:

- The granules should be in a three-dimensional moving powder bed
- No new nuclei should be created during the granulation process
- Granules should not agglomerate during the granulation process
- Forces experienced by the granules should be high enough to allow the granules to consolidate
- Forces experienced by the granules should be as low as possible to reduce the effect of breakage and attrition
- The method must be reproducible
- Preferentially, it should be possible to compare the granules to those produced by Pitt et al. [31] to investigate the differences between dynamic and static granulation, e.g. by using a similar materials and methods of nucleus production

The first requirement is straightforward: in order to evaluate consolidation and layered growth of granules in a dynamic situation, a moving powder bed is needed. This requirement does not limit the selection of granulation equipment. Preventing nucleation during granulation can be easily solved by prenucleating the granules outside of the granulator. In fact, prenucleation was also employed by Pitt et al. [31], although they allowed the granules to grow statically after prenucleation to investigate layered growth, whereas this study focuses on dynamic growth. An additional advantage of prenucleation is the prevention of granule agglomeration, as addition of liquid during the granulation process is not required when using prenucleated granules; only the binder already present in the granules is used for consolidation and growth. To further prevent agglomeration, a sufficient amount of powder should be present. As long as surface-wet granules have access to fresh powder, granule agglomeration should not occur [157]. The slightly paradoxical need for high-force impacts to cause consolidation but low enough forces to prevent breakage and attrition leads to difficulty in selecting appropriate equipment. A delicate balance must be struck between exerting sufficient force while preventing breakage and attrition as much as possible. The reproducibility of the method should be good, as the contents of the granulator have to be extracted regularly as this study requires the monitoring of granules over time. To ensure the only difference between different batches of granules is the granulation time, a fresh batch of

prenucleated granules should be as similar as possible to the previous batch. This means the prenucleation process should be reproducible. Finally, comparison to Pitt et al.'s data should give valuable insight into the difference between static and dynamic consolidation and layered growth. Given the above criteria, an experimental method and set-up were selected. This selection is discussed in Section 4.2.

The type of equipment selected for the granulation process was a high-shear mixer. Although such mixers are capable of generating high shear, they can also be operated at low rotational speeds, which should reduce breakage and attrition. As long as a roping regime is maintained, good mixing can be achieved [7]. Even at such low speeds, it is expected that impacts are high enough to cause consolidation of granules.

4.2 Materials and methods

This initial investigation of consolidation and layered growth focused on experiments in a high-shear mixer. Granules were prenucleated outside of the mixer, granulated, extracted and analysed. A list of all experiments performed can be found in Table 4.1.

All powders were passed through a 1.14 mm sieve before use in order to remove any lumps. A powder bed was prepared in a petri dish by gently flattening the surface of the bed with a ruler. The amount of powder in the petri dish was determined, after which a total amount of powder minus the powder bed mass was added to the high-shear mixer (Key International Inc. KG-1 Granulator with a 2.3 L bowl) before granulation. For lactose and plastic beads, a total amount of 330 g was used. For zeolite, the amount was 450 g. For this granulator fill level, the powders showed roping behaviour at the selected impeller speed of 250 rpm. This behaviour was desired since the roping regime [138], characterised by powder being pushed up the walls and falling back on the impeller, indicates good mixing. To ensure a good distribution of the powder in the granulator, the mixer was run for 20 s at 250 rpm.

After preparing the powder bed and granulator, granules were prenucleated on the powder bed in the petri dish. For most experiments, this was done by hand, with a 20 mL syringe and a blunt 30 G (0.16 mm internal diameter) needle. The needle tip was kept at a height of 5 cm above the powder surface.

Table 4.1: Overview of all systems used in experiments with the high-shear mixer.

Powder	Binder	Binder delivery	# of nuclei	Times (s)	# of data points
Lactose	100 cSt silicone oil	Manual	40	3-24	4
Lactose	1000 cSt silicone oil	Manual	20	6-24	3
Zeolite	100 cSt silicone oil	Manual	40	3-24	3
Lactose	12 wt% HPMC	Manual	20	3-24	3
Plastic beads	10 cSt silicone oil	Manual	40	3-9	3
Lactose	1000 cSt silicone oil	Syringe pump	40	3-36	1
Lactose	100 cSt silicone oil	Manual	40	3-36	6 (x3)
Lactose	50 cSt silicone oil	Manual	40	3-15	4 (x3)
Lactose	10 cSt silicone oil	Manual	40	3-15	3 (x3)

When possible, 40 nuclei were produced. This was done in order to increase the precision of the results. However, for exploratory experiments with lactose-1000 cSt silicone oil and lactose-12 wt% HPMC solution, the high liquid viscosity did not allow for easy manual operation of the syringe. To ensure all nucleated granules had a similar nucleation time before addition to the granulator, only 20 nuclei were produced.

For an additional experiment using lactose and 1000 cSt silicone oil, a syringe pump (Harvard Apparatus PHD ULTRA I/W) was used for easier droplet generation. The set-up was mostly the same as for manual nucleation, but instead of connecting the syringe directly to the needle, a tube and Luer Lock connectors were used. The syringe pump was operated at a constant speed of 5 µL/s, which yielded an acceptable nucleation rate.

After nucleation, granules were immediately added to the granulator, after which the granulator was operated at 250 rpm for a set amount of time. Granulation times varied from 3 to 36 seconds. The granules were then extracted by passing all the granulator contents through a 1.4 mm sieve. Sieving was performed manually by repeatedly tapping the mesh with a spoon to allow the powder to pass through. This method was used in order to prevent breakage of the granules. The extracted granules were removed from the sieve and stored in petri dishes under ambient conditions for analysis. After a single batch was run at a specific time, a new batch was nucleated under the same conditions and the experiment was repeated for a longer granulation time.

Product granules were weighed individually using a microbalance (Mettler-Toledo XS3DU, 1 µg accuracy). This method allows for comparison to Pitt et al.'s results [31], which uses the same procedure for measuring granule growth. Additionally, Hounslow et al.'s models [30] predict the change in volume of the granules, which can be directly related to mass via density. Therefore, monitoring the growth kinetics of the granulation process can be compared to the models. For the lactose-HPMC system, granules were dried in an oven at 32.5 °C overnight before analysis to prevent fluctuations in the granule mass due to evaporating water.

The experimental work performed was split into two sets. The first set comprises the first five experiments described in Table 4.2: lactose-100 cSt silicone oil, lactose-1000 cSt silicone oil (no syringe pump), zeolite-100 cSt silicone oil, lactose-12 wt% saturated HPMC solution and plastic beads-10 cSt silicone oil. These experiments were performed to investigate the suitability of the several systems used. The second set comprised of reproducibility experiments, and was performed with lactose-based systems. A single experiment was performed with 1000 cSt silicone oil and a syringe pump, and three experiments each were performed with 10 cSt silicone oil, 50 cSt silicone oil and 100 cSt silicone oil. In the results and discussion of the experiments, Section 4.3, all liquids will be described in terms of their viscosity values, as shown in Table 4.2.

Table 4.2: Powder-binder systems used and binder dynamic viscosity.

Set	Powder	Binder	Viscosity (mPa•s)
	Lactose	100 cSt silicone oil	105
	Lactose	1000 cSt silicone oil	1043
1	Zeolite	100 cSt silicone oil	105
	Lactose	12 wt% HPMC	200
	Plastic beads	10 cSt silicone oil	13
	Lactose	1000 cSt silicone oil	1043
	Lactose	100 cSt silicone oil	105
2	Lactose	50 cSt silicone oil	52
	Lactose	10 cSt silicone oil	13

4.3 Results and discussion

The main purpose of performing the experiments with a range of systems was to explore the suitability of these systems for consolidation and layered growth studies as well as to investigate the potential of using a high-shear mixer for this purpose. In order to quantify layered growth, an increase in granule mass must be observed. Furthermore, extracted granules must remain intact, without obvious attrition or breakage. Finally, the materials should have good enough flowability to allow for rapid sieving, as large differences in extraction times might cause variations in granule properties within a single batch.

Figure 4.1 shows a selection of different granules from set 1 extracted after 3, 9 and 24 seconds of granulation. For the lactose-based systems prepared with 1043 mPa•s silicone oil and 200 mPa•s HPMC, the granules are mostly intact after 3 seconds of granulation. However, after 9 seconds, the granules show cracks, wear and deformations. After 24 seconds, very few undamaged granules remain.

This is different for zeolite and 105 mPa•s silicone oil. For all times, the granules show little wear, as well as very little breakage. This observation implies that zeolite-based granules have a higher strength than lactose-based granules. Considering the fact that the zeolite powder has smaller primary particles than lactose monohydrate, this result is logical; smaller primary particles are expected to yield stronger granules due to stronger capillary forces [62].

An additional interesting observation from visual inspection of the granules is the change in their shape. As time progresses, plastic deformation is observed for some granules; they become flatter and more elongated for all systems, although this effect is less pronounced in the zeolite-based system. This is most likely the result of collisions with the granulator impeller exceeding the yield strength of the granules. This hypothesis is supported by the observation of a build-up of granulated material on the impeller.

Lactose-1043 mPa•s silicone oil   **Zeolite-105 mPa•s silicone oil**   **Lactose-200 mPa•s HPMC**
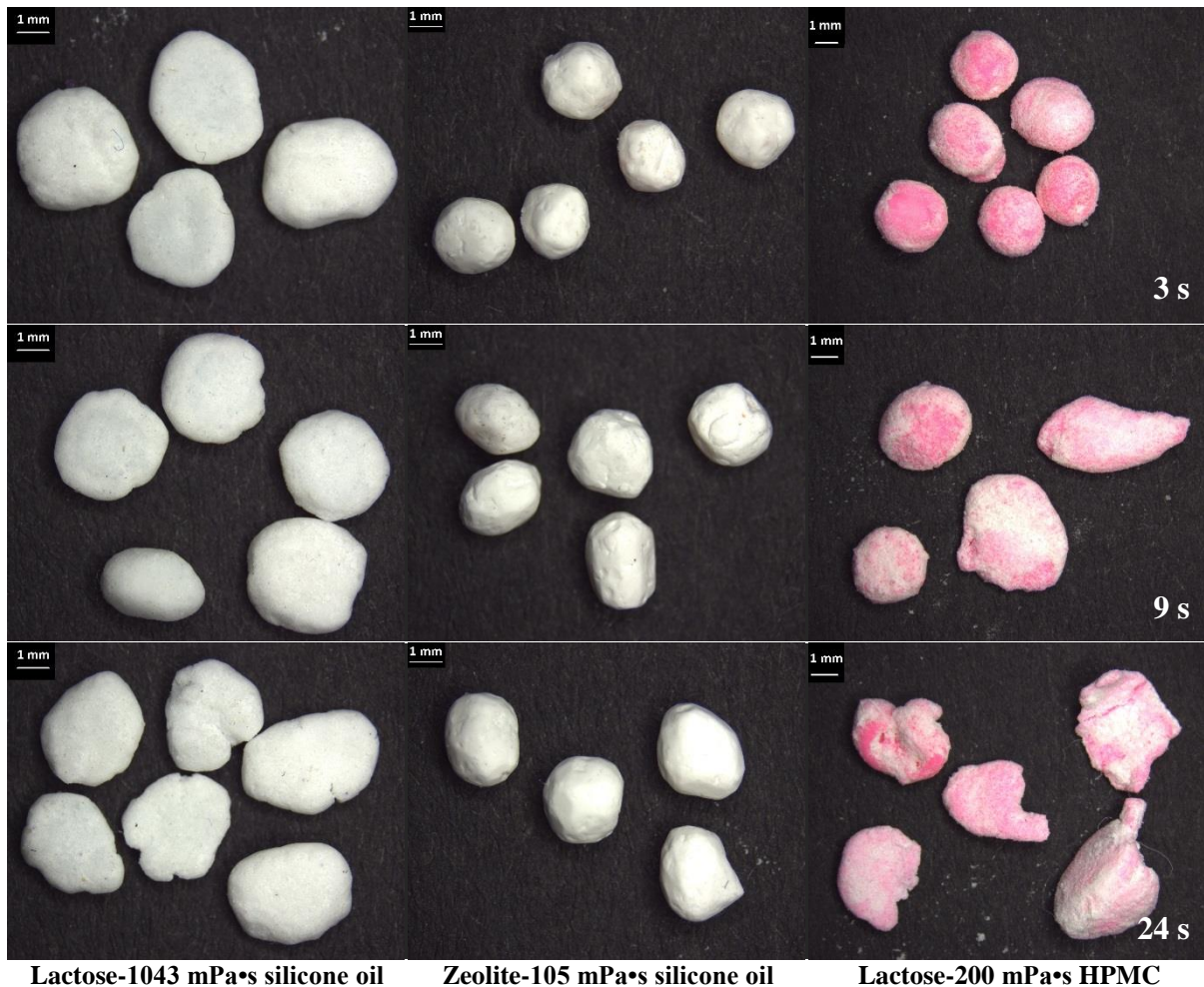
Figure 4.1: Comparison of granules produced in the high-shear mixer for three different systems. Rows show images of granules extracted after 3, 9 and 24 seconds, respectively.

Figure 4.2 shows the evolution of the granule mass as a function of time for all systems evaluated. Consistent with the observations from Figure 4.1, the systems based on lactose and silicone oil showed a slight decrease in mass, whereas the zeolite-based system showed an increase in mass. The system comprising lactose and 200 mPa•s HPMC solution showed an initial increase in mass and then a decrease. The system produced with plastic beads showed a decrease in mass and then an increase, resulting in a slight overall decrease in mass. Additionally, breakage caused the error of the granule mass to increase, as fewer granules were recovered, and damaged granules were potentially counted as intact granules. No intact granules survived more than 9 seconds of granulation. Therefore, no data is shown after this time.

Most of the observations from Figure 4.2 can be explained considering viscosity and particle size. A smaller particle size usually leads to stronger granules due to increased capillary forces [62]. Furthermore, using a higher viscosity binder should result in stronger granules, as well as slower growth due to increased viscous forces. Figure 4.2 clearly confirms that this is indeed true for zeolite-silicone oil. The combination of a high viscosity binder and small primary powder particles leads to a system that displays actual growth behaviour instead of breakage and attrition.
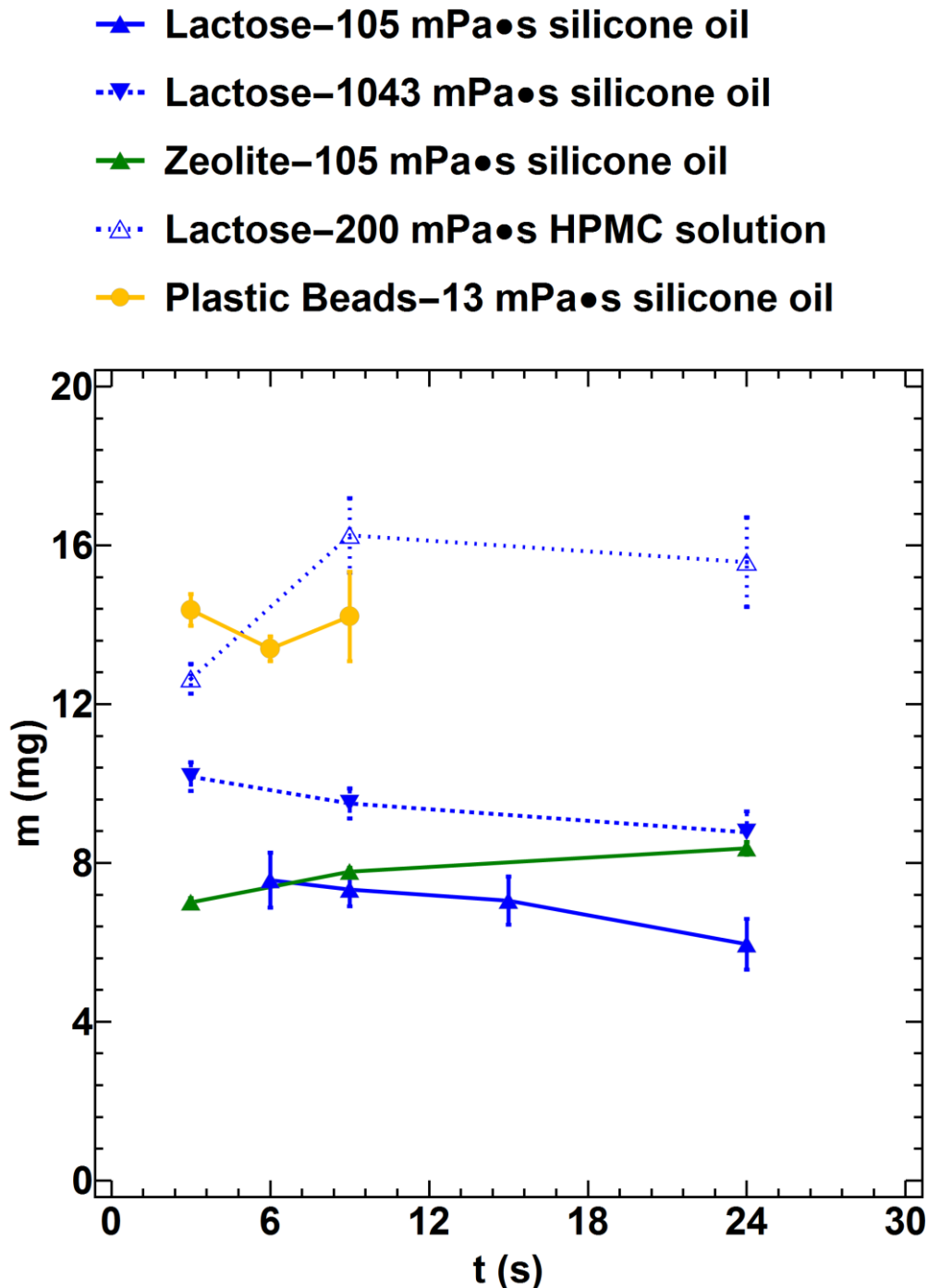
Figure 4.2: Evolution of granule mass as a function of time for five different powder binder-systems: 1. lactose-105 mPa•s silicone oil, 2. lactose-1043 mPa•s silicone oil, 3. zeolite-105 mPa•s silicone oil, 4. lactose-200 mPa•s HPMC solution and 5. plastic beads-13 mPa•s silicone oil. Lines were added for clarity and are not based on any fitted model. Errors shown are standard errors.

However, a small particle size does not make zeolite-based systems the ideal candidates for high-shear mixer granulation experiments. Due to its small particle size and cohesiveness, zeolite powder has poor flowability. This results in sieving times of over thirty minutes, which is enough time for the granules to grow significantly according to the static growth model validated by Pitt et al. [31]. Therefore, zeolite powder itself is unsuitable for this type of study.

All data sets presented thus far were single runs with each system. In order to confirm these initial findings further, repeat experiments were conducted for reproducibility purposes

71

and to determine whether the high-shear mixer results were reliable, despite the errors caused by breakage. Figure 4.3 shows a comparison between the triplicate experiments performed with lactose-silicone oil-based systems.

Within a single system, the overall behaviour is qualitatively similar between the different runs. The lowest viscosity binder (13 mPa•s) produces granules that show rapid breakage, with most of the repeats yielding no intact granules after 9 seconds of granulation. Systems with 52 mPa•s silicone oil show relatively less breakage, but display a sharp decrease in mass, indicating heavy attrition. 105 mPa•s silicone oil produces granules which show a relatively stable granule mass, but no overall growth or attrition.
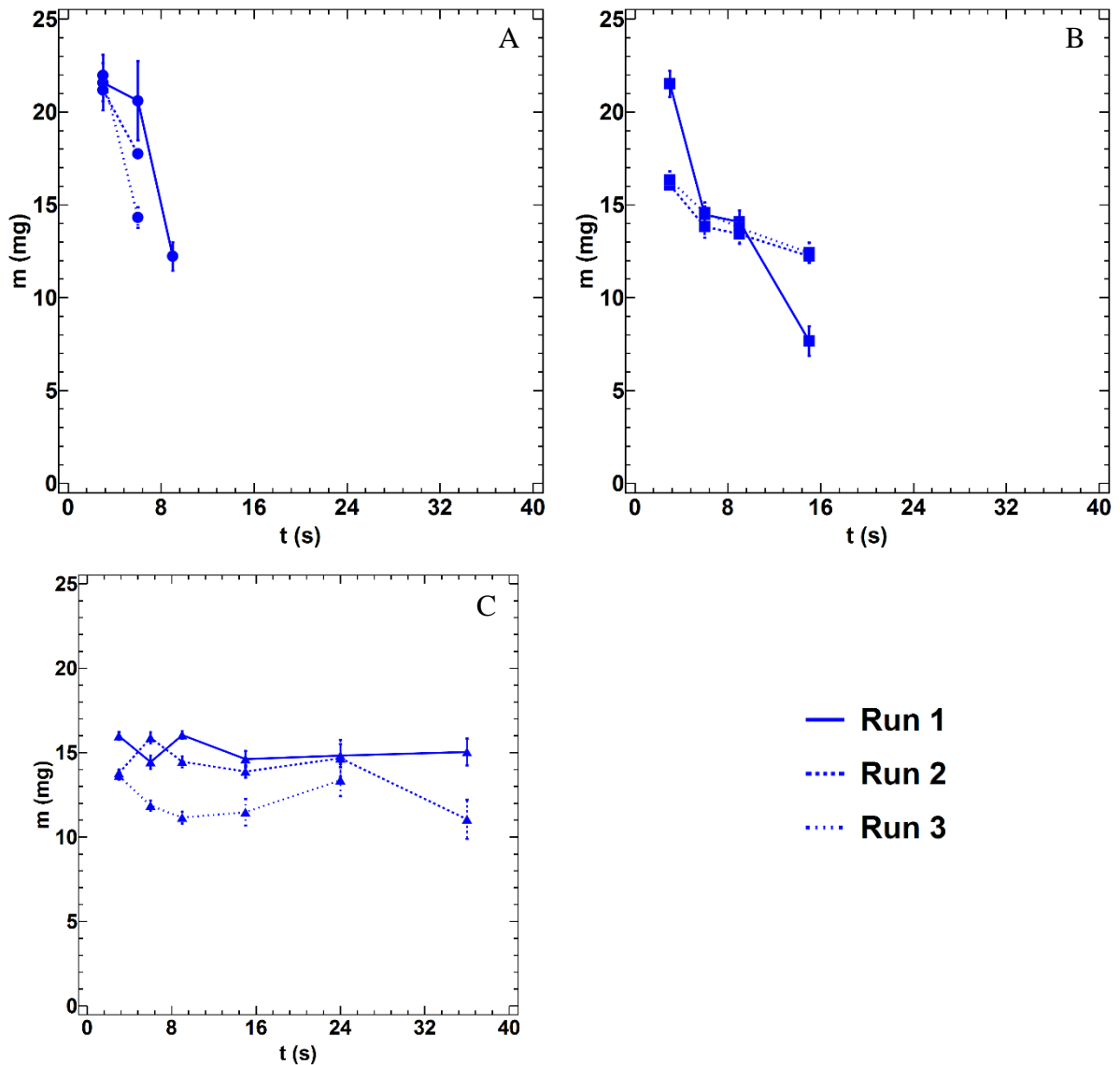
Figure 4.3: Reproducibility of granule growth behaviour for systems with lactose and A. 13 mPa•s silicone oil, B. 52 mPa•s silicone oil and C. 105 mPa•s silicone oil. Lines were added for clarity and are not based on any fitted model. Errors shown are standard errors.

The slight differences in the granule mass values within the same system may be caused by the heavy breakage and attrition observed. Attrition and partial breakage may have led to some granules being considered intact when, in fact, they had been damaged. The only system that showed any constant growth, zeolite-105 mPa•s silicone oil, had such poor powder flowability that the extraction times were deemed too long to generate meaningful and reliable results.

Overall, it can be concluded that none of the systems evaluated had a satisfactory performance for studying consolidation and layered growth due to excessive breakage. However, it is possible that by increasing the binder viscosity, systems that do display growth can be found. In order to investigate this effect of binder viscosity on the granule growth behaviour, the averaged lactose-silicone oil results were compared to those of a higher viscosity system; lactose-1043 mPa•s silicone oil. This comparison is shown in Figure 4.4.

The granulation behaviour shown in Figure 4.4 is logical when considering the binder viscosities of the systems; low-viscosity binders (13 and 52 mPa•s) show a decrease in granule mass, and demonstrate more breakage behaviour. Increasing the binder viscosity to 105 mPa•s leads to a reduction in both breakage and loss of granule mass. More interestingly, the use of a 1043 mPa•s binder does not show an improvement in growth behaviour, although a larger number of intact granules was recovered after granulation compared to the 105 mPa•s silicone oil system. This observation demonstrates that increasing binder viscosity is most likely not a solution to counter breakage in a high-shear mixer effectively for the study of consolidation and layered growth.
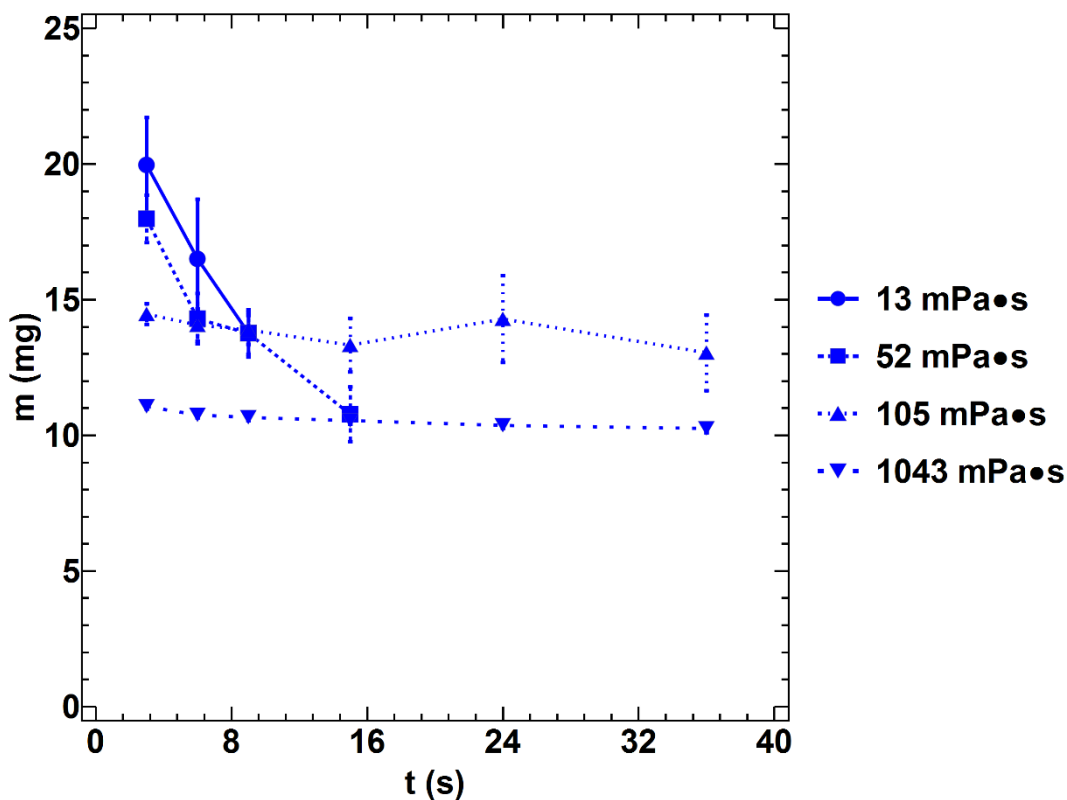
Figure 4.4: Comparison of the evolution of mass for systems with lactose and silicone oils of different viscosities. Data points for 13, 52 and 105 mPa•s silicone oil are based on the averages over three sets each. Lines were added for clarity and are not based on any fitted model. Errors shown are standard errors.

4.3.1 Summary

For the study of consolidation and layered growth, granulation experiments were performed using prenucleated granules in a high-shear mixer. The results show that granules are subject to significant breakage and attrition among all systems evaluated. Even systems with high-viscosity binders demonstrate no overall increase in mass, with the exception of the zeolite-based system. Reproducibility experiments show that the repeats demonstrate qualitative granulation behaviour. Increasing the viscosity leads to a decrease in breakage and a reduction in attrition. However, even for the highest viscosity tested, no growth was observed. Considering these observations, a high-shear mixer is not deemed a suitable piece of equipment for the study of consolidation and layered growth. However, the breakage behaviour observed makes for an interesting study in granule breakage. This topic is discussed in the following section.

4.4 Breakage behaviour in a high-shear mixer

The granules produced in the experiments in the high-shear mixer showed significant breakage behaviour. In order to evaluate the survivability of the granules and the effect of increasing the binder viscosity, the number of intact granules was tracked over time for the lactose-silicone oil data sets. Figure 4.5 shows that it is possible to fit exponential decay curves to the data using a least squares fit in Mathematica, allowing for a reasonable prediction of the number of intact granules after a certain granulation time. A list of decay rates is presented in Table 4.3. Both the figure and table clearly show that for increasing viscosity, the decay rate decreases. This finding implies that breakage is reduced by increasing the binder viscosity. This section focuses on linking the granulation time to physical parameters that might allow for the development of a model for the prediction of granule breakage.

Table 4.3: Standard errors of the fits and decay rates of breakage for the lactose-based systems evaluated.

Binder	Exponential decay rate (s^{-1})	Standard error of fit (-)
10 cSt silicone oil	0.373	0.005
50 cSt silicone oil	0.168	0.026
100 cSt silicone oil	0.088	0.019
1000 cSt silicone oil	0.013	0.015
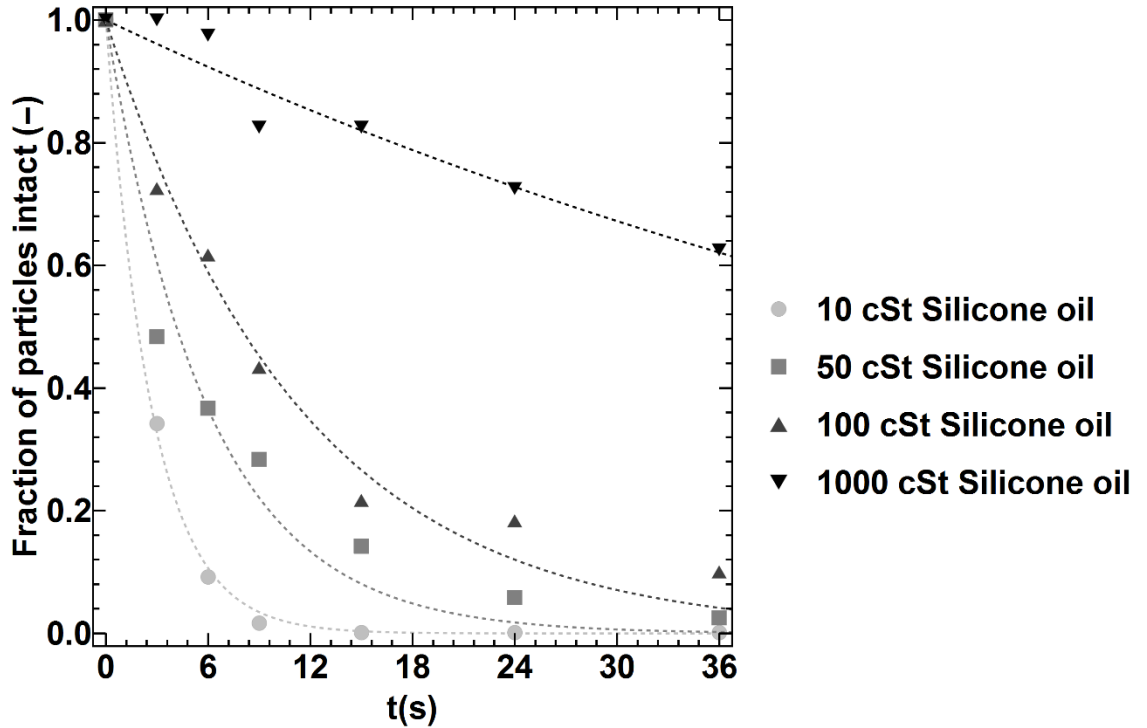
Figure 4.5: Number of surviving granules as a function of time for systems of lactose and silicone oils of different viscosities. The lines fitted are exponential decay functions of the form e^{-a*t}.

4.4.1 Model development

In the literature review in Chapter 2, two different methods of studying breakage are discussed: single granule breakage and process-scale breakage. Vogel and Peukert [117] consider single granule breakage as a stochastic process, and developed a way of calculating the probability of particle breakage S, as shown by Equation 4.1:

$$S = 1 - exp\left(-f_{Mat} * x * k * \left(W_{m,kin} - W_{m,min}\right)\right) \tag{4.1}$$

where f_{Mat} is a material parameter defining fracture behaviour of the particle, x is the particle size, k is the impact number, $W_{m,kin}$ is the kinetic energy of the particle, and $W_{m,min}$ is the minimum kinetic energy required for particle breakage. This method was implemented into population balance models to successfully model a labscale mill.

Liu et al. [16] and Smith et al. [17] developed a breakage-only granulator to study breakage on the process scale. A high-shear mixer was filled with non-granulating sand, and pre-made granules were introduced into the mixer, which was run for a set time. The granules were then extracted and analysed for breakage. Breakage was linked to the Stokes deformation number, St_{def}, and a critical number was proposed. Smith et al. specifically found that impeller shape had a strong influence on breakage behaviour [17].

For the model proposed in this work, breakage is considered as a stochastic process, with a probability of breakage. However, as shown by Liu et al. [16] and Smith et al. [17], there is a correlation between breakage and the Stokes deformation number. Therefore, the model should incorporate the Stokes deformation number in some way to predict breakage. The model considers a granulator as being divided into two zones: a zone in which breakage

occurs, and a zone in which no breakage occurs. Assuming a symmetrical granulator, these zones can be described as areas. Figure 4.6 shows a schematic cross-section of a granulator divided in such a way. Considering ideal mixing, the granules could be in either area at a specific time. Consequently, granules are assumed to be distributed over each region according to the relative size of the regions. At each time step, granules in the no-breakage zone are left intact, whereas granules in the breakage zone have a chance to break. These assumptions imply that the number of intact granules after a single collision, N, can be described using the area of the breakage zone divided by the total available area, r, and the probability of breakage, s. This relationship is shown in Equation 4.2:

$$N = N_0 * \left(1 - (r * s)\right) \tag{4.2}$$

where N_0 is the original number of granules. This expression can be rewritten to account for the number of intact granules after n impacts (Equation 4.3):

$$\frac{N}{N_0} = \left(1 - (r * s)\right)^n \tag{4.3}$$

The number of impacts n are assumed to be the product of impeller speed ω, granulation time t, and an impeller shape factor f. For example, when an impeller has three blades, a single rotation of the impeller provides three impacts for the granules to potentially break, whereas this number may be much lower for a flat plate impeller. The expression can be rewritten as an exponential function (Equation 4.4):

$$\frac{N}{N_0} = exp\left(ln\left(1 - (r * s)\right) * \omega * f * t\right)$$
$$= exp(-a * t) \tag{4.4}$$

where a is a positive, lumped parameter.
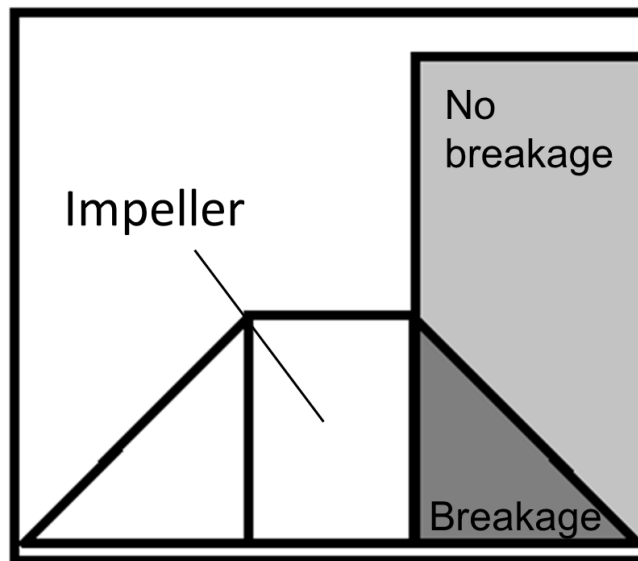
Figure 4.6: Schematic representation of a cross section of the granulator as considered by the model, with the breakage and no-breakage zone.

Equation 4.4 shows that this model agrees with the observation that the number of surviving granules decays exponentially over time. In order to illustrate this, Figure 4.7 shows how all data points collapse onto the single curve e^{-t}. This observation implies that Equation 4.4 is useful for predicting breakage behaviour. However, in order to increase the reliability of the model and its predictive abilities, it is necessary to find a full expression for a, or, more accurately, both the relative size of the breakage zone r and probability of breakage s. Of these two, r is relatively easy to determine, as it depends on the shape of the granulator, and also likely its operating speed. It should be possible to fit this single parameter to actual data. Finding an expression for s is likely to be more difficult. From the literature, it is logical to assume that s is dependent on the Stokes deformation number. This dependency is explored in the following section.

4.4.2 Determination of the probability of breakage

In order to evaluate how the probability of breakage is related to the physical properties of the granules, breakage data from Liu et al. [16] was used[1]. The data comprises 18 different experiments with systems of lactose and two grades of silicone oil, at different liquid saturations and impeller speeds, as listed in Table 4.4. Granules were prepared by extruding and cutting paste with a predetermined formula depending on liquid saturation. The granules were then granulated in a breakage-only granulator with a three-bladed impeller filled with non-granulating sand for up to one minute. The number of surviving granules over time was recorded.
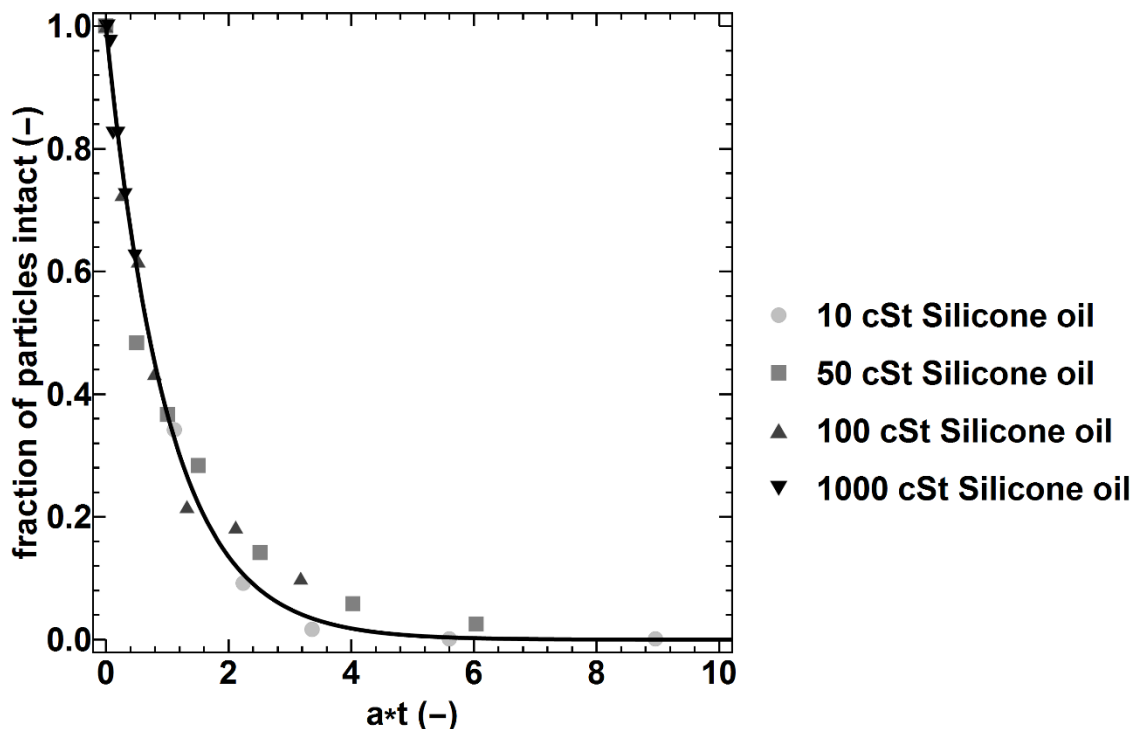
Figure 4.7: Fraction of surviving granules as a function of $a*t$ for systems consisting of lactose and silicone oils of different viscosities. All data points collapse onto the single curve e^{-t}.

---

[1] Raw data kindly provided by Dr. Lian Liu from the University of Surrey for modelling purposes.

Table 4.4: Summary of the breakage data sets evaluated in Liu et al.'s [16] work. Each possible set of conditions was used, for a total of 18 different data sets. Additionally, the table lists fit standard errors and the lumped decay parameter _a_. Data outside of the intermediate breakage range is coloured grey.

Experiment	Silicone oil Viscosity (cSt)	Liquid Saturation (-)	Impeller Speed (rpm)	Fit standard error (-)	a (s^{-1})
1	100	0.3	750	0.000	0.460
2	100	0.3	1000	0.000	0.460
3	100	0.3	1500	0.000	0.460
4	1000	0.3	750	0.002	0.155
5	1000	0.3	1000	0.002	0.155
6	1000	0.3	1500	0.010	0.148
7	100	0.5	750	0.026	0.006
8	100	0.5	1000	0.016	0.008
9	100	0.5	1500	0.031	0.011
10	1000	0.5	750	0.052	0.021
11	1000	0.5	1000	0.034	0.065
12	1000	0.5	1500	0.021	0.090
13	100	0.8	750	0.021	0.002
14	100	0.8	1000	0.037	0.008
15	100	0.8	1500	0.031	0.009
16	1000	0.8	750	0.000	0.000
17	1000	0.8	1000	0.000	0.000
18	1000	0.8	1500	0.008	0.003

Figure 4.8 shows the corresponding fit to the model proposed above, demonstrating that all data collapses neatly onto a single curve. Table 4.4 lists the fit standard errors and the fitted lumped decay parameter _a_. Of particular interest are the granules in the intermediate breakage range. Predicting full or little granule breakage simply requires _a_ to be either large ($a \geq 0.1$ s^{-1}) or very small ($a \leq 0.008$ s^{-1}), respectively, allowing for a range of values that give acceptable results. In the intermediate breakage range ($0.008 < a < 0.1$ s^{-1}), however, small changes on parameter _a_ have a large effect on the fit. The values outside of this range are coloured grey in Table 4.4.

By expressing the obtained fit parameter _a_ as shown in Equation 4.4, it is possible to study the effects of different operating conditions and granule properties on the probability of breakage. For this purpose, the Stokes deformation number St_{def} was used, as defined in the literature review (Equation 2.5). For clarity, the equation is shown below in the form used by Liu et al. (Equation 4.5):

$$St_{def} = \frac{\frac{1}{2} * \rho_g * v_c^2}{\sigma_p}$$

(4.5)

Here, ρ_g is the granule density, v_c is the granule impact velocity, and σ_p is the dynamic yield stress of the granule. For the theoretical calculation of the dynamic yield stress, the formula employed by Liu et al. [16] was used (Equation 4.6):

$$\sigma_p = AR^{-4.3} * S * \left[6 * \frac{1-\varepsilon}{\varepsilon} * \frac{\gamma * cos(\theta)}{d_{3,2}} + \frac{9}{8} * \left(\frac{1-\varepsilon}{\varepsilon}\right)^2 * \frac{9*\pi*\mu*v_p}{16*d_{3,2}} \right]$$

(4.6)
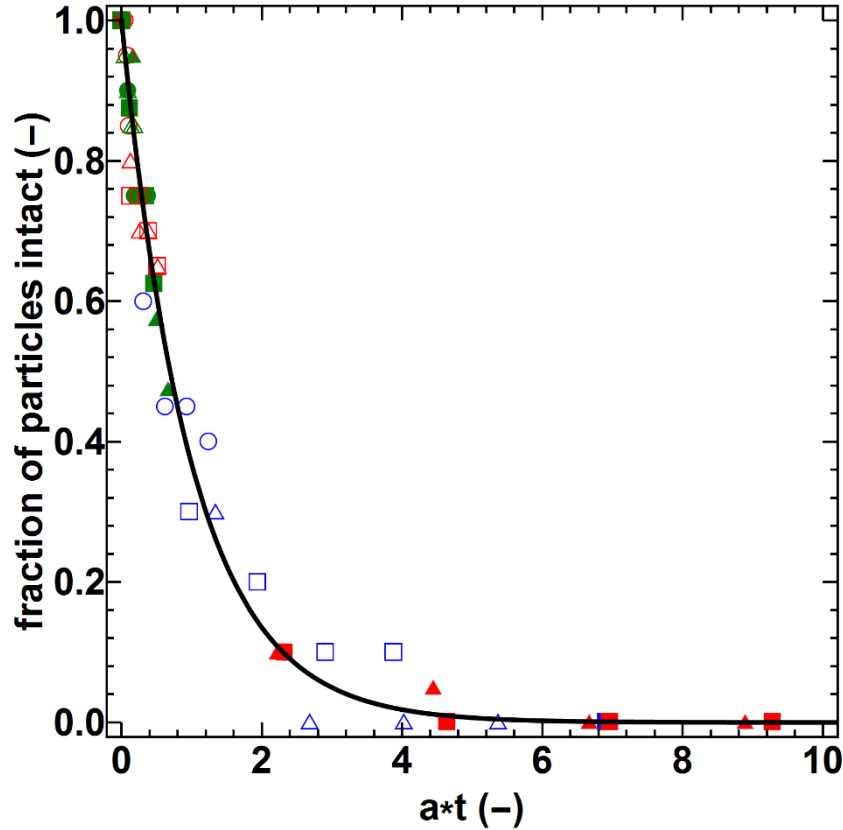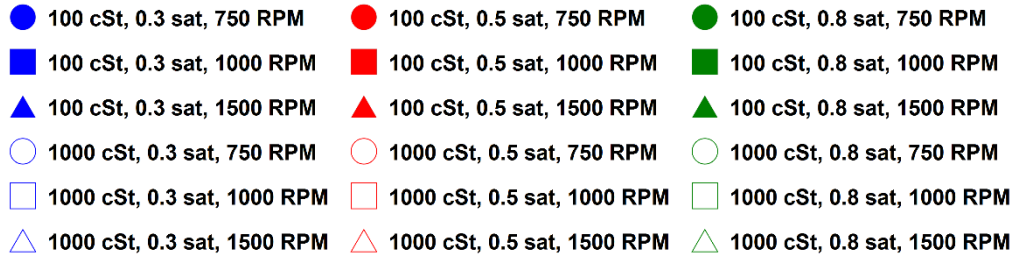
Figure 4.8: Fraction of surviving granules as a function of a*t. All curves collapse onto the single curve e^{-t}. Data was provided by Liu et al. [16].

where *AR* is the shape factor of the primary particles, *S* is the liquid saturation of the granule, ε is the porosity of the granule, γ is the surface tension, θ is the powder-liquid contact angle, $d_{3,2}$ is the primary particle Sauter diameter, μ is the binder viscosity and v_p is the relative granule velocity.

Equations 4.5 and 4.6 confirm some observations from Figure 4.8. Increasing liquid viscosity or liquid saturation reduces breakage; both these phenomena could be explained by an increase in σ_p. Increasing impeller speed, on the other hand, leads to an increase in breakage. The equations suggest that this is because the kinetic component of the St_{def} increases.

Most of the parameters in Equation 4.6 can be found in the study by Liu et al. [16], but the granule velocities are not easily obtainable without live imaging and more advanced methods such as positron emission particle tracking (PEPT). Instead, Liu et al. assumed that, based on the literature, velocity estimates between 10-20 % of the impeller speed were appropriate. Therefore, both velocity and the relative velocity were assumed to be 15 % of the impeller tip speed in their work. Figure 4.9 shows the dependency of St_{def} on this scaling factor within the 10-20 % impeller speed range. It appears only the magnitude of St_{def} is affected, and not the

general trends. Therefore, this work uses 15 % for both v_c and v_p as well. The only difference in parameters used is the contact angle. A contact angle of 0° is used in this study, whereas Liu et al. [16] used a contact angle of 45°. Liu et al. simply estimated the contact angle to be 45°, whereas actual measurements in the current work show that silicone oil wets lactose much better, with a contact angle below 20°. Consequently, the dynamic yield stress increases, and the Stokes deformation number decreases.
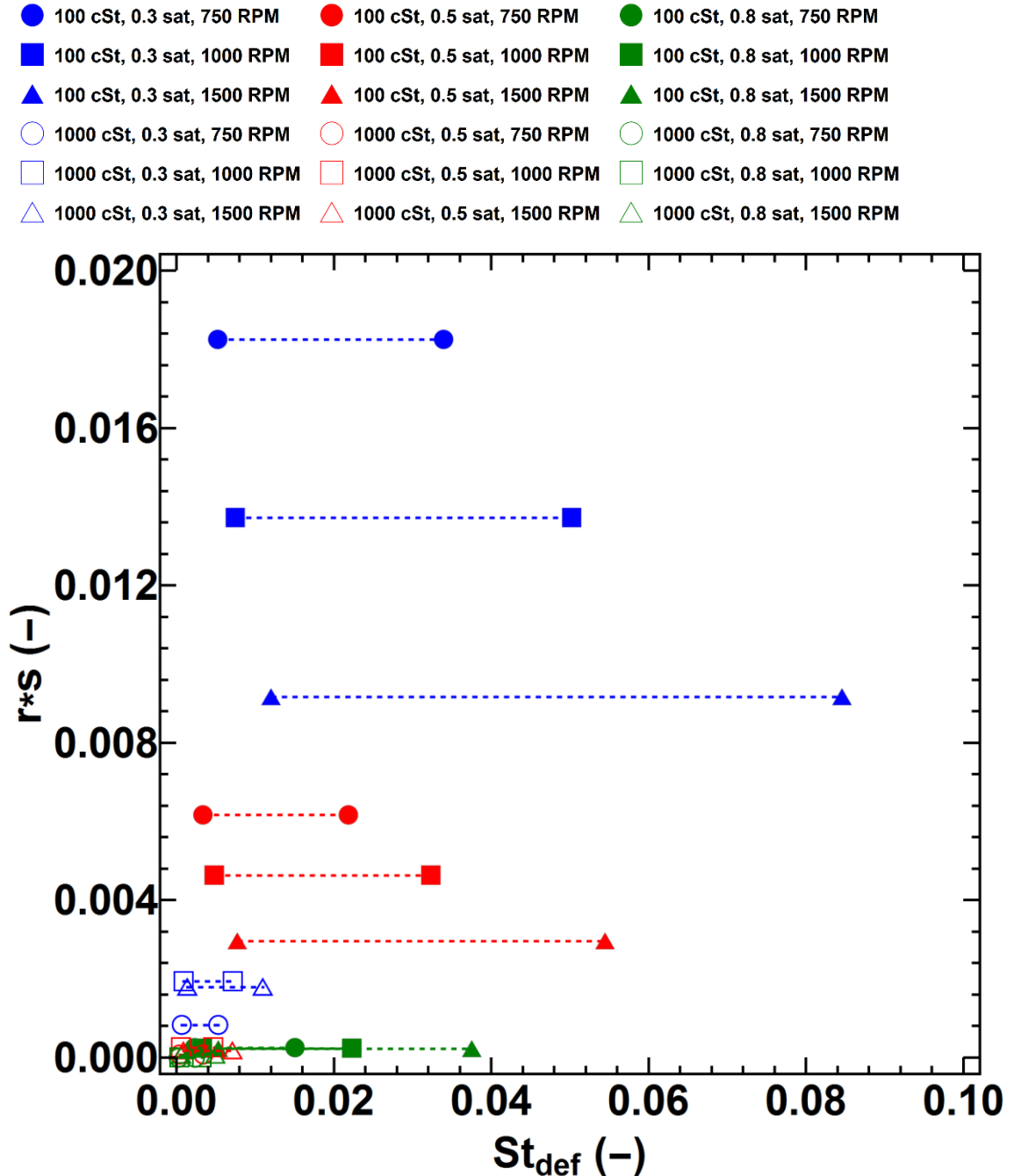
Figure 4.9 *r*s* **plotted against** *St$_{def}$* **for a range of values of** *v$_c$* **and** *v$_p$*. **Data was provided by Liu et al.** **[16].**

From Figure 4.9, it appears that there is no direct correlation between the total probability of breakage $r*s$ and St_{def}. Figure 4.10, which specifically shows the situation where both v_c and v_p are 15 % of the impeller speed, supports this conclusion. Here, three observations can be made. First of all, an increase in viscosity leads to a decrease in both St_{def} and the overall probability of breakage. This observation is logical since a more viscous liquid produces stronger liquid bridges. Second, an increase in saturation also leads to a decrease in St_{def} and overall probability of breakage. This is expected, as an increase in pore saturation leads to an increase in the dynamic yield strength σ_p, the denominator, and, in turn, a decrease in St_{def}. Third, an increase in the impeller speed results in an increase in St_{def}, but that does not automatically lead to an increase in the total probability of breakage. In fact, an increase in impeller speed appears to reduce the probability of breakage. This is not entirely illogical, as the viscous component of granule dynamic yield strength depends linearly on particle velocity v_p. Therefore, it appears that a comparison with the dynamic yield strength might be more appropriate than the Stokes deformation number.
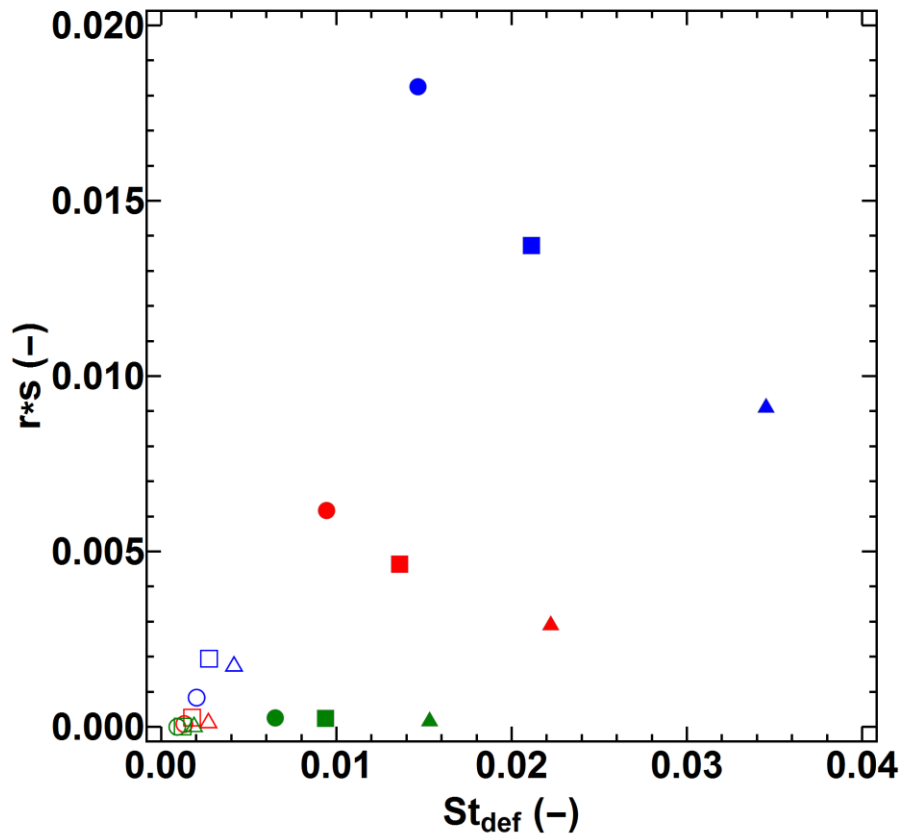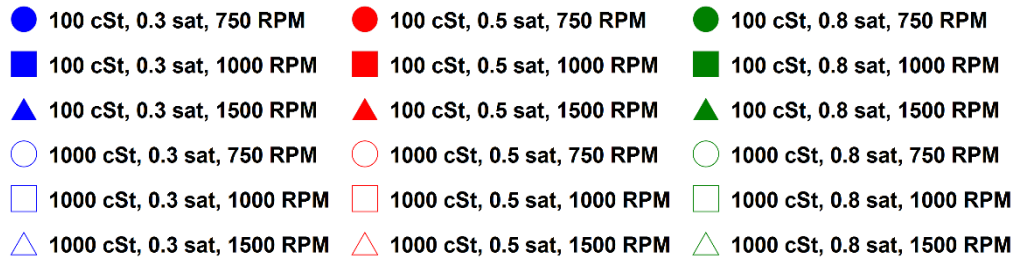
Figure 4.10: The overall probability of breakage _r*s_ plotted against the Stokes deformation number _St_{def}_. Data was provided by Liu et al. [16].

A possible candidate for a dimensionless number containing the dynamic yield strength is the *dimensionless peak flow stress*, Str^*. The number is defined as shown in Equation 4.7:

$$Str^* = \frac{\sigma_p * d_{3,2}}{\gamma * cos(\theta)} \tag{4.7}$$

where all parameters are as defined by Equation 4.6, and σ_p, is the peak flow stress, is considered to be equal to the dynamic yield strength. Smith et al. [63] found that this number corresponds linearly to the *capillary number*, *Ca*, which is defined by Equation 4.8:

$$Ca = \frac{\mu * v_p}{\gamma * cos(\theta)} \tag{4.8}$$

where, again, all parameters are as defined by Equation 4.6. Figure 4.11 shows a comparison between the two numbers.
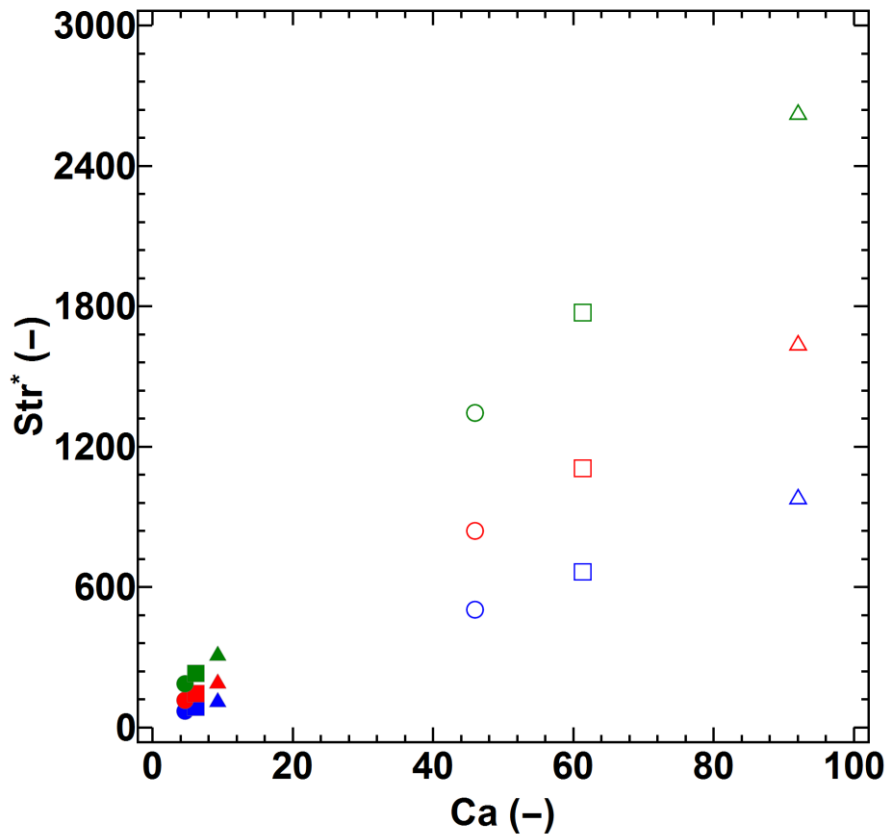
Figure 4.11: The dimensionless peak flow stress *Str** plotted against the capillary number *Ca*. Data was provided by Liu et al. [16].

Although there appears to be a linear relationship between different data sets with the same pore saturation, there is a clear difference between different pore saturations. This may be a consequence of the equation for the capillary number not taking into account the effect of the pore saturation. Regardless, since the capillary number is clearly related to the dimensionless peak flow stress and there are definite trends observable in Figure 4.11, Ca is another potential candidate for predicting the overall probability of breakage.

Since the overall probability of breakage should increase with a decrease in dimensionless peak flow stress, $r*s$ is expected to be inversely proportional to Str^*. Figure 4.12 shows that this does appear to be the case.
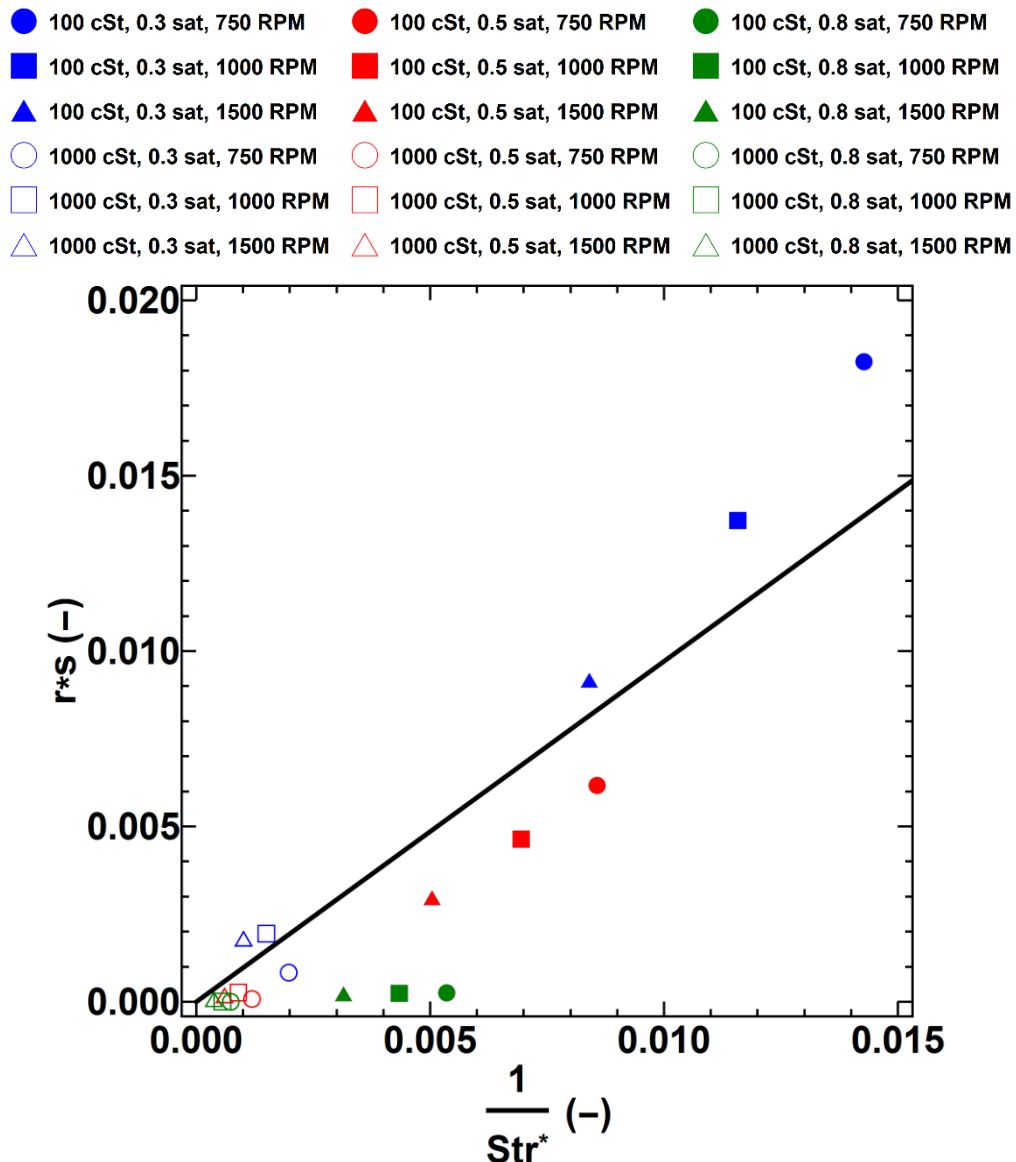
Figure 4.12: The overall probability of breakage $r*s$ plotted against the inverse of the dimensionless peak flow stress Str^*. Data was provided by Liu et al. [16].

However, not all data neatly fits a single line; especially highly saturated lactose granules do not fit the trend. In order to evaluate how accurately an inversely proportional relationship with Str^* describes r^*s, a fit in Mathematica software was performed. The fit yielded a fitting constant of 0.97, which is remarkable, since that implies that Str^* can almost directly predict the overall probability of breakage, without a fitting constant.

The obtained fitting constant was used to predict a, and the resulting fractions of intact particles were compared to the theoretical outcome as a function of time. This comparison is shown in Figure 4.13. From this figure, it becomes clear that the estimated parameter a does sufficiently describe the breakage behaviour of the granules. Breakage behaviour of granules with a high pore saturation was expected to show strong deviation, as these granules showed poor correlation with the inverse of Str^*. However, predictions in the relevant range of $0.008 < a < 0.1$ s^{-1} are not accurate either. Therefore, it appears Str^* alone is not suitable for the prediction of the overall probability of breakage.
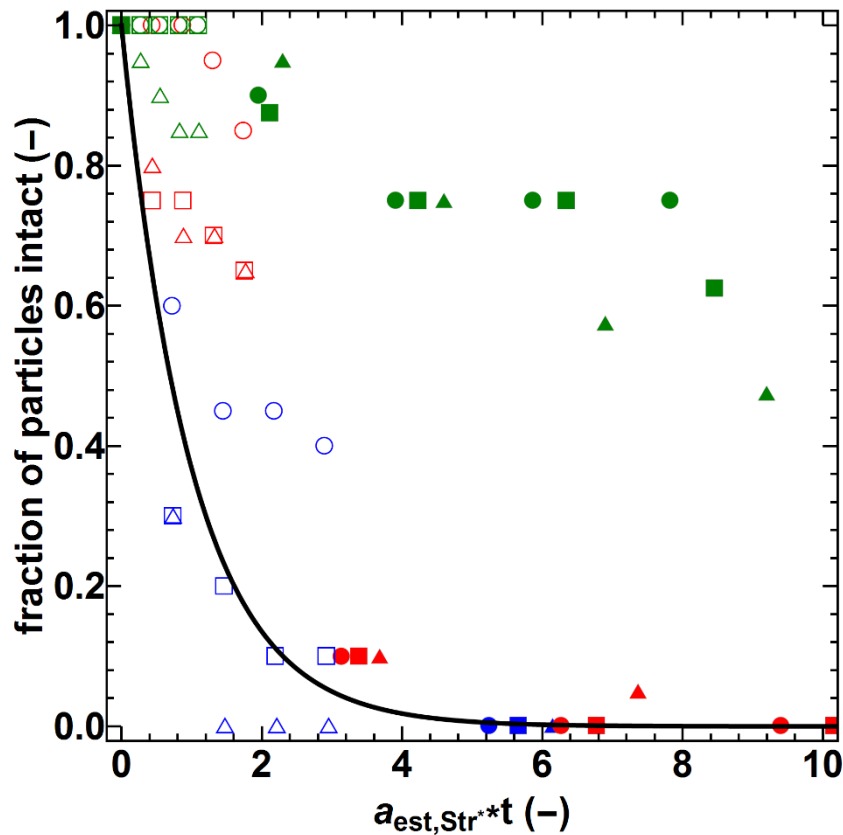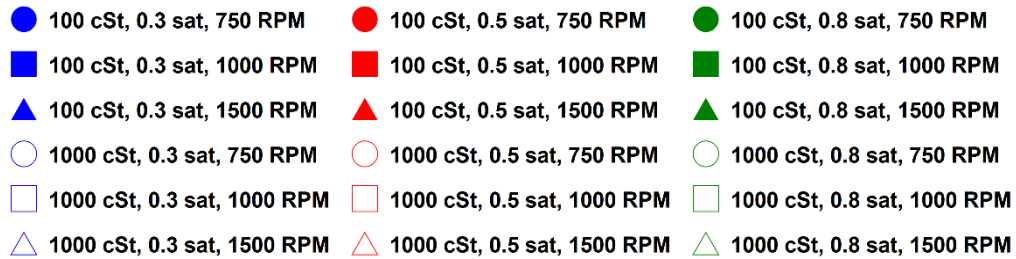
Figure 4.13: Fraction of surviving granules as a function of time, scaled with the estimated fitting parameter a_{est,Str^*}. Theoretically, all data should collapse onto a single curve. Data was provided by Liu et al. [16].

A second option for the prediction of the overall probability of breakage is to use the inverse of the capillary number Ca. As is the case for Str^*, an increase in capillary number should lead to an increase in Ca. Figure 4.14 shows the dependency of $r*s$ on Ca.

Remarkably, three linear trends can be observed: one for each of the saturation values used, which is the only different parameter between the three series. This same trend with varying S was also observed when comparing Ca to Str^*. If it were possible to find a relationship between the slope of the line and pore saturation S, $r*s$ could be related directly to the capillary number. As it turns out through least squares fitting in Mathematica, a linear relationship can be obtained, as shown in Equation 4.9:

$$r*s = \frac{exp(-7.96*S)}{Ca} \tag{4.9}$$
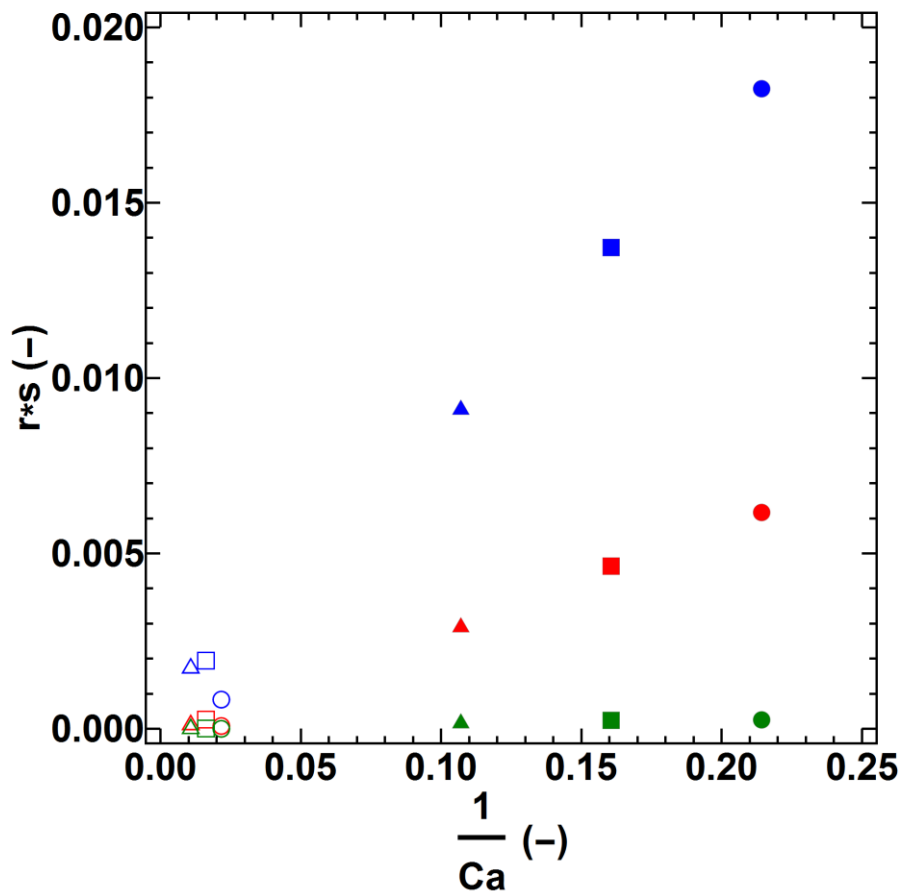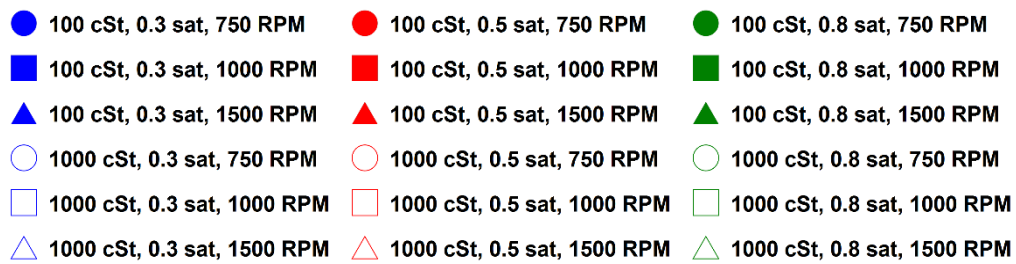
Figure 4.14: The overall probability of breakage $r*s$ plotted against the inverse of the capillary number Ca. Data was provided by Liu et al. [16].

where all parameters are as defined in by Equation 4.6. Substituting Equation 4.9 into Equation 4.4 yields Equation 4.10:

$$\frac{N}{N_0} = exp\left(ln\left(1 - \left(\frac{exp(-7.96 * S)}{Ca}\right)\right) * \omega * f * t\right) \tag{4.10}$$

This new equation allows for the straightforward calculation of the estimated lumped parameter $a_{est,Ca}$ for all data sets. Comparing the estimated parameter to the experimental data yields Figure 4.15.
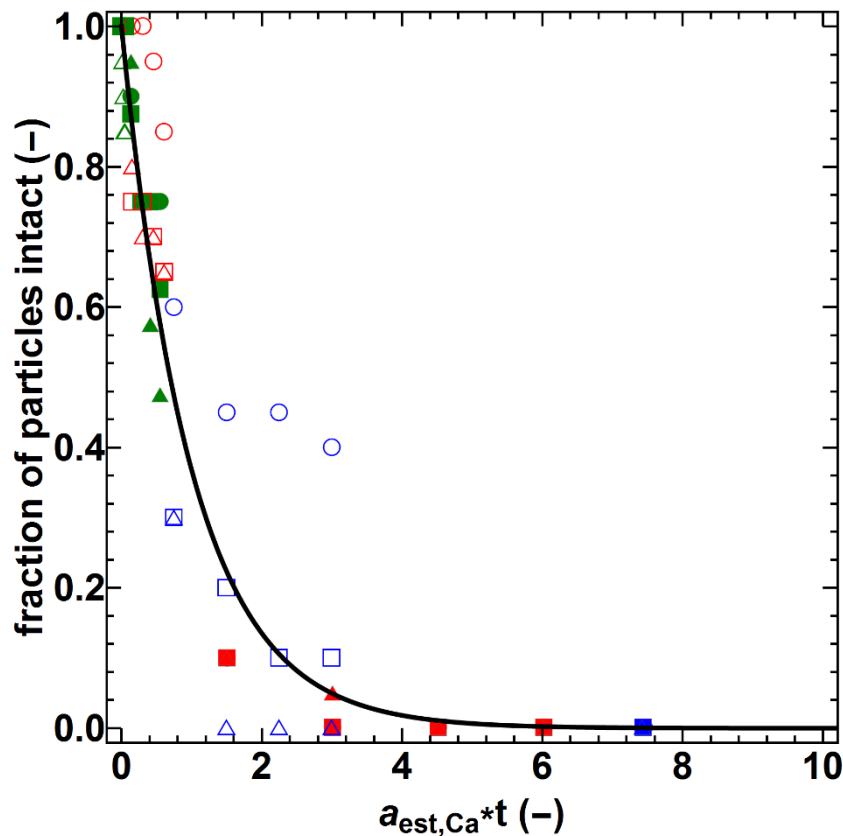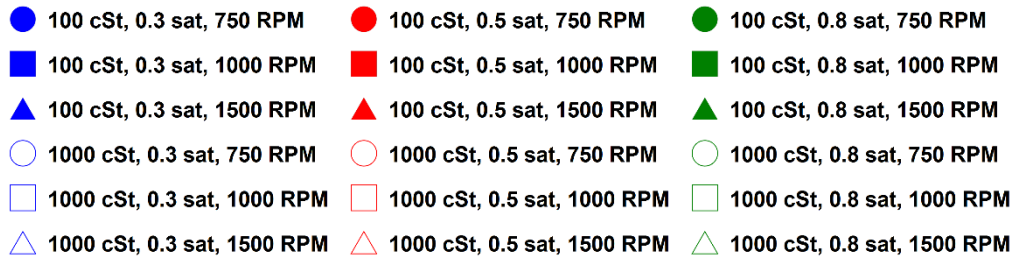
Figure 4.15: Fraction of surviving granules as a function of time, scaled with the estimated fitting parameter $a_{est,Ca}$. Theoretically, all data should collapse onto a single curve. Data was provided by Liu et al. [16].

Overall, the fit is significantly better than the one obtained with Str^*. The deviation from the exponent is much smaller in Figure 4.15 compared to Figure 4.13. Furthermore, the relationship appears to predict the breakage behaviour for high liquid saturations quite well. Sets that do not fit the line very well are all outside the range $0.008 < a < 0.1 \text{ s}^{-1}$, except the set produced with 1000 cSt silicone oil at a saturation of 0.3, granulated at 750 rpm. The fact that this set, which falls in the middle of the relevant range, deviates implies that the obtained relationship does not yet fully capture breakage behaviour.

Even if the relationship had fully predicted the breakage behaviour of the granules, however, the investigated data set is quite small. Further work in this area of research is necessary to investigate whether the obtained trend also applies to different powder-binder systems, and whether it also applies at lower shear rates. According to Iveson and Page [62], the relationship between the capillary number and dimensionless peak flow stress is much less steep. It is also possible that the value of -7.96 varies depending on the system. This would allow for the prediction of the physical properties that govern this value. Although this would be an interesting study, it is out of scope of this work.

This investigation into granule breakage has provided important insights into the predictions and modelling of breakage. First, the Stokes deformation number St_{def} only shows a qualitative relationship with the probability of breakage. Second, the dimensionless peak flow stress and dynamic yield strength appear to show an inversely proportional relationship with the probability of breakage, but no direct correlation was found. Third, the capillary number appears to have an inversely proportional relationship with the probability of breakage, but it does not account for the effect of the pore saturation. Fourth, by accounting for the pore saturation, it is possible to relate the probability of breakage to the inverse of the capillary number by introducing a factor equal to the exponent of -7.96 times the pore saturation. This value may change according to the systems evaluated, but further research is needed to confirm this.

4.5 Conclusions

The suitability of a high-shear mixer for consolidation-only granulation was evaluated using different powder-binder systems. Both image analysis and microbalance measurements showed that breakage and attrition were prevalent during the granulation process. Only the zeolite-based system showed any overall growth by layering. The growth of this system is most likely due to its smaller primary particle size compared to the other powders, as small particle size is known to increase granule strength. However, due to zeolite powder's poor flowability, it was impossible to extract the granules fast enough to guarantee the same growth times for each granule in a batch. Due to the prevalence of breakage and attrition, the high-shear mixer was deemed unsuitable for consolidation experiments.

Efforts to predict breakage behaviour using data provided by Liu et al. [16] showed positive results; the number of intact granules appears to decrease exponentially with time. The rate at which the number of intact granules decreases only depends qualitatively on the Stokes deformation number and dimensionless peak flow stress. By using an inversely proportional dependency on the capillary number and introducing the exponent of the pore saturation with a scaling factor, a reasonable prediction of the granule breakage behaviour could be achieved. However, not all breakage behaviour is fully predicted, and the investigated systems are limited to one powder and one binder with two different viscosities.

Therefore, it is recommended to investigate whether the proposed relationship holds for other systems and operating conditions. However, this would require a dedicated full study. Therefore, this investigation is out of scope for this work.

The results of this preliminary study lead to two key conclusions for future work:

- Breakage and wear play an important role in determining the suitability of a granulator for consolidation-only experiments. These must be eliminated in order to obtain useful data.
- In a high-shear mixer, the impeller causes excessive breakage and attrition. If the collisions with the impeller could somehow be reduced, the granulator might be suitable for consolidation experiments.

These results imply that either a different type of granulator should be designed, or the high-shear mixer should be modified to drastically reduce breakage and attrition. In this work, both methods are employed. However, since Hounslow et al.'s deformation-driven diffusive growth model [30] considers deformations due to collisions, a granulator that allows for the tracking of such collisions is expected to yield results that are more useful for the fulfilment of the objectives of this thesis. Therefore, Chapter 5 presents, the development of a novel, consolidation-only granulator that allows the granules to experience a quantifiable number of impacts. In Chapter 6, a modified high-shear granulator is used to further investigate the critical parameters found in Chapter 5.

Chapter 5.   Development   of   a   consolidation-only granulator

5.1 Introduction

From the results in Chapter 4, it is evident that a high-shear mixer is not suitable for the study of consolidation and layered growth. Although it was possible to eliminate nucleation and agglomeration during granulation, the granules experienced significant breakage and attrition. In order to reduce breakage and attrition during the experiments, a different type of equipment is required. Therefore, a new type of granulator was designed, so that the collisions experienced by the granules could be quantified. In this way, the results can be compared to models available in literature [30,31], as described in Section 5.4. To this purpose, a novel consolidation-only granulator (COG) was developed, based on a linear shaker. This design should allow for consistent, countable impacts on the granules for the study of consolidation and layered growth.

The aims of this study are:

- To develop a granulator specifically for studying consolidation and layered growth.
- To determine the feasibility of such a granulator.
- To use the data to develop a kinetic model for consolidation and layered growth.
- To compare the kinetics found to the results from static nucleation experiments performed by Pitt et al. [31] in order to investigate the difference between static and dynamic situations in granulation.

The overall concept for the experimental design was the same as that for the experiments described in Chapter 4. Again, to eliminate the effect of nucleation within the granulator, granules were prenucleated. However, to produce granules rapidly regardless of viscosity, a syringe pump was used. Instead of a high-shear mixer, the newly designed consolidation-only granulator (COG) was used to granulate the nuclei with powder for a set amount of time. The resulting granules were extracted and weighed to obtain their growth as a function of time.

The results were then compared to Hounslow et al.'s models [30] and Pitt et al.'s static nucleation results [31]. In this way, a model for dynamic granulation can be proposed, and the performance and viability of the COG can be evaluated.

5.2 Consolidation-only granulator design

The design of the consolidation-only granulator (COG) was based on the principle of a linear shaker. This type of motion was selected in order to ensure homogenous impacts experienced by all granules. In order to achieve this, it was decided that the granulation vessel itself would move so that its motion would be imparted to its contents. Initial manual impact tests showed that a stroke of approximately 20 cm at a rate of 5 strokes per second, with a fill level of 50-75% of the vessel, resulted in appreciable impacts on the granules. An adapted version of the Froude number, described in Equation 2.23, can be calculated in this case, according to Equation 5.1:

$$Fr = \frac{D * f^2}{g} \tag{5.1}$$

Here, D is the distance of a single stroke, f is the frequency and g is the acceleration due to gravity. Using these values, a Froude number of 0.51 are obtained, and an average velocity of 1 m/s. This Froude number is relatively low for mixer granulators [10,141,158]. However, since the investigated motion was linear instead of rotary and good powder flow was observed, it was decided to design a granulator based on these specifications. A schematic design of the COG is shown in Figure 5.1, and the final set-up, manufactured at the University of Sheffield, is shown in Figure 5.2.

The moving granulation vessel should be removable from the granulator, as it would have to be filled and emptied for every experiment, as well as cleaned. In order to make it possible to monitor the flow behaviour of the powder in the granulator, the walls and lid of the vessel were made of acrylic glass. The base was made of stainless steel. The moving part of the granulator itself was a stainless steel carriage on a rail (Hepcomotion), with a flywheel imparting the motion via a movable crank. The carriage contained a slot for the granulation vessel, with two screws allowing for the quick fastening and removal of the vessel. The flywheel itself was powered by a 0.75 kW electromotor (TEC Electric) that could achieve speeds of 300 rpm in this set-up. In order to compensate for the forces exerted on one side of the flywheel by the crank, a movable counterweight was added to the opposing side.

For safety purposes, the flywheel-rail system was encased in an acrylic glass cage, which could only be removed when the granulator was not running. Accidental access to the electromotor and electronics was prevented by stainless steel sheets covering the sides of the granulator. The whole rig was placed on legs with swivel casters that could be manually locked in position. This type of design was selected for several reasons. Since the flywheel converts rotational motion to a linear motion, the apparatus was expected to vibrate significantly due to residual lateral (i.e. not in the direction of the shaking motion) forces.
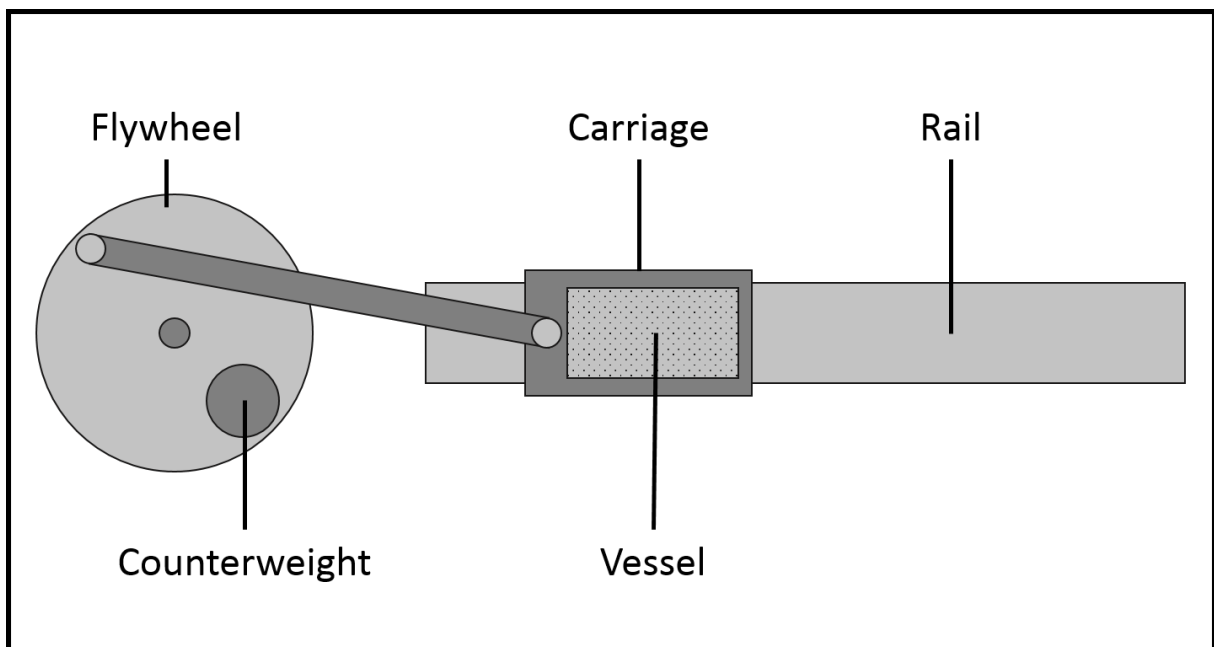
Figure 5.1: Schematic drawing of the consolidation-only granulator. A flywheel, powered by an electrical motor, is connected to a carriage on a rail. Attached to the carriage is a detachable container that serves as the granulation vessel.
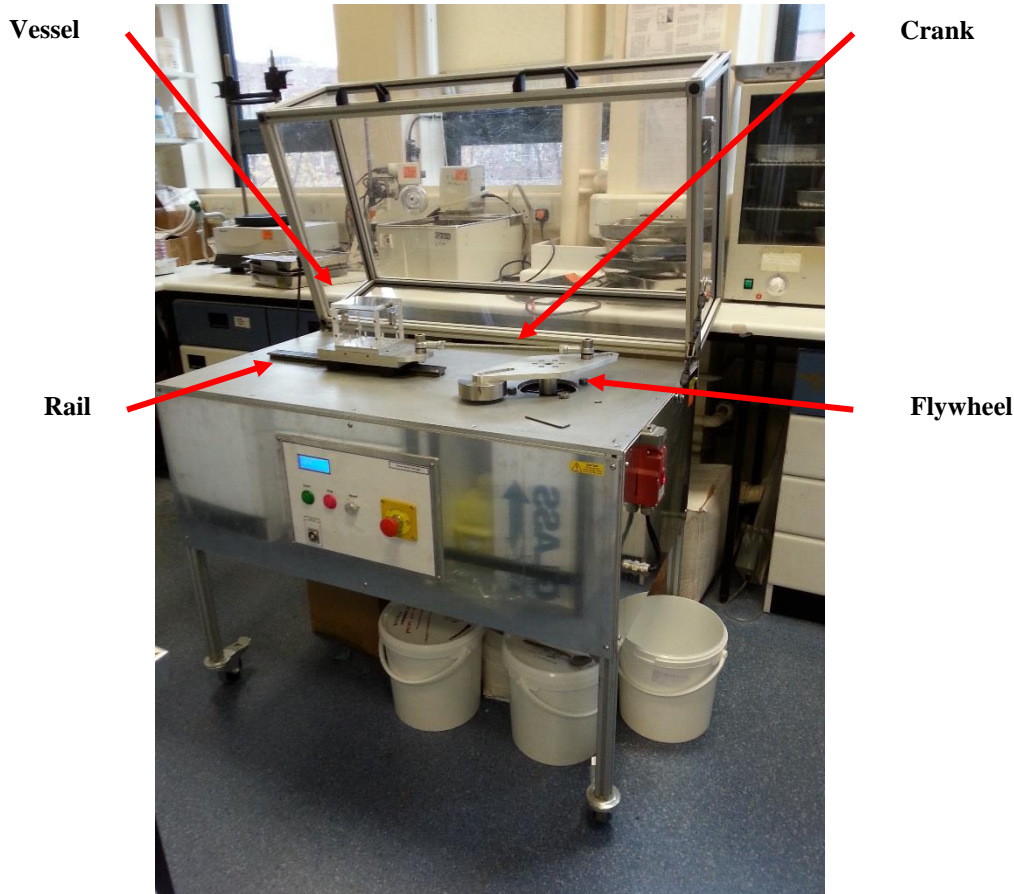
Figure 5.2: Final design for the consolidation-only granulator (COG); a vessel for powder on a rail driven by a flywheel and crank.

Placing the set-up directly on a bench might result in damage to both the bench and surroundings, as well as to the equipment due to feedback forces. By placing the apparatus on legs, the forces are dissipated by the legs first. In addition, the swivel casters can be locked at a slight angle, which helps stabilise the system. Test runs with the apparatus showed that the combination of the counterweight and the swivel casters was effective in reducing the vibration to acceptable levels; the granulator could be run constantly for over two hours.

The movable crank was fixed at 10 cm from the centre of the flywheel, for a total stroke of 20 cm, as specified by the manual tests. This distance implies that the granules in the vessel travel 40 cm in a single rotation of the flywheel. The selected motor speed was set to 150 rpm, or 2.5 s^{-1}. This setting results in the specified five impacts per second; both when the crank pushes and pulls the carriage.

A possible issue with the design of the COG is the motion of the flywheel: Due to its design, the acceleration is at its highest in the middle of a stroke, and at its lowest at the end of a stroke. However, provided the motion is fast enough, inertia can still cause an impact of the granules with the walls. Again, the Froude number can be calculated according to Equation 5.2:

$$Fr = \frac{\langle v \rangle^2}{g * D} = \frac{\left(2f \int_0^{\frac{1}{2f}} v(t)\, dt \right)^2}{g * D} = \frac{\left(2f \left(s\left(\frac{1}{2f}\right) - s(0) \right) \right)^2}{g * D} = \frac{4 * D * f^2}{g} \tag{5.2}$$

where $<v>$ is the average vessel velocity, f is the frequency of the flywheel, v is the vessel velocity, t is the time, g is the acceleration due to gravity, D is the distance of a single stroke, and s is the position of the carriage on the rail. The average velocity is calculated by integrating the acceleration over the selected interval since this is exactly a full stroke, or half a rotation of the flywheel. A single stroke should therefore take $(2*f)^{-1}$ or 0.2 seconds at the selected speed of 2.5 s^{-1}. Since the integral of the velocity is the location, the average velocity can be found simply by dividing the distance travelled by the time a single stroke takes.

The velocity, however, is simply the derivative of the position along the rail, or the horizontal position of the crank on the flywheel. Consequently, the Froude number can be calculated simply by using the overall displacement, leading to a straightforward expression to calculate the Froude number. The result, 0.51, is the same as the value originally specified by manual testing. This value is generally considered too low for a roping regime, as gravitational forces dominate the inertial forces at this point. However, this is an average Froude number. The peak Froude number can be calculated from the highest attainable velocity, which can be found using Equation 5.3:

$$v(t) = \frac{ds}{dt} = \frac{d\left(\frac{D}{2} - \frac{D}{2}\cos\left(2*\pi*f*\frac{1}{4f}\right)\right)}{dt} = D*\pi*f*\sin\left(\frac{\pi}{2}\right) \tag{5.3}$$

Solving this equation for $t = (4*f)^{-1}$ or 0.1 s yields a peak velocity of 1.6 m/s, which translates to a peak Froude number of 1.3. In this scenario, it is much more likely that a turbulent, well-mixed flow can be developed. Actual test runs using the COG (Figure 5.2) with powder showed that this was indeed the case; powder flow was observed throughout the vessel.

5.3 Materials and methods

A novel consolidation-only granulator (COG) was developed specifically to isolate consolidation and layered growth by eliminating breakage and attrition. In total, ten different powder-binder systems were evaluated, as shown in Table 5.1. For easier comparison, all liquids will be referred to by their viscosity values in the results and discussion: 13, 52, 105 and 1043 mPa•s for 10, 50, 100 and 100 cSt silicone oil, respectively, 130 and 3192 mPa•s for 50 wt% PEG 4000 and PEG 20000, respectively, and 95 mPa•s for molten PEG 600, as shown in the table.

The experimental procedure was similar to that of the high-shear mixer experiments described in Chapter 4, with prenucleation of granules, granulation, extraction and granule analysis. First, powder was sieved through a 1.14 mm sieve, after which a powder bed was prepared for granule prenucleation. The surface was levelled by using the ruler to gently sweep off powder above the edge of the dish. This method was used in order to decrease the variance of the amount of powder in the powder bed.

Table 5.1: Overview of all systems used in experiments with the COG.

Powder	Binder	Viscosity (mPa•s)	Times (min)	# of data points
Lactose	10 cSt silicone oil	13	1-64	7
Lactose	50 cSt silicone oil	52	1-64	7
Lactose	100 cSt silicone oil	105	1-128	7 (x2), 8
Lactose	50 wt% PEG 4000	130	1-64	12
Lactose	50 wt% PEG 20000	3192	0.5-64	8
Lactose	Liquid PEG 600	95	1-128	8
Glass Beads	50 cSt silicone oil	52	0.5-4	6
Glass Beads	100 cSt silicone oil	105	0.5-8	8
Glass Beads	1000 cSt silicone oil	1043	1-16	7
Glass Beads	50 wt% PEG 4000	130	0.5-96	14

Next, half of the volume of the COG vessel was filled with powder. For lactose, the amount used was 200 g, whereas the amount used for glass beads was 400 g due to differences in bulk density. Granules were prenucleated by depositing liquid droplets on the powder bed using a syringe pump (Harvard Apparatus PHD ULTRA I/W). To improve flow and reduce pressure build-up, the syringe in the pump was connected to a 25 G (0.26 mm inner diameter) plastic tapered flow tip instead of a needle. Because of this type of tip, a flow rate of 10 μl/s could be achieved. The tip was mounted 5 cm above the powder bed.

Some breakage of granules occurred during granulation, especially at long granulation times. In order to extract a sufficient number of intact granules, between 20 and 60 granules were nucleated, depending on the expected amount of granule breakage. Granules were added to the container, after which a final layer of powder was added in order to prevent the granules from adhering to the COG vessel wall. The total amount of powder used was 300 g for lactose and 600 g for glass beads. Both amounts filled the container to approximately 75-80 % of the available volume of 0.7 L.

The granulator was run for a set amount of time at 150 rpm (or 300 impacts), after which all granules were extracted and separated from the powder using a 1.4 mm sieve by gently tapping the sieve with a spoon. After extraction, a new batch of granules was nucleated as described above, and the experiment was repeated for a longer granulation time. Granulation times varied between 0.5 and 128 minutes. Each series of experiments was stopped after an insufficient number of intact granules (i.e. less than ten) was obtained as a result of breakage.

Extracted granules were weighed using a microbalance (Mettler-Toledo XS3DU, 1 μg accuracy). In the case of granules being produced with 50 wt% PEG solution, granules were dried for 6 days under ambient conditions before analysis in order for their mass to stabilise. Granules produced with liquid PEG were stored in a refrigerator at 5 °C for 2 weeks to stabilise their weight. By tracking the mass, the results can be compared to the static experiments from Pitt et al. [31], as well as to the models proposed by Hounslow et al. [30].

From each data set, a number of granules were analysed with helium pycnometry and powder pycnometry to obtain their respective true and envelope densities. Granules were selected depending on their granulation time. Preferentially, granules with the lowest and highest granulation times were selected, but this was not always possible due to breakage. As a rule, the set with the lowest and highest granulation time and a minimum of 15 surviving granules was used. For helium pycnometry, a small number of granules, usually 3-6, was analysed at the same time, yielding an average true density. This experiment was repeated

another two times, each with a different set of granules, for a total of three experiments per data set evaluated. For the powder pycnometry, a larger number of granules was required to fill the sample chamber to the minimum volume needed for analysis, usually 6-10. In order to increase reliability of the results, repeats with the pycnometer were performed on the same granules. For granules produced with PEG, this proved to be a reliable method. However, for granules produced with silicone oil, the granules decreased in density after each repeat.

A select number of granules were analysed with X-ray tomography to investigate the structural changes over time. Two sets of granules were evaluated: lactose-105 mPa•s silicone oil, and glass beads-105 mPa•s silicone oil. These sets were compared to sets produced by static nucleation where nuclei were left to grow in the petri dish without any additional granulation. For each set, two different granulation times were selected: one of the early granulation times and one at the end of the experiments. For each time, three different representative granules were evaluated, for a total of 24 images.

5.4 Results and discussion

This section is divided into three parts. The first part focuses on the growth data obtained from the experiments using the COG. The second part discusses the mechanisms by which consolidation and layered growth occur. Finally, the third part is an evaluation of the validity of the COG as a granulator for studying consolidation and layered growth.

5.4.1 Layered growth in a consolidation-only granulator

An increase in overall granule mass with time was observed for all systems. However, the kinetics and overall growth behaviour varied between systems. Therefore, growth behaviour is initially discussed separately for each individual system. Figure 5.3 shows the growth behaviour of the lactose-silicone oil based systems in terms of granule mass over time.

The black lines in Figure 5.3 that have been added for visual clarity follow the Hounslow et al. model [30] for surface tension-driven growth as shown in Equation 2.11. The full implications of this finding are discussed in Section 5.4.2. For now, it suffices to observe that the model appears to predict the growth behaviour of the granules quite well, with the exception of early and late growth behaviour. This observation is true for all systems evaluated in this study.

Initial growth behaviour of the lactose-silicone oils systems was characterised by a significant increase in granule mass, after which the growth rate slowly decreased. The final data point represents the maximum granulation time for which a sufficient number of intact granules could be extracted from the granulator. Although breakage and attrition were significantly reduced compared to high-shear granulation, they were still present; visual observation revealed that both fracturing of the granules occurred, as well as breakage of the outer layers of the granules. This increase in damage to granules is reflected by the standard error for each system; the standard error increases for longer granulation times due to greater variation in granule mass, caused by breakage and attrition.

A different lactose-based system, using 50 wt% PEG solutions of different viscosities as binders, is shown in Figure 5.4.
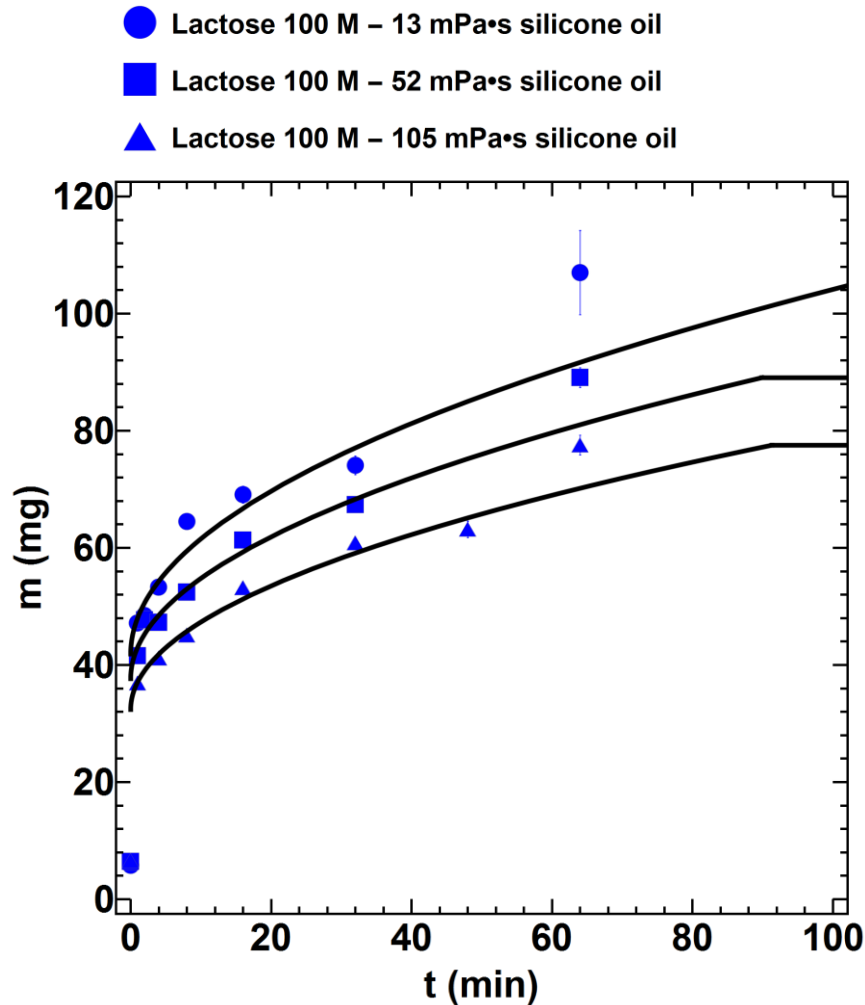
Figure 5.3: Granule mass as a function of time for three lactose-silicone oil systems of different viscosities. Error bars indicate standard errors, and lines were fitted by using Hounslow et al.'s model for surface tension-driven growth [30].

Compared to silicone oils, the systems showed different behaviour. No slow, steady growth was observed; after an initial rapid increase in mass, which represents the transition from liquid droplet to granule, the granule mass remained more or less constant. This effect was probably caused by the drying of the binder liquid. This led to a reduction of the standard error of the data points. However, more importantly, this effect also caused the kinetics of layered growth to be difficult to obtain.

Similar to lactose-silicone oil-based systems, it appears as though an increase in viscosity from 130 to 3192 mPa•s causes slower growth kinetics. Combined with drying, this effect may have resulted in a reduction of the final granule mass for the higher viscosity PEG solution. Regardless of the cause, the quick levelling off of the growth rate makes systems based on lactose and PEG solution unsuitable for the study of isolated consolidation and layered growth. The rapid growth-no growth behaviour of the PEG solution-based systems is different from the more steady growth behaviour observed with the silicone oil-based systems. Interestingly, the final mass achieved with the lowest-viscosity PEG solution, 130 mPa•s, is much lower than the final mass achieved with a silicone oil of a similar viscosity (105 mPa•s).
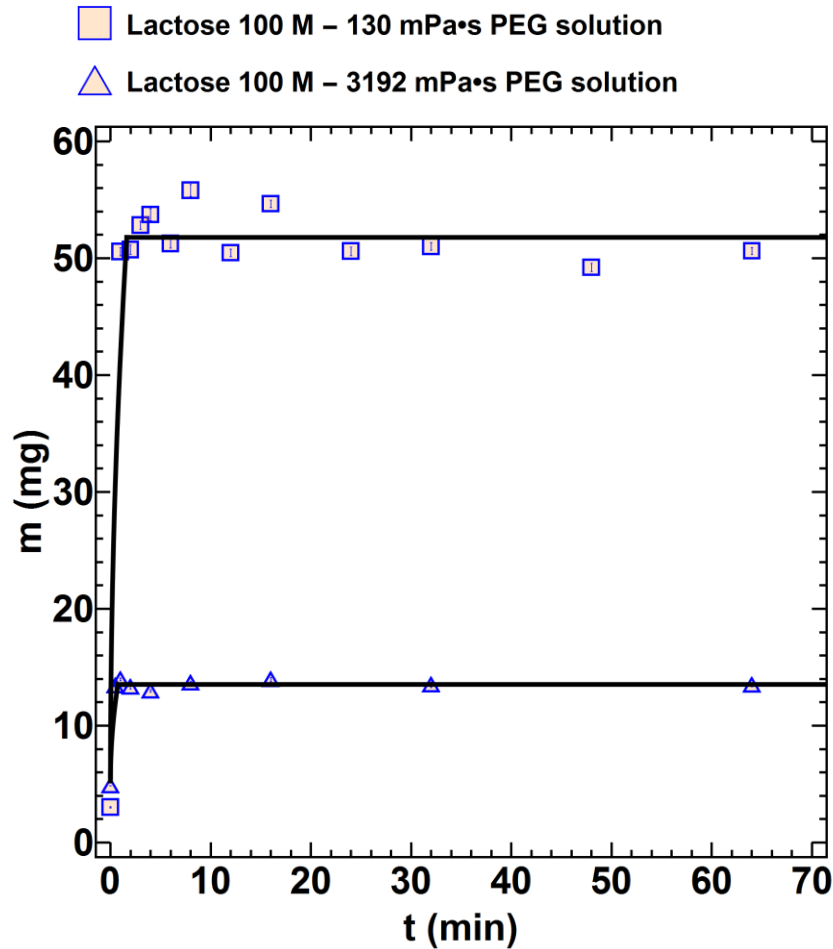
Figure 5.4: Granule mass as a function of time for two lactose-50 wt% PEG solution systems of different viscosities. Error bars indicate standard errors, and lines were fitted by using Hounslow et al.'s model for surface tension-driven growth [30].

Figure 5.5 shows the growth behaviour of a system based on lactose and molten PEG 600, with an initial viscosity of 95 mPa•s at 32.5 °C. After an initial leap in granule mass, the system shows a decreasing growth rate without levelling off until the experiments were stopped due to breakage and attrition.

Compared to the other systems, this growth behaviour is mostly similar to the growth behaviour of silicone oil-based granules. When comparing PEG 600 to the similar-viscosity 105 mPa•s silicone oil, the final mass is much higher. It should be noted, however, that the initial droplet mass was also higher. As such, it is more interesting to study the critical-packing liquid volume fraction, ϕ_{cp}, as discussed in Section 5.4.2.1.

Although the observed growth behaviour of this lactose-PEG system is promising for the study of consolidation and layered growth, there is a potential issue that should be addressed. PEG 600 increases in viscosity due to cooling, from 95 to 132 mPa•s at 25 °C, which may cause a decrease in the growth rate. Eventually, the binder will solidify, halting growth altogether.
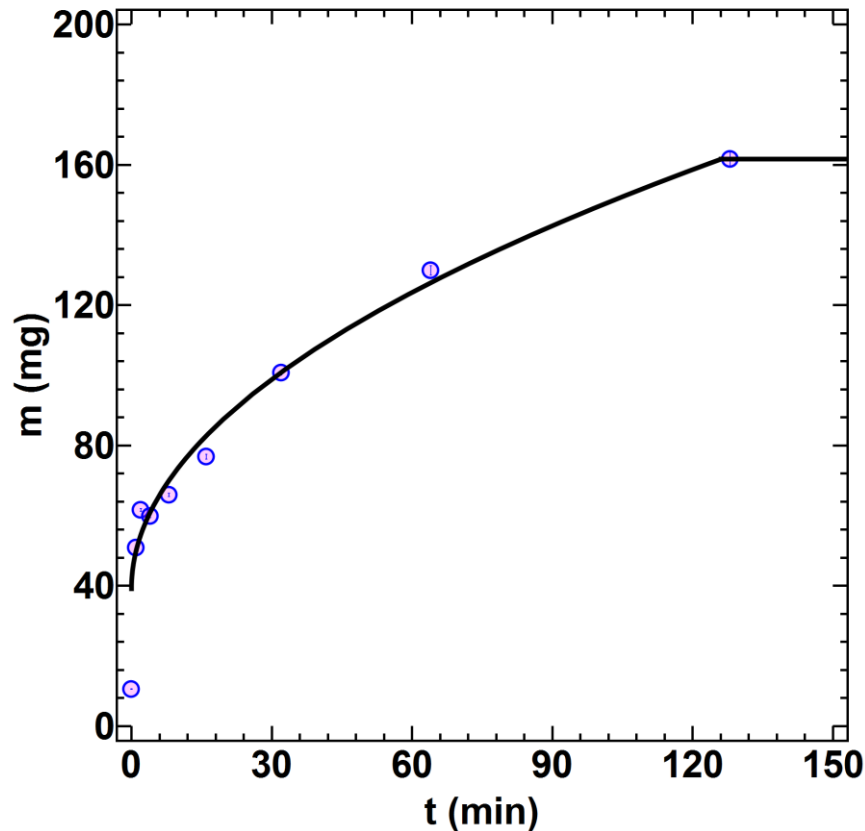
Figure 5.5: Granule mass as a function of time for a lactose-liquid PEG 600 system. Error bars indicate standard errors, and the line was fitted by using Hounslow et al.'s model for surface tension-driven growth [30].

Taking into account the growth data, it appears as though the increase in viscosity does not have a deeply pronounced effect. This could be the result of either slow cooling, or a limited effect of the viscosity on the kinetics, or a combination of both. Since the contents of the granulator were often close to room temperature after granulation times longer than 10 min, the effect of increasing viscosity is likely not to be very significant. This is predicted by Hounslow et al.'s model surface tension-driven growth model: the growth rate is inversely proportional to the square root of the viscosity [30]. Hence, a change from 95 to 132 mPa•s would only result in a reduction of the growth rate by a factor 0.84, or a 16 % deviation.

The growth behaviour of glass beads-silicone oil-based systems is shown in Figure 5.6.

Growth behaviour is similar to that of lactose-silicone oil-based systems, with a steep initial increase in granule mass, steady growth behaviour and significant breakage at longer granulation times; this effect of breakage is reflected by the larger standard errors visible at long granulation times. A major difference, however, is the total granulation time before experiments were halted due to breakage; overall granulation times were much shorter than those of lactose, even using higher viscosity binders.
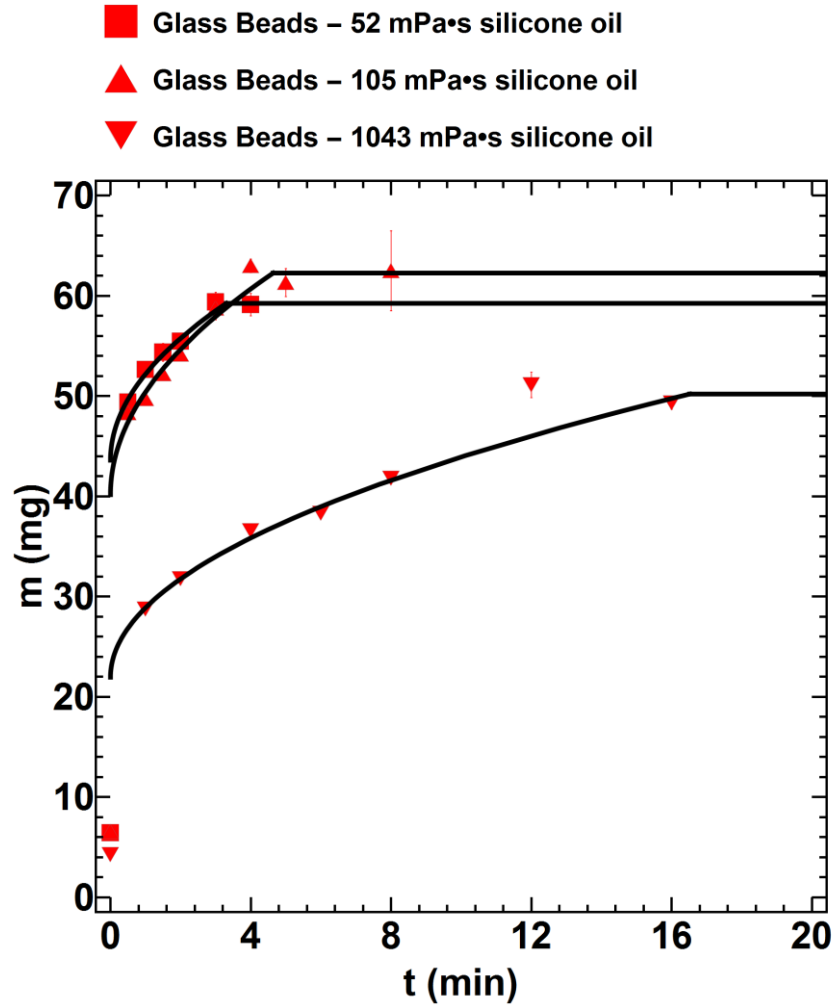
Figure 5.6: Granule mass as a function of time for three glass-silicone oil systems of different viscosities. Error bars indicate standard errors, and lines were fitted by using Hounslow et al.'s model for surface tension-driven growth [30].

The growth behaviour of the final system evaluated in this study, glass beads-130 mPa•s PEG solution, is shown in Figure 5.7. This system behaves similarly to its lactose-based counterparts; a steep initial jump in granule mass is observed, after which no further increase is observed. This system, however, shows an increase and then a decrease in overall mass after approximately 12 min. Since the granule mass had been stable over quite a few measurements, it is unlikely that this increase was caused by further growth, but rather by fluctuations in mass due to breakage. Compared to the glass beads-105 mPa•s silicone oil-based system, the growth behaviour is different, as no steady growth is observed. However, a similar granule mass is achieved. This is most likely coincidence, as the masses shown are dry droplet masses. Additionally, the initial growth rate is much higher for the PEG-based system, and if drying had not occurred, the granules might have grown more.
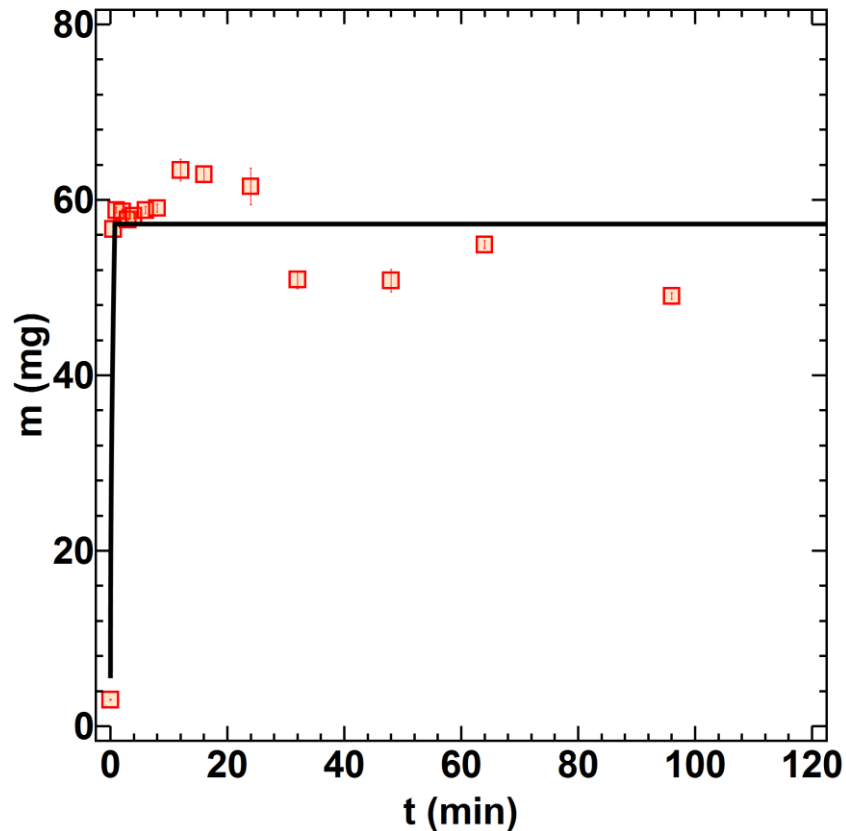
Figure 5.7: Granule mass as a function of time for a glass beads-50 wt% PEG solution (130 mPa•s) system. Error bars indicate standard errors, and the line was fitted by using Hounslow et al.'s model for surface tension-driven growth [30].

The decrease in mass can be explained by drying; after the granules were sufficiently dried in the granulator, breakage and attrition started occurring. This behaviour would be consistent with the observations from Figure 5.6, where no drying occurs. The reason why the glass beads-PEG solution-based granules show a more prominent decrease in mass than the lactose-PEG solution-based granules is most likely the result of the different shapes of the primary particles. Glass beads are spherical and lactose particles are rougher, allowing for mechanical interlocking [16]. Therefore, systems based on glass beads are likely to produce weaker granules than those based on lactose.

The overall growth behaviour of all systems evaluated is shown in Figure 5.8, scaled according to Hounslow et al.'s model for surface tension-driven growth [30], as shown in Equation 2.11. The surface tension-driven model shows remarkable agreement with the scaled data, although a few assumptions for this scaling have to be mentioned.

First and most important of all, data was scaled based on the observed maximum granule mass achieved for each data set. This mass was not necessarily the final granule mass; in the case of systems based on silicone oils and liquid PEG, experiments were halted due to significant breakage before a final granule mass was observed. The final granulation time was calculated based on a fit of the data points in the growth regime; the data before the maximum size was achieved. This assumption could skew the data to the left, as well as give a misrepresentation of the stage at which growth levels off. However, taking into account the data, this assumption can be justified. Further growth would lead to an increase in granule mass. Compared to the current data, this effect would lead to a slightly steeper slope of the fitting line, but the overall linear relationship with the square root of time would remain.

Hence, although the comparison is quantitatively not fully representative of the actual growth kinetics, the qualitative relationship still holds.

A second issue that must be addressed is the cluster of points to the left of the normalised curve; at $\tau^{1/2}$ values between 0.8-1. This range is the transition from the growth to no growth regime. These data points deviate significantly from the other points. There are two factors that could explain this effect. The first factor is the aforementioned assumption of the final observed granule mass being the maximum attainable granule mass. This holds for systems using silicone oils and liquid PEG as binders, which make up the majority of the points in the cluster. The second factor holds for systems based on 50 wt% PEG solutions. These systems displayed no growth after the initial increase in granule mass and, as such, do not provide reliable data in the growth regime of the curve.
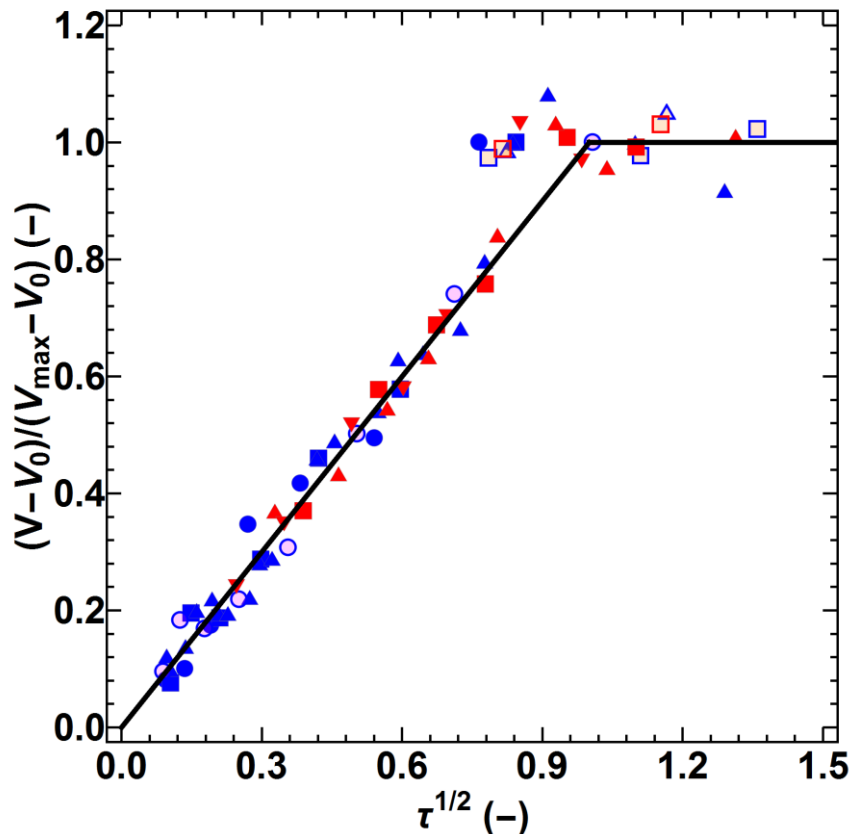
Figure 5.8: Dimensionless granule volume difference as a function of the square root of dimensionless time for all experiments performed. The black line represents Hounslow et al.'s model for surface tension-driven growth [30].

To demonstrate that the observed trend is not a simple matter of good fitting, Figure 5.9 shows a fit with Hounslow et al.'s proposed model for deformation-driven growth [30]. The model predicts exponential decay of growth, with time scale depending on material properties and the critical-packing liquid volume fraction ϕ_{cp}; the liquid volume fraction at the maximum size attainable by the granule for the system. Clearly, the predictions by the model do not at all describe the observed behaviour. Since the model is based on deformations caused by impacts, this finding implies that the actual collisions are not an important factor in layered growth for the non-breaking conditions examined here.
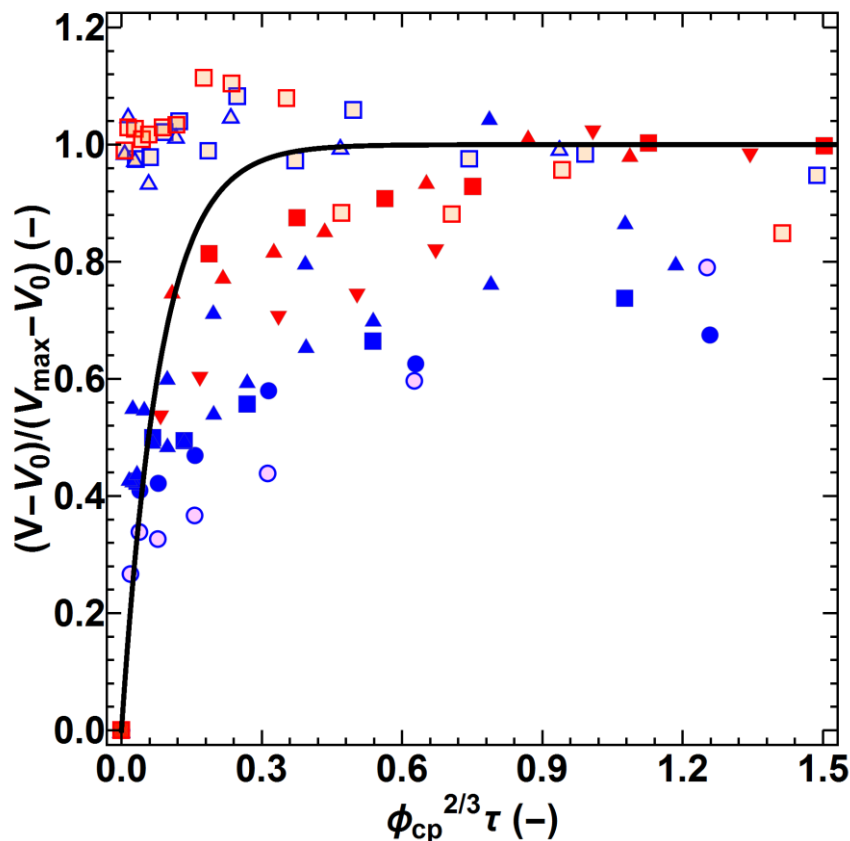
Figure 5.9: Dimensionless granule volume difference as a function of the dimensionless time scaled with the critical-packing liquid volume fraction according to Hounslow et al.'s model for deformation-driven growth [30]. The black line represents the theoretical curve on which all lines should collapse.

In spite of the obvious caveats with interpreting the data obtained with the COG, Figure 5.8 demonstrates that it is possible to study growth behaviour of granules, provided that the systems actually display growth. Furthermore, growth appears to proceed linearly with the square root of time, as predicted by Hounslow et al.'s model for surface tension-driven growth [30]. This finding implies that surface tension, not collision force, is the key driving mechanism in layered growth, even in a dynamic granulation situation. The consequences of this implication are discussed in Section 5.4.2, as well as the question whether this implication extends to consolidation.

5.4.2 Mechanisms of consolidation and layered growth

The analysis of granule growth behaviour showed that granule growth is proportional to the square root of time. An overall qualitative agreement was found with Hounslow et al.'s model for surface tension-driven growth [30], but there were several issues that should be addressed before a fully predictive model can be proposed. This section deals with the kinetics found in this study, as well as showing a comparison to Pitt et al.'s work on static granule nucleation [31]. In their work, Pitt et al. demonstrated that static nucleation is predicted extremely well by Hounslow et al.'s model of surface tension-driven growth, as shown in Figure 5.10. Considering the differences between static nucleation in a powder bed and granulation using equipment that actively agitates the nuclei, the fact that the results presented in this study are predicted by a model for static growth is remarkable. To discern the exact kinetics of layered growth, however, several issues must be addressed. Additionally, although the kinetics of layered growth are predicted by the model, those of consolidation are not. Hounslow et al.'s model assumes no air is present in the granules. Since growth in the model occurs by adding powder volume only, the liquid fraction decreases and granules automatically consolidate. However, the assumption of no air present in the granules is not a realistic assumption unless the granules considered are heavily saturated with liquid. These points are all discussed in the following sections.

5.4.2.1   The kinetics of layered growth

To understand how the kinetics in layered growth are affected by agitation, the results in this work can be compared to the static growth results obtained by Pitt et al. [31]. An effective method of comparing the growth data is to consider the critical-packing liquid volume fraction ϕ_{cp}, and the final consolidation time t_{max} for granules that were grown statically in a powder bed and dynamically in the COG.

Figure 5.10: Dimensionless granule volume difference as a function of the square root of dimensionless time for Pitt et al.'s data [31]. The black line represents Hounslow et al.'s model for surface tension-driven growth [30].

However, comparing the two methods is not straightforward. There is a time difference of approximately one minute between introducing prenucleated granules into the COG and actually starting the granulation. This gap is necessary to seal the vessel, fasten the vessel to the carriage, and close the lid of the COG. Additionally, extraction takes approximately five minutes, as there is a large quantity of powder that needs to be separated from the granules. Static growth, on the other hand, starts as soon as the drop hits the powder bed. Furthermore, Pitt et al.'s method [31] uses far smaller quantities of powder, allowing for rapid extraction of the granules. Of the issues of start-up and extraction, the former is likely to have the most profound effect. The fastest growth occurs at the start of granulation; static growth afterwards

would be slower, and might be insignificant compared to the dynamic growth experienced before this.

Fortunately, there is a way to account for the initial growth between nucleation and the start of granulation. Pitt et al. [31] actually dealt with a similar problem for some systems in static nucleation, where the first data point of granules that could be collected had a relatively high initial mass. The other data points were predicted by Hounslow et al.'s model, showing a linear relationship with the square root of time for all points including the initial granule data point. However, there was a large discrepancy between the initial droplet mass and the first granule mass measured. Pitt et al.'s solution [31] is shown in Figure 5.11.

Figure 5.11 shows the grey data points with the fitted curve (red), from which the maximum granule volume v_{max} and the apparent time until the maximum critical-packing liquid volume fraction has been achieved, t_{max}^{app}, can be calculated. The method proposed by Pitt et al. [31] is based on the principle that an *apparent initial droplet volume*, v_0^{app}, can be calculated by using the slope of the line fitted to the data to extrapolate to the intersection with the y-axis. The actual growth curve starting at initial droplet volume v_0 can then be reconstructed (blue) to calculate the true time until the critical-packing liquid volume fraction has been achieved, t_{max} (Equation 5.4).
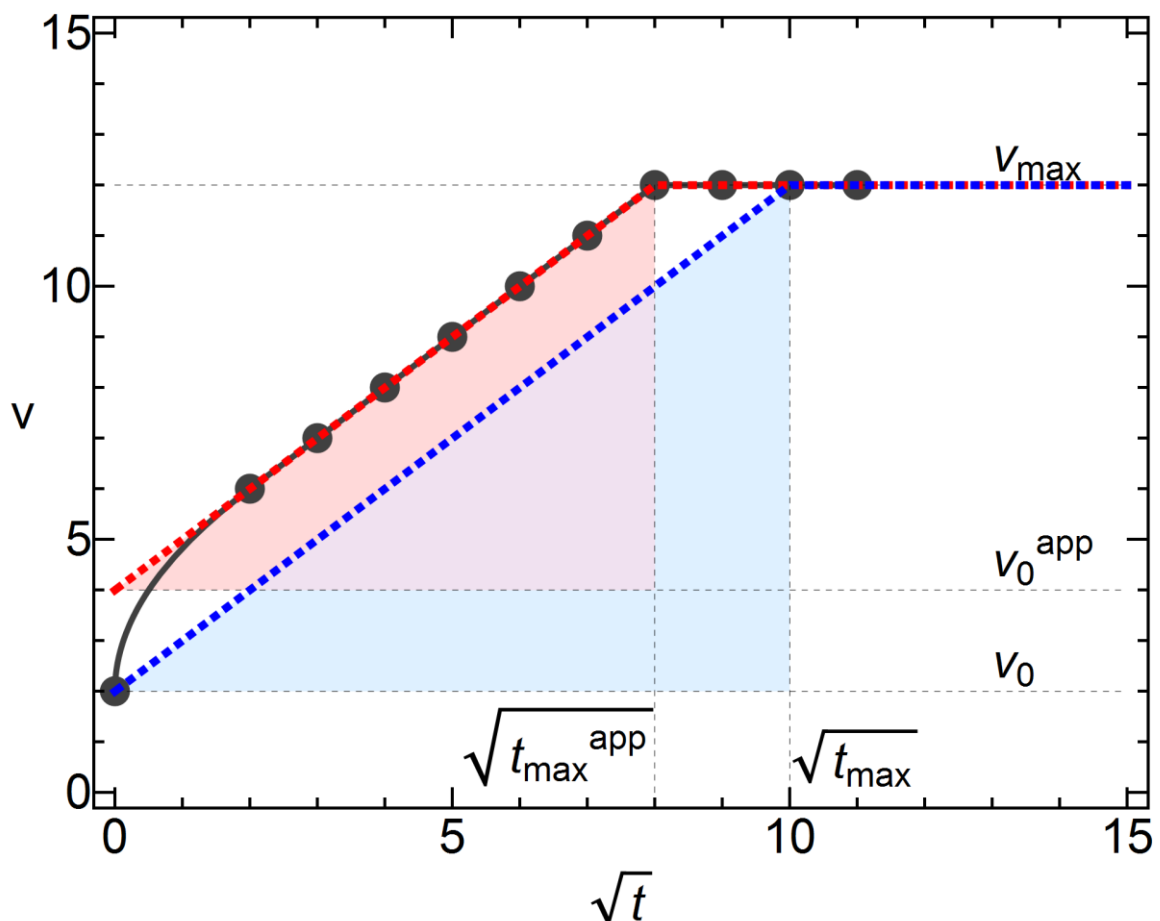
Figure 5.11: Pitt et al.'s method of calculating the true time until critical-packing liquid volume fraction t_{max} using similar triangles on a plot with granule volume as a function of the square root of time [31].

$$t_{max} = t_{max}^{app} \left(\frac{v - v_0}{v - v_0^{app}} \right)^2 \tag{5.4}$$

where all symbols are as described above. Using this method, t_{max} can be compared to the values obtained by Pitt et al. [31], as well as the theoretical values proposed by Hounslow et al. [30], which can be calculated using Equation 5.5:

$$t_{max} = \frac{18.75 * \mu * h_0^2}{\gamma * \cos(\theta) * d} \frac{1 - \phi_{cp}^{1/3}}{\phi_{cp}^3} \tag{5.5}$$

where μ is the binder viscosity, h_0 is the initial droplet radius, γ is the binder surface tension, θ is the powder-binder contact angle, and d is the primary particle diameter. From the equation, it becomes clear that the critical-packing liquid volume fraction ϕ_{cp} plays an important role; a difference of about 0.1 in the determined fraction can lead to an order of magnitude difference in t_{max}. Table 5.2 lists the ϕ_{cp} values for systems evaluated using static nucleation and dynamic nucleation. For lactose-silicone oil based systems, literature values from Pitt et al. were used [31].

Table 5.2 clearly shows that the COG consistently produces granules that have grown more than granules grown in a static powder bed. More specifically, ϕ_{cp} appears to change from approximately 0.2 to 0.1 in dynamic situations. Therefore, the final powder mass gained is approximately doubled for dynamic situations compared to simple static growth. This finding implies that ϕ_{cp} is not only influenced by the powder and binder properties, but also by the equipment used. It is possible that by using a different type of equipment to granulate the same system, ϕ_{cp} changes depending on how strong the impacts exerted on the granules by the equipment are. Care should be taken with this conclusion, however, as granules nucleated by depositing a droplet on a static powder bed do not actually grow in three dimensions. It is possible that the doubling of mass for dynamic situations simply represents the granule growing in full spheres instead of quasi-hemispheres.

Since ϕ_{cp}, is predicted to affect t_{max}, the kinetics of growth are expected to change depending on the equipment used as well. Table 5.3 compares the theoretical granulation times to the times as interpolated using Pitt et al.'s method of compensating for the initial rapid increase in granule mass for both static and dynamic situations. Comparing the theoretical times for static growth and growth in the COG, two major factors influence t_{max}. The first factor is ϕ_{cp}, as explained above. The second difference is in droplet size. ϕ_{cp} accounts for approximately a factor 10. This is confirmed by the lactose-PEG system, which shows about an order of magnitude difference between the static and dynamic situation.

Table 5.2: Comparison of critical-packing liquid volume fractions ϕ_{cp} for both static (s) and dynamic (d) situations.

System	$\phi_{cp,s}$ (-)	$\phi_{cp,d}$ (-)
Lactose-13 mPa•s silicone oil	0.22[*]	0.09
Lactose-52 mPa•s silicone oil	0.21[*]	0.11
Lactose-105 mPa•s silicone oil	0.20[*]	0.13
Lactose-95 mPa•s PEG	0.18	0.09

* calculated using data from Pitt et al. [31]

Table 5.3: Comparison of theoretical times until the critical-packing liquid volume fraction for both static (s) and dynamic (d) situations to the times determined using Pitt et al.'s method [31].

System	$t_{max,theory-s}$ (min)	$t_{max,theory-d}$ (min)	$t_{max,s}$ (min)	$t_{max,d}$ (min)
Lactose-13 mPa•s silicone oil	0.07[*]	4.67	2.23[*]	264.20
Lactose-52 mPa•s silicone oil	0.43[*]	7.76	21.14[*]	232.14
Lactose-105 mPa•s silicone oil	1.00[*]	9.91	34.57[*]	200.12
Lactose-95 mPa•s PEG	1.57	17.59	118.16	191.70

* calculated using data from Pitt et al. [31]

The much larger disagreement between Pitt et al.'s results is caused by differences in initial droplet size; Pitt et al.'s initial droplet size was much smaller than the droplet sizes used in the experiments in this study. The difference between theoretical time and interpolated times, however, are less straightforward to explain. Pitt et al. found that the predictions by Hounslow et al.'s proposed model for t_{max} was unsatisfactory when applied to real situations. However, a general trend can be observed in the static observed times, where an increase in viscosity within the same system leads to an increase in the observed t_{max}. For the dynamic situation, this is not the case. All values are similar in magnitude, and, interestingly, an increase in viscosity appears to lead to a decrease in t_{max}. This conclusion would not be logical, however. There is clear evidence in the literature, as well in Pitt et al.'s results, that an increase in viscosity slows down growth [30,31,55]. A more logical cause of this discrepancy is the fact that the true values for v_{max}, and in extension t_{max}, were never observed due to breakage.

A different method of evaluating the kinetics of growth is by solely considering the slope of the growth line. The slope can be determined by rewriting Equation 2.11 in terms of ϕ_{cp} to produce Equation 5.6:

$$v = v_0 + v_0 * \left(\frac{1 - \phi_{cp}}{\phi_{cp} * \sqrt{t_{max}}} \right) * \sqrt{t} = v_0 + v_0 * a * \sqrt{t} \tag{5.6}$$

With the initial droplet volume v_0 known, the only unknown parameters in this function are t_{max} and ϕ_{cp}, which can be lumped into parameter a. By comparing parameter a between all data sets, a general trend may be observed, as shown by Table 5.4. Increasing viscosity in a single powder-binder system clearly lowers the growth rate, which is as expected. Interestingly, the overall growth rate for lactose-silicone oil systems appears to decrease when changing to a dynamic system. From Equation 5.6, it can be inferred that this change in growth rate can be attributed to an increase in t_{max}, as the experimental results clearly show a decrease in ϕ_{cp}. A potential cause could be the attrition and breakage of the granules, which is more prevalent in the COG than in a static situation.

Table 5.4: Lumped growth parameter a for both static (s) and dynamic (d) situations.

System	a_s (min$^{1/2}$)	a_d (min$^{1/2}$)
Lactose-13 mPa•s silicone oil	2.37[*]	0.65
Lactose-52 mPa•s silicone oil	0.82[*]	0.52
Lactose-105 mPa•s silicone oil	0.68[*]	0.47
Lactose-95 mPa•s PEG	0.41	0.73

* calculated using data from Pitt et al. [31]

On the other hand, the lactose-PEG system appears to have a larger growth rate in a dynamic situation. This phenomenon is not caused by shear thinning, as both silicone oil and PEG showed no such behaviour. Breakage and attrition may also be the cause of the difference in kinetics between lactose with silicone oil or PEG as a binder. However, a more thorough investigation is required to confirm this possibility.

Finally, it should be noted that the initial droplet size influences the kinetics of layered growth; a larger droplet size will increase the overall growth rate. Since larger initial droplet sizes were used in this work, the overall kinetics are faster than those obtained by Pitt et al. [31].

5.4.2.2   The kinetics of consolidation

A final assumption that must be discussed is the actual air content of the granules. Hounslow et al. [30] assume that no air is present in the initial granule, and the increase in mass is based purely on the layering of powder. In reality, the granules will contain air. As demonstrated by the comparison of all systems in Figure 5.8, the fact that granules are porous has no effect on the actual qualitative growth behaviour of the granules, although it will likely affect the maximum attainable granules size, v_{max}, and the time needed to reach this size, t_{max}.

To determine how the porosity of the granules changed during the granulation time in the COG, granules with short and long granulation times were analysed using both helium and powder pycnometry to obtain the true and envelope density of the granules, respectively. Table 5.5 lists the initial and final porosity of all granules analysed, as well as the relative change in porosity.

Interestingly, changes appear very slight, sometimes falling within the margin of error for of the values. Furthermore, there is no general trend visible; for some systems, the porosity increases slightly, whereas it decreases for other systems. The overall effect of the impacts produced by the COG on porosity seems non-existent; it appears that no actual consolidation occurs. This is a remarkable result, considering the COG generates forces capable of causing attrition and breakage of the granules. Consequently, it appears as though the decrease in critical-packing liquid volume fraction compared to Pitt et al.'s results [31] is indeed partially caused by the transition from a 2.5-D to a 3-D situation; for the set-up in this study, the nucleus can grow in all directions, as opposed to Pitt et al.'s method where a nucleus can only grow into a hemispherical volume.

Table 5.5: Granule porosities at the start and end of granulation. Standard errors are shown in parentheses.

System	ε_{start} (-)	ε_{end} (-)	Change (%)
Lactose-13 mPa•s silicone oil	0.428 (0.003)	0.408 (0.008)	-5 (2)
Lactose-52 mPa•s silicone oil	0.408 (0.007)	0.431 (0.003)	6 (2)
Lactose-105 mPa•s silicone oil	0.40 (0.06)	0.43 (0.01)	7 (15)
Lactose-130 mPa•s PEG solution	0.68 (0.01)	0.695 (0.009)	2 (2)
Lactose-3192 mPa•s PEG solution	0.37 (0.01)	0.36 (0.01)	-4 (5)
Lactose-95 mPa•s PEG	0.43 (0.04)	0.442 (0.005)	2 (2)
Glass beads-52 mPa•s silicone oil	0.490 (0.007)	0.447 (0.005)	-9 (2)
Glass beads-105 mPa•s silicone oil	0.406 (0.009)	0.433 (0.008)	7 (3)
Glass beads-1043 mPa•s silicone oil	0.39 (0.01)	0.383 (0.007)	-3 (4)
Glass beads-130 mPa•s PEG solution	0.31 (0.01)	0.342 (0.006)	12 (4)

5.4.2.3   The mechanism of layering

In the previous section, it was established that there is no clear consolidation occurring in the granules during granulation in the COG. However, layering clearly occurs, and it appears there is a difference between static growth in a powder bed and dynamic growth in the COG. There is a possibility that this difference in caused by the transition from a 2.5-D static bed to a 3-D granulator. This section aims to elucidate the mechanism by which layering takes place in both situations.

In order to investigate this, the difference in the internal structure between statically and dynamically grown granules was studied using X-ray computed tomography. Figure 5.12 shows a comparison of representative tomography images for a system using lactose as the powder and 105 mPa•s silicone oil as the binder liquid. Note that the rings around the granules are part of the sample container. Statically and dynamically grown granules are compared both after a short granulation time and after the granules stopped growing. These times are not equal, as demonstrated by the results presented in Section 5.4.1.

Several interesting observations can be made from Figure 5.12. From all images, two different basic regions can be discerned; the core and the outer shell. This is logical, as the core of all granules was originally a liquid drop. However, there is a difference in cores and shells between granules grown in the COG and statically grown granules. Granules grown in the COG show clear voids, represented by the black areas. These are likely cracks formed by the impacts in the COG, and they appear even after 2 min of granulation. Statically grown granules show no such cracks.

Apart from the obvious cracks in the granules, the cores of the dynamically grown granules show larger voids than the much more tightly packed cores of granules grown in a static powder bed for both times. During growth, the cores of statically grown granules appear to have slightly more voids, whereas this effect is much less pronounced in dynamically grown granules. The increase in voidage in the static case can be attributed to movement of the binder liquid; cavities originally filled with liquid might be drained due to liquid spreading. It is possible that the wider availability of contact area in the COG promotes this drainage. This theory is supported by the fact that the core of the granule after short dynamic granulation looks very similar to that of the dynamically grown granule at the end of its growth.

A final remarkable difference between the statically and dynamically grown granules is the structure of their outer shells. The statically grown granules have a clear shell layer, but the shell does not have a specific structure, with loosely packed powder surrounding the core. There is, however, a clear layer-like structure to the powder shell found around the core of the granules grown in the COG. The powder has grown around the core in layers, and the layers are much more compacted than the layers in the statically grown granules. In both cases, the shell layer is clearly thicker after a long granulation time compared to the shorter times. This finding demonstrates that there is definitely a consolidating effect found in granulation with the COG. However, it appears as though consolidation and the formation of macrovoids by fracturing result in an overall neutralising effect on the porosity values obtained, as demonstrated earlier in Table 5.5.
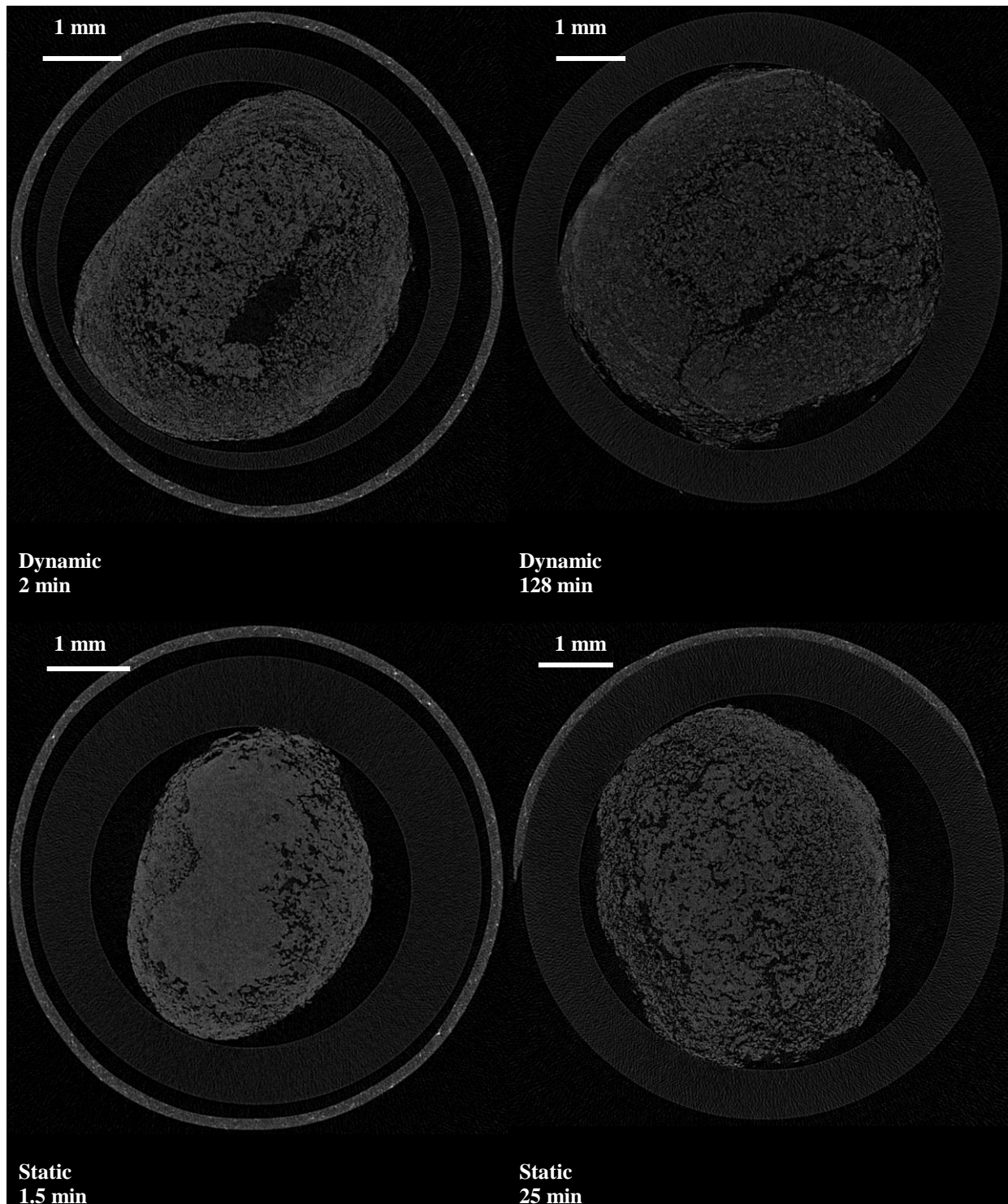
Figure 5.12: Comparison of X-ray tomography images of lactose-100 cSt silicone oil at the early and late growth times for static and dynamic situations. The rings are part of the sample container.

The core-shell structure found could explain the two modes of breakage observed for lactose-based granules: fracturing of the whole granule, caused by the cracks formed in the core, and breakage of the outer layer of the granules, caused by the poor connection between core and shell.

The effect of powder particle shape can be investigated by comparing the growth behaviour of lactose-based systems to that of systems based on glass beads. Figure 5.13 shows a comparison between granules produced from glass beads and 100 mPa•s silicone oil after different growth times in the COG and a static powder bed.
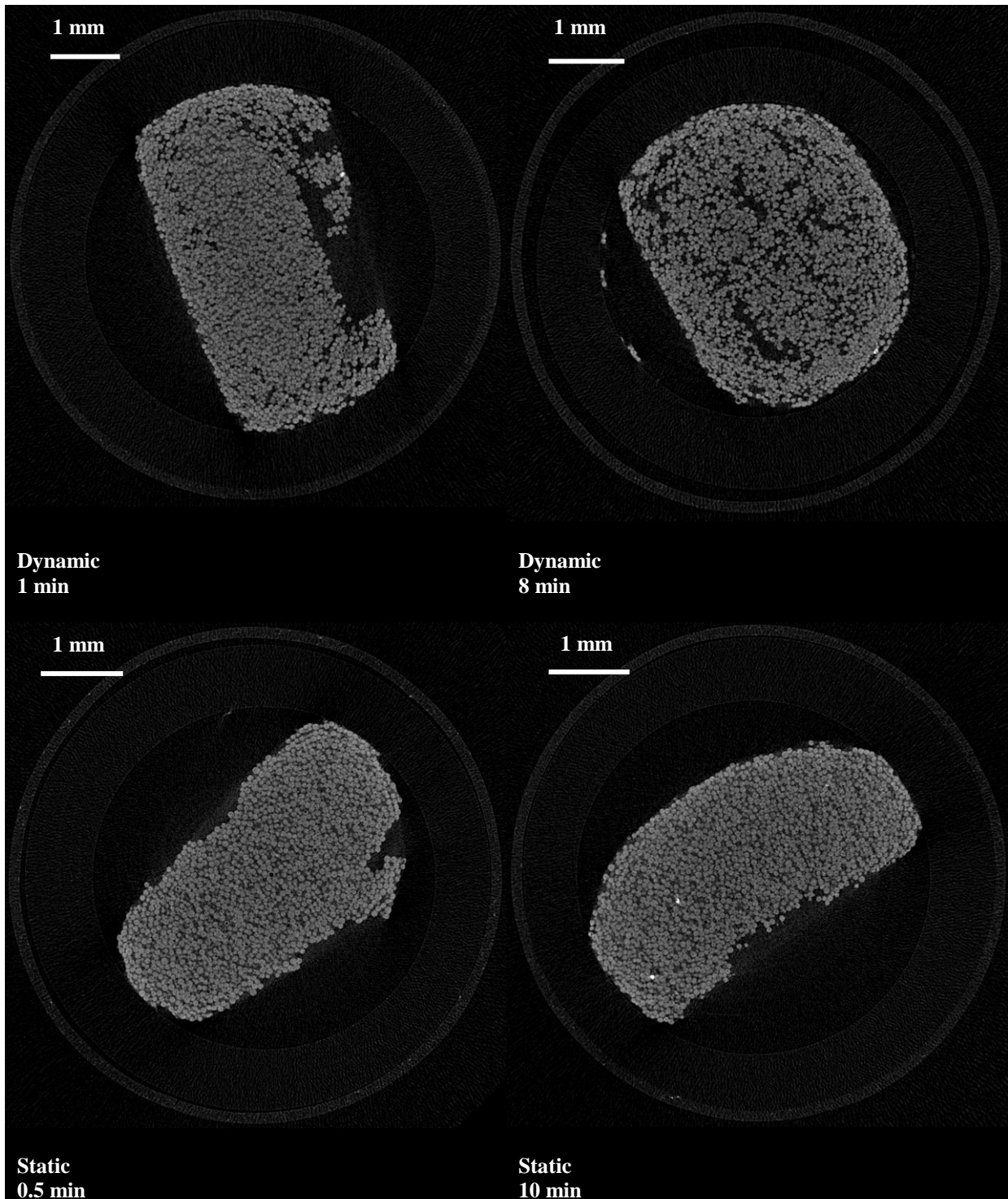
Figure 5.13: Comparison of X-ray tomography images of glass beads-100 cSt silicone oil at the start and end of growth for static and dynamic situations. The rings are part of the sample container.

The glass beads-based granules in Figure 5.13 show different behaviour compared those based on lactose from Figure 5.12. There is no clear core-shell separation for the glass-based system. Additionally, no voids are present in the statically grown granules. However, the granules grown in the COG clearly show the development of macrovoids in the granule, particularly after 8 min of granulation time. This can be partially attributed to internal fracturing. The reason for fracturing is also obvious from the images, as well as visual observations of the granules; statically nucleated granules and granules that have been granulated in the COG for short times are disc-shaped. In the COG, the granules deform and become more spherical after granulation due to the 3-dimensional nature of the powder bed and the impacts in granulator. These deformations, which are not present in statically grown granules, have resulted in internal fractures.

The differences in internal structure between lactose and glass beads-based systems can be explained by powder particle shape. Glass beads are spherical and move easily, whereas lactose-based granules are stronger due to the irregular shape of the powder [62]. This enables the glass-based systems to deform more easily into tightly packing structures, whereas lactose-based systems develop larger voids. Additionally, glass beads are slightly larger than lactose particles (74 compared to 49 μm for lactose), and have a narrow particle size distribution. This difference causes lactose-based granules to be stronger, and less prone to plastic deformation [63]. Therefore, the lactose-based systems show a clear distinction between the original core of the granule and the shells formed around it, whereas the glass beads-based granules show no such distinction. Therefore, there is no possibility of tighter packing for glass beads-based systems, and consolidation is unlikely to be observed. This is also the reason why glass-beads based systems show shorter growth time ranges than lactose-based systems. The tightly packed glass beads have few voids to impede the binder; therefore, the granule reaches its maximum size much faster than with lactose-based granules.

In conclusion, there appears to be a consolidating effect by the COG, but this is only visible in systems with a powder that is not already tightly packed. The consolidating effect does not lead to an overall decrease in the porosity due to the formation of macrovoids during granulation.

5.4.3 Viability of the COG for studying consolidation and layered growth

The results obtained using the COG have led to interesting observations and results. However, the question remains as to whether this newly developed equipment is useful for the study of consolidation and layered growth. This question concerns both the reliability of the results presented, as well as the actual process by which granulation takes place in the COG.

The repeatability of the COG was evaluated by performing a triplicate series of experiments with lactose-105 mPa•s silicone oil. The results are shown in Figure 5.14. For short granulation times, i.e. times when the maximum attainable granule mass has not been reached, the results show good agreement. However, as the granulation process progresses, the spread in data points becomes larger. For longer granulation times, which are not shown in the figure, the agreement between the three sets completely vanishes. This increase in error could be the result of breakage and attrition, which causes inaccuracies in the measured granule mass.

Overall, it appears as though the reliability of the COG is sufficient for obtaining growth data for intermediate granulation times. However, the accuracy and precision of the COG are both greatly reduced for long granulation times. As a result, a different method is needed to determine the maximum attainable granule size for a specific system.

An additional limitation of the COG is the fact that the granules it produces provide no useful data with which to investigate granule consolidation. Although X-ray tomography images suggest that at least some consolidation occurs in the outer shell of the granule, no overall consolidation is observed from pycnometry measurements. This effect is most likely caused due to the balance of consolidation with fracture formation. It is possible that in industrial granulation, a combination of consolidation, breakage and reagglomeration causes the overall decrease in porosity. Alternatively, an increase in the pore saturation by the constant addition of liquid binder might also promote the deformability of the granules, which could aid in the reduction of the macrovoid volume due to deformation.

Regardless of the actual mechanisms, the COG is designed in such a way that the data it provides cannot provide clear data concerning consolidation. Increasing consolidating forces would also increase breakage, invalidating the growth data, as would promoting agglomeration and reagglomeration.
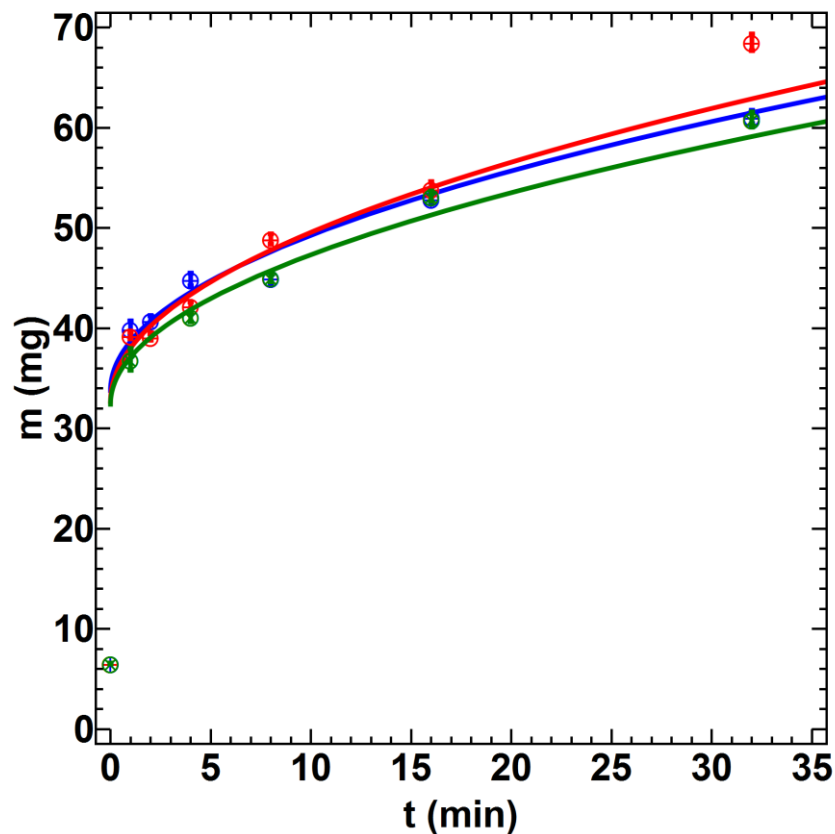
Figure 5.14: Comparison of granule mass as a function of time for three lactose-105 mPa•s silicone oil data sets. Lines were fitted by using Hounslow et al.'s model for surface tension-driven growth [30].

In spite of its limitations, the COG provides kinetics of layered growth that appear to describe granule growth behaviour quite well. The resulting growth rate, a fitting constant a, could be used for modelling of the process. Ideally, an expression to estimate critical-packing liquid volume fraction ϕ_{cp} should be found to determine the maximum attainable granule size and the time needed to reach this size, as well as the full predictive kinetics. As a final remark, it is interesting that the typically found growth times are in the order of minutes to hours for the systems evaluated. This suggests that the critical-packing liquid volume fraction is never reached during practical granulation processes, unless perhaps aggressive consolidation and breakage is applied to force growth.

5.5 Conclusions

In this study, granule consolidation and layered growth behaviour was studied using a newly developed consolidation-only granulator (COG). Experiments were set up in such a way that the effects of wetting and nucleation as well as agglomeration were eliminated, and the effect of breakage and attrition was greatly reduced. The data obtained in the experiments was compared with predictions from existing models in the literature in order to elucidate the mechanisms and kinetics of growth. In this way, three of the key objectives of this work were addressed; the development of an experimental method to study consolidation and layered growth, the generation of experimental data using this method, and the identification of a model that describes the kinetics of layered growth.

Layered growth proceeded linearly with the square root of time, as predicted by Hounslow et al.'s model on surface tension-driven growth [30]. This model uses the critical-packing liquid volume fraction ϕ_{cp} and final granulation time t_{max} as the only two unknown parameters for determining growth kinetics. The fact that this model predicts granule growth implies that powder-binder interaction is the driving force behind layering. There was very little qualitative difference between static growth data from Pitt et al. [31] and the dynamic growth data obtained in this work. Quantitatively, however there were differences in both the observed and interpolated t_{max}, and no trends were found to predict it accurately. Furthermore, the obtained critical-packing liquid volume fraction is smaller for dynamic situations compared to the static case. This effect can partially be attributed to the fact that static growth requires a 2.5-D bed, whereas more realistic dynamic growth takes place in a 3-D environment.

From porosity calculations using pycnometry, it appears as though no overall consolidation of the granules occurred in the COG. In spite of this, X-ray computed tomography revealed that the additional powder mass layered around the granule has a higher density than the core. However, fractures negate the effect this denser layer would have on the overall granule porosity. Comparison with statically grown granules showed that such granules grow differently, with fewer macrovoids inside the granules, but a less dense grown layer around the core. It appears as though consolidation, in practice, occurs via either stronger impacts that force breakage and reagglomeration, or by constant wetting, which increases the deformability of the granules.

Overall, the COG was successful in isolating layered growth from other granulation mechanisms, and the growth kinetics obtained are a major leap in understanding and modelling layered growth. However, there are several limitations to experiments using the COG. In eliminating the effect of wetting and nucleation by prenucleation, the liquid fraction

of the granules can only decrease. In combination with the relatively weak impacts of the COG to eliminate breakage and attrition, overall consolidation does not occur. Therefore, the COG is not suitable for studying consolidation. Moreover, breakage and attrition is not fully eliminated, and the granules show attrition and fracturing after long granulation times. Although results for short and intermediate granulation times are consistent, results for long granulation times show significant variation between different repeats. In addition, determining t_{max} and the final granule volume is impossible due to significant breakage after long granulation times. A final limitation of the COG is the fact that early growth behaviour cannot be measured, although Pitt et al. proposed a method of addressing the initial leap in granule mass at the start of granulation [31].

Using the kinetic data successfully obtained with the COG, the initial workings of a model have been put in place. However, works needs to be performed to accurately determine the key parameters ϕ_{cp} and t_{max}. The following chapter focuses on addressing this issue.

Chapter 6.   Layered growth in a mixer with a flat plate impeller

6.1 Introduction

The consolidation-only granulator (COG) presented in Chapter 5 was successful in demonstrating that layered growth behaviour of granules can be predicted qualitatively using Hounslow et al.'s model for surface tension-driven growth [30]. In this model, granules grow linearly with the square root of time until a *critical-packing liquid volume* fraction, ϕ_{cp}, has been reached. ϕ_{cp} determines the maximum attainable granule size, and the time it takes to reach this maximum size is termed t_{max}. According to the model, both ϕ_{cp} and t_{max} determine the kinetics of granule growth. However, the experiments in the COG did not yield these values, as the maximum granule size was not reached due to granule breakage. In order to allow for the quantitative modelling of granule growth behaviour, this issue needs to be addressed. Furthermore, an initial rapid increase in granule mass was observed in the experiments, which is not predicted by the model. Although Pitt et al. [31] found a method to compensate for this leap, it is necessary to account for the rapid increase if a mechanistic model is developed. The purpose of the work described in this chapter is to identify a method with which to reach maximum consolidation, as well as discuss methods to account for initial granule growth.

The aims of the work described in this chapter are:
- To design a method to reach maximum attainable granule size
- To determine ϕ_{cp} and t_{max} for the system evaluated
- To investigate methods to calculate these values
- To evaluate the effect of the initial rapid increase in granule mass

Instead of using the COG, a high-shear mixer with a flat plate impeller is used to provide a moving 3-D bed without causing significant breakage. The overall method used, discussed in Section 6.2, was similar to that of the growth experiments described in Chapter 4, Section 4.2 and Chapter 5, Section 5.3. However, instead of granulating prenucleated granules, paste prepared from powder and binder was cut and granulated. The resulting granules were weighed and analysed for their densities. Additionally, X-ray tomography was performed on a selection of granules to study their internal structure.

The values and kinetics obtained were compared to data from Chapter 5, and an extension of Hounslow et al.'s model [30] was proposed in order to estimate ϕ_{cp} and t_{max}. Additionally, data provided by Shukri [159] was used to discuss rapid initial growth and its consequences on the model predictions.

6.2 Method development

In the work thus far, the breakage of granules has been a significant limiting factor for an adequate study of consolidation and layering mechanisms. Even the design of the consolidation-only granulator (COG), which aims to reduce breakage as much as possible, did not succeed in completely eliminating granule breakage, as demonstrated in Chapter 5. Therefore, an attempt was made to develop a method which limited granules impacts, while still providing a moving powder bed and deformation forces. For this purpose, a high-shear mixer with a flat plate impeller was selected as the granulator. In order to ensure good mixing, the granulator was operated at speeds at which the roping regime was observed.

Instead of using droplet nucleated granules, a paste was made by mixing powder and binder liquid, then cut and added to the granulator. This was done for two reasons. Firstly, using paste granules essentially starts the growth process in the 'middle' of granulation, ignoring the initial rapid increase in granule mass observed in the experiments performed with the COG described in the previous chapter. Without this initial leap, it should be easier to predict growth behaviour using the model, as there would be no need to account for apparent t_{max}; the time needed to reach the granulation end point from the mass after the initial leap occurred. Secondly, as a result of to the premixing of powder and binder, the paste-based granules are expected to be more homogenous than droplet-nucleated granules. Since the shell grown around prenucleated granules was observed to be brittle and low in liquid content, a more homogenous granule should show less wear and breakage.

For the scope of this study, it was decided that a single powder-binder system would be evaluated, and that the focus would lie on the repeatability of the experiments. In this way, the maximum attainable granule size and ϕ_{cp}, as well as t_{max}, could be determined as accurately as possible for this set-up.

6.3 Materials and methods

Similar to the high-shear mixer study described in Chapter 4 and the consolidation-only granulator (COG) studies described in Chapter 5, the method of the experiments performed was based on prenucleation of granules outside of the granulator, followed by granulation, extraction and analysis. Experiments were performed using a high-shear mixer (Key International Inc. KG-1 Granulator) to compare results to the data obtained using the COG. In order to minimise breakage and attrition, a flat plate impeller was used (2.5 L bowl), and granules were prenucleated from paste as described below to make the nuclei less fragile. To investigate the effect of impeller speed, the granulator was operated at two different speeds in the roping regime; 500 and 750 rpm. Additionally, an experiment at a single granulation time (25 min) was repeated seven times in order to investigate the reproducibility of the method. The consolidation performance of the flat impeller was compared to that of a three-bladed impeller (2.3 L bowl) in the same granulator operated at the minimum speed required for the well-mixed roping regime (250 rpm). All operating set-ups used in this study are shown in Table 6.1.

Table 6.1: Overview of all conditions used in experiments with the high-shear mixer.

Impeller	Speed (rpm)	Times (min)	Nucleation	# of data points
Flat plate	500	0.25-30	Ruler	11
Flat plate	750	0.25-20	Grid	11
Three-bladed	250	0.05-0.3	Grid	6
Flat plate	500	0.25-25	Grid	11
Flat plate	750	0.25-25	Grid	11 (x2)
Flat plate	750	25	Grid	7

For comparison, the same powder-binder system, lactose-105 mPa•s silicone oil, was used in all experiments. First, the powder was passed through a 1.14 mm sieve, and the granulator was loaded with 350 g of powder. The powder was then premixed at the desired speed for 20 s. Next, the paste was prepared with the powder and binder liquid. The *liquid volume fraction* used was chosen in such a way that the paste could be cleanly cut, but was wet enough to be extruded properly. For this particular system, the optimal liquid volume fraction was found to be 0.45, which corresponds to a liquid to solid ratio of 0.53. Using the true densities of the solid and liquid, the required masses of the materials were calculated, weighed and thoroughly mixed in a bowl. After mixing, the materials were loaded into a baker's syringe with a blunt nozzle, of which the 4.78 mm orifice was large enough to enable extrusion of the paste. The paste, shown in Figure 6.1, was extruded on cling film and cut into 5 mm cylinders with a spatula. For the first series of experiments, at 500 rpm, a ruler was used to cut the granules to size, but a 5 mm paper grid underneath the cling film was used for all further experiments in order to reduce variation in paste piece size. Each piece of paste was immediately introduced into the granulator. After 20 nuclei had been produced and added to the granulator, the paste was granulated for a set amount of time. Granulation times depended on the impeller used; the flat impeller granulated more slowly and produced more intact granules than the three-bladed impeller. The granules were then extracted, separated from the powder using a 1.4 mm sieve and weighed individually using a microbalance (Mettler-Toledo XS3DU, 1 μg accuracy). The experiment was repeated for a longer granulation time until no further increase in mass was observed.

The true and envelope density of granules were determined using helium and powder pycnometry, respectively, for early and late stages of growth. In this way, the porosity could be evaluated at the start and end of granulation.
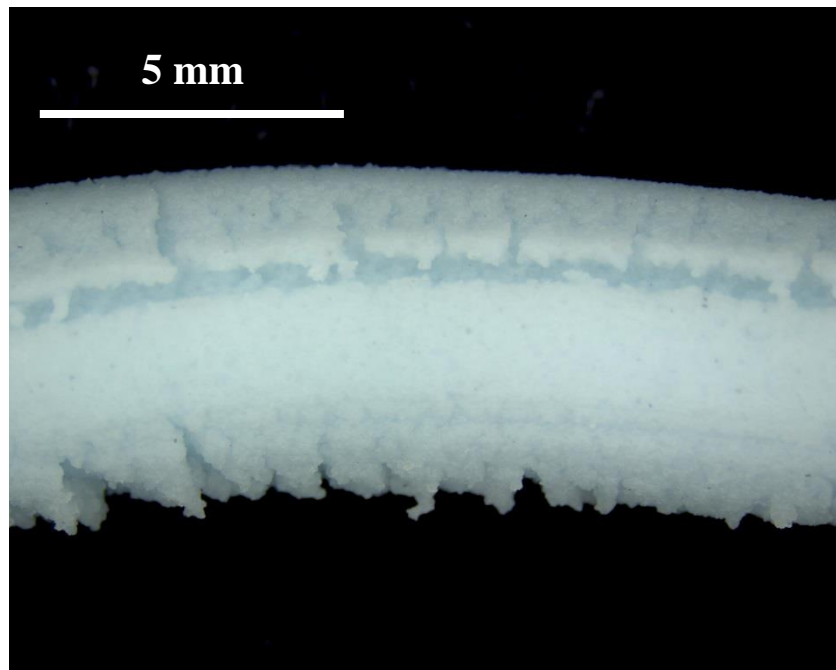
Figure 6.1: Extruded lactose-100 cSt silicone oil paste.

Additionally, X-ray tomography was used to investigate the changes in internal structure over time of the produced granules. A single set of granules (produced at 750 rpm) was investigated at two different times; after 0.5 and 20 min of granulation. For each time, three different representative granules were evaluated, for a total of 6 images.

6.4 Results and discussion

This section is divided into three parts. Section 6.4.1 presents and discusses the results of the experiments performed. In Section 6.4.2, an attempt is made to extend Hounslow et al.'s surface tension-driven growth model [30] to account for the observed consolidation behaviour. Finally, Section 6.4.3 focusses on initial granule growth, and ways to predict the observed rapid initial granule growth.

6.4.1 Growth behaviour of paste-based granules

Growth of the paste-based granules was observed for all conditions evaluated, but the growth behaviour varied for the different operating speeds and impellers used. Therefore, growth behaviour is initially discussed separately for each operating condition. Figure 6.2 shows the first condition; paste granules which have been granulated at 500 rpm using a flat plate impeller.
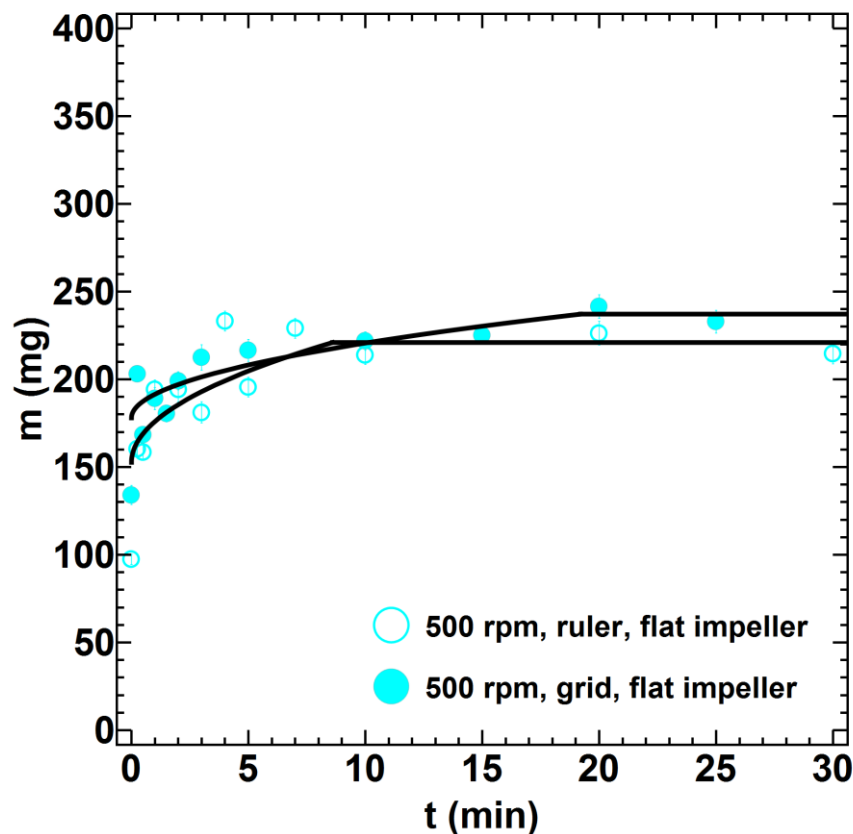
Figure 6.2: Granule mass as a function of time for granules produced from paste cut using either a ruler or a grid and granulated at 500 rpm with a flat plate impeller. Error bars indicate standard errors, and lines were fitted using Hounslow et al.'s model for surface tension-driven growth [30].

Figure 6.2 shows that the paste granules show steady growth until a maximum has been reached, much like droplet-nucleated granules. There also does not appear to be a large difference between paste prepared with a ruler and paste prepared with a grid, although the grid method does appear to produce less variation in the data points; more points fall on the fitted curve. Therefore, this method was used for subsequent experiments.

Figure 6.2 also shows that there is still an initial fast increase in granule mass, which is not accounted for by the model. It is possible that this is caused by the method of addition to the granulator; paste granules are added as they are cut, leaving a few minutes for the paste to sit in a static powder bed. Another potential cause for the initial leap is the presence of liquid at the surface of the paste granule. Therefore, no liquid movement is required to produce the first initial layer around the granule, causing the initial growth to occur instantaneously. This topic of initial growth is discussed in more detail in Section 6.4.3.

The observation of growth and the end of the growth regime in the high-shear mixer with a flat impeller blade clearly demonstrates that paste-based granules remain intact in the mixer. In order to investigate whether paste-based granules could survive higher shear, the effect of using a three-bladed impeller was investigated. Figure 6.3 shows the growth behaviour of paste granulated using the three-bladed impeller at 250 rpm. Growth occurred at much shorter time scales compared to the flat plate impeller. The data set shows an overall increase in mass of about 50% after 4 seconds. After this increase, no further growth is observed. At a first glance, growth appears to occur without an initial rapid increase.
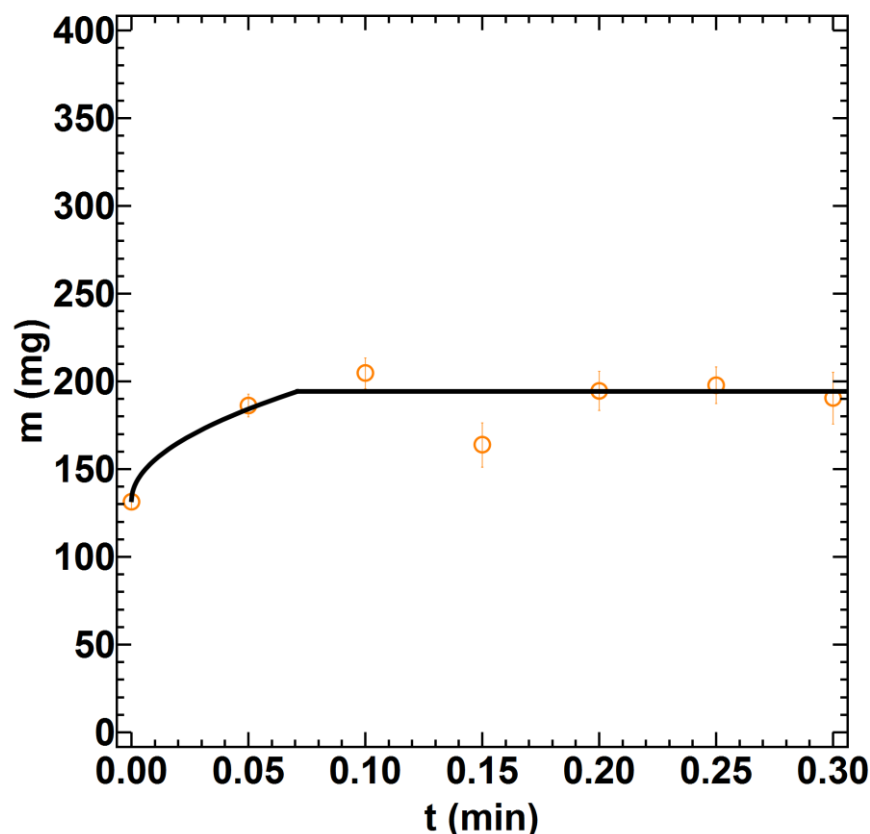
Figure 6.3: Granule mass as a function of time for granules produced from paste at 250 rpm with a bladed impeller. Error bars indicate standard errors, and lines were fitted using Hounslow et al.'s model for surface tension-driven growth [30].

However, this absence of a leap is caused by a lack of growth after the first measured data point at 0.05 min. Since the maximum size is reached at this point, any line fitted between these two points automatically follows the data.

The cause for the observed lack of further growth is obvious from visual inspection: the granules show signs of breakage and attrition, which is reflected by the relatively large standard error bars in Figure 6.3. Despite the obvious damage, the system does display overall growth. The porosity of the granules produced with the three-bladed impeller is compared to that of granules produced with a flat plate impeller in Section 6.4.1.2.

Figure 6.4 shows the growth behaviour of the three sets of paste granulated at 750 rpm with a flat plate impeller. After an initial steep increase, the granule mass increased steadily according to Hounslow et al.'s model for surface tension-driven growth [30]. After approximately 20-30 minutes (23 min average), growth stopped, and the final granule size was reached. Apart from the slight variation in apparent t_{max}, the granules show comparable growth behaviour. Compared to the system cut on a grid and granulated at 500 rpm, two observations can be made, as shown in Figure 6.5.
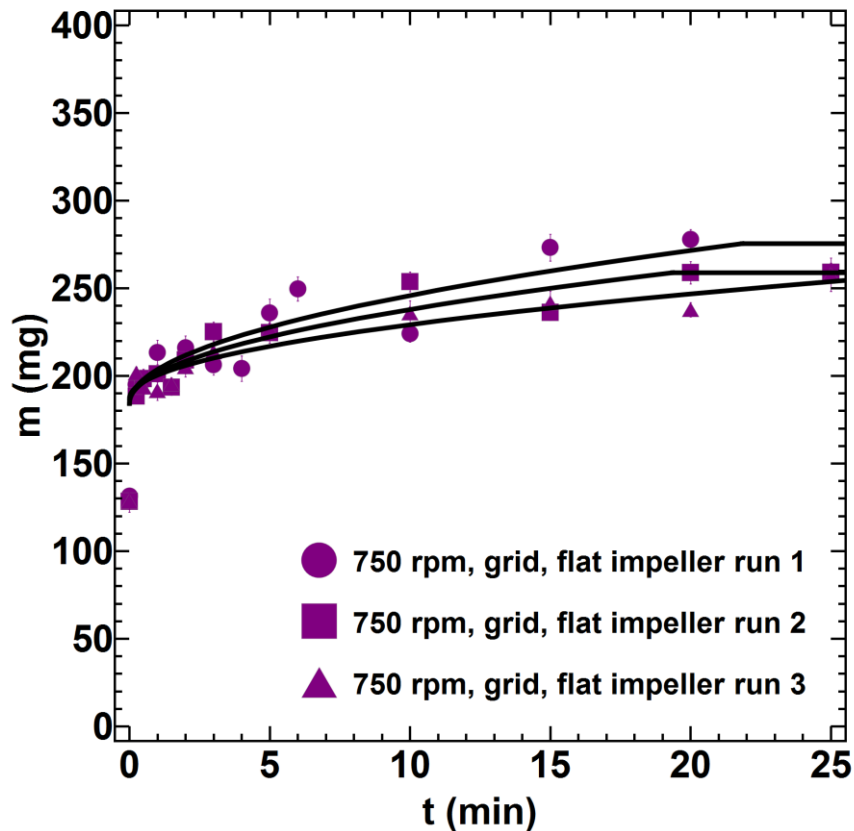
Figure 6.4: Granule mass as a function of time for granules produced from paste at 750 rpm with a flat plate impeller. Error bars indicate standard errors, and lines were fitted using Hounslow et al.'s model for surface tension-driven growth [30].

First of all, the final granule mass obtained is slightly smaller for the 500 rpm set than for the 750 rpm sets; 237 mg and an average mass of 264 mg, respectively. The time it takes to achieve this mass is also slightly shorter for the 500 rpm set, with t_{max} only being 19 min. Secondly, it turns out that this effect does not even out completely; the mass gain rate is 13.5 mg/min$^{1/2}$ for the 500 rpm set, and 16.7 mg/min$^{1/2}$ (averaged) for the 750 rpm sets. This finding implies that the impeller speed does have a positive effect on the growth rate; in this case, a 50 % increase in impeller speed leads to a 23 % decrease in growth rate. This value is close to 22 %; the square root value of a 50 % increase.

The obtained value could suggest a square root relationship between impeller speed and growth rate (Equation 6.1). However, the possible range of rotational speeds (500-750 rpm) is too narrow to properly investigate this with the current set-up.

$$\frac{r_1}{r_2} \propto \sqrt{\frac{\omega_1}{\omega_2}} \qquad\qquad (6.1)$$

In Equation 6.1, r is the growth rate, and ω is the impeller frequency of rotation.
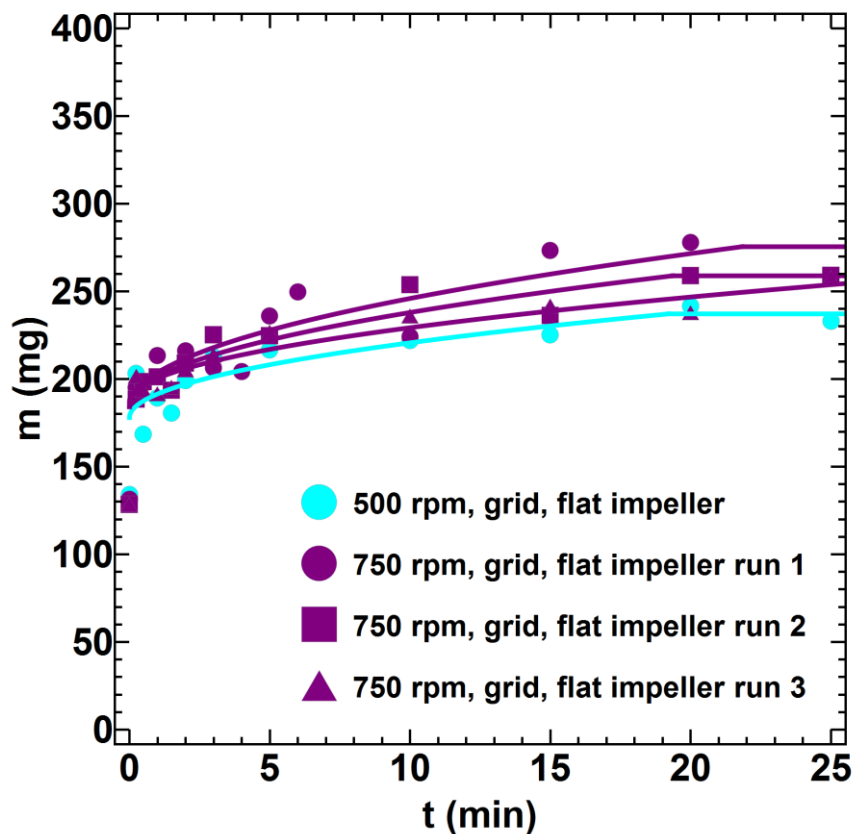
Figure 6.5: Comparison of granule mass as a function of time for granules produced from paste at 500 and 750 rpm with a flat plate impeller. Error bars indicate standard errors, and lines were fitted using Hounslow et al.'s model for surface tension-driven growth [30].

Figure 6.6 shows the dimensionless growth scaled according to Hounslow et al.'s model for surface tension-driven growth [30] for the 500 and 750 rpm sets, using paste cut on a grid. Several observations can be made from the figure. First of all, qualitatively, the granules appear to demonstrate linear growth with the square root of time. However, the deviation from the expected growth line is much larger than the deviation from the scaled growth line demonstrated by the COG-produced granules in Figure 5.8 of the previous chapter; the prenucleated granule data only showed deviations at the transition between steady growth and no growth. The larger deviations in Figure 6.6 may be caused by the difference in nucleation methods; granules cut from paste show inherently more deviation in mass than droplets produced by a syringe pump; initial drop-nucleated granules have a relative standard error of 0.1-1.7 %, as opposed to 3.0-4.8 % for cut paste. Hence, results show more variation. This explanation is also supported by the fact that the standard errors for the paste-based granule masses are significantly larger than those of the drop-nucleated granules in Figure 5.3-Figure 5.7 in Chapter 5.
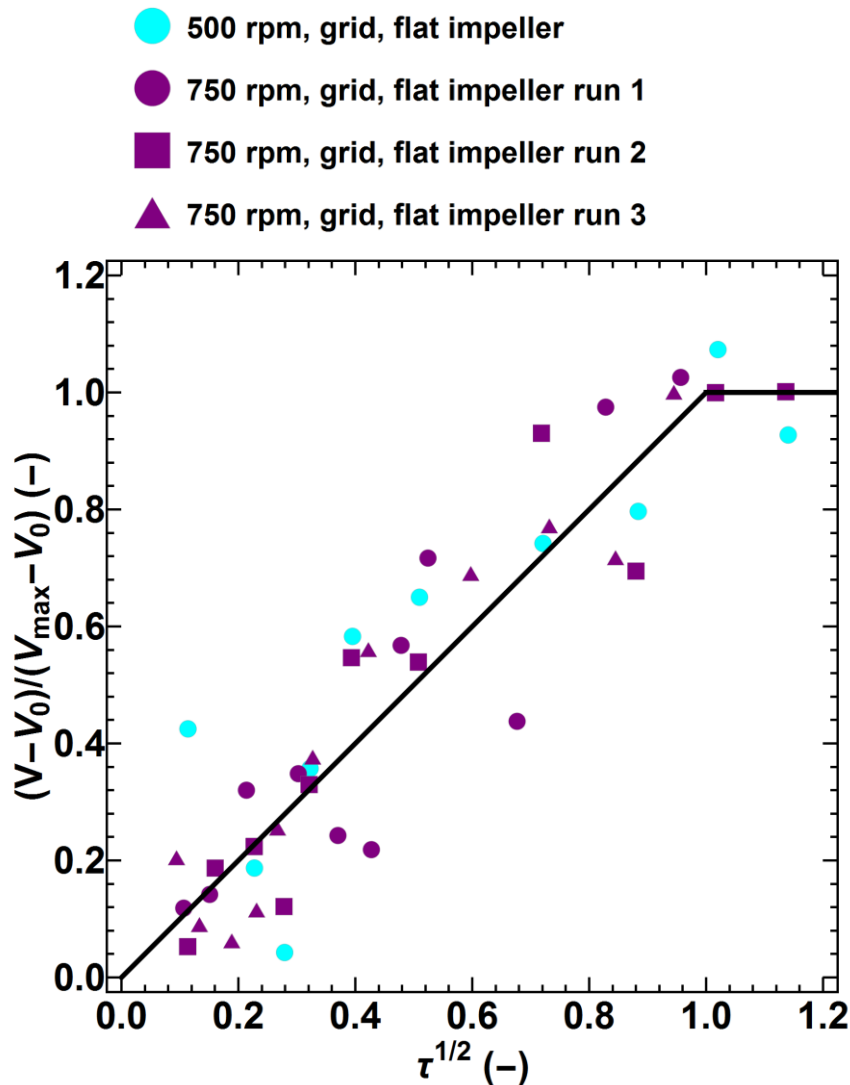
Figure 6.6: Dimensionless granule volume difference as a function of the square root of dimensionless time for all granules produced from paste cut on a grid. The black line represents Hounslow et al.'s model for surface tension-driven growth [30].

In the previous chapter, it was also established that there were deviations from the predicted line in the range of 0.8-1 for $\tau^{1/2}$. It was proposed that these deviations might be caused by breakage, and the absence of an actual observed maximum granule mass. In Figure 6.6, despite the wider scatter of the data, no particularly strong deviations are present. For the granulation experiments with paste, no granule breakage was observed, but end points in growth were definitely observed. This observation supports the theory that the large deviations from predictions at the transition between the growth and no-growth regime observed using the COG in the previous chapter were caused by breakage and scaling errors.

A final issue that must be addressed when considering the results is the matter of repeatability, since the data in Figure 6.6 showed significant deviations from the predicted growth line. Figure 6.7 compares the three repeats from Figure 6.4 to the data points from single time (25 min) repeated experiments at 750 rpm. The repeated single data point experiments in Figure 6.7, marked with diamonds, fall in a similar range as the other experiments performed. Interestingly, the repeated experiments show decreasing mass values for each iteration; the values decline in order of the experiments performed.
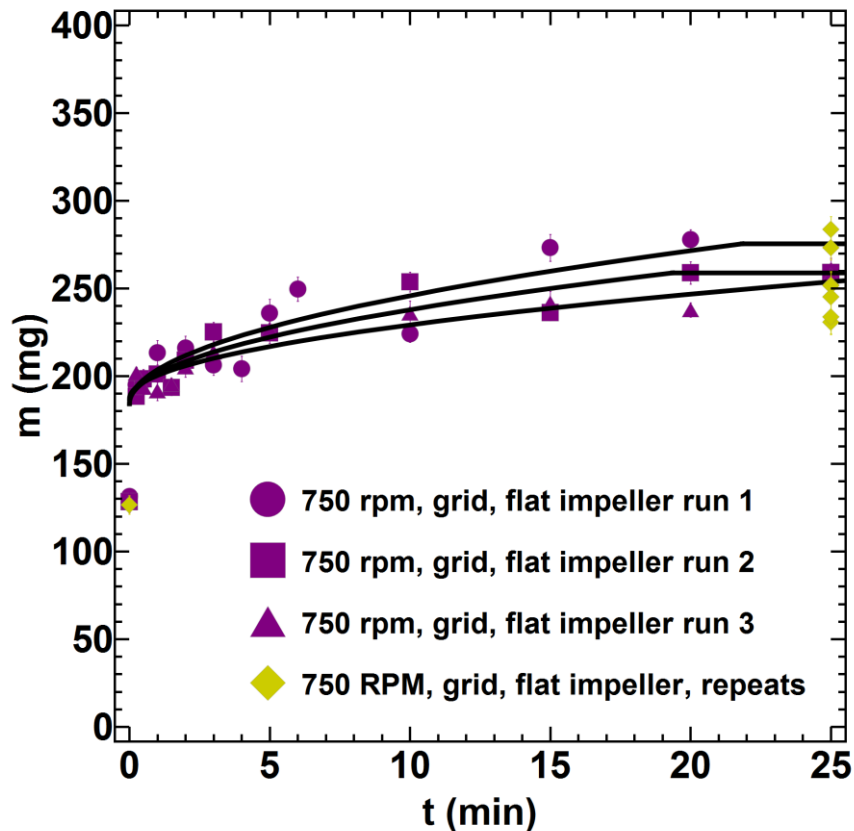
Figure 6.7: Comparison of granule mass as a function of time for all systems granulated at 750 rpm. Lines were fitted using Hounslow et al.'s model for surface tension-driven growth [30].

From experimental observations, there is an explanation for this decline. For all experiments performed, the paste became more difficult to extrude as the experiments progressed. This reduction in flowability was most likely caused by a slight loss of binder liquid during extrusion. The proof for this explanation is discussed in more detail in the following section. The question remains as to whether the loss of binder liquid has consequences on the results. From initial trial runs, it was shown that slight variations in the liquid volume fraction had a large impact on the flowability of the paste; it was impossible to manually extrude paste with a liquid volume fraction of 0.4 using the current set-up. This result implies that liquid loss was less than 10%, as it was still possible to extrude the paste, albeit with effort. Consequently, a variation of about 10% is expected in the results. However, due to the method of initial paste granule production, there already exists some variation in the results. The fact that all single experiment repeated points fall within the same range as the full range triplicate experiments supports this assumption. Therefore, the error due to liquid loss as a result of the experimental method does not invalidate the results, although care should be taken when using the results for the estimation of the kinetics.

6.4.1.1   Kinetics of growth

The critical-packing liquid volume fraction ϕ_{cp} was determined for all sets cut on a grid using the maximum granule mass and the initial liquid mass present in the paste. Table 6.2 shows a comparison between the theoretically calculated ϕ_{cp} and ϕ_{cp} obtained from helium pycnometry data. The first observation that can be made from the table is that for both methods, the systems granulated at 750 rpm have a lower ϕ_{cp} than the system granulated at 500 rpm. Therefore, it is possible that increasing the impeller speed promotes growth. In the study using the consolidation-only granulator (COG) described in the previous chapter, the effect of impact and movement on granule growth could not be established; the transition from a 2.5-D (static) to a 3-D (dynamic) bed might have caused the observed decrease in ϕ_{cp}. The observation made here, however, implies that there is at least some effect of increasing the forces experienced by granules.

The second observation that can be made from Table 6.2 is the clear difference in liquid volume fraction when comparing the two calculation methods. Helium pycnometry clearly indicates that the liquid volume fraction is actually lower than the calculated liquid volume fraction. This finding implies that liquid is lost either during or before granulation. This is supported by the observation that the paste becomes less easy to handle as more paste is extruded, as described above.

Table 6.2: Comparison of critical-packing liquid volume fraction as calculated from the final granule mass (c) and as determined from the skeletal density (ρ). Standard errors are shown in parentheses.

System	$\phi_{cp,c}$ (-)	$\phi_{cp,\rho}$ (-)
500 rpm, grid, flat	0.28 (0.01)	0.250 (0.001)
750 rpm, grid, flat run 1	0.24 (0.09)	0.215 (0.001)
750 rpm, grid, flat run 2	0.24 (0.02)	0.190 (0.001)
750 rpm, grid, flat run 3	0.25 (0.02)	0.200 (0.001)

When comparing these ϕ_{cp} values to those obtained with the COG, values are significantly lower for the COG than for the flat plate impeller mixer. The ϕ_{cp} values obtained with helium pycnometry, which should be closest to the true values, are comparable to the results obtained by Pitt et al. [31]. This finding further supports the hypothesis that impacts on granules do promote layered growth.

As in the previous chapter, the calculated ϕ_{cp} values were used to determine the theoretical final granulation times. These times were compared to the actual final granulation times, t_{max}, as calculated using Pitt et al.'s method [31]. The results are shown in Table 6.3. Again, the theoretical values strongly deviate from the observed values. The theoretical values show good agreement for 750 rpm. For 500 rpm, the theoretical value is significantly lower. This is logical, as the calculation method only takes into account the value of ϕ_{cp}, not the impacts or impeller speed [30].

For the extrapolated values, two interesting observations can be made. First of all, the value for the third run at 750 rpm clearly deviates from the other values. It is possible that the value is an outlier; Figure 6.7 does show that the system demonstrates the slowest growth, and has no real data point beyond its final granule size. This means that it is more difficult to accurately extrapolate the time. Secondly, the system granulated at 500 rpm has a significantly higher t_{max} than the system granulated at 750 rpm. This phenomenon could be explained by the increase in impeller speed, which might have promoted granule growth due to an increase in the number and magnitude of the collisions experienced by the granules.

When comparing the values of t_{max} to those obtained with the COG in the previous chapter, the value for 500 rpm is very close to the value obtained for the dynamic 100 cSt silicone oil system. However, the values for 750 rpm are much lower, except for the third repeat, which shows a significantly higher value. Although this may be due to the value being an outlier, this finding implies that the estimation of the final consolidation time shows wide variation. There does appear to be consistency in the order of magnitude, however.

To compare the kinetics of the data sets at 500 rpm and 750 rpm, the same method as in the previous chapter was used (Equation 6.2) to calculate the growth rate:

$$v = v_0 + v_0 * \left(\frac{1 - \phi_{cp}}{\phi_{cp} * \sqrt{t_{max}}} \right) * \sqrt{t} = v_0 + v_0 * a * \sqrt{t} \qquad (6.2)$$

where v is the original droplet volume, v_0 is the initial droplet volume, and a is the lumped parameter that contains information on ϕ_{cp} and t_{max}.

Table 6.3: Comparison of theoretical times until the critical-packing liquid volume fraction is reached to times determined using Pitt et al.'s method [31], as described in Chapter 5.

System	$t_{max,theory}$ (min)	t_{max} (min)
500 rpm, grid, flat	2.81	202.66
750 rpm, grid, flat run 1	4.80	140.21
750 rpm, grid, flat run 2	4.17	162.93
750 rpm, grid, flat run 3	4.11	258.59

The values for *a* are shown in Table 6.4. Growth rates appear to be higher for the 750 rpm system, with the exception of the third dataset, which may be an outlier. Overall, it appears as though parameter *a* increases with an increasing impeller speed, and the same relationship between the growth rate and the square root of the impeller speed is obtained.

Interestingly, when comparing the growth rates to the rates obtained with the COG in the previous chapter, the rates obtained with the flat plate mixer are much lower. The breakage in the high-shear mixer was significantly lower than the breakage in the COG after long granulation times, which implies that breakage and attrition are not the only factors influencing granule growth. Had this been the case, then the growth rate should fall within the static-dynamic value range. It is possible that gravity is also a relevant property for droplet penetration; this may explain the higher growth rates in the 2.5-D powder beds used by Pitt et al. [31]. Due to the movements in dynamic beds, gravity should not play as much of a role in that case.

6.4.1.2   Consolidation

Table 6.5 shows granule porosity values obtained with helium pycnometry, including standard errors, as well as the relative porosity change between early and late granulation times. As was the case for granules produced with the COG described in the previous chapter, no overall changes were observed, with porosity staying at approximately the same value at the start and end of granulation. The few observed differences do not show enough change to surpass the relatively high standard errors. Considering the results from the previous chapter, these findings are not surprising. In particular, breakage and attrition in the mixer with the flat plate impeller was significantly lower than the breakage observed in the COG. This finding suggests that the impacts experienced by the granules were much lower for the mixer compared to the COG. Consequently, consolidation is expected to be less for the mixer.

Table 6.4: Lumped growth parameter *a* for all sets cut on a grid.

System	a $(\mathrm{min}^{1/2})$
500 rpm, grid, flat	0.19
750 rpm, grid, flat run 1	0.27
750 rpm, grid, flat run 2	0.24
750 rpm, grid, flat run 3	0.19

Table 6.5: Granule porosities at the start and end of granulation, as well as the relative change in porosity. Standard errors are shown in parentheses.

Experiment	ε_{start} (-)	ε_{end} (-)	Change (%)
500 rpm, ruler, flat plate	0.388 (0.007)	0.407 (0.007)	5 (3)
250 rpm, ruler, three-bladed	0.397 (0.008)	0.41 (0.01)	3 (3)
500 rpm, grid, flat plate	0.397 (0.007)	0.391 (0.008)	-1 (3)
750 rpm, grid, flat plate run 1	0.398 (0.007)	0.397 (0.006)	0 (2)
750 rpm, grid, flat plate run 2	0.378 (0.006)	0.377 (0.008)	0 (3)
750 rpm, grid, flat plate run 3	0.384 (0.004)	0.390 (0.009)	+1 (3)

However, when comparing the actual porosity values obtained, the values appear to be higher for the COG, implying the mixer results in more consolidation. The values are still fairly close, however, and the values obtained with the COG have relatively high standard errors. In the case where the porosity actually would be lower for the mixer, this can be explained by the preparation method of the granules. Paste nucleation is more likely to produce a homogenous granule core, which may lead to a reduction in fracturing. To investigate this, X-ray tomography was performed on cut paste granulated at 750 rpm, as shown in Figure 6.8.

Similar to the images of drop-nucleated granules granulated using the COG described in the previous chapter, Figure 6.8 clearly shows that there is a core-shell structure in the granulated paste. Interestingly, the paste does not appear to be completely close-packed; small voids are present, even at the early stages of granulation. When comparing to the images from the previous chapter, however, the voids are significantly less than those for dynamically grown granules, and comparable to the statically grown granules. In the figure, the granule cores appear to maintain a similar porosity, although the porosity appears to have increased over time, as the colour of the core darkens a bit and small microcracks may be observed. However, the outer shell clearly becomes denser during granulation. In fact, the darker colour and relatively numerous voids in the image for short granulation times indicates that the shell has a higher porosity than the core. On the other hand, the shell has fewer voids and a lighter colour for longer granulation times, indicating that the porosity is actually lower than that of the core.

As in the previous chapter, this finding implies that consolidation is definitely happening, but it mostly occurs in the outer layers of the granule, and not so much in the core. It would therefore be interesting to investigate the effect of this difference in porosity on the growth model.
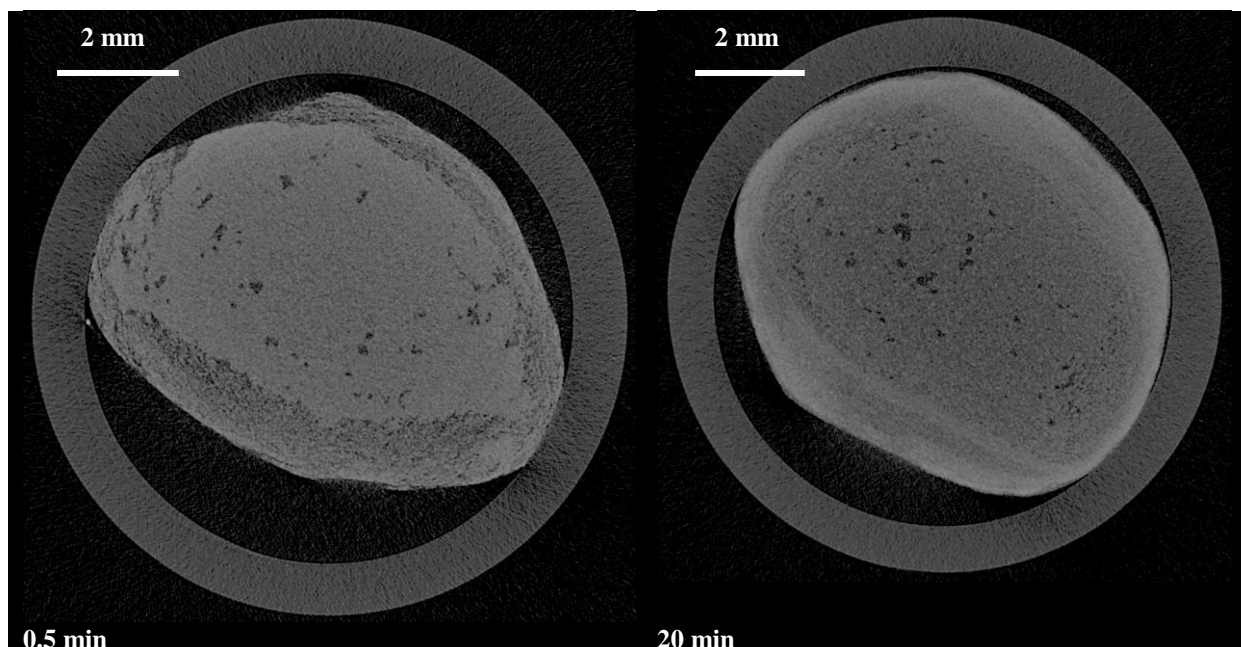
Figure 6.8: Comparison of X-ray tomography images of granules consisting of lactose-100 cSt silicone oil at the start and end of growth for paste granulated in a high-shear mixer with flat plate impeller at 750 rpm. The rings are part of the sample container.

6.4.2 The effect of porosity differences on surface tension-driven growth

Experiments with the COG and high-shear mixer have shown that no overall consolidation occurred. However, the X-ray tomography images clearly show that some sort of local consolidation is occurring, giving the granules a clear core-shell structure. This section aims to propose an explanation for this phenomenon and investigate the impact on the surface tension-driven growth model.

From the images, it seems as though there is a porosity difference between the core and shell, with the shell apparently having a lower porosity than the core. This difference in porosities is most likely the result of impacts on the granule. Logically, different porosities cause flow of liquid, as capillary force drives the liquid to move to the lower-porosity region, enabling more powder layers to form. This phenomenon would partially explain why Hounslow et al.'s surface tension-driven growth model [30] drastically underpredicts the theoretical t_{max}; if impacts cause a reduction in porosity of the outer layer, further growth is possible, but it is limited by the frequency and force of the impacts. This theory is supported by the observation of an increased growth rate for higher impeller speeds in the high-shear mixer.

It is not unrealistic to assume that growth occurs in two phases; Maxim et al. proposed a similar approach for their modelling of granule consolidation and layered growth [53], as described in Chapter 2, Section 2.3.2.4. Initially, there is the static growth observed by Pitt et al. [31], causing the granule to grow until it reaches ϕ_{cp}. This behaviour is predicted by Hounslow et al.'s model for surface tension-driven growth [30]. However, even in this situation, t_{max} is not predicted accurately. Two factors may contribute to this discrepancy. First of all, some voids may be closed off to the liquid, causing the liquid to spread further overall than would be the case in absence of these voids. Second, pores in the surrounding powder are not equally sized and the liquid may migrate from larger pores to smaller ones, causing the granule to keep growing.

In the second, dynamic, growth phase, growth is driven by a porosity difference caused by impacts. Again, liquid migrates to the lower porosity region, in this case the shell. This process will continue until the granule has stopped deforming, either because the porosity is equal throughout the granule, or because further densification of the core is not possible, causing growth to cease. Possibly, the latter phenomenon has been observed with X-ray tomography.

Although the two stages of static and dynamic surface tension-driven growth are likely to occur simultaneously, it is relevant for our understanding of layered growth to look at the extreme of the two phases occurring sequentially. For this approach, the granules are assumed to grow regardless of impacts until the nucleus has reached the critical-packing liquid volume fraction ϕ_{cp}, or ϕ_1, which could be valid for prenucleation or very fast liquid penetration. Next, impacts cause the shell to have a new ϕ_{cp}, labelled ϕ_2. The growth then continues until the entire granule has reached the new critical-packing liquid volume fraction. From the observed growth behaviour, this assumption is not completely valid, as growth stops before the entire granule has reached the new ϕ_{cp}. For modelling purposes, however, the growth kinetics are exactly the same; the only difference is that the growth will cease sooner, leading to an overestimation of t_{max}. The actual value of ϕ_2 and the percentage of the granule consolidated to ϕ_2 would depend on the impact force and frequency in the granulator.

This assumption allows for the repurposing of the model to account for the observed core-shell growth behaviour, as well as for the comparison with experimental growth behaviour. Before this model can be developed for a three-dimensional scenario, the 1-D case must be evaluated first, however. This is described in the following section.

6.4.2.1   One-dimensional porosity difference-driven growth

Figure 6.9 presents a one-dimensional situation for growth; similar to Hounslow et al.'s planar slab-shaped nucleus [30], a granule that has reached ϕ_{cp} is placed in a situation where the surrounding powder has a lower porosity due to impacts. The granule starts out at original size h_{max}, at liquid volume fraction ϕ_{cp}. These are renamed h_1 and ϕ_1, respectively, to indicate that the granule will grow further. The core with liquid volume fraction ϕ_1 is then expected to decrease in size (b), whereas the total granule size (h) is expected to increase until the granule has reached a new maximum size (h_2) at a new critical-packing liquid volume fraction (ϕ_2).

The change of the high liquid-fraction core size b and the total granule size h can be expressed in terms of the liquid flux (J_L) at the interface between the two phases, J. The terms for the core and shell size changes are similar to those of Hounslow et al. [30], although the expression for the change in b contains both the first and second critical volume liquid fraction, ϕ_1 and ϕ_2 (Equation 6.3 and 6.4):

$$\frac{db}{dt} = -\frac{J}{\phi_1 - \phi_2} \tag{6.3}$$

$$\frac{dh}{dt} = \frac{J}{\phi_2} \tag{6.4}$$
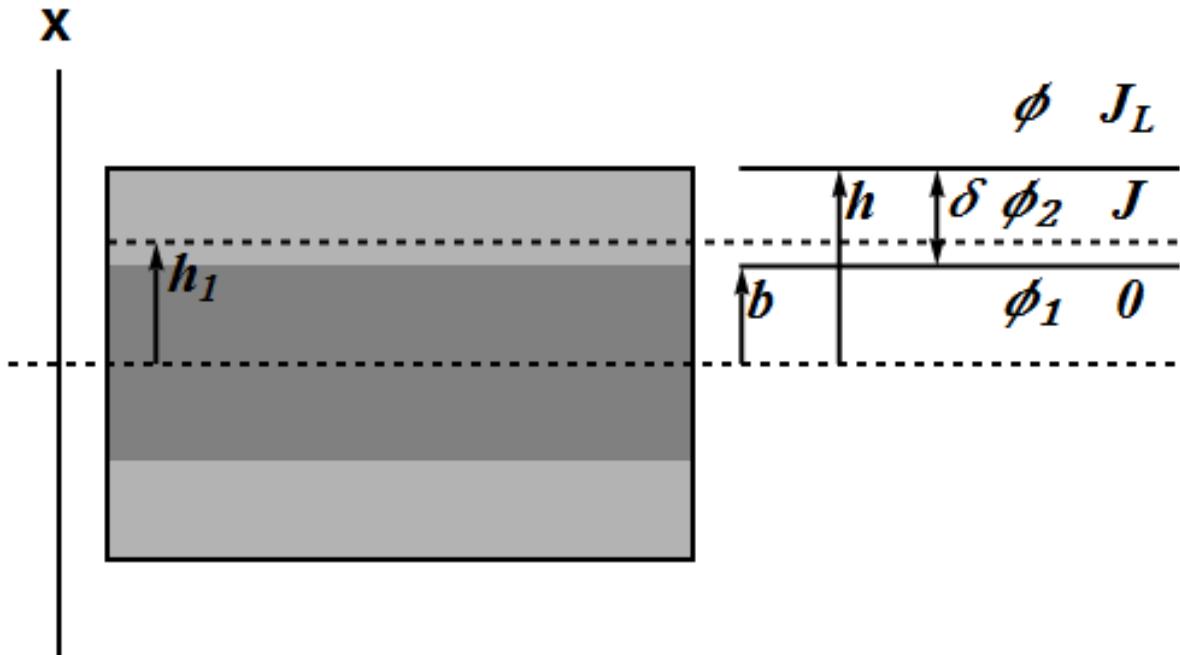
Figure 6.9: Schematic representation of one-dimensional granule growth for a granule with a core-shell system.

Furthermore, the difference between h and b is termed δ (Equation 6.5):

$$\delta = h - b \tag{6.5}$$

Since δ is equal to the difference between h and b, the derivative of δ can be considered the difference between the derivatives of h and b (Equation 6.6):

$$\frac{d\delta}{dt} = \frac{\phi_1}{\phi_2} * \frac{J}{(\phi_1 - \phi_2)} \tag{6.6}$$

Using Equation 6.5, a liquid volume balance (Equation 6.7) can be used to derive an expression for the granule size h, as shown in Equation 6.8:

$$h_1 * \phi_1 = h_0 = (b * \phi_1) + (\delta * \phi_2) \tag{6.7}$$

$$h = \frac{h_0}{\phi_1} + \frac{(\phi_1 - \phi_2)}{\phi_1} * \delta \tag{6.8}$$

Next, the Blake-Kozeny equation (Equation 6.9) and the capillary force (Equation 6.10) can be used to derive an expression for the liquid flux (Equation 6.11). The results are the same as those obtained by Hounslow et al. [30].

$$\frac{dp}{dx} = -\frac{150 * \mu}{d^2} * \frac{(1 - \phi_2)}{\phi_2{}^3} * J \tag{6.9}$$

where p is the pressure, x is the height, μ is the liquid viscosity and d is the powder particle diameter.

$$\frac{dp}{dx} = -\frac{4 * \gamma}{\delta * d} * (1 - \phi_2) \tag{6.10}$$

where γ is the surface tension.

$$J = \frac{\gamma * d * \phi_2{}^3}{37.5 * \mu * \delta} \tag{6.11}$$

With the expression for the liquid flux J known, Equation 6.6 can be rewritten (Equation 6.12) and integrated to yield an expression for δ (Equation 6.13):

$$\frac{d\delta}{dt} = \frac{\gamma * d}{37.5 * \mu * \delta} * \frac{\phi_1 * \phi_2{}^2}{(\phi_1 - \phi_2)} \tag{6.12}$$

$$\delta = \left(\frac{\gamma * d}{18.75 * \mu} * \frac{\phi_1 * \phi_2{}^2}{(\phi_1 - \phi_2)} * t \right)^{1/2} \tag{6.13}$$

This expression can then be substituted into Equation 6.8 to yield an expression for h (Equation 6.14). At the time t_2, the granule stops growing and h reaches the size h_0/ϕ_2. This time is defined in Equation 6.15.

$$h = \frac{h_0}{\phi_1} + \left(\frac{\gamma * d}{18.75 * \mu} * \frac{(\phi_1 - \phi_2) * \phi_2{}^2}{\phi_1} * t \right)^{1/2} \qquad (6.14)$$

$$t_2 = \frac{18.75 * \mu * h_0{}^2}{\gamma * d} * \frac{(\phi_1 - \phi_2)}{\phi_1 * \phi_2{}^4} \qquad (6.15)$$

With the expression for t_2 known, dimensionless expressions can be constructed for t (Equation 6.16), δ (Equation 6.17), b (Equation 6.18 and 6.19) and h (Equation 6.20), indicated by a circumflex:

$$\hat{t} = \frac{t}{t_2} \qquad (6.16)$$

$$\hat{\delta} = \frac{\hat{t}^{1/2}}{\phi_2} \qquad (6.17)$$

$$\frac{d\hat{b}}{d\hat{t}} = -\frac{1}{2 * \hat{t}^{1/2}} * \frac{1}{\phi_1} \qquad (6.18)$$

$$\hat{b} = \frac{1}{\phi_1} \left(1 - \hat{t}^{1/2} \right) \qquad (6.19)$$

$$\hat{h} = \hat{b} + \hat{\delta} = \frac{1}{\phi_1} + \frac{\phi_1 - \phi_2}{\phi_1 * \phi_2} * \hat{t}^{1/2} \qquad (6.20)$$

These expressions are fairly similar to those obtained by Hounslow et al. [30], but they account for an initial liquid volume fraction that is not equal to 1. In fact, setting ϕ_1 to 1 and ϕ_2 to ϕ_{cp} yields the same expression Hounslow et al. arrived at. Furthermore, the expression for the dimensionless volume change (Equation 6.21) and the overall volume as a function of time (Equation 6.22) can be derived to be equivalent to those of Hounslow et al. [30], provided the initial liquid volume fraction is 1:

$$\frac{v - v_1}{v_2 - v_1} = \frac{\hat{h} - \hat{h}_1}{\hat{h}_2 - \hat{h}_1} = \frac{\hat{h} - \frac{1}{\phi_1}}{\frac{1}{\phi_2} - \frac{1}{\phi_1}} = \hat{t}^{1/2} \qquad (6.21)$$

$$v = \frac{v_0}{\phi_1} + \left(v_0 * \frac{\phi_1 - \phi_2}{\phi_1 * \phi_2} \right) * \left(\frac{t}{t_2} \right)^{1/2} \qquad (6.22)$$

6.4.2.2 Three-dimensional porosity difference-driven growth

With the expansion of the 1-D model proposed by Hounslow et al. [30], it is possible to investigate the 3-D spherical case, shown in Figure 6.10. The figure shows the three-dimensional equivalent of Figure 6.9. As with the one-dimensional case, the Blake-Kozeny equation (Equation 6.23) and the capillary force (Equation 6.24 and 6.25) can be used to find an expression for the liquid flux. However, since the coordinates are spherical, the flux may be expressed in terms of q, the constant liquid flux, independent of the radius. Solving the equations for q results in an expression of q in terms of the liquid and powder properties, ϕ_2 and the core and total granule size (Equation 6.26).

$$\Delta p = -\frac{4*\gamma}{d}*(1-\phi_2) \tag{6.23}$$

$$\frac{dp}{dr} = -\frac{150*\mu}{d^2}*\frac{(1-\phi_2)}{\phi_2^3}*\frac{q}{r^2} \tag{6.24}$$

$$\Delta p = -\frac{150*\mu}{d^2}*\frac{(1-\phi_2)}{\phi_2^3}*q\int_b^h\frac{dr}{r^2} = -\frac{150*\mu}{d^2}*\frac{(1-\phi_2)}{\phi_2^3}*q*\frac{h-b}{h*b} \tag{6.25}$$

$$q = -\frac{\gamma*d*\phi_2^3}{37.5*\mu}*\frac{h*b}{h-b} \tag{6.26}$$
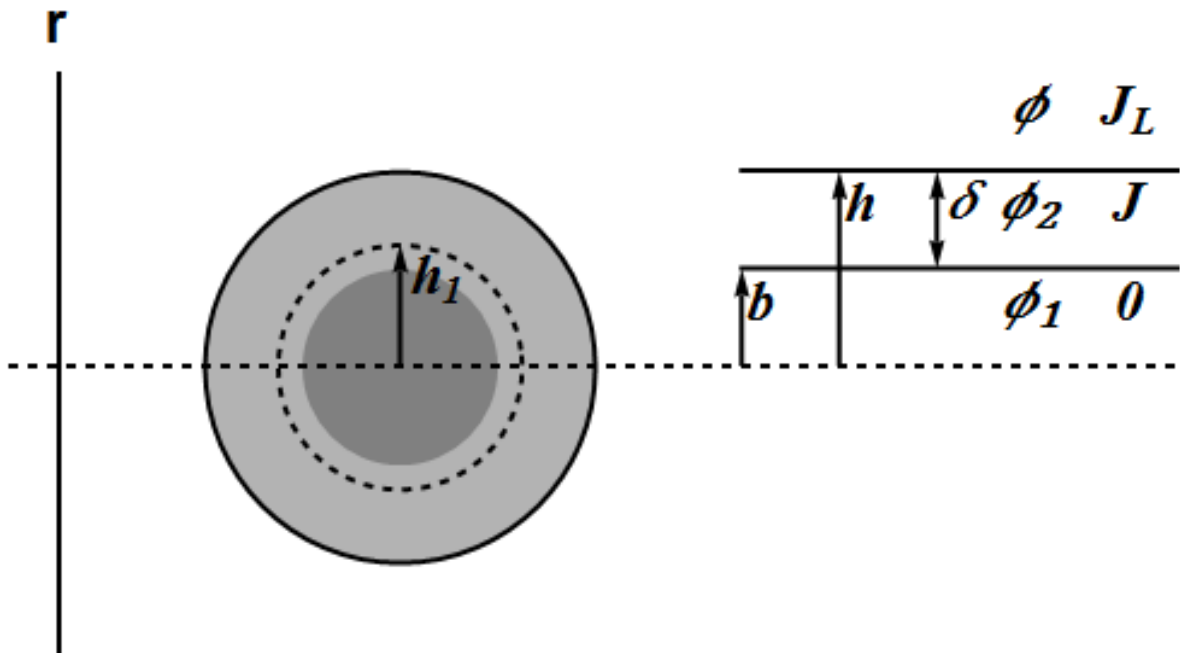
Figure 6.10: Schematic representation of three-dimensional granule growth for a granule with a core-shell system.

135

which is the expression as derived by Hounslow et al. [30]. However, the expressions for the change in b (Equation 6.27), h (Equation 6.28) and the liquid mass balance (Equation 6.29) are slightly different, incorporating terms for both ϕ_1 and ϕ_2:

$$\frac{db}{dt} = -\frac{q/b^2}{\phi_1 - \phi_2} = -\frac{\gamma * d}{37.5 * \mu} * \frac{\phi_2^3}{\phi_1 - \phi_2} * \frac{h}{b * (h - b)} \tag{6.27}$$

$$\frac{dh}{dt} = \frac{q/h^2}{\phi_2} = \frac{\gamma * d}{37.5 * \mu} * \phi_2^2 * \frac{b}{h * (h - b)} \tag{6.28}$$

$$h_1^3 * \phi_1 = h_0^3 = (b^3 * \phi_1) + \left((h^3 - b^3) * \phi_2\right) \tag{6.29}$$

which are all similar to the expressions obtained by Hounslow et al. [30]. In order to solve the equations and find an expression for time as a function of the total granule size, it is convenient to derive dimensionless equations for the change in core size (Equation 6.30), overall size (Equation 6.31) and the liquid mass balance (Equation 6.32) first using the expression for t_2 presented in Equation 6.15:

$$\frac{d\hat{b}}{d\hat{t}} = -\frac{1}{2} * \frac{1}{\phi_1 * \phi_2} * \frac{\hat{h}}{\hat{b} * (\hat{h} - \hat{b})} \tag{6.30}$$

$$\frac{d\hat{h}}{d\hat{t}} = \frac{1}{2} * \frac{\phi_1 - \phi_2}{\phi_1 * \phi_2^2} * \frac{\hat{b}}{\hat{h} * (\hat{h} - \hat{b})} \tag{6.31}$$

$$1 = (\hat{b}^3 * \phi_1) + \left((\hat{h}^3 - \hat{b}^3) * \phi_2\right) \tag{6.32}$$

Equation 6.31 can then be solved by rewriting the mass balance to find an expression for the dimensionless core size (Equation 6.33) and substituting this into the equation (Equation 6.34). Rewriting the equation into Equation 6.35 and integrating to give Equation 6.36 yields the expression for the dimensionless time. Finally, applying the initial condition that the dimensionless granule size is equal to ϕ_1^{-1} allows for the solution of the integration constant K, yielding Equation 6.37.

$$\hat{b} = \left(\frac{\left(1 - (\hat{h}^3 * \phi_2)\right)}{\phi_1 - \phi_2}\right)^{1/3} \tag{6.33}$$

$$\frac{d\hat{h}}{d\hat{t}} = \frac{1}{2} * \frac{\phi_1 - \phi_2}{\phi_1 * \phi_2{}^2} * \frac{\left(\dfrac{\left(1 - (\hat{h}^3 * \phi_2)\right)}{\phi_1 - \phi_2}\right)^{1/3}}{\hat{h}^2 - \left(\hat{h} * \left(\dfrac{\left(1 - (\hat{h}^3 * \phi_2)\right)}{\phi_1 - \phi_2}\right)^{1/3}\right)} \tag{6.34}$$

$$\frac{2 * \phi_1 * \phi_2{}^2}{\phi_1 - \phi_2} * \left(\frac{\hat{h}^2}{\left(\dfrac{\left(1 - (\hat{h}^3 * \phi_2)\right)}{\phi_1 - \phi_2}\right)^{\frac{1}{3}}} - \hat{h}\right) * d\hat{h} = d\hat{t} \tag{6.35}$$

$$\hat{t} = -\frac{\phi_1 * \phi_2{}^2}{\phi_1 - \phi_2} * \left(\frac{\phi_1 - \phi_2}{\phi_2} * \left(\dfrac{\left(1 - (\hat{h}^3 * \phi_2)\right)}{\phi_1 - \phi_2}\right)^{\frac{2}{3}} + \hat{h}^2\right) + K \tag{6.36}$$

$$\hat{t} = \frac{\phi_1 * \phi_2}{\phi_1 - \phi_2} *$$
$$\left(\frac{\phi_2}{\phi_1{}^{2/3}} * (1 - \hat{h}^2 * \phi_1{}^{2/3}) + (\phi_1 - \phi_2)^{1/3} * \left(\left(1 - \frac{\phi_2}{\phi_1}\right)^{2/3} - (1 - \hat{h}^3 * \phi_2)^{2/3}\right)\right) \tag{6.37}$$

Although the obtained expression for dimensionless time looks relatively daunting, setting ϕ_1 equal to 1 again results in the same expression as found by Hounslow et al. [30]. Similarly, performing a Taylor expansion around a value $\phi_2{}^{-1}$ for the dimensionless height yields equivalent expressions for dimensionless time (Equation 6.38) and the dimensionless granule height (Equation 6.39):

$$\hat{t} = \left(\frac{\phi_1 * \phi_2}{\phi_1 - \phi_2}\right)^2 * \left(\hat{h} - \frac{1}{\phi_1{}^{1/3}}\right)^2 \tag{6.38}$$

$$\hat{h} = \frac{1}{\phi_1{}^{1/3}} + \frac{\phi_1 - \phi_2}{\phi_1 * \phi_2} * \hat{t}^{1/2} \tag{6.39}$$

Furthermore, using a dimensionless height of $\phi_2{}^{-1}$ in Equation 6.37 yields the expression of the dimensionless maximum growth time (Equation 6.40) and actual maximum growth time t_2 (Equation 6.41):

$$\hat{t}_{max} = \frac{\phi_1 * \phi_2}{\phi_1 - \phi_2} * \left(\phi_1{}^{1/3} - \phi_2{}^{1/3}\right) \tag{6.40}$$

$$t_2 = \frac{18.75 * \mu * h_0{}^2}{\gamma * d} * \frac{\phi_1{}^{1/3} - \phi_2{}^{1/3}}{\phi_2{}^3} \tag{6.41}$$

Using the same approximation as Hounslow et al. [30], the granule volume can then be expressed using Equation 6.42:

$$v = \frac{v_0}{\phi_1} + \left(v_0 * \frac{\phi_1 - \phi_2}{\phi_1 * \phi_2}\right) * \left(\frac{t}{t_2}\right)^{1/2} \tag{6.42}$$

Finally, an expression for the overall granule size can be constructed by assuming that the first type of growth occurs independently at different times. First, the granule grows independent of impacts until it reaches its natural saturation at ϕ_1 after time t_1. Next, the granule starts growing due to compacted powder around its core, changing the liquid volume fraction to ϕ_2. From t_1, this process takes time t_2. This means that the overall observed growth time equals the sum of t_1 and t_2. Below, expressions are presented for t_1 (Equation 6.43), t_2 (Equation 6.44) and the overall granule volume v (Equation 6.45):

$$t_1 = \frac{18.75 * \mu * h_0{}^2}{\gamma * d} * \frac{1 - \phi_1{}^{1/3}}{\phi_1{}^3} \tag{6.43}$$

$$t_2 = \frac{18.75 * \mu * h_0{}^2}{\gamma * d} * \frac{\phi_1{}^{\frac{1}{3}} - \phi_2{}^{\frac{1}{3}}}{\phi_2{}^3} = \left(\frac{\phi_1}{\phi_2}\right)^3 * \frac{\phi_1{}^{\frac{1}{3}} - \phi_2{}^{\frac{1}{3}}}{1 - \phi_1{}^{1/3}} * t_1 \tag{6.44}$$

$$v = \begin{cases} v_0 + \left(v_0 * \dfrac{1 - \phi_1}{\phi_1}\right) * \sqrt{\dfrac{t}{t_1}} & t < t_1 \\[3ex] \dfrac{v_0}{\phi_1} + \left(v_0 * \dfrac{\phi_1 - \phi_2}{\phi_1 * \phi_2}\right) * \sqrt{\dfrac{t - t_1}{t_2}} & t_1 \leq t < t_1 + t_2 \\[3ex] \dfrac{v_0}{\phi_2} & t \geq t_1 + t_2 \end{cases} \tag{6.45}$$

Two observations can be made from Equation 6.45. First of all, if ϕ_1 equals 1 or ϕ_2 the expression is equivalent to Hounslow et al.'s model [30]. Second, nondimensionalisation of the overall expression has become more complicated. In order to ensure that the dimensionless volume change has values between 0 and 1, it is scaled by the initial droplet volume and the final granule volume, v_2. Time is scaled by the overall time $t_1 + t_2$. However, due to the different growth regimes of Equation 6.45, this scaling results in nonlinear growth as a function of dimensionless time.

Figure 6.11 demonstrates this behaviour for varying values of ϕ_1. As expected, for a ϕ_1 value of 1, the growth behaviour is indeed linear with the square root of time. Initial growth behaviour appears to be consistently linear with the square root of time, but the shift by t_1 for the second growth regime in Equation 6.45 causes nonlinear behaviour in the second regime. Furthermore, it appears as though the further apart the values of ϕ_1 and ϕ_2 are, the closer the overall growth behaviour appears to be linear.

Figure 6.11: Dimensionless volume change as a function of the square root of dimensionless time according to Equation 6.45 for varying values of ϕ_1.

Figure 6.12 demonstrates the effect of varying ϕ_2. Again, for the case where ϕ_1 and ϕ_2 are equal, the behaviour is linear. For other values of ϕ_2, however, the behaviour is similar to that in Figure 6.11, with linear behaviour for the first regime, and nonlinear behaviour for the second regime. As in Figure 6.11, the overall behaviour is closer to linear when the difference between ϕ_1 and ϕ_2 is larger.

When considering the overall curve, it is entirely feasible to fit a linear line to a set of data points behaving according to Equation 6.45. Therefore, there is no clear way of determining whether this behaviour or a simpler model holds for the granulation process. The fact that the actual growth process might be a combination of static (ϕ_1) and dynamic (ϕ_2) growth further complicates matters, as such data points would be even easier to fit on a straight line. However, the question remains whether which type of behaviour is actually happening is even relevant for the purposes of modelling the growth behaviour. If Hounslow et al.'s original surface tension-driven growth model [30] is sufficiently capable of predicting the general growth kinetics, a more complicated expression is neither needed nor does it provide a closer representation of reality.

To investigate how strongly the model deviates from a straight line, several combinations of ϕ_1 and ϕ_2 values were tested. For ϕ_1, values in the range of Pitt et al.'s typical ϕ_{cp} were selected (0.2) [31], whereas for ϕ_2, values around typical COG experiments (0.1) were used. In practice, Pitt et al. may have found values beyond the growth regime intended by Hounslow et al. due to the presence of smaller pores. However, that would only have increased the difference between ϕ_1 and ϕ_2, making the curve more linear.
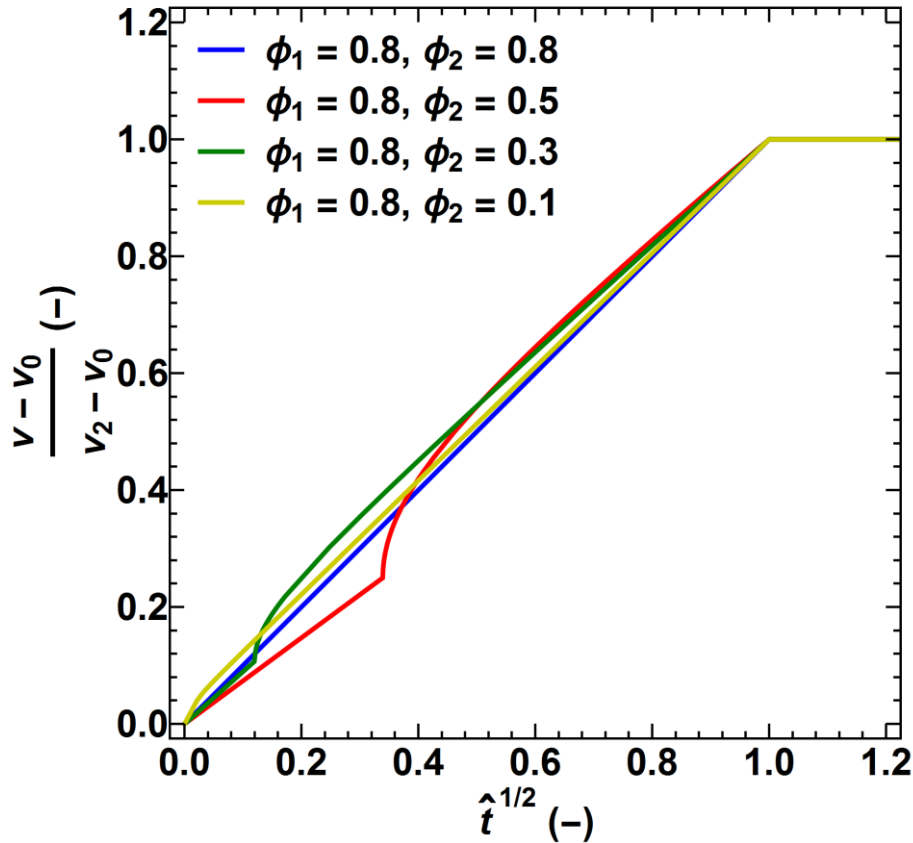
Figure 6.12: Dimensionless volume change as a function of the square root of dimensionless time according to Equation 6.45 for varying values of ϕ_2.

Figure 6.13 shows the effect of slight variations in the values of 0.2 and 0.1 for ϕ_1 and ϕ_2, respectively, and a comparison with Hounslow et al.'s model for surface tension-driven growth [30] and experimental data obtained with the COG. For relatively large differences in ϕ_1 and ϕ_2, the curve is very close to linear, with a linear line underestimating the granule size slightly in the second growth regime. The smaller the size difference, the more dramatic the change from the first growth regime to the second growth regime, and the shorter the second growth regime is. At the extreme situation of $\phi_1 = 0.18$ and $\phi_2 = 0.12$, the curve deviates strongly from linear behaviour, and the original model drastically overestimates the granule size. Additionally, both the granulation time as well as the initial granule size are severely underestimated. In this situation, Hounslow et al.'s model [30] would not at all give an accurate prediction of the growth behaviour.

However, such behaviour has not been observed in the data produced both by Pitt et al. [31] and in this study, as demonstrated by the experimental data in Figure 6.13. This either implies that the difference observed between ϕ_1 and ϕ_2 is sufficiently large, or that the two processes of static and dynamic surface tension-driven growth overlap in such a way that a linear model is sufficient. This means that a linear surface tension-driven growth model can be used, but that Hounslow et al.'s expression for t_{max} [30] does not reflect the actual growth time for granulation. Therefore, both ϕ_{cp} and t_{max} are variables that do not only depend on powder and binder properties, but also on the operating parameters and equipment used. For the purpose of developing a population balance model, it is therefore sufficient to use the original model developed by Hounslow et al.
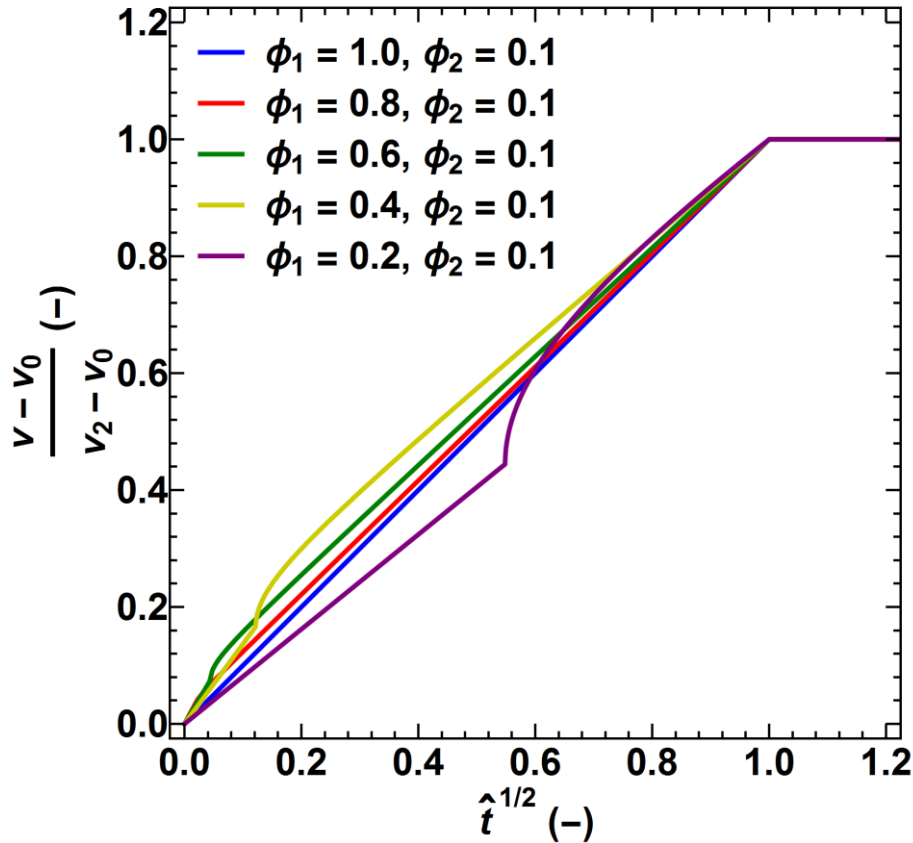
140
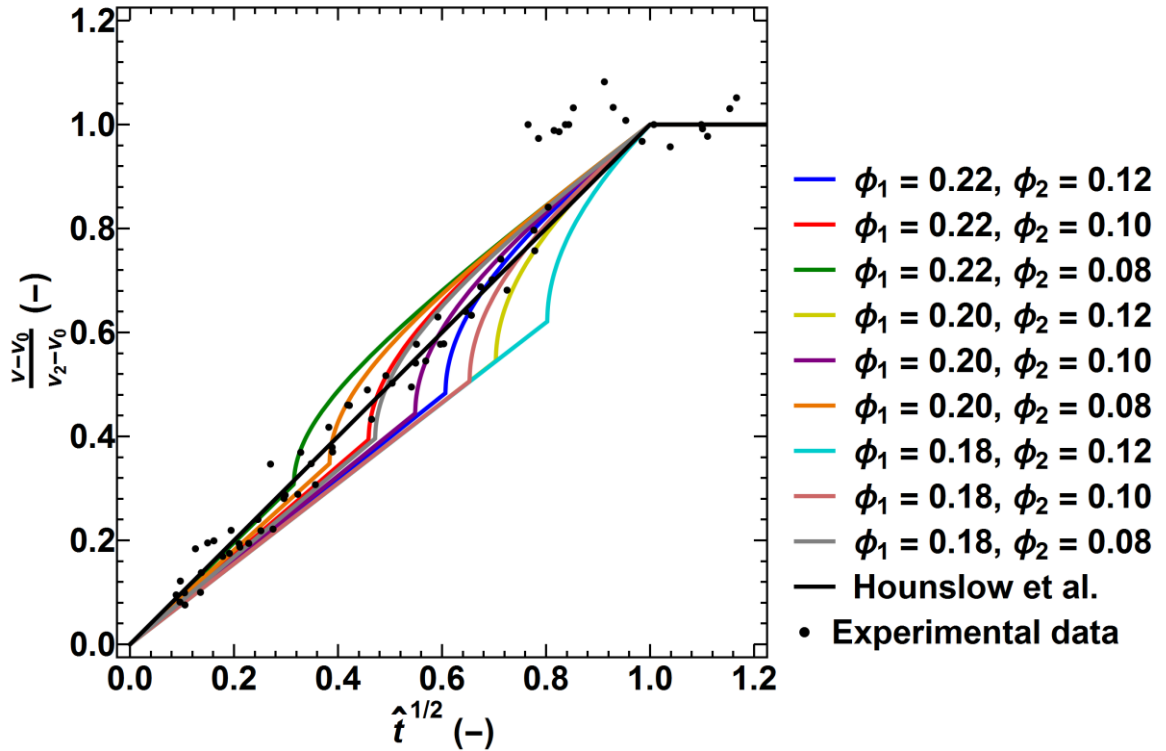
Figure 6.13: Dimensionless volume change as a function of the square root of dimensionless time according to Equation 6.45 for varying values of ϕ_1 and ϕ_2, compared to Hounslow et al.'s surface tension-driven growth model [30] and experimental data obtained with the COG.

6.4.3 Initial growth behaviour of granules

So far, this study has focused on developing methods for determining the kinetics of layered growth, as well as evaluating the critical-packing liquid volume fraction and final granulation time. A final phenomenon that should be addressed is that of the initial growth behaviour of granules, i.e. the difference between the initial granule mass *observed* from data plots and the *known* initial granule mass. For all experiments performed, both with the COG and the high-shear mixer, the initial granule mass predicted by the growth line was significantly higher than the actual granule mass. After this initial rapid increase, growth would proceed according to Hounslow et al.'s model for surface tension-driven growth [30]. In order to propose a model, it is important to identify the source of the initial leap in granule mass.

The first source of the rapid increase in granule mass could be the transition from static to dynamic surface tension-driven growth, as described in Section 6.4.2. If the first growth regime is fast, and only the second regime is observed, nonlinear growth behaviour could be found. However, that is only the case if the first and second growth regime are sufficiently separated. If there is insufficient separation, the line should appear much more linear, and the leap less pronounced. Furthermore, Pitt et al. [31] also observed a rapid increase in granule mass for some systems, and their work did not include any dynamic experiments. Therefore, different explanations for the initial rapid increase in granule mass should be investigated.

Shukri [159] specifically investigated the early static growth behaviour of granules using a set-up similar to that of Pitt et al. [31]. Granules were drop-nucleated using a syringe, and grown statically. The granules were then extracted and weighed, but instead of using a sieve,

Shukri extracted all granules individually using pins. In this way, the early growth of granules could be studied much more precisely. It was found that there was actually no initial rapid increase in granule growth in early stages, but that the method used to extract the granules did influence the observed masses; Shukri's pin method was capable of extracting the granule without significantly affecting the granule mass, as opposed to granule-powder separation with a sieve, which might lead to granule attrition. As such, it was not possible to connect different data sets that used different methods, but the qualitative kinetic growth behaviour held in the study.

The conclusion in Shukri's work most relevant to this study is that, provided the employed method is the same, growth will show the same kinetics, i.e. linear growth with the square root of time. This implies that, for both modelling and in practice, if a granule is nucleated *inside* a granulator, it directly starts growing according to known kinetics. Since there is no change in extraction method, there will be no initial leap in granule mass. Granules with different nucleation times will grow at different rates, however, as determined by their liquid content. For the development of a model for use in practical granulation, this difference may result in a wide spread of growth rates if long liquid addition times are used, causing nucleation at different times. However, it should still be possible to model the rates provided the liquid content of the granules is known.

Interestingly, for the studies performed in this chapter, the initial rapid increase in granule mass was observed despite starting in the middle of granulation. This behaviour provides some clues about the cause for the observed leap. It is likely that the large growth at the start of granulation is caused by the immediate uptake of powder by the liquid. For some set-ups, the overall effect will be more pronounced than for other set-ups, as demonstrated by Shukri's results [159]. However, for the purpose of understanding nucleation, as well as explaining the behaviour observed in this work, it is interesting to consider the exact mechanism of powder uptake from a wet droplet. The following section explores how the granule layer is formed in terms of the powder layer formed around it.

6.4.3.1 Layer by layer powder uptake

Observed granule growth behaviour is generally characterised by linear behaviour with the square root of time. However, the initial granule mass is rarely predicted correctly, except in perhaps the static experiments performed by Pitt et al. [31]. This exclusion of the first data point can partially be attributed to a small time difference between addition to the granulator of nuclei or paste, and actual granulation. This time gap might cause some static growth, which has been demonstrated to have different, albeit qualitatively similar, kinetics. However, this time difference does not completely account for the powder uptake, as demonstrated by the large differences between actual and predicted granulation end times.

It is possible that a nucleus or paste granule immediately gains a layer of powder when it is added to the powder bed. This is logical, as the surface of the granule is wet; there is no requirement for consolidation before layering occurs. Assuming there is a limit to the thickness of the powder layer that can be taken in by the nucleus in that first moment of granulation, the effect on the granule mass will vary per granule size and the amount of liquid available. For smaller granules, the total added powder mass should be lower than that for larger granules, since the wet surface area is smaller for the former. However, the relative increase in granule mass can be much higher for smaller granules, as the uptake of powder

will rapidly increase their mass. Droplet-nucleated granules also have a higher amount of liquid available, and should, therefore, show a large relative increase in mass compared to paste-nucleated granules. A comparison of the drop-nucleated granules produced with the COG in the previous chapter and paste-based granules described here is shown in Table 6.6. The table shows that most of these predictions appear to be valid. Small granules with a large amount of available liquid show a sharper increase in granule mass than the larger, less wet paste-based granules. The total mass increase is larger for the paste-based granules, however, especially when considering the fact that the drop-nucleated granules were not granulated immediately due to the time between nucleation and start-up of the COG.

An additional interesting observation is the fact that viscosity appears to have an effect on the uptake of powder. The lower the viscosity, the larger the uptake of powder. This observation supports the prediction that the availability of binder influences powder uptake; a lower-viscosity binder is more mobile in a powder bed, i.e. the penetration time is shorter compared to higher-viscosity binders. It is also consistent with Hapgood et al.'s work on liquid penetration into powder beds [12,55].

For the paste-based granules, the results are quite consistent, although the 500 rpm batch deviates slightly from the others. When considering the actual interpolated values (178 mg for 500 rpm as opposed to 185 mg for 750 rpm), the overall difference is not that significant.

Although Table 6.6 is useful for observing the relative increases in granule mass, it does not show how the exact layering mechanism works. Table 6.7 shows how many layers the granules actually gain when comparing the actual nucleus mass to the interpolated mass, assuming a single layer is approximately a powder particle diameter in height.

Interestingly, when comparing drop-nucleated lactose and glass beads granules, it appears as though lactose-based granules show significantly more layered growth. This may be the result of particle size and shape; glass beads are larger and more spherical than lactose particles, which may lead to weaker powder-liquid bonds and more difficult powder uptake due to less mechanical interlocking of the particles [62].

Table 6.6: Comparison of initial nuclei masses to the masses as extrapolated using Hounslow et al.'s model for surface tension-driven growth [30].

System	m_0 (µL)	$m_{0,extrapolated}$ (µL)	Change (%)
Lactose-13 mPa•s silicone oil	5.7	41.9	638.2
Lactose-52 mPa•s silicone oil	6.4	37.7	485.4
Lactose-105 mPa•s silicone oil	6.6	33.0	401.7
Lactose-95 mPa•s PEG	10.6	39.2	269.0
Glass beads-52 mPa•s silicone oil	6.4	43.6	577.8
Glass beads-105 mPa•s silicone oil	6.6	40.2	511.0
Glass beads-1043 mPa•s silicone oil	4.3	21.9	416.4
500 rpm, grid, flat plate	134.1	178.0	32.8
750 rpm, grid, flat plate run 1	131.3	184.2	40.2
750 rpm, grid, flat plate run 2	128.4	184.5	43.8
750 rpm, grid, flat plate run 3	128.3	187.1	45.8

Table 6.7: Comparison of initial nucleus radius to the radius as extrapolated using Hounslow et al.'s model for surface tension-driven growth, as well as the number of powder layers required to achieve the radius difference.

System	r_0 (mm)	$r_{0,obs}$ (mm)	Layers (-)
Lactose-13 mPa•s silicone oil	1.1	1.9	16
Lactose-52 mPa•s silicone oil	1.2	1.9	14
Lactose-105 mPa•s silicone oil	1.2	1.8	12
Lactose-95 mPa•s PEG	1.3	1.9	11
Glass beads-52 mPa•s silicone oil	1.2	1.7	8
Glass beads-105 mPa•s silicone oil	1.2	1.7	7
Glass beads-1043 mPa•s silicone oil	1.0	1.4	5
500 rpm, grid, flat plate	2.9	3.2	5
750 rpm, grid, flat plate I	2.9	3.2	6
750 rpm, grid, flat plate II	2.9	3.2	6
750 rpm, grid, flat plate III	2.9	3.2	7

Comparing the paste-based granules to the droplet nucleated granules shows that the layered growth is less pronounced in the paste. This is in agreement with the observations recorded in Table 6.6. It should be noted that the immediate number of layers gained by nucleation with paste is quite small; it is not hard to imagine that the sheer impact of the paste with the powder bed allows 5-7 single layers of powder to form around the granule. Taking Shukri's conclusions [159] into consideration, it appears reasonable to assume that the granule takes up only a few powder layers upon deposition. For larger granules, the effect on both granule mass and volume is less pronounced, and for non-prenucleated granules, the effect should not be noticeable during the granulation process.

6.5 Conclusions

In this study, an attempt was made to find expressions for key parameters in Hounslow et al.'s model [30], which is one of the main objectives of this work. These key parameters are the critical-packing liquid volume fraction, ϕ_{cp}, and the granulation time needed to reach critical packing, t_{max}. Additionally, behaviour of experiments performed using the consolidation-only granulator (COG) that deviated from Hounslow et al.'s model was elucidated in order explore the validity of the model.

Paste granulation was performed in order to determine end points in granule layered growth, as well as find methods to predict these values. To minimise granule breakage and attrition and reach the end point of layered growth, a high-shear mixer was fitted with a flat plate impeller, and paste was cut and granulated in the mixer. The data obtained was compared to that of the drop-nucleated granules granulated in the COG as described in the previous chapter.

It was found that paste-based granules showed similar behaviour to drop-nucleated granules, although the paste method had an inherently wider variation in initial granule mass. The method was still found to be fairly consistent. Overall, less growth was observed compared to growth in the COG, and the final granulation time was similar to that of the COG growth experiments. Consequently, growth rates were lower than those obtained in the COG. Additionally, it was found that increasing the impeller speed appeared to promote growth, with the growth rate being proportional to the square root of the impeller speed.

Porosity was found to be comparable to the granule porosities obtained with the COG, and X-ray tomography revealed a similar core-shell structure. However, the core in this study was

found to decrease in density, and the shell to increase in density. No overall densification was observed.

An extension of Hounslow et al.'s surface tension-driven growth model [30] was proposed to account for the densification of the granule shell by impacts in the granulator. However, it was concluded that considering growth as having a separate static and impact-driven dynamic phase did not agree with experimentally observed behaviour. Therefore, it was recommended to use Hounslow et al.'s model [30] for predicting granule growth, as well as for the development of a population balance model. However, both ϕ_{cp} and t_{max} can most likely not be simply calculated, as they could be dependent on the operating procedure and equipment used as well as on the system properties. These parameters should be determined experimentally.

Unexpectedly, the initial rapid increase in granule mass after nucleation was still present in this study, even for paste-based granules. Evaluation of the results using Shukri's work [159] led to the conclusion that the initial leap in granule mass is most likely not present in practical granulation. Further investigation into the layering mechanism revealed that a layer of several primary particle sizes wide was formed around the granules immediately after addition to the granulator. This phenomenon was most likely caused by the immediate availability of binder liquid in the granules, and it was not expected to significantly influence the granulation process. Therefore, it is not necessary to account for the uptake of powder in the population balance model developed in Chapter 7.

Chapter 7. Modelling layered growth with population balances

7.1 Introduction

In Chapter 5, an effort was made to identify models that predict granulation and consolidation behaviour. It was found that layered growth occurred as predicted by Hounslow et al.'s model for surface tension-driven growth [30]. In Chapter 6, a method was proposed to account for some of the observed deviations from the model, such as the initial rapid increase in granule mass. Furthermore, methods to predict important model parameters, such as the liquid volume fraction when layered growth stops, ϕ_{cp}, and the time it takes to reach this value, t_{max}, were investigated. In this chapter, the information from the previous chapters is used to develop a population balance model (PBM). This type of model tracks the distribution of one or multiple properties, in this case particle number or volume of solid, liquid and air, over time.

Although the results from Chapter 5 and Chapter 6 show that layered growth can be predicted using Hounslow et al.'s model, that does not make the model directly suitable for application in population balance modelling. The equations need to be converted into population balance equations, and several assumptions have to be made for process parameters and conditions in order to solve the equations. Additionally, the performance of the developed model has to be evaluated, at least qualitatively, in order for the model to be deemed successful.

The aims of the work described here are:

- To provide a summary of all the results from Chapter 5 and Chapter 6 with which to develop the PBM.
- To evaluate information from the literature review in Chapter 2 on PBM relevant to this study.
- To develop a layered growth kernel for PBM using discretisation.
- To implement the model using Mathematica software and perform a short simulation.
- To compare the results of the simulation to the granulation data obtained using the consolidation-only granulator described in Chapter 5.

Two types of model are presented here. The first model is based on the volume approach proposed by Verkoeijen et al. [68] for a three-dimensional PBM. Due to its relative complexity, this model is not evaluated in this study. The second model is a one-dimensional PBM solved using discretisation. The latter model is run using Mathematica software. The results are compared to the experimental data obtained in Chapter 5, and the viability of the proposed model and assumptions are evaluated.

7.2 Properties of the surface tension-driven growth model

From Chapter 5, it becomes clear that granule layered growth is linear with the square root of time. This behaviour is predicted by Hounslow et al.'s model for surface tension-driven growth [30], which implies that the interaction between powder and binder is the driving force behind layering (Equation 7.1):

$$v = v_0 + (v_{max} - v_0) * \sqrt{\frac{t}{t_{max}}} \qquad (7.1)$$

Here, v is the granule volume, v_0 is the initial droplet volume, v_{max} is the maximum attainable granule volume, dependent on critical-packing liquid volume fraction ϕ_{cp}, and t_{max} is the time needed to attain the maximum granule volume.

Although the model predicted growth behaviour quite well, there were two complications that needed to be addressed. First of all, the initial granule volume, v_0, did not agree with the observed initial volume when extrapolating obtained growth rates. Generally, an initial steep increase in granule mass, and therefore volume, was observed. A second issue that arose was that the final granule mass, and therefore the final granule volume and critical-packing liquid volume fraction, ϕ_{cp}, could not be determined accurately; granule breakage lowered the observed granule mass and prevented the recovery of a sufficient number of intact granules to accurately determine the final granule mass.

The work described in Chapter 5 needs two additional remarks. Firstly, it was concluded that, although local consolidation appeared to occur in the outer layer of the granules, no overall granule consolidation occurred. Therefore, no model can be developed to incorporate consolidation as well as layering. Secondly, the method to calculate and use the granule volume in Hounslow et al.'s model [30] does not take into account the porosity of the granule. It is possible that ϕ_{cp} and t_{max} are dependent on granule porosity, but no such effect was found in the model. Therefore, when creating a population balance model, the amount of air present in the granules has to be taken into account for the change in granule size.

In Chapter 6, the issues of the initial rapid increase in granule mass and the determination of the final granule mass were addressed. From Shukri's work [159], it was concluded that the initial increase in granule mass was most likely an artefact of the prenucleation times. For practical granulation, the effect of the initial uptake of powder should be significantly less pronounced. The final granule mass was determined using a mixer with a flat blade impeller and cut paste instead of prenucleated granules. The advantage of this method is the fact that the effect of the rapid initial growth was reduced. The observed granulation times again did not agree with Hounslow et al.'s surface tension-driven growth model [30], most likely due to changes in the porosity by impacts in the granulator. Therefore, an attempt was made to extend Hounslow et al.'s model to account for the liquid flow due to porosity changes. It was found, however, that for practical purposes, ϕ_{cp} and t_{max} could not be calculated in this way, and that the kinetics of Hounslow et al.'s model were adequate for describing the growth kinetics. Therefore, this model is used for the development of the population balance models in the following section.

7.3 Population balance modelling

In this study, two different kernels for PBMs were developed. The first model, a 3-D PBM, was proposed, whereas the second model, a 1-D PBM, was discretised and analysed using Mathematica software. The shape the equations take is largely determined by the type of solution method used to solve the equations, as well as several other factors, described in Chapter 2, Section 2.4. The reasons why it was decided to develop these two models specifically are evaluated in this section.

There are several methods of solving PBMs. First of all, there are the *discretisation* methods [22,75-77], which are based on splitting the population balance equations up into several integrals that cover different size classes of granules. Second, there are the *Monte Carlo* (MC) methods [93-95], which are slower than discretisation models, but provide information on the individual particles involved in collisions. Third, there is the *quadrature method of moments* (QMOM) [100-102], which preserves only the lower order moments of a particle size distribution (PSD). There exist other techniques, but for the purpose of this study, only these three categories of techniques are considered [103-105].

The study on solution methods in Chapter 2 concludes with the following factors that need to be taken into account when selecting a solution system for PBMs:

- Dimensionality of the population balance equations
- Mechanisms considered (e.g. nucleation, coalescence, breakage, growth)
- Required accuracy for the application
- Acceptable computational time for the application
- Hardware (e.g. number of cores, available CPU)
- Desired synergy with other models, such as CFD and DEM

Each of these points is considered in the following sections.

7.3.1 The dimensionality of the population balance equations

Population balance models (PBMs) are a type of simulation in which one or multiple properties of a system are tracked over time [26,65], depending on the dimensionality of the model. In the case of a one-dimensional PBM for granulation, that property is often number of granules of a specific size. Usually, a population balance model has several terms, describing *growth* (the change of a property), *birth* (the increase in number of granules of a certain size) and *death* (the removal of granules of a certain size), referred to as *kernels* [64]. In multidimensional PBMs, multiple properties are tracked. For example, some models track size, porosity and liquid content [24], whereas others track volumes of solid, liquid and air [68].

For the purpose of the layering model, a 3-D PBM sounds attractive: the volume-based model meshes well with population balance equations based on volumes of solid, liquid and air. However, there are few programs that allow for the fast direct simulation of such a complex model. Therefore, a 3-D PBM is proposed, but a simpler 1-D PBM is also developed for evaluation using Mathematica software.

7.3.2 The mechanisms considered in the model

The model considered in this study is chiefly designed for predicting layered growth. However, it should be kept in mind that the model should be compatible with models for other mechanisms such as agglomeration, nucleation, consolidation and breakage. Furthermore, when developing a model, liquid addition may play a role, as well as the availability of powder in the granulator. This means the model needs to incorporate these processes, or at least be adaptable so that these processes can be easily added.

7.3.3 Accuracy, computational time, hardware and synergy

For the initial validation of the model, the most interesting factor is qualitative behaviour. This means that the model accuracy does not have to be very high. Therefore, the computational time is also expected to be low. Consequently, hardware is not a limiting factor. Finally, the model is kept as simple as possible for this first evaluation, and does not yet need any synergy with DEM.

7.3.4 Other considerations

Two different types of equations are developed for modelling purposes, and both should be compared to existing models in the literature. Therefore, it was decided that the 3-D PBM would be shaped like Verkoeijen et al.'s set of equations [68], which is a Hounslow discretised system [22]. Since this type of discretisation is the most straightforward approach, the one-dimensional layered growth kernel for Mathematica is also solved by discretisation. In this kernel, the growth rate is considered a function of the granule diameter. Since standard discretisation is known to lead to errors due to the division into bins [22], an additional two alternatives to standard discretisation are explored; Marchal et al.'s dicretisation [23] and a variant of Bertin et al.'s discretisation [84].

7.4 Model development

This section is divided into two subsections describing the two different models. For the first model, a 3-D PBM is developed according to Verkoeijen et al.'s method [68]. The second model consists of a fairly straightforward one-dimensional discretised rate expression for the change in granule diameter.

7.4.1 3-D PBM based on volume of solid, liquid and air

In 3-D PBMs, multiple properties of a system are tracked at the same time. Although this method increases the complexity of the equations and the computation time, it allows for the simulation of more realistic property distributions. Verkoeijen et al. [68] proposed a method for a volume-based approach of population balance modelling, tracking the volume density distribution of solid, liquid and air, as shown in Equation 7.2:

$$\frac{\partial \underline{q}}{\partial t} + \frac{\partial (G * \underline{q})}{\partial L} = \underline{B} - \underline{D} \tag{7.2}$$

where $\underline{q}$ is a vector containing the volume densities of liquid, solid, and air, L is particle size, G is growth, $\underline{B}$ is the birth vector and $\underline{D}$ is the death vector.

Considering the fact that the model proposed by Hounslow et al. [30] uses liquid and solid volume of a single granule, this type of model appears to be well suited to Verkoeijen et al.'s approach. Although such a model would not be able to predict the granule porosity due to the exclusion of an air term from the equations, the model would be able to predict the solid and liquid content of the granules. In order to develop an appropriate rate equation, Equation 7.1

firstly needs to be rewritten slightly to reflect the fact that the equation only takes into account the volumes of solid and liquid (Equation 7.3):

$$v_{S+L} = v_L + (v_{max} - v_L) * \sqrt{\frac{t}{t_{max}}} \tag{7.3}$$

Here, v_{S+L} is the total granule volume excluding air, v_L is the liquid volume, which may be dependent on time, v_{max} is the maximum attainable granule size, t is the granulation time and t_{max} is the time needed to reach the v_{max}. The most important modification in this equation is that v_L can be dependent on time, depending on whether liquid is added or evaporation occurs during the simulated granulation process. Since v_{max} can vary if the liquid volume in the granule is variable, it is more useful to express Equation 7.3 in terms of the critical-packing liquid volume fraction ϕ_{cp}. Additionally, it is more convenient to consider only the solid volume v_S instead of the total volume v_T (Equation 7.4):

$$v_S = (v_{max} - v_L) * \sqrt{\frac{t}{t_{max}}} = v_L * \left(\frac{1 - \phi_{cp}}{\phi_{cp}}\right) * \sqrt{\frac{t}{t_{max}}} \tag{7.4}$$

This equation is not suitable for direct implementation in population balance modelling, however; a population balance equation should be a rate expression to make it possible to combine the equation with other kernels. As such, the derivative of Equation 7.4 needs to be taken, as shown in Equation 7.5:

$$\frac{d\,v_S}{d\,t} = \frac{d\,v_L}{d\,t} * \left(\frac{1 - \phi_{cp}}{\phi_{cp}}\right) * \sqrt{\frac{t}{t_{max}}} + v_L * \left(\frac{1 - \phi_{cp}}{\phi_{cp}}\right) * \frac{1}{2\,t_{max} * \sqrt{\frac{t}{t_{max}}}} \tag{7.5}$$

The expression for growth by layering now contains two terms: the increase or decrease in the surface tension-driven growth rate caused by liquid addition or evaporation (blue), as well as the surface tension-driven growth rate in absence of changes in the liquid volume (red). For evaluation as a PBM, t should be removed from the equation, as the start of growth is potentially different for every single granule (if nucleation occurs). Both terms can be expressed in terms of v_S, eliminating t from the equation (Equation 7.6):

$$\frac{d\,v_S}{d\,t} = \frac{d\,v_L}{d\,t} * \frac{v_S}{v_L} + \frac{v_L{}^2}{v_S} * \left(\frac{1 - \phi_{cp}}{\phi_{cp}}\right)^2 * \frac{1}{2\,t_{max}} \tag{7.6}$$

In this way, both the term for liquid addition (blue) and regular surface tension-driven growth (red) are expressed in quantifiable parameters and variables. In the case where no liquid addition or evaporation occurs, the blue term can be eliminated, leaving Equation 7.7:

$$\frac{d\,v_S}{d\,t} = \frac{v_L{}^2}{v_S} * \left(\frac{1 - \phi_{cp}}{\phi_{cp}}\right)^2 * \frac{1}{2\,t_{max}} \tag{7.7}$$

which is the same rate expression as the one proposed by Hounslow et al. [30]. Naturally, this expression only holds for $v_L/v_S > \phi_{cp}$; at the critical-packing liquid volume fraction, no further growth occurs.

7.4.2 1-D PBM based on granule diameter growth rate

A typical one-dimensional population balance model represents the change in number density function n in terms of particle size L, growth G, birth B and death D, as shown in Equation 2.16 of Chapter 2, which is also presented below (Equation 7.8):

$$\frac{\partial n}{\partial t} + \frac{\partial (G * n)}{\partial L} = B - D \tag{7.8}$$

For the purpose of the simulation using Mathematica software, birth and death are neglected, reducing the equation to Equation 7.9:

$$\frac{\partial n}{\partial t} = -\frac{\partial (G * n)}{\partial L} \tag{7.9}$$

Here, the growth rate G is expressed in terms of the change of granule diameter as a function of time, dL/dt. To convert the population balance equation into an equation usable for a 1-D PBM, Equation 7.7 must be converted into an expression dependent on the granule diameter.

7.4.2.1   Expressing the growth rate as a function of the granule diameter

In order to express the growth rate as a function of the diameter instead of solid volume v_S and liquid volume v_L, the total granule volume v_T is needed. However, it was found during experiments that Hounslow et al.'s model [30] does not take into account the volume of air v_A. Therefore, this variable must be added, even if no consolidation occurs (Equation 7.10), to account for the effect porosity has on the size of the granule.

$$v_T = v_S + v_L + v_A \tag{7.10}$$

Using this equation, the porosity ε can be expressed in terms of these volumes, as shown in Equation 7.11. In turn, this equation can be rewritten to express v_A as a function of v_T, v_L and ε (Equation 7.12):

$$\varepsilon = \frac{v_L + v_A}{v_T} \tag{7.11}$$

$$v_A = v_T * \varepsilon - v_L \tag{7.12}$$

Substituting this equation into Equation 7.10 yields Equation 7.13:

$$v_T = v_S + v_L + v_T * \varepsilon - v_L = \frac{v_S}{1 - \varepsilon} \tag{7.13}$$

Now, the total granule volume has been expressed in terms of the volume of solid and the porosity. Using the total volume, the granule diameter L can be calculated (Equation 7.14):

$$L = \sqrt[3]{\frac{6}{\pi} * v_T} = \sqrt[3]{\frac{6}{\pi} * \frac{v_S}{1-\varepsilon}} \tag{7.14}$$

The growth rate G is effectively the derivative of the granule diameter with respect to time. Therefore, the derivative of this equation has to be taken. Note that the porosity may be dependent on time due to consolidation, and this has also to be taken into account, yielding Equation 7.15:

$$G = \frac{d\,L}{d\,t} = \frac{\frac{d\,v_S}{d\,t} * (1-\varepsilon) + v_S * \frac{d\,\varepsilon}{d\,t}}{\frac{\pi}{2} * (1-\varepsilon)^2 * \sqrt[3]{\left(\frac{6}{\pi} * \frac{v_S}{1-\varepsilon}\right)^2}} \tag{7.15}$$

Since it is undesirable to have the rate expression for solid volume in the equation, Equation 7.6 can be substituted into this expression to yield Equation 7.16:

$$\frac{d\,L}{d\,t} = \frac{\left(\frac{d\,v_L}{d\,t} * \frac{v_S}{v_L} + \frac{v_L^2}{v_S} * \left(\frac{1-\phi_{cp}}{\phi_{cp}}\right)^2 * \frac{1}{2\,t_{max}}\right) * (1-\varepsilon) + v_S * \frac{d\,\varepsilon}{d\,t}}{\frac{\pi}{2} * (1-\varepsilon)^2 * \sqrt[3]{\left(\frac{6}{\pi} * \frac{v_S}{1-\varepsilon}\right)^2}} \tag{7.16}$$

Here, the numerator describing the granule growth rate is composed of three terms: changes in surface tension-driven growth due to the addition or evaporation of liquid (blue), regular surface tension-driven growth (red), and changes in surface tension-driven growth due to variations in the porosity (green). This equation is still quite complex; information on the liquid density and porosity is needed, as well as the solid volume. In the experiments performed in this work, no liquid was added during the experiments, and no overall consolidation was observed. Therefore, Equation 7.16 can be simplified by removing the liquid addition (blue) and consolidation (green) terms to produce Equation 7.17. If it is desired to include these phenomena, separate equations to describe them must be developed. For the liquid volume, it should be possible to use the equation for determining the liquid mass fraction, which is used in PBM for mechanistic collision kernels [112]. Likewise, porosity is already considered in some population balance models [24]. Therefore, adapting the model presented here to implement these parameters for more advanced models should be possible.

$$\frac{d\,L}{d\,t} = \frac{\frac{v_L^2}{v_S} * \left(\frac{1-\phi_{cp}}{\phi_{cp}}\right)^2 * \frac{1}{2\,t_{max}}}{\frac{\pi}{2} * (1-\varepsilon) * \sqrt[3]{\left(\frac{6}{\pi} * \frac{v_S}{1-\varepsilon}\right)^2}} \tag{7.17}$$

With the porosity and initial droplet size as constants, the only parameters that need to be considered are the critical-packing liquid volume fraction ϕ_{cp} and the time to achieve the maximum granule size t_{max}. These two parameters can be determined experimentally.

Before discretising Equation 7.17, two special cases must be addressed. The first case is the end of the growth regime, where the growth rate is zero. This condition is simply satisfied by comparing the volume of solid and liquid to the critical-packing liquid volume fraction. The other special case is the initial growth, where there is not enough powder taken into the nucleus for the porosity constraint to hold. In this scenario, the total volume v_T is considered to be equal to $v_L + v_S$. This regime is true until a critical solid volume has been reached; v_{crit}, according to Equation 7.18:

$$v_{crit} = v_L \frac{1-\varepsilon}{\varepsilon} \tag{7.18}$$

where ε is the constant porosity once the granule has grown beyond the critical solid volume. As long as the sum of the solid and liquid volume is smaller than this value, the granule is assumed to not contain any air. Since no liquid is added to the granules, the granule will start incorporating air during growth in order to maintain a constant porosity. Applying these conditions to Equation 7.17 leads to the following equation (Equation 7.19):

$$G = \begin{cases} \dfrac{\dfrac{v_L{}^2}{v_S} * \left(\dfrac{1-\phi_{cp}}{\phi_{cp}}\right)^2 * \dfrac{1}{2\,t_{max}}}{\dfrac{\pi}{2} * \sqrt[3]{\left(\dfrac{6}{\pi} * (v_S + v_L)\right)^2}} & v_S < v_{crit} \\[3em] \dfrac{\dfrac{v_L{}^2}{v_S} * \left(\dfrac{1-\phi_{cp}}{\phi_{cp}}\right)^2 * \dfrac{1}{2\,t_{max}}}{\dfrac{\pi}{2} * (1-\varepsilon) * \sqrt[3]{\left(\dfrac{6}{\pi} * \dfrac{v_S}{1-\varepsilon}\right)^2}} & \dfrac{v_L}{v_L + v_S} > \phi_{cp} \\[3em] 0 & \dfrac{v_L}{v_L + v_S} \le \phi_{cp} \end{cases} \tag{7.19}$$

7.4.2.2   Discretisation of granule growth

There are several discretisation methods available in the literature for the term $\mathrm{d}(G*n)/\mathrm{d}L$. Here, three different discretisation methods are used: standard discretisation [22], discretisation as performed by Marchal et al. [23] and a variant of discretisation employed by Bertin et al. [84].

As explained in Chapter 2, discretisation is based on the partial integration of the expression of the equation with respect to the particle size, effectively dividing the differential equation up into a series of differential equations dependent on time only. Each differential equation describes the birth, death and growth in a single bin, or particle size range, and bins usually increase exponentially according to a fixed bin size ratio r. Using many narrow bins leads to a higher accuracy of the solution, but also to increased computational load. The final result is a series of equations describing the number of particles in a bin over time, $N_i(t)$.

Discretisation of Equation 7.19 requires the replacement of all volumes v_S by the discrete bin diameter L_i by relating the volume v_T to the diameter; according to Equation 7.14 for the normal growth (red) regime, and as the total volume minus the liquid volume for the initial growth (blue) regime (Equation 7.20):

$$G_i = \begin{cases} \dfrac{v_L{}^2 * \left(\dfrac{1-\phi_{cp}}{\phi_{cp}}\right)^2 * \dfrac{1}{2\,t_{max}}}{\dfrac{\pi}{2} * (L_i + d_p)^2 * \left(\left(\dfrac{\pi}{6} * (L_i + d_p)^3\right) - v_L\right)} & i = 1 \\[4ex] \dfrac{v_L{}^2 * \left(\dfrac{1-\phi_{cp}}{\phi_{cp}}\right)^2 * \dfrac{1}{2\,t_{max}}}{\dfrac{\pi}{2} * L_i{}^2 * \left(\left(\dfrac{\pi}{6} * L_i{}^3\right) - v_L\right)} & \left(\dfrac{\pi}{6} * L_i{}^3\right) - v_L < v_{crit} \\[4ex] \dfrac{v_L{}^2 * \left(\dfrac{1-\phi_{cp}}{\phi_{cp}}\right)^2 * \dfrac{1}{2\,t_{max}}}{\dfrac{\pi^2}{12} * (1-\varepsilon)^2 * L_i{}^5} & \dfrac{v_L}{v_L + \left((1-\varepsilon) * \dfrac{\pi}{6} * L_i{}^3\right)} > \phi_{cp} \\[4ex] 0 & \dfrac{v_L}{v_L + \left((1-\varepsilon) * \dfrac{\pi}{6} * L_i{}^3\right)} \le \phi_{cp} \end{cases}$$

(7.20)

Note that there is one problem with this equation; for cases where $v_T \le v_L$, the equation is not valid. This can be solved by ensuring no bin smaller than the bin currently under consideration exists in the model. Additionally, for L_1, which is set equal to the initial droplet volume, the size of the bin is considered to be $L_1 + d_p$, where d_p is the diameter of a single powder particle. This effectively means that a liquid droplet is assumed to take in a single layer of powder. Provided that the powder particles are small compared to the droplet size, this appears to be a reasonable assumption.

After the discretisation of the growth rate G, it is necessary to define terms for the change into and out of the bins in terms of G_i and N_i. The first and most straightforward option is standard discretisation [22] which assumes the growth into bin i is equal to the number of particles in the bin i-1 multiplied by the growth rate, divided by the width of that bin. Likewise, the growth out of a bin i is equal to the number of particles in the bin divided by the width of bin i. In summary, the differential equations become (Equation 7.21):

$$\frac{d\,N_i}{d\,t} = \begin{cases} -\dfrac{G_i * N_i}{L_{i+1} - L_i} & i = 1 \\[3ex] \dfrac{G_{i-1} * N_{i-1}}{L_i - L_{i-1}} - \dfrac{G_i * N_i}{L_{i+1} - L_i} & 1 < i < q \\[3ex] \dfrac{G_{i-1} * N_{i-1}}{L_i - L_{i-1}} & i = q \end{cases}$$

(7.21)

Here, there are special cases for the first and last (q^{th}) bin; no extra granules are produced at the lowest bin, and no granules can grow out of the highest bin. The latter constraint is not a result of the end of the growth regime predicted by the model, but rather a necessity to conserve the number of granules present. For the growth kernel presented here, no granules

are expected to reach the final bin, but this could occur if agglomeration or liquid addition kernels were added.

Equation 7.21 can be rewritten more elegantly in terms of L_i only by using the fixed bin size ratio r. The rewritten equation then becomes Equation 7.22:

$$\frac{d\,N_i}{d\,t} = \begin{cases} \dfrac{-(G_i * N_i)}{(r-1) * L_i} & i = 1 \\[3mm] \dfrac{(r * G_{i-1} * N_{i-1}) - (G_i * N_i)}{(r-1) * L_i} & 1 < i < q \\[3mm] \dfrac{(r * G_{i-1} * N_{i-1})}{(r-1) * L_i} & i = q \end{cases} \tag{7.22}$$

A second option for discretisation is presented by Marchal et al. [23]. Instead of simply considering the influx and outflow of granules in a bin to be a function of the previous and current bin sizes, Marchal et al. take the average growth between bins. This leads to Equation 7.23:

$$\frac{d\,N_i}{d\,t} = \begin{cases} \dfrac{-\left((G_i * N_i) + \left(\frac{1}{r} * G_i * N_{i+1}\right)\right)}{2 * (r-1) * L_i} & i = 1 \\[4mm] \dfrac{(r * G_{i-1} * N_{i-1}) + ((G_{i-1} - G_i) * N_i) - \left(\frac{1}{r} * G_i * N_{i+1}\right)}{2 * (r-1) * L_i} & 1 < i < q \\[4mm] \dfrac{(r * G_{i-1} * N_{i-1}) + (G_{i-1} * N_i)}{2 * (r-1) * L_i} & i = q \end{cases} \tag{7.23}$$

Bertin et al. [84] present a third option for discretisation of the growth equation. The particle size frequency distribution in a single bin, n_i, is considered as a function of two arbitrary constants, $C_{1,i}$ and $C_{2,i}$, according to Equation 7.24:

$$n_i(L, t) = \left(C_{1,i} * L\right) + C_{2,i} \tag{7.24}$$

The parameters $C_{1,i}$ and $C_{2,i}$ may be found by solving the integral for any of the moments. Bertin et al. use the zeroth (Equation 7.25) and third moment (Equation 7.26):

$$\int_{L_i}^{L_{i+1}} \left(\left(C_{1,i} * L\right) + C_{2,i}\right) d\,L = N_i \tag{7.25}$$

$$\int_{L_i}^{L_{i+1}} \left(\left(C_{1,i} * L^4\right) + \left(C_{2,i} * L^3\right)\right) d\,L = N_i * L_{p,i}{}^3 \tag{7.26}$$

where $L_{p,i}$ is the representative granule size for each bin. Bertin et al. then proceeded to rewrite the equations with an additional set of equations to calculate this size for each bin. However, since the aim of this study is to create as simple a model as possible, $L_{p,i}$ is assumed to be equal to the geometric mean of the bin size, $\bar{L}_i = (L_i * L_{i+i})^{1/2}$. This assumption

can underestimate or overestimate the actual representative particle size, as demonstrated by Figure 7.1.

Figure 7.1 presents several possible scenarios for the number density function, some of which are explored by Bertin et al. [84]. The representative particle size corresponds to the particle size that encloses half of the total number of particles in the bin, i.e. half the area of the positive part the density function. In case I, the density function is initially negative but becomes positive; in case II, the density function starts out positive and further increases. In case III, the number density is evenly distributed over the bin. In these three scenarios, the representative particle size is expected to be underestimated. According to Equation 7.26, this underestimation is expected to lead to an overestimation of the growth rate. On the other hand, cases IV and V, the opposites of cases I and II, respectively, lead to an overestimation of representative particle size $L_{p,i}$ and an underestimation of the growth rate. Since the initial condition states that granules grow from the smallest bin, it is likely that, at least initially, the growth rate is underestimated slightly.
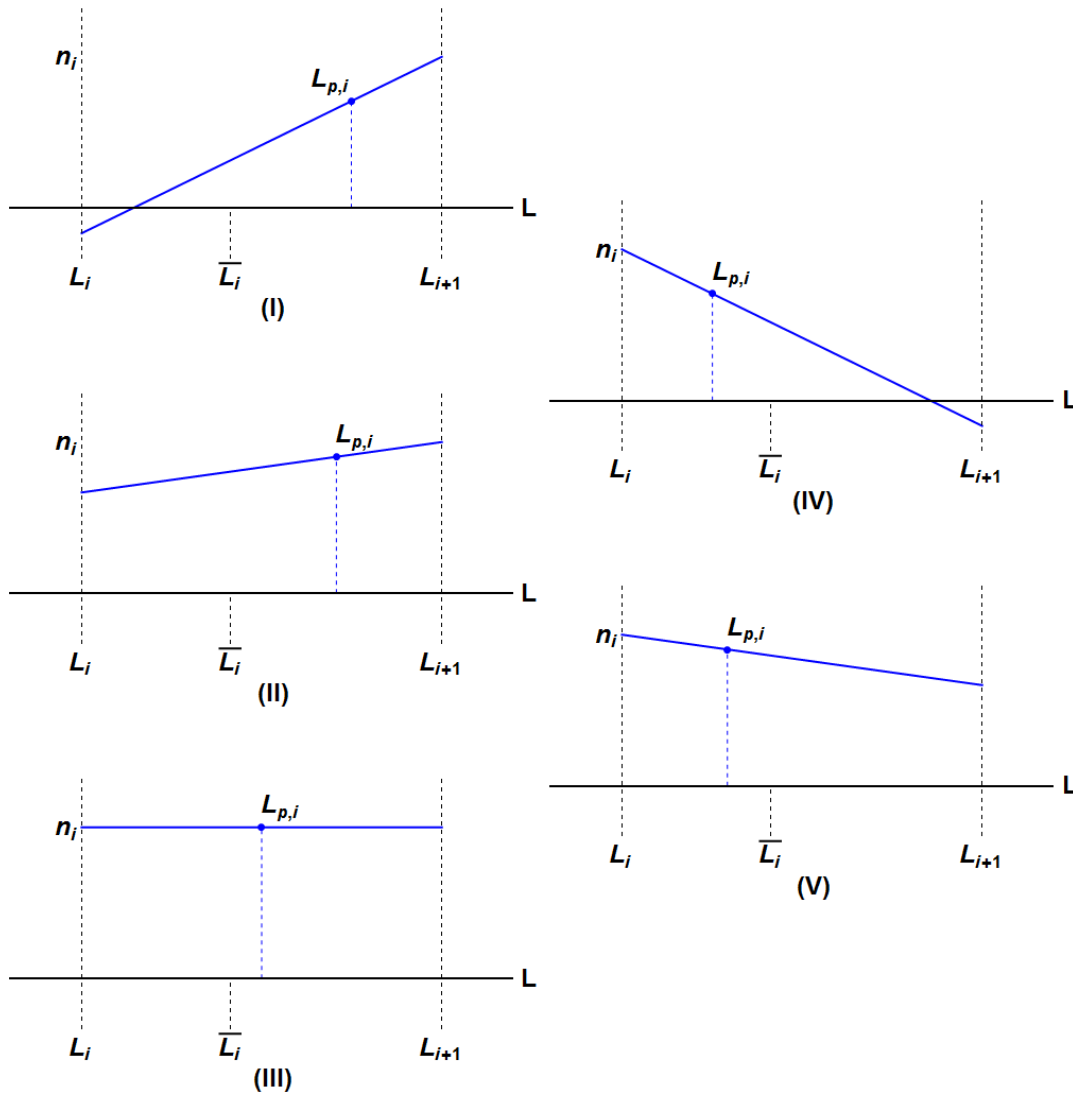

Figure 7.1: Different cases for which the assumption $L_{p,i} = \bar{L}_i$ is incorrect. In cases I-III, the representative particle size is underestimated; for cases IV and V, the representative particle size is overestimated.

Solving the equations using this assumption leads to the following expressions for $C_{1,i}$ (Equation 7.27) and $C_{2,i}$ (Equation 7.28):

$$C_{1,i} = \frac{\frac{r^4 - 1}{r - 1} - \left(4 * r^{3/2}\right)}{\left(\frac{1}{2} * (r^4 - 1) * (r + 1)\right) - \left(\frac{4}{5} * (r^5 - 1)\right)} * \frac{N_i}{L_i{}^2} \qquad (7.27)$$

$$C_{2,i} = \frac{N_i - \left(\frac{C_{1,i}}{2} * L_i{}^2 * (r^2 - 1)\right)}{L_i * (r - 1)} \qquad (7.28)$$

In order to ensure the expression is continuous, Equation 7.24 must satisfy the following constraint (Equation 7.29):

$$n_i = \left(C_{1,i-1} * L_i\right) + C_{2,i-1} \qquad (7.29)$$

This leads to the following differential equation (Equation 7.30):

$$\frac{d N_i}{d t} = \begin{cases} -\alpha_i * G_{i+1} * \left(\left(C_{1,i} * L_{i+1}\right) + C_{2,i}\right) & i = 1 \\[2mm] \left(\alpha_{i-1} * G_i * \left(\left(C_{1,i-1} * L_i\right) + C_{2,i-1}\right)\right) & \\ -\left(\alpha_i * G_{i+1} * \left(\left(C_{1,i} * L_{i+1}\right) + C_{2,i}\right)\right) & 1 < i < q \\[2mm] \alpha_{i-1} * G_i * \left(\left(C_{1,i-1} * L_i\right) + C_{2,i-1}\right) & i = q \end{cases} \qquad (7.30)$$

where α_i equals 1 for the case where the outcome of Equation 7.29 is positive, and 0 where Equation 7.29 is negative. This constraint is used in order to ensure the number of particles in a bin is always positive.

The three sets of discretised population balance equations presented in Equation 7.22, Equation 7.23 and Equation 7.30 were solved using Mathematica software. The results were compared and the performance of the different sets of equations was evaluated, as described in the following section.

7.5 Model implementation

In order to evaluate the performance of the developed 1-D model, it was implemented using Mathematica software for the three different discretisation methods presented in Equation 7.22, Equation 7.23 and Equation 7.30, as shown by Figure 7.2. To supply data for values of initial liquid volume v_L, critical-packing liquid volume fraction ϕ_{cp}, porosity ε, and time needed to achieve critical packing t_{max}, experimental data was used. All available granulation data from the experiments performed using the consolidation-only granulator (COG) with the lactose-100 cSt silicone oil system as described in Chapter 5 was combined. The combined data points were used to calculate the fitted line and the values for ϕ_{cp} and t_{max}, and the pycnometry data was used to calculate the overall porosity. It should be noted that the

values used do not represent the actual physical values; after all, it was not possible to obtain the real values of ϕ_{cp} and t_{max} in the work performed using the COG. However, the behaviour observed does not change, and the experimental data does conform to Hounslow et al.'s model for surface tension-driven growth [30], which serves the purpose of evaluating the population balance model. The results are shown in Table 7.1.

Table 7.2 shows the other parameters used to perform the simulation. The lowest bin size was set to the diameter of the initial liquid droplet, and the number of particles simulated was set to 1000. The latter has no real effect on the actual simulation, but serves as a useful tool to ensure the zeroth moment is conserved. For the size ratio between neighbouring bins r, two different values were used; a ratio of $2^{1/3}$, and a ratio of $2^{1/9}$. The former value was also applied by Hounslow et al. [22] in their discretisation of the growth term. The latter value was selected to increase the accuracy of the discretisation, at the cost of increasing the number of bins evaluated, as shown in Table 7.2. The actual number of bins was selected based on the bins size ratio r; the number of bins should be sufficient to account for all possible granule sizes. To ensure the final granule size was well within the limits of the simulated bin sizes, an additional number of bins was added to the minimum number of bins required.

The parameters shown in Table 7.1 and Table 7.2 were used for standard discretisation [22], Marchal et al's discretisation [23] and Bertin et al.'s discretisation [84], as presented in Section 7.4.2.2, for a total of six simulations. All simulations were solved using Mathematica software's NDSolve function for a total simulation time of 250 minutes to capture all experimental data, as well as to ensure the fits had reached the no-growth regime. The obtained time-dependent particle size distributions (PSDs) were then converted to time-dependent number-based average particle sizes in order to compare them with experimental data. The results of the first set of simulations, with $r = 2^{1/3}$, are shown in Figure 7.3.

Table 7.1: Parameters from experimental data used for the model in Equation 7.20.

Parameter (units)	Value
v_L (µL)	6.785
ε (-)	0.43
ϕ_{cp} (-)	0.13
t_{max} (min)	156

Table 7.2: Simulation parameters used for the model.

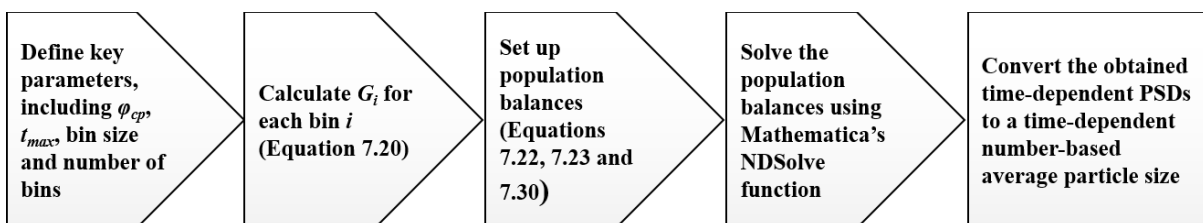| Simulation type	Number of granules	L_1 (mm)	r (-)	Number of bins (-)
Simulation 1	1000	2.349	$2^{1/3}$	10
Simulation 2			$2^{1/9}$	20

Figure 7.2: Block diagram of the calculations performed using Mathematica software.

Figure 7.3: Comparison of particle size as a function of time for both the experimental and simulated data for all three discretisation methods with $r = 2^{1/3}$.

All three models shown in Figure 7.3 demonstrate an increase in particle size over time, but Marchal et al.'s discretisation method [23] shows the most unstable behaviour. After a rapid increase in particle size, the size fluctuates. This fluctuation is related to the number of granules present in each bin; inspection of the individual bins regularly shows a negative number of granules. Bertin et al.'s discretisation method [84] yields stable growth, but the growth rate is generally underestimated compared to the fit to the experimental data. The standard discretisation method [22] appears to yield the smallest deviation from the fitted curve, slightly overestimating both the growth rate and the final granule size. The theoretical maximum granule size as fitted to the experimental data is 5.49 mm, whereas the predicted maximum according to the standard discretisation method is 5.92 mm, a deviation of 7.8 %. This means the volume of the granule is overestimated by 25 %.

The overestimation of the final granule size is not surprising, as the final size is dependent on the last bin in which growth occurs. Creating narrower bins by changing r to $2^{1/9}$ should improve the accuracy of the solution; this is demonstrated in Figure 7.4.

Compared to Figure 7.3, the modelled curves in Figure 7.4 more closely match the fit to the experimental data. Marchal et al.'s method [23] displays small deviations and appears to predict a final granule size similar to that of the standard discretisation method [22]. However, the method still displays negative granule numbers for bins, which is undesirable. Bertin et al.'s method [84], which greatly underpredicted the final granule size as well as the growth rate, appears to more closely predict the final granule size, with a deviation of 0.18 % in diameter, or 0.55 % in volume. The standard discretisation method appears to capture the kinetics of growth extremely well. However, the method still overestimates the final granule size by 7.8 %.
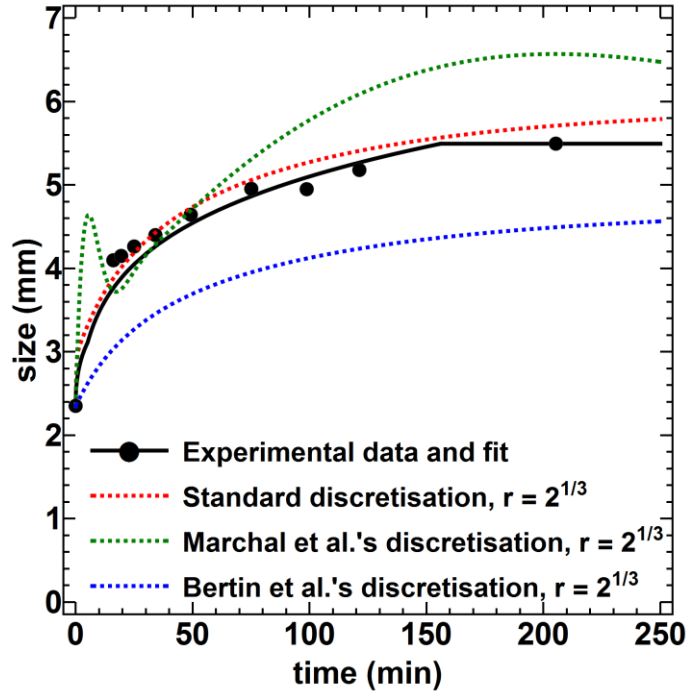
Figure 7.4: Comparison of particle size as a function of time for both the experimental and simulated data for all three discretisation methods with $r = 2^{1/9}$.

This difference between the standard discretisation method and Bertin et al.'s method [84] is caused by their different approaches. The latter method is an upwind scheme, which takes into account the granule size of the next bin. This method inherently underpredicts granule growth, as growth decreases with increasing granule size. Therefore, the solution is likely to predict the maximum granule size as the bin size *before* the actual maximum granule size. The standard discretisation method, on the other hand, uses the previous bin to calculate growth. Therefore, it uses smaller granule sizes compared to Bertin et al.'s method, and consequently overpredicts growth. As a result, the standard discretisation method is likely to designate the bin size *after* the actual maximum granule size as the maximum.

Because of the inherent flaws of discretisation methods, no single method can accurately predict the final granule size. However, the kinetics of the growth process can be captured. Figure 7.5 shows how the solutions converge for the extreme case where the bin size ratio r is equal to $2^{1/81}$. In this scenario, both standard discretisation and Bertin et al.'s method [84] show agreement with the analytical solution. However, Marchal et al.'s method [23] deviates from the solution even at this low value for r. Furthermore, the solution keeps fluctuating beyond the final time of 250 minutes, never fully converging to the analytical solution. Therefore, it is not recommended to use this method for the simulation of growth if the growth parameter G is not a constant.

From the simulations performed, it appears as though standard discretisation is the most reliable method for the prediction of the kinetics, especially considering the fact that real simulations are expected to run for much shorter granulation times. Although Bertin et al.'s method [84] shows good convergence to the analytical solution, it underestimates the actual granule size too much for shorter granulation times, particularly at large values of r.
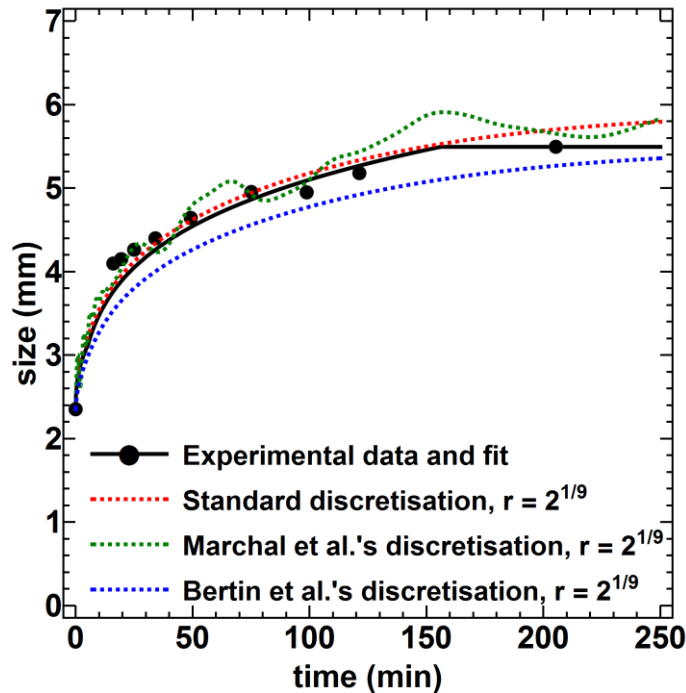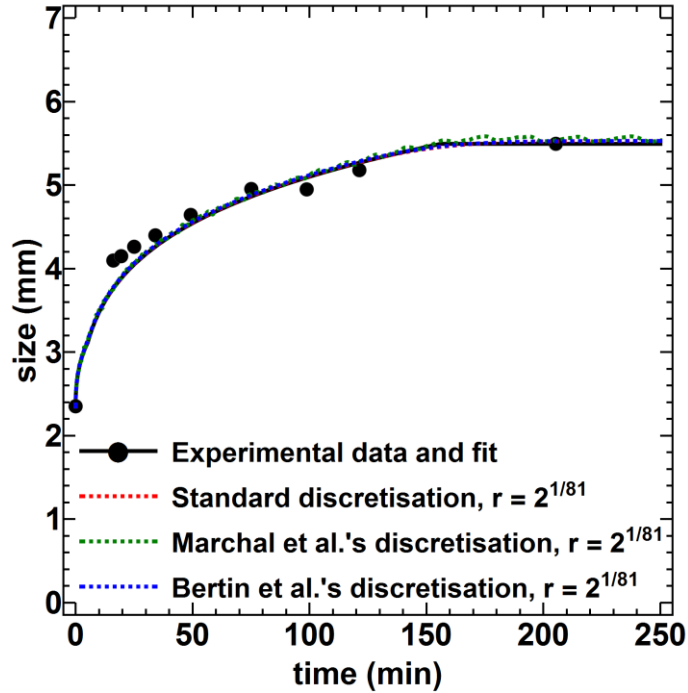
Figure 7.5: Comparison of particle size as a function of time for both the experimental and simulated data for all three discretisation methods for the extreme case $r = 2^{1/81}$.

In order to improve the accuracy of the prediction of the final granule size, the bins surrounding the final granule size should be narrow, i.e. the value for r should be reasonably small. However, reducing r increases the number of bins and, consequently, the computational load. Moreover, simulating other granulation mechanisms, such as agglomeration, in conjunction with growth would further increase the possible granule sizes, the number of bins, and the computation time. Therefore, it is not recommended to decrease r if simulation speed is important.

Since layered growth most likely never reaches the no-growth regime in simulations of industrial processes, the predicted growth rate is much more significant than the predicted final granule size. As such, upwind methods such as Bertin et al.'s discretisation method [84] are not recommended. Standard discretisation appears to better predict the kinetics, although it deviates significantly for large bins sizes. It should be possible to develop a discretisation method that better captures the kinetics by using a more representative granule size for each bin. Marchal et al.'s attempt [23] to average the flows in and out of bins resulted in instabilities and negative numbers of granules in some bins, which is undesirable. Different averaging methods might be more suitable.

It should also be noted that the case studied here was the most straightforward simulation of growth possible. No liquid addition was considered, and it was assumed that there was no consolidation. These two processes will greatly influence the complexity of the equations. Furthermore, nucleation, agglomeration, breakage and attrition were not considered. There was no mass balance for powder available for layering; it was assumed that, as with the COG experiments, powder was not the limiting factor. However, in practical granulation, this is not the case. It is likely that the layering rate decreases with a decreasing amount of fines. As such, the model evaluated here is just the first step in the mechanistic simulation of layered growth. The further development of models capable of simulating this type of growth could

provide industry with the tools to better understand the granulation process, as well as facilitate easier granulation process design.

7.6 Conclusions

In the study presented here, two novel population balance models (PBMs) were developed for layered granule growth by finding a mechanistic expression for the growth rate in order to address the final objective of this thesis; to develop and evaluate a mechanistic population balance model. The first model was a 3-D PBM based on Verkoeijen et al.'s work [68], which tracks volumes of solid, liquid and air per size bin. The second model, a 1-D PBM tracking only particle number for each size bin, was discretised using three different discretisation methods and evaluated using Mathematica software.

Results showed that standard discretisation predicted the growth rate best for narrow bins, but that it could not accurately predict the final granule size due to the limits of discretisation. Other methods deviated more from the curve fitted to experimental data, especially for wider bins, which are more likely to be used for simulations when simulation times should be short. It is therefore recommended to either use standard discretisation, or develop a discretisation scheme that better represents the expected growth rate.

Overall, the results of the simulation showed that the developed model is capable of predicting granule growth behaviour. Future development of the population balance equations should focus on the inclusion of other processes such as consolidation, liquid addition, nucleation, agglomeration, breakage and attrition.

Chapter 8.   Conclusions and recommendations

8.1 Conclusions

The key objective of this work was to develop a mechanistic population balance model for layered growth by elucidating the kinetics of the layering mechanism. To this purpose, a novel granulator was designed to isolate the layering and consolidation. The obtained kinetics were compared to available models in literature, and an appropriate predictive model was selected. Further experiments were then performed to evaluate the validity of the model and to determine the key parameters needed. Finally, two different population balance models were proposed, one of which was further evaluated.

8.1.1 Method development

In order to develop an experimental method to investigate consolidation and layered growth in isolation, a novel, consolidation-only granulator (COG) was developed. Prenucleation outside of the granulator was used to successfully prevent the effects of wetting and nucleation, as well as agglomeration. The development of this method allows, for the first time, the observation of the kinetics of layered growth. Additionally, the design of the COG would allow for the study of other rate processes, such as attrition, using a slightly different set-up.

8.1.2 Consolidation and layering studies

Several key findings were observed in the experimental studies of consolidation and layering using the COG and a flat plate impeller mixer:

- The COG was a suitable method of evaluating the kinetic behaviour of layered growth. The method had several limitations, however. Breakage and attrition prevented the study of late layered growth behaviour, as well as the observation of the end points. Furthermore, initial layered growth behaviour could not be observed using this method.
- Qualitative growth behaviour was predicted by Hounslow et al.'s model for surface tension-driven growth [30], with the granules growing linearly with the square root of time until a critical-packing liquid volume fraction, ϕ_{cp}, had been reached. This finding implies that layered growth behaviour is dominated by capillary forces. Furthermore, it allows for the description of the full growth behaviour using only two parameters: ϕ_{cp} and the granulation time required to achieve ϕ_{cp}, t_{max}.
- No overall consolidation was observed for the systems evaluated. However, X-ray tomography demonstrated that local density differences did develop in the granules during granulation. A clear core-shell structure was observed, with the core being less dense than the surrounding shell. This was most likely the result of impacts experienced by the granules. This finding implies that breakage may play an important role in the full consolidation of granules.

8.1.3 Model evaluation

Hounslow et al.'s model for surface tension-driven growth [30] was converted into two different population balance models (PBMs). The first PBM was three-dimensional, based on the work performed by Verkoeijen et al. [68]. Due to its relatively higher complexity, this model PBM was not evaluated. However, the equations should be useful for the future development of a fully predictive 3-D model.

The second, one-dimensional PBM was based on the frequency distribution of the number of granules as a function of granule size. Hounslow et al.'s model was adapted to account for the inclusion of a fixed porosity, and used to develop an expression for the layered growth term G. This growth term was used to formulate layered a layered growth equation, which was solved using three different discretisation schemes. It was demonstrated that the PBM, when solved with standard discretisation [22], was capable of predicting the experimental data reasonably well.

This study proposes the first mechanistic population balance kernel for layered growth. This model allows for the evaluation of granulation processes as a whole by combination with existing kernels for other rate processes, and provides industry with the tools to improve the understanding of granulation as well as facilitate granulation process design.

8.1.4 Summary

This work presents, for the first time, a study of consolidation and layered growth in dynamic systems. It has been found that layered growth of granules can be qualitatively predicted according to Hounslow et al.'s model for surface tension-driven growth [30], and that layered growth occurs linearly with the square root of time. The observed trend has been used to develop a population balance kernel that can be used to better understand granulation in general as well as aid in the design of granulation processes.

8.2 Recommendations for future work

This work has demonstrated that it is possible to model layered granule growth using surface tension as the driving force, as proposed by Hounslow et al. [30]. This result opens the way for the development of more mechanistic population balance models (PBMs), and increases our fundamental understanding of layered granule growth. Additionally, this study has contributed to the area of experimental research of granulation by means of the development of a novel consolidation-only granulator, which could also be adapted to study other granulation mechanisms such as breakage and attrition. Naturally, this work has generated more questions than answers, as most studies do. Key areas for future research have been identified and listed below:

- The influence of the presence of air in the granules on the growth rate is most likely part of the reason why final growth time t_{max} and critical-packing liquid volume fraction ϕ_{cp} can, as of yet, not be estimated. Elucidating the relationship and identifying expressions to approximate these values would greatly contribute to our understanding of layered growth.

- Consolidation has so far been observed mostly locally, not for the entire granule. The exact mechanism of consolidation so far is still unknown, and provides an interesting avenue of research.
- In the area of population balance modelling, research should focus combining the model with other kernels, and experimentally validating the results. Additionally, solution methods should be developed that better predict the final granule size.
- It this work is has been demonstrated that there is some kind of relationship between the capillary number, liquid saturation and granule breakage. However, the physics of this process are, as of yet, unclear. Therefore, experiments with a wider variety of powder-binder systems could shed some light on the mechanisms involved.

Bibliography

1. K. Hapgood and M. Rhodes, *Size Enlargement*, in *Introduction to Particle Technology*, M. Rhodes, Editor. 2008, John Wiley & Sons Ltd: Chichester.
2. S.M. Iveson, et al., *Nucleation, growth and breakage phenomena in agitated wet granulation processes: a review.* Powder Technology, 2001. **117**(1-2): p. 3-39.
3. D.M. Parikh, *Introduction*, in *Handbook of Pharmaceutical Granulation Theory*, D.M. Parikh, Editor. 2005, Taylor & Francis Group, LLC: Boca Raton.
4. B.J. Ennis, *Agglomeration and size enlargement - Session summary paper.* Powder Technology, 1996. **88**(3): p. 203-225.
5. J.D. Litster, *Scaleup of wet granulation processes: science not art.* Powder Technology, 2003. **130**(1-3): p. 35-40.
6. J. Litster, B.J. Ennis, and L. Liu, *The Science and Engineering of Granulation Processes.* 2004, Dordrecht: Kluwer Academic Publishers.
7. Y. He, X. Liu, and J.D. Litster, *Scale-Up Considerations in Granulation*, in *Handbook of Pharmaceutical Granulation Theory*, D.M. Parikh, Editor. 2005, Taylor & Francis Group, LLC: Boca Raton.
8. P.R. Mort, *Scale-up of binder agglomeration processes.* Powder Technology, 2005. **150**(2): p. 86-103.
9. A. Hassanpour, et al., *Effect of granulation scale-up on the strength of granules.* Powder Technology, 2009. **189**(2): p. 304-312.
10. G.I. Tardos, et al., *Stress measurements in high-shear granulators using calibrated "test" particles: application to scale-up.* Powder Technology, 2004. **140**(3): p. 217-227.
11. S. Hibare and K. Acharya, *Scale-up of detergent granules in a high shear mixer.* Powder Technology, 2014. **254**: p. 265-273.
12. K.P. Hapgood, J.D. Litster, and R. Smith, *Nucleation regime map for liquid bound granules.* AIChE Journal, 2003. **49**(2): p. 350-361.
13. L.X. Liu, et al., *Coalescence of deformable granules in wet granulation processes.* Aiche Journal, 2000. **46**(3): p. 529-539.
14. S.M. Iveson and J.D. Litster, *Growth regime map for liquid-bound granules.* AIChE Journal, 1998. **44**(7): p. 1510-1518.
15. A.D. Salman, et al., *Breakage in Granulation*, in *Handbook of Powder Technology*, A.D. Salman, M.J. Hounslow, and J.P.K. Seville, Editors. 2007, Elsevier Science B.V. p. 979-1040.
16. L.X. Liu, R. Smith, and J.D. Litster, *Wet granule breakage in a breakage only high-hear mixer: Effect of formulation properties on breakage behaviour.* Powder Technology, 2009. **189**(2): p. 158-164.
17. R.M. Smith, L.A.X. Liu, and J.D. Litster, *Breakage of drop nucleated granules in a breakage only high shear mixer.* Chemical Engineering Science, 2010. **65**(21): p. 5651-5657.
18. S.M. Iveson and J.D. Litster, *Fundamental studies of granule consolidation - Part 2. Quantifying the effects of particle and binder properties.* Powder Technology, 1998. **99**(3): p. 243-250.
19. F. Stepanek and M.A. Ansari, *Computer simulation of granule microstructure formation.* Chemical Engineering Science, 2005. **60**(14): p. 4019-4029.
20. K.V.S. Sastry and D.W. Fuerstenau, *SIZE DISTRIBUTION OF AGGLOMERATES IN COALESCING DISPERSED PHASE SYSTEMS.* Industrial & Engineering Chemistry Fundamentals, 1970. **9**(1): p. 145-149.

21. F. Gelbard and J.H. Seinfeld, *Numerical solution of the dynamic equation for particulate systems.* Journal of Computational Physics, 1978. **28**(3): p. 357-375.

22. M.J. Hounslow, R.L. Ryall, and V.R. Marshall, *A DISCRETIZED POPULATION BALANCE FOR NUCLEATION, GROWTH, AND AGGREGATION.* AIChE Journal, 1988. **34**(11): p. 1821-1832.

23. P. Marchal, et al., *CRYSTALLIZATION AND PRECIPITATION ENGINEERING .1. AN EFFICIENT METHOD FOR SOLVING POPULATION BALANCE IN CRYSTALLIZATION WITH AGGLOMERATION.* Chemical Engineering Science, 1988. **43**(1): p. 59-67.

24. S.M. Iveson, *Limitations of one-dimensional population balance models of wet granulation processes.* Powder Technology, 2002. **124**(3): p. 219-229.

25. I.N. Bjorn, et al., *Empirical to mechanistic modelling in high shear granulation.* Chemical Engineering Science, 2005. **60**(14): p. 3795-3803.

26. I.T. Cameron, et al., *Process systems modelling and applications in granulation: A review.* Chemical Engineering Science, 2005. **60**(14): p. 3723-3750.

27. B. Freireich, et al., *Incorporating particle flow information from discrete element simulations in population balance models of mixer-coaters.* Chemical Engineering Science, 2011. **66**(16): p. 3592-3604.

28. J. Bouffard, F. Bertrand, and J. Chaouki, *A multiscale model for the simulation of granulation in rotor-based equipment.* Chemical Engineering Science, 2012. **81**: p. 106-117.

29. M. Sen and R. Ramachandran, *A multi-dimensional population balance model approach to continuous powder mixing processes.* Advanced Powder Technology, 2013. **24**(1): p. 51-59.

30. M.J. Hounslow, M. Oullion, and G.K. Reynolds, *Kinetic models for granule nucleation by the immersion mechanism.* Powder Technology, 2009. **189**(2): p. 177-189.

31. K. Pitt, et al., *Kinetics of immersion nucleation driven by surface tension.* Submitted to Powder Technology (2018).

32. D.M. Parikh and M. Mogavero, *Batch Fluid Bed Granulation*, in *Handbook of Pharmaceutical Granulation Theory*, D.M. Parikh, Editor. 2005, Taylor & Francis Group, LLC: Boca Raton.

33. E.I. Keleb, et al., *Continuous twin screw extrusion for the wet granulation of lactose.* International Journal of Pharmaceutics, 2002. **239**(1-2): p. 69-80.

34. R.M. Dhenge, et al., *Twin screw wet granulation: Effect of powder feed rate.* Advanced Powder Technology, 2011. **22**(2): p. 162-166.

35. A.S. El Hagrasy and J.D. Litster, *Granulation Rate Processes in the Kneading Elements of a Twin Screw Granulator.* AIChE Journal, 2013. **59**(11): p. 4100-4115.

36. C. Vervaet and J.P. Remon, *Continuous granulation in the pharmaceutical industry.* Chemical Engineering Science, 2005. **60**(14): p. 3949-3957.

37. T. Chirkot and C. Propst, *Low-Shear Granulation*, in *Handbook of Pharmaceutical Granulation Theory*, D.M. Parikh, Editor. 2005, Taylor & Francis Group, LLC: Boca Raton.

38. R. Gokhale, Y. Sun, and A.J. Shukla, *High-Shear Granulation*, in *Handbook of Pharmaceutical Granulation Theory*, D.M. Parikh, Editor. 2005, Taylor & Francis Group, LLC: Boca Raton.

39. M.A. Jarvinen, et al., *Comparison of a continuous ring layer wet granulation process with batch high shear and fluidized bed granulation processes.* Powder Technology, 2015. **275**: p. 113-120.

40. H.N. Emady, et al., *Granule formation mechanisms and morphology from single drop impact on powder beds.* Powder Technology, 2011. **212**(1): p. 69-79.

41. H.R. Charles-Williams, et al., *Granule nucleation and growth: Competing drop spreading and infiltration processes.* Powder Technology, 2011. **206**(1-2): p. 63-71.

42. K.P. Hapgood and B. Khanmohammadi, *Granulation of hydrophobic powders.* Powder Technology, 2009. **189**(2): p. 253-262.

43. K. van den Dries and H. Vromans, *Quantitative proof of liquid penetration-involved granule formation in a high shear mixer.* Powder Technology, 2009. **189**(2): p. 165-171.

44. W.I.J. Kariuki, et al., *Distribution nucleation: Quantifying liquid distribution on the particle surface using the dimensionless particle coating number.* Chemical Engineering Science, 2013. **92**: p. 134-145.

45. J.D. Litster, et al., *Liquid distribution in wet granulation: dimensionless spray flux.* Powder Technology, 2001. **114**(1-3): p. 32-39.

46. W.J. Wildeboer, et al., *A novel nucleation apparatus for regime separated granulation.* Powder Technology, 2007. **171**(2): p. 96-105.

47. B.J. Ennis, *Theory of Granulation: An Engineering Perspective*, in *Handbook of Pharmaceutical Granulation Theory*, D.M. Parikh, Editor. 2005, Taylor & Francis Group, LLC: Boca Raton.

48. B.J. Ennis, G. Tardos, and R. Pfeffer, *A MICROLEVEL-BASED CHARACTERIZATION OF GRANULATION PHENOMENA.* Powder Technology, 1991. **65**(1-3): p. 257-272.

49. S.M. Iveson, et al., *Growth regime map for liquid-bound granules: further development and experimental validation.* Powder Technology, 2001. **117**(1-2): p. 83-97.

50. C.E. Capes and G.C. Danckwerts, *Granule formation by the agglomeration of damp powders. Part I: The mechanism of granule growth.* TRANS. INSTN CHEM. ENGRS., 1965. **43**.

51. F. Hoornaert, et al., *Agglomeration behaviour of powders in a Lodige mixer granulator.* Powder Technology, 1998. **96**(2): p. 116-128.

52. P.A.L. Wauters, et al., *Growth and compaction behaviour of copper concentrate granules in a rotating drum.* Powder Technology, 2002. **124**(3): p. 230-237.

53. R. Maxim, et al., *Modelling effects of processing parameters on granule porosity in high-shear granulation.* Granular Matter, 2004. **6**(2-3): p. 131-135.

54. W.D. Tu, et al., *Exploring the regime map for high-shear mixer granulation.* Chemical Engineering Journal, 2009. **145**(3): p. 505-513.

55. K.P. Hapgood, et al., *Drop penetration into porous powder beds.* Journal of Colloid and Interface Science, 2002. **253**(2): p. 353-366.

56. K. van den Dries, et al., *Granule breakage phenomena in a high shear mixer; influence of process and formulation variables and consequences on granule homogeneity.* Powder Technology, 2003. **133**(1-3): p. 228-236.

57. S. Antonyuk, et al., *Breakage behaviour of spherical granulates by compression.* Chemical Engineering Science, 2005. **60**(14): p. 4031-4044.

58. X. Pepin, et al., *Hardness of moist agglomerates in relation to interparticle friction, granule liquid content and nature.* Powder Technology, 2001. **117**(1-2): p. 123-138.

59. S.M. Iveson, N.W. Page, and J.D. Litster, *The importance of wet-powder dynamic mechanical properties in understanding granulation.* Powder Technology, 2003. **130**(1-3): p. 97-101.

60. S. Antonyuk, et al., *Impact breakage of spherical granules: Experimental study and DEM simulation.* Chemical Engineering and Processing, 2006. **45**(10): p. 838-856.

61. S.M. Iveson, J.A. Beathe, and N.W. Page, *The dynamic strength of partially saturated powder compacts: the effect of liquid properties.* Powder Technology, 2002. **127**(2): p. 149-161.

62. S.M. Iveson and N.W. Page, *Dynamic strength of liquid-bound granular materials: The effect of particle size and shape.* Powder Technology, 2005. **152**(1-3): p. 79-89.

63. R.M. Smith and J.D. Litster, *Examining the failure modes of wet granular materials using dynamic diametrical compression.* Powder Technology, 2012. **224**: p. 189-195.

64. T. Abberger, *Population Balance Modelling of Granulation*, in *Handbook of Powder Technology*, A.D. Salman, M.J. Hounslow, and J.P.K. Seville, Editors. 2007, Elsevier Science B.V. p. 979-1040.

65. M.J. Hounslow, *The population balance as a tool for understanding particle rate processes.* Kona Powder and Particle Journal, 1998. **16**: p. 179-193.

66. A. Kumar, et al., *Model-based analysis of high shear wet granulation from batch to continuous processes in pharmaceutical production - A critical review.* European Journal of Pharmaceutics and Biopharmaceutics, 2013. **85**(3): p. 814-832.

67. C.F.W. Sanders, et al., *Development of a predictive high-shear granulation model.* Powder Technology, 2003. **138**(1): p. 18-24.

68. D. Verkoeijen, et al., *Population balances for particulate processes - a volume approach.* Chemical Engineering Science, 2002. **57**(12): p. 2287-2303.

69. A. Darelius, et al., *A volume-based multi-dimensional population balance approach for modelling high shear granulation.* Chemical Engineering Science, 2006. **61**(8): p. 2482-2493.

70. M.J. Hounslow, J.M.K. Pearson, and T. Instone, *Tracer studies of high-shear granulation: II. Population balance modeling.* AIChE Journal, 2001. **47**(9): p. 1984-1999.

71. C.A. Biggs, et al., *Coupling granule properties and granulation rates in high-shear granulation.* Powder Technology, 2003. **130**(1-3): p. 162-168.

72. D. Barrasso and R. Ramachandran, *A comparison of model order reduction techniques for a four-dimensional population balance model describing multi-component wet granulation processes.* Chemical Engineering Science, 2012. **80**: p. 380-392.

73. A. Chaudhury, I. Oseledets, and R. Ramachandran, *A computationally efficient technique for the solution of multi-dimensional PBMs of granulation via tensor decomposition.* Computers & Chemical Engineering, 2014. **61**: p. 234-244.

74. C.L. Marshall, P. Rajniak, and T. Matsoukas, *Numerical simulations of two-component granulation: Comparison of three methods.* Chemical Engineering Research & Design, 2011. **89**(5A): p. 545-552.

75. S. Kumar and D. Ramkrishna, *On the solution of population balance equations by discretization .1. A fixed pivot technique.* Chemical Engineering Science, 1996. **51**(8): p. 1311-1332.

76. S. Kumar and D. Ramkrishna, *On the solution of population balance equations by discretization .2. A moving pivot technique.* Chemical Engineering Science, 1996. **51**(8): p. 1333-1342.

77. J. Kumar, et al., *Improved accuracy and convergence of discretized population balance for aggregation: The cell average technique.* Chemical Engineering Science, 2006. **61**(10): p. 3327-3342.

78. S. Kumar and D. Ramkrishna, *On the solution of population balance equations by discretization - III. Nucleation, growth and aggregation of particles.* Chemical Engineering Science, 1997. **52**(24): p. 4659-4679.

79.   J. Chakraborty and S. Kumar, *A new framework for solution of multidimensional population balance equations.* Chemical Engineering Science, 2007. **62**(15): p. 4112-4125.

80.   I. Nopens, D. Beheydt, and P.A. Vanrolleghem, *Comparison and pitfalls of different discretised solution methods for population balance models: a simulation study.* Computers & Chemical Engineering, 2005. **29**(2): p. 367-377.

81.   J. Kumar, et al., *An efficient numerical technique for solving population balance equation involving aggregation, breakage, growth and nucleation.* Powder Technology, 2008. **182**(1): p. 81-104.

82.   J. Kumar, et al., *The cell average technique for solving multi-dimensional aggregation population balance equations.* Computers & Chemical Engineering, 2008. **32**(8): p. 1810-1830.

83.   A. Chaudhury, et al., *An extended cell-average technique for a multi-dimensional population balance of granulation describing aggregation and breakage.* Advanced Powder Technology, 2013. **24**(6): p. 962-971.

84.   D. Bertin, et al., *Population balance discretization for growth, attrition, aggregation, breakage and nucleation.* Computers & Chemical Engineering, 2016. **84**: p. 132-150.

85.   F. Filbet and P. Laurencot, *Numerical simulation of the Smoluchowski coagulation equation.* Siam Journal on Scientific Computing, 2004. **25**(6): p. 2004-2028.

86.   S. Qamar and G. Warnecke, *Solving population balance equations for two-component aggregation by a finite volume scheme.* Chemical Engineering Science, 2007. **62**(3): p. 679-693.

87.   S. Qamar and G. Warnecke, *Numerical solution of population balance equations for nucleation, growth and aggregation processes.* Computers & Chemical Engineering, 2007. **31**(12): p. 1576-1589.

88.   C.D. Immanuel and F.J. Doyle, *Computationally efficient solution of population balance models incorporating nucleation, growth and coagulation: application to emulsion polymerization.* Chemical Engineering Science, 2003. **58**(16): p. 3681-3698.

89.   C.D. Immanuel and F.J. Doyle, *Solution technique for a multi-dimensional population balance model describing granulation processes.* Powder Technology, 2005. **156**(2-3): p. 213-225.

90.   M.A. Pinto, C.D. Immanuel, and F.J. Doyle, *A feasible solution technique for higher-dimensional population balance models.* Computers & Chemical Engineering, 2007. **31**(10): p. 1242-1256.

91.   J.M.H. Poon, et al., *A three-dimensional population balance model of granulation with a mechanistic representation of the nucleation and aggregation phenomena.* Chemical Engineering Science, 2008. **63**(5): p. 1315-1329.

92.   J.M.H. Poon, et al., *Experimental validation studies on a multi-dimensional and multi-scale population balance model of batch granulation.* Chemical Engineering Science, 2009. **64**(4): p. 775-786.

93.   J.A. Gantt and E.P. Gatzke, *A stochastic technique for multidimensional granulation modeling.* AIChE Journal, 2006. **52**(9): p. 3067-3077.

94.   A. Braumann, et al., *Modelling and validation of granulation with heterogeneous binder dispersion and chemical reaction.* Chemical Engineering Science, 2007. **62**(17): p. 4717-4728.

95.   A. Braumann, M. Kraft, and W. Wagner, *Numerical study of a stochastic particle algorithm solving a multidimensional population balance model for high shear granulation.* Journal of Computational Physics, 2010. **229**(20): p. 7672-7691.

96. R.I.A. Patterson, W. Wagner, and M. Kraft, *Stochastic weighted particle methods for population balance equations.* Journal of Computational Physics, 2011. **230**(19): p. 7456-7472.

97. K.F. Lee, et al., *A multi-compartment population balance model for high shear granulation.* Computers & Chemical Engineering, 2015. **75**: p. 1-13.

98. K.F. Lee, et al., *Stochastic weighted particle methods for population balance equations with coagulation, fragmentation and spatial inhomogeneity.* Journal of Computational Physics, 2015. **303**: p. 1-18.

99. X. Yu, M.J. Hounslow, and G.K. Reynolds, *Accuracy and optimal sampling in Monte Carlo solution of population balance equations.* AIChE Journal, 2015. **61**(8): p. 2394-2402.

100. R. McGraw, *Description of aerosol dynamics by the quadrature method of moments.* Aerosol Science and Technology, 1997. **27**(2): p. 255-265.

101. V. Alopaeus, M. Laakkonen, and J. Aittamaa, *Solution of population balances with breakage and agglomeration by high-order moment-conserving method of classes.* Chemical Engineering Science, 2006. **61**(20): p. 6732-6752.

102. P. Rajniak, et al., *A combined experimental and computational study of wet granulation in a Wurster fluid bed granulator.* Powder Technology, 2009. **189**(2): p. 190-201.

103. A. Majumder, et al., *Lattice Boltzmann method for population balance equations with simultaneous growth, nucleation, aggregation and breakage.* Chemical Engineering Science, 2012. **69**(1): p. 316-328.

104. A. Majumder, et al., *Lattice Boltzmann method for multi-dimensional population balance models in crystallization.* Chemical Engineering Science, 2012. **70**: p. 121-134.

105. Y. Liu and I.T. Cameron, *A new wavelet-based method for the solution of the population balance equation.* Chemical Engineering Science, 2001. **56**(18): p. 5283-5294.

106. J. Utomo, et al. *Numerical studies of wavelet-based method as an alternative solution for population balance problems in a batch crystalliser.* in *ADCHEM 2009.* 2009. Koç University: Elsevier Ltd.

107. R. Ramachandran, et al., *A mechanistic model for breakage in population balances of granulation: Theoretical kernel development and experimental validation.* Chemical Engineering Research & Design, 2009. **87**(4A): p. 598-614.

108. K. Lee, et al., *Integrated run-to-run and on-line model-based control of particle size distribution for a semi-batch precipitation reactor.* Computers & Chemical Engineering, 2002. **26**(7-8): p. 1117-1131.

109. A.A. Adetayo, et al., *POPULATION BALANCE MODELING OF DRUM GRANULATION OF MATERIALS WITH WIDE SIZE DISTRIBUTION.* Powder Technology, 1995. **82**(1): p. 37-49.

110. A.A. Adetayo and B.J. Ennis, *A new approach to modeling granulation processes for simulation and control purposes.* Powder Technology, 2000. **108**(2-3): p. 202-209.

111. A.A. Adetayo and B.J. Ennis, *Unifying approach to modeling granule coalescence mechanisms.* AIChE Journal, 1997. **43**(4): p. 927-934.

112. L.X. Liu and J.D. Litster, *Population balance modelling of granulation with a physically based coalescence kernel.* Chemical Engineering Science, 2002. **57**(12): p. 2183-2191.

113. A. Darelius, et al., *High shear wet granulation modelling - a mechanistic approach using population balances.* Powder Technology, 2005. **160**(3): p. 209-218.

114. M. Smoluchowski, *Versuch einer matematischen Theorie der Koagulationskinetic kolloider Lösungen.* Zeitschrift für Physikalische Chemie, 1917. **92**: p. 129-168.

115. A. Chaudhury, et al., *A mechanistic population balance model for granulation processes: Effect of process and formulation parameters.* Chemical Engineering Science, 2014. **107**: p. 76-92.

116. D.A. Pohlman and J.D. Litster, *Coalescence model for induction growth behavior in high shear granulation.* Powder Technology, 2015. **270**: p. 435-444.

117. L. Vogel and W. Peukert, *Characterisation of grinding-relevant particle properties by inverting a population balance model.* Particle & Particle Systems Characterization, 2002. **19**(3): p. 149-157.

118. A. Chaudhury, M.E. Armenante, and R. Ramachandran, *Compartment based population balance modeling of a high shear wet granulation process using data analytics.* Chemical Engineering Research & Design, 2015. **95**: p. 211-228.

119. X. Yu, M.J. Hounslow, and G.K. Reynolds, *Representing spray zone with cross flow as a well-mixed compartment in a high shear granulator.* Powder Technology, 2016. **297**: p. 429-437.

120. D. Barrasso and R. Ramachandran, *Qualitative Assessment of a Multi-Scale, Compartmental PBM-DEM Model of a Continuous Twin-Screw Wet Granulation Process.* Journal of Pharmaceutical Innovation, 2016. **11**(3): p. 231-249.

121. J.A. Gantt and E.P. Gatzke, *High-shear granulation modeling using a discrete element simulation approach.* Powder Technology, 2005. **156**(2-3): p. 195-212.

122. J.A. Gantt, et al., *Determination of coalescence kernels for high-shear granulation using DEM simulations.* Powder Technology, 2006. **170**(2): p. 53-63.

123. D. Barrasso and R. Ramachandran, *Multi-scale modeling of granulation processes: Bi-directional coupling of PBM with DEM via collision frequencies.* Chemical Engineering Research & Design, 2015. **93**: p. 304-317.

124. D. Barrasso, et al., *A multi-scale, mechanistic model of a wet granulation process using a novel bi-directional PBM-DEM coupling algorithm.* Chemical Engineering Science, 2015. **123**: p. 500-513.

125. T. Kulju, et al., *Modeling continuous high-shear wet granulation with DEM-PB.* Chemical Engineering Science, 2016. **142**: p. 190-200.

126. D. Barrasso, A. Tamrakar, and R. Ramachandran, *A reduced order PBM-ANN model of a multi-scale PBM-DEM description of a wet granulation process.* Chemical Engineering Science, 2014. **119**: p. 319-329.

127. H.M. Yu, et al., *Prediction of the Particle Size Distribution Parameters in a High Shear Granulation Process Using a Key Parameter Definition Combined Artificial Neural Network Model.* Industrial & Engineering Chemistry Research, 2015. **54**(43): p. 10825-10834.

128. W.H. AlAlaween, M. Mahfouf, and A.D. Salman, *Predictive modelling of the granulation process using a systems-engineering approach.* Powder Technology, 2016. **302**: p. 265-274.

129. H.S. Tan, et al., *Building population balance model for fluidized bed melt granulation: lessons from kinetic theory of granular flow.* Powder Technology, 2004. **142**(2-3): p. 103-109.

130. H.S. Tan, et al., *Population balance modelling of fluidized bed melt granulation - An overview.* Chemical Engineering Research & Design, 2005. **83**(A7): p. 871-880.

131. M. Khalilitehrani, et al., *Continuum modeling of multi-regime particle flows in high-shear mixing.* Powder Technology, 2015. **280**: p. 67-71.

132. A.C.S. Lee and P.E. Sojka, *Drop Impact and Agglomeration Under Static Powder Bed Conditions.* AIChE Journal, 2012. **58**(1): p. 79-86.

133. L.X. Liu, et al., *A nuclei size distribution model including nuclei breakage.* Chemical Engineering Science, 2013. **86**: p. 19-24.

134. K.P. Hapgood, M.X.L. Tan, and D.W.Y. Chow, *A method to predict nuclei size distributions for use in models of wet granulation.* Advanced Powder Technology, 2009. **20**(4): p. 293-297.

135. K. Washino, et al., *A new capillary force model implemented in micro-scale CFD-DEM coupling for wet granulation.* Chemical Engineering Science, 2013. **93**: p. 197-205.

136. I. Talu, G.I. Tardos, and M.I. Khan, *Computer simulation of wet granulation.* Powder Technology, 2000. **110**(1-2): p. 59-75.

137. R. Plank, et al., *Quantifying liquid coverage and powder flux in high-shear granulators.* Powder Technology, 2003. **134**(3): p. 223-234.

138. P.R. Mort, *Scale-up and control of binder agglomeration processes - Flow and stress fields.* Powder Technology, 2009. **189**(2): p. 313-317.

139. H. Nakamura, H. Fujii, and S. Watano, *Scale-up of high shear mixer-granulator based on discrete element analysis.* Powder Technology, 2013. **236**: p. 149-156.

140. M. Bardin, P.C. Knight, and J.P.K. Seville, *On control of particle size distribution in granulation using high-shear mixers.* Powder Technology, 2004. **140**(3): p. 169-175.

141. S. Forrest, et al., *Flow patterns in granulating systems.* Powder Technology, 2003. **130**(1-3): p. 91-96.

142. Y. Saito, et al., *A new approach to high-shear mixer granulation using positron emission particle tracking.* Chemical Engineering Science, 2011. **66**(4): p. 563-569.

143. A.M. Nilpawar, et al., *Surface velocity measurement in a high shear mixer.* Chemical Engineering Science, 2006. **61**(13): p. 4172-4178.

144. A. Darelius, et al., *Measurement of the velocity field and frictional properties of wet masses in a high shear mixer.* Chemical Engineering Science, 2007. **62**(9): p. 2366-2374.

145. V. Rimpilainen, et al., *Electrical capacitance tomography as a monitoring tool for high-shear mixing and granulation.* Chemical Engineering Science, 2011. **66**(18): p. 4090-4100.

146. S. Watano, et al., *A fuzzy control system of high shear granulation using image processing.* Powder Technology, 2001. **115**(2): p. 124-130.

147. V. Wenzel and H. Nirschl, *Validation of an inline particle probe in a high-shear mixer for particle size determination.* Powder Technology, 2015. **269**: p. 178-184.

148. P.C. Knight, *AN INVESTIGATION OF THE KINETICS OF GRANULATION USING A HIGH-SHEAR MIXER.* Powder Technology, 1993. **77**(2): p. 159-169.

149. S. Watano, T. Tanaka, and K. Miyanami, *A METHOD FOR PROCESS MONITORING AND DETERMINATION OF OPERATIONAL END-POINT BY FREQUENCY-ANALYSIS OF POWER-CONSUMPTION IN AGITATION GRANULATION.* Advanced Powder Technology, 1995. **6**(2): p. 91-102.

150. A. Goldszal and J. Bousquet, *Wet agglomeration of powders: from physics toward process optimization.* Powder Technology, 2001. **117**(3): p. 221-231.

151. *A basic guide to particle characterization.* 2012, Malvern Instruments Limited.

152. G. Paroline, *Basics of applied rheology.* 2016, Anton Paar USA.

153. Y. Yuan and T.R. Lee, *Chapter 1 - Contact Angle and Wetting Properties*, in *Surface Science Techniques*, G. Bracco and B. Holst, Editors. 2013, Springer: Berlin, Heidelberg.

154. R.P. Woodward, *Surface tension measurements using the drop shape method.* First Ten Angstroms.

155. S.J.R. Simons, *Liquid Bridges in Granules*, in *Handbook of Powder Technology*, A.D. Salman, M.J. Hounslow, and J.P.K. Seville, Editors. 2007, Elsevier Science B.V. p. 1257-1316.

156. L. Farber, G. Tardos, and J.N. Michaels, *Use of X-ray tomography to study the porosity and morphology of granules.* Powder Technology, 2003. **132**(1): p. 57-63.

157. P.A.L. Wauters, et al., *Liquid distribution as a means to describing the granule growth mechanism.* Powder Technology, 2002. **123**(2-3): p. 166-177.

158. P.C. Knight, et al., *An investigation of the effects on agglomeration of changing the speed of a mechanical mixer.* Powder Technology, 2000. **110**(3): p. 204-209.

159. A.H.B. Shukri, *The effect of material properties on the kinetics of granule nucleation*, in *Chemical and Biological Engineering*. 2017, University of Sheffield: Sheffield.